AEROSPACE ENGINEERING

MARCH, 2018

Master Thesis Report

Analysis of an Over the Wing Based Distributed Propulsion System

Arash Khajehzadeh

TU Delft Delft University of Technology

"The greatest enemy of knowledge is not ignorance, it is the illusion of knowledge"

-Stephen Hawking

Analysis of an Over the Wing Based Distributed Propulsion System

A Numerical Study

Master of Science Thesis

For obtaining the degree of Master of Science in Aerospace Engineering

(Flight Performance and Propulsion) at Delft University of Technology

Arash Khajehzadeh

March 2018

Thesis committee members

Prof. L.L.M. Veldhuis +31 15 27 82009 L.L.M.Veldhuis@tudelft.nl Professor at Aerospace Faculty of Delft University of Technology	Dr. S.J. Hulshoff +31 15 27 81538 S.J.Hulshoff@tudelft.nl Assistant Professor at Aerodynamics Faculty of Delft University of Technology	Dr. M. Voskuijl +31 15 27 83992 M.Voskuijl@tudelft.nl Assistant Professor at Aerospace Faculty of Delft University of Technology

DELFT UNIVERSITY OF TECHNOLOGY

AEROSPACE FACULTY

The undersigned, hereby, certify that they have read and recommended to the faculty of Aerospace Engineering of Delft University of Technology for acceptance of the thesis entitled "*Analysis of an Over the Wing based Distributed Propulsion System*" by Arash Khajehzadeh in fulfillment of the requirements for the degree of Master of Science.

Date: March 2018

X

Prof. Dr. Ir. L.L.M Veldhuis

X

Dr. S. J. Hulshoff

X

Dr. M. Voskuijl

Table of Contents

Acknowledgment

I would like to express my special thanks and gratitude to my supervisors Prof. Leo Veldhuis and Dr. Steven Hulshoff, who gave me the opportunity to do this project. I am thankful for their guidance and teachings that helped me to develop my engineering skills and finalize this project successfully.

I would like to thank my parents, Roya Nikfam and Morteza Khajehzadeh, for making it possible for me to study abroad. They have given me everything during the past eight years so that I can pursue my dreams of building a bright future. I would like them to know that I will always remember and appreciate their effort and I will do anything not to waste the opportunity that they have provided me.

I would like to thank Nigora Atta that designed the cover page of this report. She also helped me to keep my moral high during challenging times, and for that, I am forever grateful.

Arash Khajehzadeh

Abstract

The purpose of this report is to investigate propeller wing interaction of an over the wing (OTW) based distributed propulsion (DP) system with the addition of a secondary wing. This research explored the opportunities that OTW configuration provides to DP concept, such as improving the lifting performance of system by inducing the flow over the upper surface of wing. Secondary wing is oriented in a biplane configuration above propeller and intends to improve propeller's performance by decreasing propeller's inflow velocity. This research aimed to investigate the influence of shape and position modification on the system's aerodynamic performance and overall propulsive efficiency. The influence of spacing between the wings, position of propeller, secondary wing's angle of attack and secondary wing's initial lift coefficient on aerodynamic performance and overall propulsive efficiency of DP system was investigated in this project.

The analysis of this particular configuration was performed with the help of Euler calculations. Eliminating viscous effects from the analysis, reduced the demanded computational cost of this study and could help this research to perform a broader investigation. The influence of isothermal flow condition on Euler calculation was examined to reduce the computational cost of optimization study; This study showed that the drag coefficient of system is sensitive to this assumption and that only by simulating the initial and final points of the optimization study with adiabatic flow condition, the use of isothermal flow condition could be justified. The secondary wing's shape was optimized to study the influence of its shape variation on the system's aerodynamic performance. The first optimization study aimed to decrease the drag coefficient of system, and as a result, overall propulsive efficiency of was improved. The second optimization study aimed to improve the lifting performance of system. As a result, the drag coefficient of system significantly increased, however, the overall propulsive efficiency was again improved. The flow decelerated between main wing and secondary wing since the lifting performance of secondary wing improved, which increased the propeller's thrust according to blade element method (BEM) calculation.

List of Figures

List of Tables

NOMENCLATURE

Latin Symbols

A ..... Area

C_D ..... Drag coefficient

C_{D_0} ..... Initial drag coefficient

C_{L_0} ..... Initial lift coefficient

C_L ..... Lift coefficient

C_P ..... Pressure coefficient

C_f ..... Friction coefficient

C_{main} ..... Chord length of main wing

C_q ..... Torque coefficient

C_{sec} ..... Chord length of secondary wing

C_t ..... Thrust coefficient

D ..... Drag force

$D(r)$ ..... Local diameter of propeller

D_0 ..... Initial design's drag force

D_P ..... Propeller's diameter

E_T ..... Total energy

F_x ..... Axial resultant force acting on system

$F_{x_{main}}$ ..... Axial resultant force acting on main wing

$F_{x_{sec}}$ ..... Axial resultant force acting on secondary wing

$F_{y_{main}}$ ..... Normal resultant force acting on main wing

$F_{y_{sec}}$ ..... Normal resultant force acting on secondary wing

l ..... Length

L ..... Lift force

L_0 ..... Initial design's lift force

L/D ..... Lift to drag ratio

M ..... Mach number

n ..... Rotational speed of the propeller [1/s]

P ..... Static pressure

P_o ..... Order of convergence

P_t ..... Total pressure

P_r ..... Prandtl number

$P_{r_{h=0}}$ ..... Value of a parameter at zero grid spacing

q ..... Dynamic pressure

$Q(r)$ ..... Propeller's torque as a function of radius

r ..... Mesh refinement factor

R ..... Gas constant

Re ..... Reynolds number

s_{main} ..... Spacing between main wing's surface and propeller's tip

S_{ref} ..... Reference planform area of wing

s_{sec} ..... Spacing between secondary wing's surface and propeller's tip

t ..... Time

T ..... Static temperature

t_P ..... Actuator disc's thickness

$T(r)$ ..... Propeller's thrust as a function of radius

T_t ..... Total temperature

u ..... Velocity in x-direction

U_j ..... Jet velocity

v ..... Velocity in y-direction

V ..... Volume

V_∞ ..... Freestream velocity

V_{in} ..... Inlet velocity

w ..... Velocity in z-direction

x_p ..... Chordwise position of propeller

$y_{P_{main}}$ ..... Distance from propeller's tip to main wing's chord line

$y_{P_{sec}}$ ..... Distance from propeller's tip to secondary wing's chord line

y_s ..... spacing between secondary wing's chord line and main wing's chord line

z ..... Height

Greek Symbols

Δt ..... Time step

Δx ..... Cell length

η_{pp} ..... Overall propulsive efficiency

η_{pp_0} ..... Initial design's overall propulsive efficiency

η_{prop} ..... Propeller's efficiency

η_{prop_0} ..... Initial design's propeller's efficiency

γ ..... Heat ratio

μ ..... Kinematic viscosity

ν ..... Dynamic viscosity

π ..... The number Pi

ρ ..... Density

τ_{ij} ..... Component of stress tensor

Abbreviations

AR ..... Advance ratio

BLI ..... Boundary Layer Ingestion

BTW ..... Below The Wing

BWB ..... Blended Wing Body

CEL ..... CFX Expression Language

CFD ..... Computational Fluid Dynamics

CFL ..... Courant-Friedrichs-Lewy number

CST ..... Parametric Geometry Presentation Method

DP ..... Distributed Propulsion

FPR ..... Fan Pressure Ratio

HLD ..... High Lift Device

LES ..... Large Eddy Simulations

MDF ..... Main Distributed Frame

MDO ..... Multidisciplinary Design Optimization

N+i..... Specifying the aircraft generation

NASA ..... The National Aeronautics and Space Administration

OTW ..... Over the wing

RANS ..... Reynold Averaged Navier-Stokes

RPM ..... Revolutions Per Minute

TeDP ..... Turbo-electric Distributed Propulsion

VLM ..... Vortex Lattice Method

1 Introduction

Every aircraft manufacturer is facing significant competition in the aviation industry. Many companies invest in scientific studies to improve the efficiency of their products in order to remain competitive against their rivals. Reducing cost and negative environmental impacts of airplanes are the main factors that attract more clients and raise the stakes in the market. In October of 2011, NASA published a review of propulsion technologies for subsonic vehicle concepts [Ref.1]. In this report, experts from Glenn Research Center in Cleveland (Ohio) explained their goals and milestones to improve fuel burn, noise, and emission reduction for new generation of aircraft, which could be viable in 2035. "N+i" is a term used to describe the sequence of future generations of airplanes, where "N" stands for the current generation of aircraft (2011) and "i" represents a specific generation of aircraft beyond the current generation "N" [Ref.1]. Figure [1] shows, goals and objectives set by NASA for N+1 (2015), N+2 (2020) and N+3 (2035) generations of aircraft. As it is mentioned in Figure [1], N+3 goals include the fuel burn performance of aircraft, which should be lowered by 70% in 2035 with respect to the current generation "N" (2011). Such significant improvements require researchers to explore and implement different concepts that could significantly increase aerodynamic performance as well as propulsive efficiency of planes.

CORNERS OF THE TRADE SPACE	N+1 (2015)*** Technology Benefits Relative to a Single Aisle Reference Configuration	N+2 (2020)*** Technology Benefits Relative to a Large Twin Aisle Reference Configuration	N+3 (2025)*** Technology Benefits
Noise (cum below Stage 4)	- 32 dB	- 42 dB	- 71 dB
LTO NOx Emissions (below CAEP 6)	-60%	-75%	better than -75%
Performance Aircraft Fuel Burn	-33%**	-50%**	better than -70%
Performance Field Length	-33%	-50%	exploit metroplex* concepts

*** Technology Readiness Level for key technologies = 4-6
** Additional gains may be possible through operational improvements
* Concepts that enable optimal use of runways at multiple airports within the metropolitan areas

Figure 1: NASA N+i goals [Ref.1] (This figure has been adopted for detailed visualization)

During past two decades, many concepts of propulsion have been developed to increase aircraft's efficiency. Exploring advantages and disadvantages of these concepts could help this study to motivate the choice of the model's configuration and investigate its working principles further.

1. Conventional propulsion systems
   1.1. BWB configuration (BLI)
   1.2. OTW configuration
   1.3. Tractor configuration
   1.4. Pusher configuration
2. Distributed propulsion systems
   2.1. BWB configuration (BLI)
   2.2. OTW configuration
   2.3. Tractor configuration
   2.4. Pusher configuration

Analyzing BWB configuration that benefits from BLI effect is out of this project's scope because flow's viscous effects were ignored in this project (more details in chapter 2.2). However, the publications and studies that isolated viscous effects and considered the influence of DP systems in a BWB configuration were used to motivate the goals of this project.

The abovementioned propulsion systems were categorized based on the number and orientation of engines. Conventional propulsion systems usually make use of two or four engines. However, DP systems usually utilize more than four engines over the wingspan. The current generation of airplanes use a limited number of engines, which could not be integrated into the airframe due to their size. The conventional method of mounting an engine to an aircraft is pylon nacelle configuration. In this setting, the engine is connected by a pylon to either wing or fuselage externally in pusher, tractor or OTW configuration.

Some publications suggest [Ref.2] [Ref.3] [Ref.4] that pylon nacelle configuration is less efficient compared to distributed propulsion systems integrated in the airframe of aircraft. According to Rossow, Godard, Schmitt [Ref.5] and Obert [Ref.2], pylon nacelle configuration suffers from added installation drag due to pylon wing interference and the total lift coefficient of the aircraft decreases compared to a clean wing at a constant incident angle.

According to Ko, Schetz, Manson [Ref.6] and Kim [Ref.7], one of the critical reasons that DP systems could improve the aerodynamic performance of aircraft is that the outflow of engines can fill the wake of a wing uniformly and improve the drag performance of an airplane. As the number of engines in conventional propulsion systems decreases, wake filling becomes more inconsistent and damages the drag performance of aircraft.

1.1 Distributed Propulsion systems

DP systems are array of smaller engines in a row, comparative to conventional engines. This is in contrasts with the limited number of engines in pylon nacelle configurations. Looking at the history and the work of other scientists on DP systems helped this project find the necessary motives for the application of such configurations. The first airplanes that exploited DP systems were not meant to take advantage of this principle as means of reducing fuel consumption. Instead, engineers and designers often added extra propellers to aircraft for a more comfortable and safer take-off and landing by increasing the lifting force with the help of thrust vectoring.

In 1924, Manzel[1] proposed the idea of DP system for airships as means for landing [Ref.8] (Figure [2-A]). Later in 1932, Altieri[2] used propellers on the front and aft of the wing (Figure [2-B]) for a shorter landing runway [Ref.8]. These auxiliary propellers were also meant to increase lift force for low-speed flight conditions. In 1954, Griffith[3] made use of gas turbines instead of propellers, with a master combustion engine and with a number of gas turbine units on an array located on the aircraft's wing [Ref.8] (Figure [2-C]). The main idea behind this design was to make use of thrust vectoring to increase the lift force of the aircraft for shorter take-off and landing runway. In 1964, Reyle[4] introduced an idea (Figure [2-D]) that used gas engines positioned between ducting surfaces and nuclear engines in the engine nacelles [Ref.8]. This concept contributed to power to weight ratio enhancement, but also recognized possible radiation concerns in the event of an

[1] Manzel CW. Propelling mechanism for airships and the like. Serial no. 321,008, United States Patent Office, 1,487,872; 1924.
[2] Altieri A. Auxiliary propeller for aircraft. Serial no. 531,020, United States Patent Office, 1,850,066; 1932.
[3] Griffith AA. Improvements relating to aircraft and aircraft engine installations. United Kingdom Patent, 720,394; 1954.
[4] Reyle W. Aircraft. United Kingdom Patent, 1,066,360; 1967.

aircraft crash. In 1983, Philips[5] presented the idea of solar powered aircraft with a cruciform wing structure (Figure [2-F]) equipped with solar cells [Ref.8]. The propeller's position on the wingtips keeps the solar cells orientation normal to sun's rays. This concept was a giant leap forward in the development of solar airplanes. In 1988, NASA proposed different concepts, one of which was SnAPII (Figure [2-G]). This aircraft made use of fuselage boundary layer ingestion, smart inlet, and nozzle technology. Furthermore, this design utilized the DP principle to eliminate the possibility of total engine failure for either one of the fuselages [Ref.8].

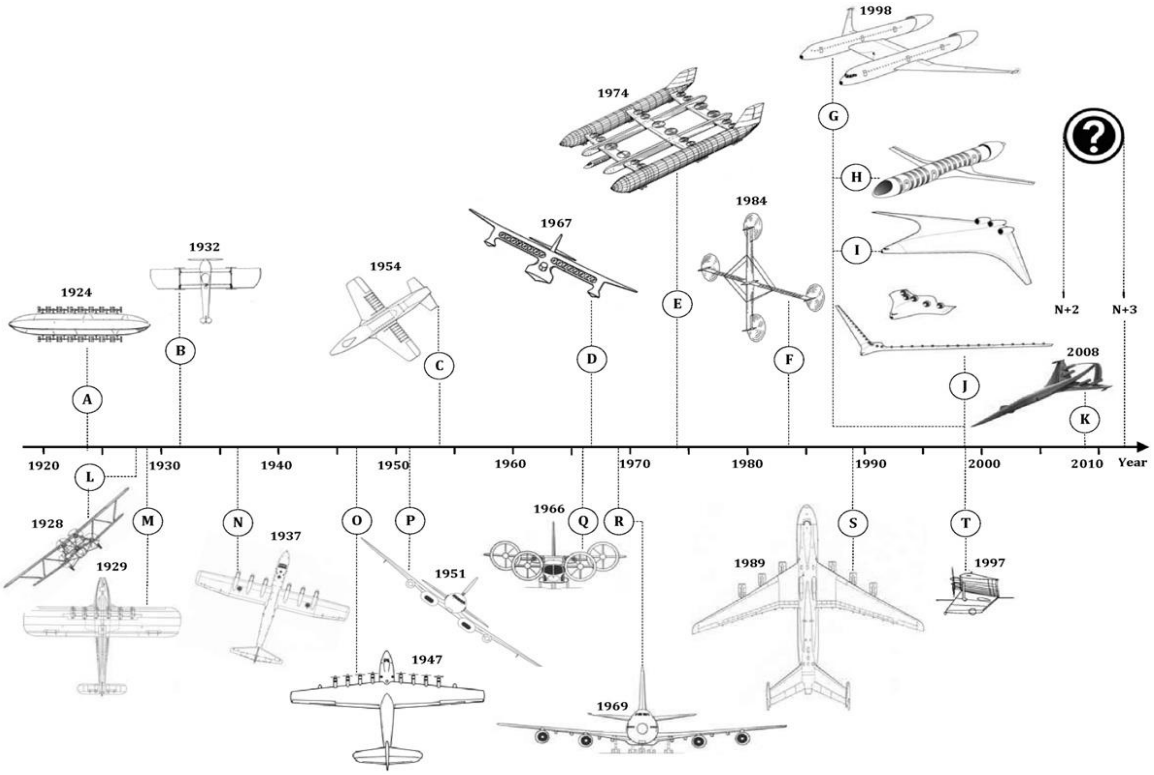

Figure 2: Evolution and Application of Distributed Propulsion system [Ref.8] (This figure has been adopted for detailed visualization)

According to Isyanov, Lukovnikov, and Mirzoyan [Ref.9]: "Application of DP systems on long range airplanes is a new engineering solution, which may allow meeting the future advanced efficiency goals." This study focuses on BLI as well as DP systems, and it is difficult to isolate the inviscid influence of DP on aerodynamic performance. However, this study shows the possibilities and opportunities that DP concept provides.

[5] Phillips WH. Solar powered aircraft. United States Patent Office, 4,415,133; 1983.

Reynolds, Nguyen, Ting, and Urnes [Ref.10] conducted a wind tunnel test on a scaled (200:11) model of the NASA generic transport model, which utilizes two generators per wing with an addition of four fans. According to Reynolds, Nguyen, Ting, and Urnes [Ref.10]: "The flexible wing distributed propulsion aircraft concept was shown to achieve a 4% improvement in lift to drag ratio over a mission profile consisting of a minimum fuel climb, minimum fuel cruise, and continuous descent." It should be noted that the research conducted by Reynolds, Nguyen, Ting, and Urnes [Ref.10] does not include BLI effects on aerodynamic performance of the system. However, this research includes the influence of wing's flexibility (aeroelasticity) and compares the results to a rigid wing to isolate the effect of DP on the overall efficiency. This study conclusively states that DP increased lift to drag ratio of aircraft by at least 3% with a rigid wing depending on the range of aircraft.

Most of the conventional propulsion systems involve utilization of chemical fuels such as kerosene as energy source. However, by reducing engine size and the amount of demanded thrust per engine, DP systems can make the application of electromotors in airplanes possible. Application of electromotors on airplanes can improve the noise, weight (depending on the weight of the cooling system for superconductors) and emission characteristics of the aircraft to meet environmental demands [Ref.3] [Ref.11].

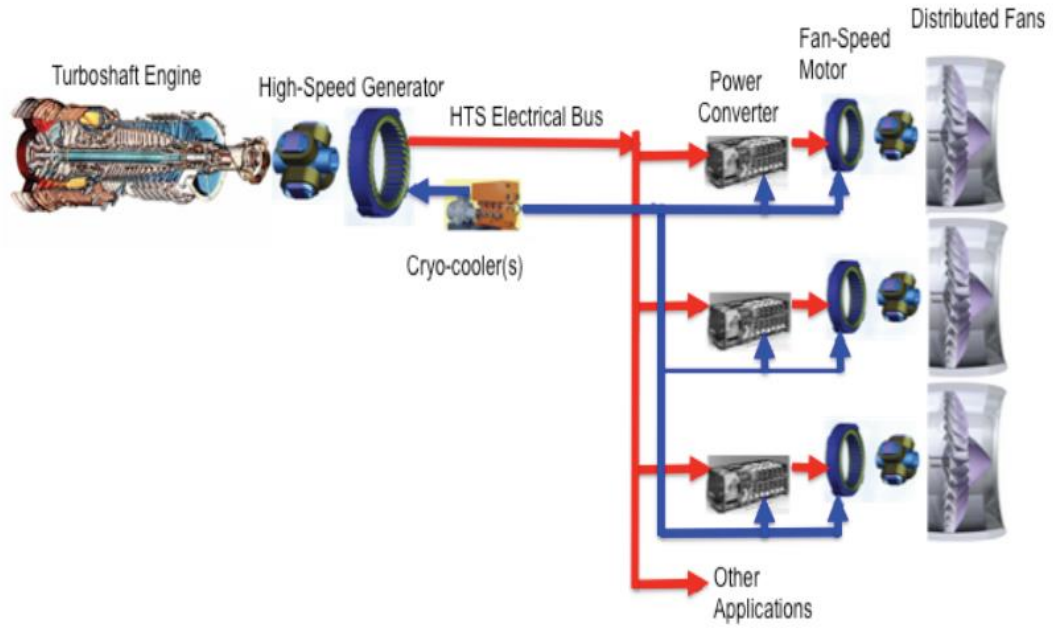

Figure 3: A schematic of turboelectric distributed propulsion system [Ref.3]

According to the work of Kim, Felder, and Tong [Ref.3], implementation of DP systems could reduce energy consumption of N3-X by 70-72% compared to 777-200LR for the same mission depending on the weight of the cooling system needed for the application of superconducting electric motor driving fans. One of the challenges of DP systems is the added weight that limits the efficiency of this principle. However, by successfully implementing the superconducting technology in electrical and propulsion system of N3-X aircraft, it is possible to reduce the weight of the propulsion system compared to 777-200LR and take full advantage of the benefits of this principle.

Table 1: N3-X baseline gross takeoff weight, mission fuel, and energy consumption compared to Boeing 777-200LR class vehicle [Ref.3], BSCCO/Cryocooler and MgB2/LH2 are two different type of cooling systems for the application of the superconducting electromotor driven fans

Superconducting Material / Cooling Method	GTOW - lbm	Mission Fuel Consumption – lbm	Mission Energy Consumption – BTU	Mission energy reduction compared to 777-200LR
777-200LR Class Vehicle	768,000	279,800	5.20E+09	
BSCCO/Cryocooler	514,933	84,992	1.58E+09	70%
MgB_2/LH_2	496,174	76,171	1.47E+09	72%

A numerical study by Felder, Brown, and Kim [Ref.12] shows that the energy consumption of N3-X aircraft with two different propulsion configurations has been obtained and compared, i.e., the conventional pylon nacelle setup and DP configuration both in OTW configuration. This study shows that DP eliminates many installation penalties compared to pylon nacelle configuration. For example, DP system on N3-X aircraft weighs about 25% less than the pylon nacelle configuration on N3-A aircraft according to this paper. Moreover, installation drag penalties of pylon nacelle configuration require N3-A to carry more fuel which increases the maximum take-off weight of aircraft. This study shows that fuel burn could be reduced by up to 20% by only implementing DP system. This fuel burn reduction includes BLI effect, which is not considered in this project. However, 4% fuel burn reduction due to wake filling of DP system in Figure [5] shows the advantage of DP system in this case. Moreover, implementing electromotors is only possible because of DP system. Although it is difficult to separate BLI influence on fuel burn reduction in this study, the contribution of electromotors' application to fuel burn reduction, which is made possible by DP system, should not be overlooked.

Figure 4: on left: N3-X FLOPS Model with distributed propulsion system on right: N3A FLOPS Model with pylon and nacelle configuration [Ref.12] FLOPS: Flight Optimization System Developed by NASA

As Figure [5] shows, the major difference in fuel burn reduction between N3-A and N3-X model is advanced triboelectric distributed propulsion, which was made possible by implementing DP system.

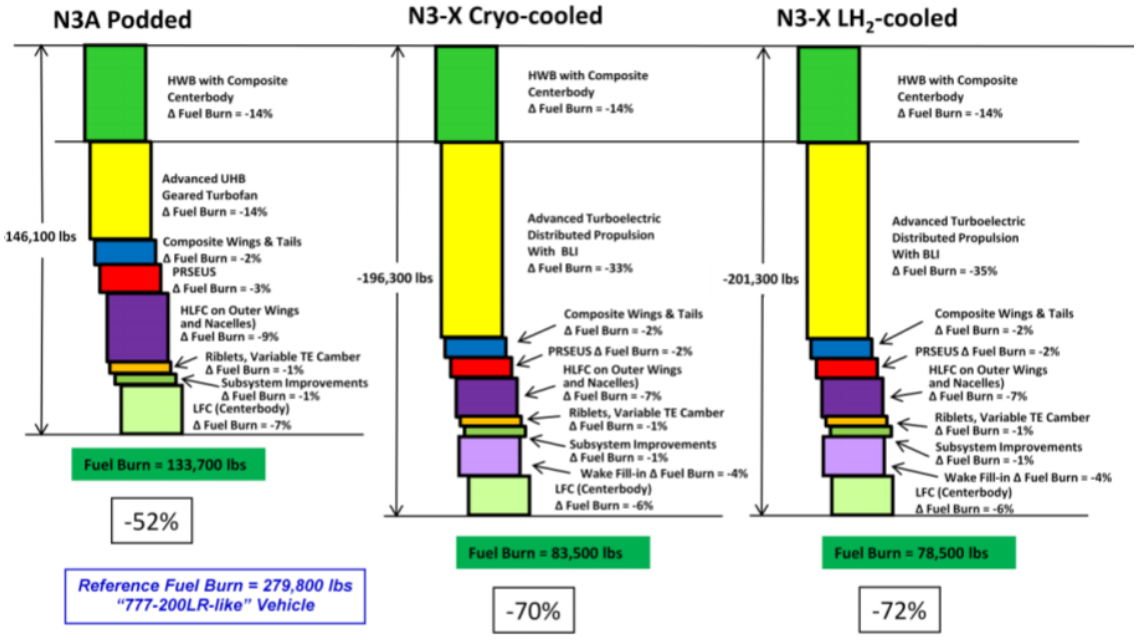

Figure 5: Fuel burn Reduction breakdown N3A: pylon and nacelle configuration, N3X: distributed propulsion system with two different cooling systems [Ref.12], 4% fuel reduction only by filling the wake

Kiner, Raffaelli, Rolt, and Laskaridis [Ref.13] compare the fuel saving of two different propulsion systems, namely pylon nacelle configuration and DP. According to this study, with a wing tube configuration aircraft, distributed propulsion system could achieve 4.1% fuel burn reduction compared to conventional pylon nacelle configuration.

In a following related study [Ref.14], in BWB configuration, 5.3% fuel burn reduction was obtained with the help of DP. According to these two studies [Ref.13]

[Ref.14], principle of DP can reduce fuel burn of an aircraft more than 4.1%, in the case of wing tube configuration, and about 5.3%, in the case of BWB configuration. Due to the technological obstacles (necessary cooling system for superconductors), this principle suffers from extra added weight penalties. The comparison between these two studies could partially separate influence of BLI in BWB configuration from DP system's effects (other than BLI related effects) that reduces fuel burn of aircraft.

Ko, Leifsson, Manson, Schetz, and Grossman [Ref.15] demonstrate the application of Multidisciplinary Design Optimization (MDO) on a BWB transport aircraft with DP system. By optimizing DP system, they could reduce fuel consumption by 5.4%. Moreover, the gross take-off weight of aircraft reduced by 7.8%. Therefore, solely comparing conventional and distributed propulsion configurations cannot reveal the full potential of this concept. Merely altering the propulsion system to create a comparable example does not show the full possibilities that DP can offer. According to Ko, Leifsson, Manson, Schetz, and Grossman [Ref.15], optimizing a design implemented with distributed propulsion can undoubtedly reveal a better perspective of how much this principle can help engineers to achieve a more efficient and greener design to meet nowadays demands.

1.1.1 Wing Propeller Configurations

Reviewing the references shows that the influence of propeller on lifting bodies could not be overlooked. Researchers aim to take advantage of propeller wing interactions to improve aerodynamic performance of aircraft. According to the work and observations of Obert [Ref.2], Veldhuis [Ref.16], and Catalano [Ref.17] on propeller wing interactions, the influence of propeller's slipstream on wing could be directly observed by evaluating the spanwise lift distribution over the wing. Figure [6] shows the influence of a tractor propeller's

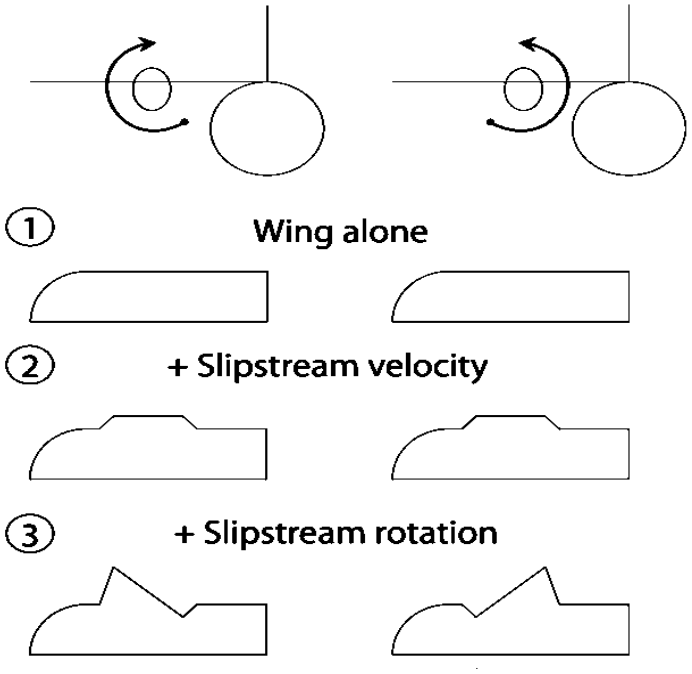

Figure 6: Influence of the propeller's slipstream on the spanwise lift distribution over the wing [Ref.2]

slipstream on the wing. As Figure [6] shows, the elliptical lift distribution of the wing is disturbed by this effect. However, this interaction results in higher total lift generated by the wing, which is motivating to investigate. When the wing is placed in propeller's slipstream, it experiences a different flow field relative to freestream flow, which alters the flow's pressure on the wing's surface and results in local lift variations over wingspan.

The propeller can also be installed in pusher configuration where the wing is not placed in propeller's slipstream. The engine should be located behind the airplane's center of mass to be considered in a pusher configuration, which is usually behind aircraft's wing.

The work of Catalano [Ref.18] [Ref.19] on the influence of pusher propeller on wing shows that propeller induces the flow over the wing's surface and therefore increases lift and pressure drag of the wing. Moreover, the propeller's inflow also delays transition by preserving laminar flow over a smooth wing up to 80% chordwise position.

Three related studies conducted by Muller, Heinze, Kožulovic, Hepperle, and Radespiel [Ref.20] [Ref.21] [Ref.22] reveal another possible propeller wing configuration. Positioning the propeller in an over the wing (OTW) configuration could introduce a nearly undisturbed spanwise lift distribution that impacts the drag coefficient of wing. Figure [8] shows the spanwise drag coefficient of OTW configuration is even smaller than the clean wing. In this case, propeller wing interaction reduces the drag coefficient of the system by inducing an angle of attack.

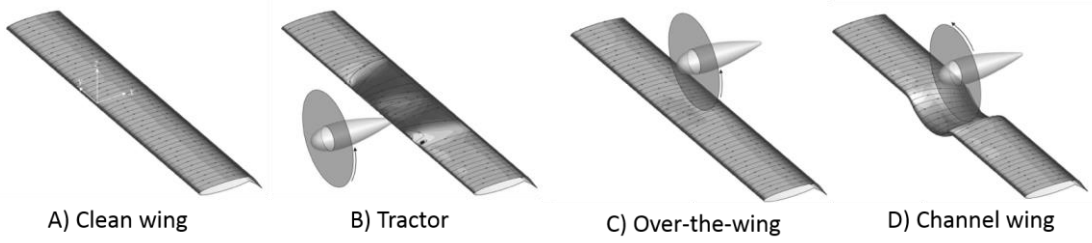

Figure 7: Four different configurations that were studied by Muller, Heinze, Kožulovic, Hepperle, and Radespiel [Ref.22], A) Clean wing without the influence of the propeller, B) Propeller and wing are in tractor configuration, and the wing experiences the propeller's slipstream, C) the propeller is placed over the wing and induces the flow un the suction surface of the wing D) the shape of the wing is modified in a way that the distance from the propeller's tip to the wing surface remains a constant value

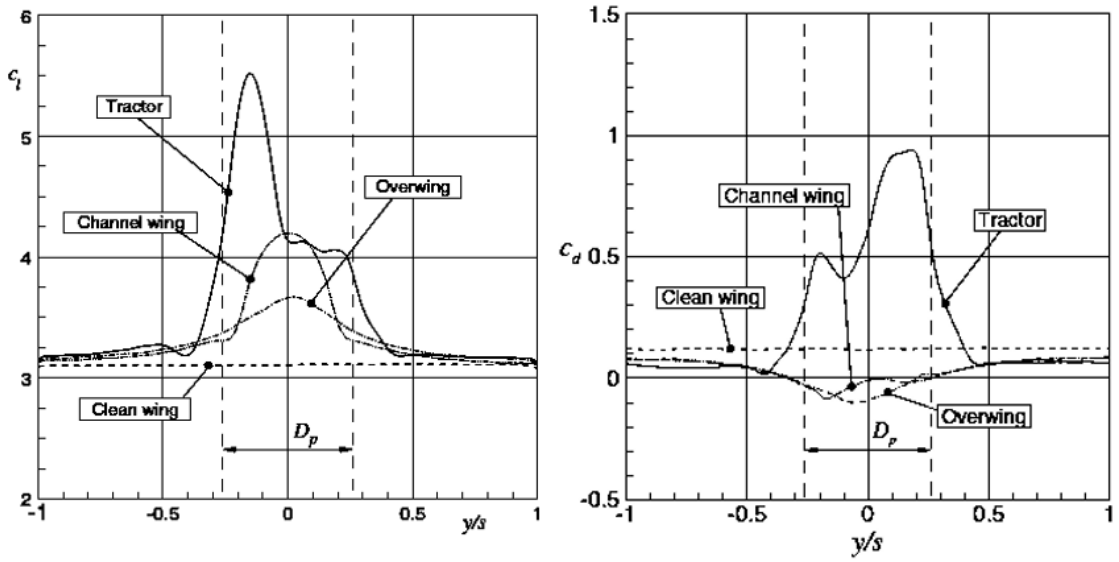

Figure 8: On the left: Spanwise lift distribution of the wing in different configurations with the propeller, On the right: Spanwise Drag distribution of the wing in different configurations with the propeller [Ref.22]

Moreover, according to Muller and his colleagues [Ref.20] [Ref.21] [Ref.22], lift performance and overall efficiency is improved at low Mach numbers compared to the case where propeller is in tractor configuration. OTW configuration can benefit from the influence of propeller's inflow on the wing's suction side. Furthermore, propeller's chordwise position may be optimized to maximize overall propulsive efficiency.

Muller, Heinze, Kožulovic, Hepperle, and Radespiel [Ref.20] [Ref.21] [Ref.22] concluded that propeller wing interactions are more advantageous in OTW configuration than pusher, tractor or channeled wing configuration. Moreover, OTW configuration seems to benefit more from propeller wing interaction than other configurations regarding both lift and drag performance. However, it is not yet entirely clear which parameters influence the interaction between propeller and wing. Muller, Heinze, Kožulovic, Hepperle, and Radespiel [Ref.20] [Ref.21] [Ref.22] recommend investigating the influence of wing shape on the aerodynamic performance in cruise condition where the lift to drag ratio is more sensitive to the drag coefficient.

1.1.2 Secondary wing

Introducing a secondary wing in biplane configuration can reduce drag and increase lift to drag ratio of the system substantially compared to a monoplane configuration according to Olson and Selberg [Ref.23]. According to this study stagger, decalage angle and the gap between wings affects these improvements. However, this study did not include the influence of propeller on biplane configuration.

Configuration	L/D_{max}	$\Delta(L/D_{max})$ (%)	C_D ($C_L = 0.175$)	ΔC_D (%)	C_{Lmax}	ΔC_{Lmax} (%)
Monoplane	8.988	0	0.028	0	0.943	0
Biplane Case I GA = 1.0 ST = 0.875 De = −6 deg	10.49	+16.7	0.021	−25	0.722	−23.4
Biplane Case II Ga = 1.0 St = 0.875 De = −5 deg	11.788	+31.2	0.022	−21.4	0.734	−22.2
Biplane Case III Ga = 0.875 St = 1.0 De = −6 deg	10.449	+16.3	0.024	−14.3	0.840	−10.6

Figure 9: The experimental results of the biplane configuration with different Gap (Ga) (proportional to chord length), Stagger (ST) (Proportional to chord length) and decalage angle (DA) [Ref.23]

In another study by Hongbo, Xiaoping, and Zhou, the influence of propeller on biplane configuration is investigated [Ref.24]. This study shows that the scaled double airfoils propeller (SDAPC) configuration benefits from the presence of secondary wing. In this study, the propeller is modeled with a singular geometry actuator disc model. Hongbo, Xiaoping, and Zhou [Ref.24] conclude that this configuration can improve lift and drag performance of the entire system compared to the case where the scaled secondary wing is not present (Figure [11]).

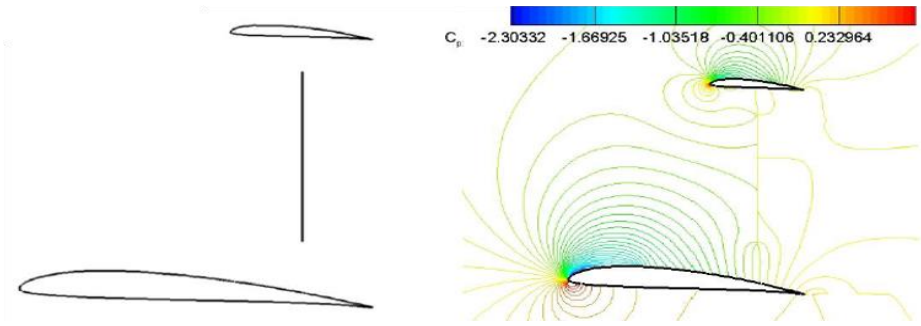

Figure 10: On the left: The Scaled double airfoils propeller configuration (SDAPC), On the right: The Pressure coefficient plot of SDAPC generated with Fluent program including RANS models in the evaluation of this plot [Ref.24]

More importantly, improvements on lift and drag performance of the system have a direct relationship with the propeller's thrust (Figure [11]). This study indicates that influence of the propeller on aerodynamic performance of this configuration is significant and can be considered beneficial. Moreover, this research [Ref.24] concluded that aerodynamic performance of the whole system could benefit from adding a scaled secondary wing in biplane configuration.

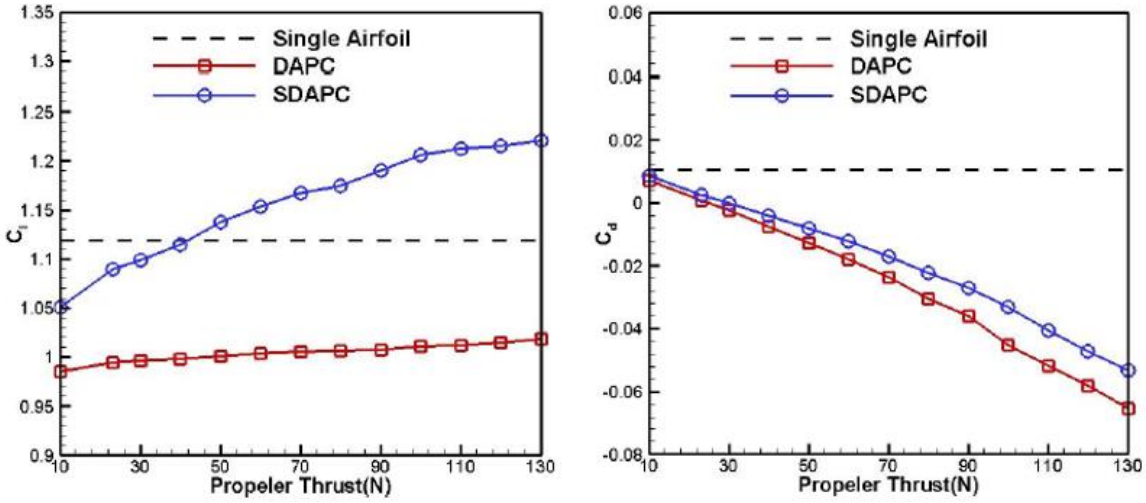

Figure 11: On the left: The total lift coefficient of the model as a function of propeller's thrust [N], On the right: The total drag coefficient of the model as a function of Propeller's thrust [N], SDAPC: Scaled double airfoils propeller configuration, DAPC: double airfoils propeller configuration (The second wing is not scaled and has the same length as the main wing) [Ref.24]

According to the observations made by Olson, Selberg [Ref.23], Hongbo, Xiaoping, and Zhou [Ref.24], adding a secondary wing to an OTW propeller induces pressure coefficient on the main wing's upper surface, which improves the lifting performance of the system. Furthermore, it was observed from these publications [Ref.23] [Ref.24] that flow velocity in the duct between the main wing and the secondary wing becomes more uniform compared to the case where the secondary wing is not present. It was recommended by Hongbo, Xiaoping, and Zhou [Ref.24] to optimize the secondary wing shape and observe the influence of altered flow field on the propeller's performance and overall efficiency of the system.

Muller, Heinze, Kožulovic, Hepperle, and Radespiel [Ref.20] [Ref.21] [Ref.22] recommended studying the integration of a ducted propfan above the wing's trailing edge to take advantage of the drag reduction effect and reduced inflow velocity to the rotor. Implementing a secondary wing relates this project closer to this particular recommendation [Ref.20] [Ref.21] [Ref.22].

1.2 Thesis project and Research Questions

This research aims to investigate the influence of an OTW based DP system with addition of a newly introduced element called secondary wing. This project intends to evaluate the inviscid flow effect of wing propeller interaction by including the flow vorticity in the solutions. The choice of the analytical approach is based on the requirements of this project, the recommendations of references in chapter 1.1 and the discussion in chapter 2.2. Furthermore, this project examined the relationship between a certain number of parameters and the model's performance to illustrate the working principle of propeller wing interactions in this particular configuration.

Most of the mentioned studies in chapter 1.1 suffer from high demanded computational power. The mentioned studies in chapter 1.1 applied RANS models and included viscous effects in the solutions. The viscous effects are ignored in this research to reduce the simulations' cost and broaden the scope of this study. Moreover, Mani shows [Ref.26] that Euler calculation is efficient in design optimization and Euler solvers are commonly coupled to optimization schemes to produce practical design procedures. Comparing RANS and Euler solutions could examine the influence of viscous effects, which shows how valuable this study could be for researchers aiming to include the viscous effects in later studies.

Muller, Heinze, Kožulovic, Hepperle, and Radespiel [Ref.20] [Ref.21] [Ref.22] suggest, that further investigation requires optimization studies to take advantage of OTW configuration since the resulting aerodynamic benefit against the tractor concept may be necessary to compensate the expected increase in structural weight.

Hongbo, Xiaoping, and Zhou [Ref.24] also suggest that addition of the secondary wing may exploit OTW configuration's potentials through an optimization study. Further effort should be spent on investigating the propeller characteristics and a three dimensional flow simulation because of the more complicated problems for a 3D configuration.

The publications mentioned in chapter 1.1 investigated many issues regarding the influence of DP system on fuel consumption, application of electromotors, propeller wing interaction, different propeller wing configurations and application of a scaled biplane. Therefore, this project is motivated to investigate the influence of geometry modification and identify different parameters that could affect aerodynamic performance and overall propulsive efficiency of the DP system in OTW configuration. The following research questions are formulated based on recommendation of the reference.

1) How do the main wing and secondary wing geometry variations affect overall propulsive efficiency and aerodynamic performance of the system?
2) Which design changes can provide desired velocity profile over the upper surface of the main wing to result in an optimum interaction between both wings and propeller?
3) Does the CFD simulation resemble and capture the reality of the physical phenomenon and occurrences? (CFD simulation verification and validation)

Answering these questions provides sufficient information on OTW based DP system with addition of the secondary wing. However, answering the first two questions was rather challenging, since they involve examining different aspects of the DP system. Therefore, it was more sensible to break down each research question into sub questions and set smaller goals by separating the different aspects that influence the outcome of this research. The first two research questions were broken into the following smaller sub questions.

1) What are the advantages and disadvantages of propeller wing interactions in this particular orientation?
2) By including the secondary wing, is this model's orientation comparable to any known topology?
3) What is the impact of the secondary wing orientation on aerodynamic performance and propulsive efficiency of the system?
4) What is the impact of the propeller's position on aerodynamic performance and propulsive efficiency of the system?
5) How do the main wing and the secondary wing influence performance of the propeller?

2 Distributed Propulsion Model

This project studied the inviscid flow effects of an OTW based DP system with addition of a secondary wing. Figure [14] and Figure [15] show that the propeller is located between the main wing and the secondary wing. In this configuration, the propeller experiences ducted flow conditions, which could enhance the propeller's performance by decreasing the inflow velocity of the propeller. This chapter further explains how the CFD model was constructed and what type of analytical approach was required to simulate this model accurately.

A reference aircraft was required to use the same scales of dimensions for the consistency in the analysis. This reference aircraft helps the research to obtain the geometry and the corresponding flight condition and to construct a consistent model. Muller, Heinze, Kožulovic, Hepperle, and Radespiel [Ref.22] recommended investigating the influence of the OTW based propeller in cruise conditions, where thrust effects are small and the lift to drag ratio is more sensitive to drag. Muller, Kožulovic, and Radespiel [Ref.20] show that the drag coefficient due to the influence of the propeller's thrust of OTW configuration depends on the freestream Mach number and OTW configuration is most effective where the freestream Mach number is about 0.4. Therefore, the reference aircraft is required to have low cruise Mach number and preferably a wing based turboprop engine to rescale the model easier to a DP system. After careful considerations, it seems that ATR72 (Figure [14]) fits the requirements of this project. In this case, the consistency between the engine's specification, propeller's dimensions, wing dimensions and the flying condition is achieved by introducing a reference aircraft. This choice does not further influence the analysis of this project.

Figure 12: ATR72's picture [Ref.25]

2.1 CFD Model

This project uses ANSYS CFX software as a CFD solver to perform the necessary calculation. The option of choosing a CFD program is limited to the resources provided to the researcher. ANSYS CFX is a commercial software which is validated and produces acceptable solutions based on Navier-Stokes formulas. This program uses finite volume method of calculation to solve the Navier-Stokes formulas. In ANSYS software suite, there are two different finite volume based CFD programs that are able to perform the required calculations, i.e., Fluent and CFX. According to Acharya [Ref.27] CFX solver requires less number of iterations compared to FLUENT and performs simulations faster. Furthermore, Acharya [Ref.27] explains that CFX has more tolerance toward meshes than FLUENT. The tolerance of CFX toward the mesh quality is advantageous in the optimization process, where the mesh is repetitively deformed.

In this project, one of the engines in the DP array (closest to Mean Aerodynamic Chord (MAC)) was simulated, and the problem was resolved by assuming that the aerodynamic features of the considered piece are periodically reoccurring in the rest of the engines. This assumption can reduce the calculation cost of the analysis significantly. Using the periodic boundary condition in this case is an accurate assumption to model at least 3 neighboring propellers since ATR72's wing has 3 degrees quarter chord sweep angle and a taper ratio of 0.6 [Ref.31]. Therefore, it was assumed the aerodynamic characteristics of this periodic model represents the DP system.

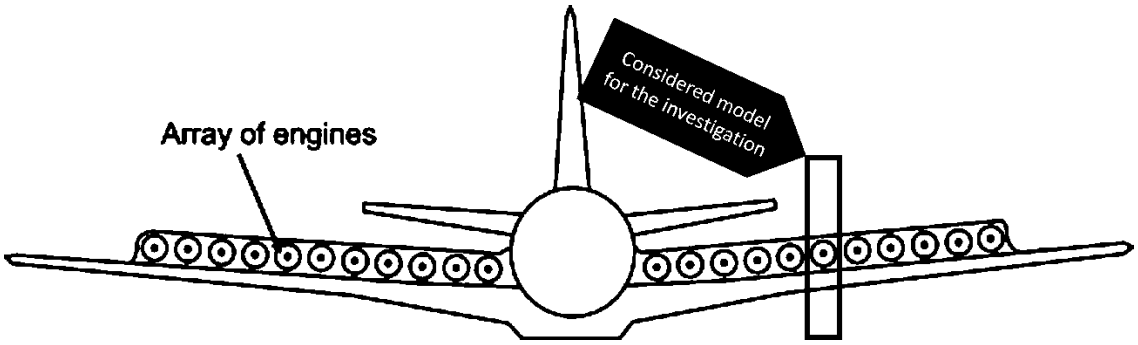

Figure 13: Distributed Propulsion in an Over the wing configuration [Ref.28] (This figure has been adopted for detailed visualization)

The model's potential improvements were obtained by geometry and position variation of the different elements, and they were studied based on their aerodynamic performance and the propulsive efficiency of the propeller. Luijendijk [Ref.29] and Marcus [Ref.30] investigated the consequence of the OTW based propeller and they showed that the chordwise position of the propeller (with respect to the main wing) affects the performance of the design significantly. Moreover, the spacing between the disc and the main wing's surface can, in fact, influence the interactions between the propeller and the main wing.

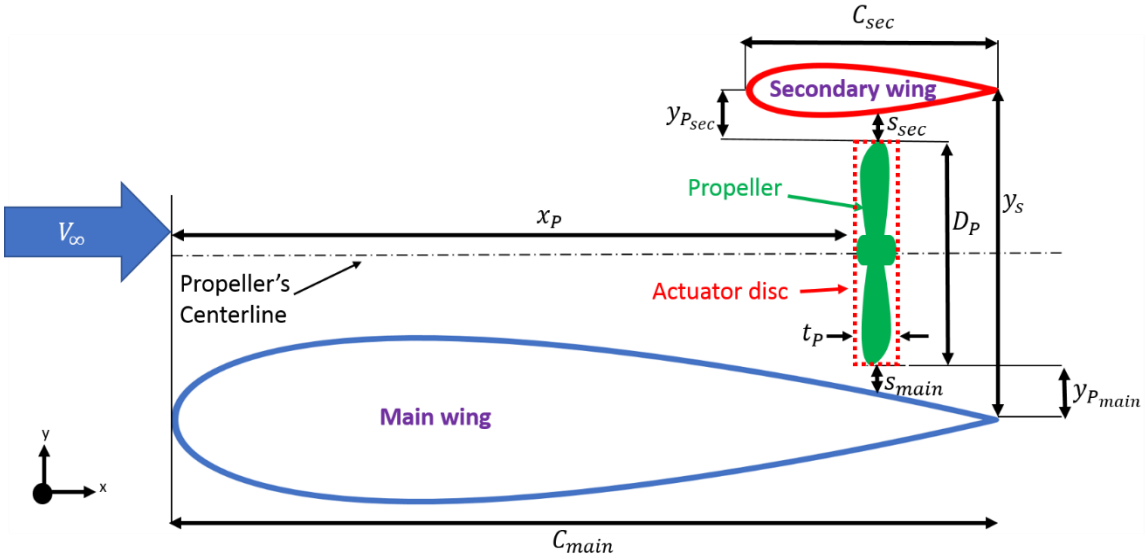

Figure 14: Cross-section sketch of the CFD model's orientation with the required parameters and variables to define the geometry shape and the position of the elements with respect to each other.

Figure [14] illustrates the cross section drawing of the CFD model and shows the orientation of each element in an OTW configuration. The distance from the propeller's tip to the main wing and the secondary wing's chord line and the distance between the main wing and the secondary wing's chord line are respectively specified as $y_{P_{main}}$, $y_{P_{sec}}$and y_s. These parameters were used to construct the model with the help of ICEM[6]. However, the distance from the main wing and the secondary wing's surface to the propeller's tip were specified respectively by s_{main} and s_{sec}. These parameters were important to compare the solution of different cases where the propeller's chordwise position (x_p) was modified. The distance from the propeller's tip to the main wing and the secondary wing's chord line could remain constant, while the tip clearance from the wing

[6] ANSYS ICEM CFD is a popular proprietary software package used for Computer-Aided Design (CAD) and mesh generation

surface changed as the chordwise position of the propeller was varied. Therefore, the tip clearance of the propeller to the surface of the wing was considered as a variable in the analysis. The rest of the parameters define the dimension of the main wing, secondary wing and the propeller. C_{main}, C_{sec}, t_P and D_P respectively define the main wing and the secondary wing's chord length, actuator disc thickness and the propeller's outer diameter.

In this project, the design variables that define the geometry and the location of each element are manipulated to identify the layouts that could increase the performance of the system. It is nearly impossible to study the shape variation of the elements without the help of optimization algorithms because it could be extremely costly. However, in some cases, it was essential to separately test the effect of some parameters and compare the cases to each other to reduce the complexity of the shape optimization algorithms.

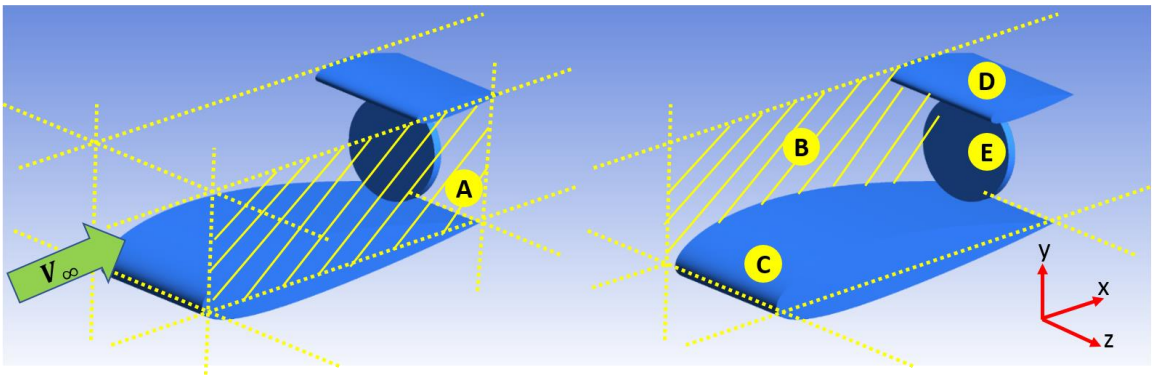

Figure 15: Model's configuration and the Elements, A) Periodic boundary of the fluid domain on the left side of the model, B) Periodic boundary of the fluid domain on the right side of the model,(A and B are facing each other and cover the whole fluid domain), C) The main wing scaled by the mean aerodynamic chord of ATR72, D) The secondary wing that is placed on the top of the propeller, E) The actuator disc model that represents the propeller

The position of the propeller with respect to the main wing and the secondary wing can affect the overall performance of this model significantly [Ref.29] [Ref.30]. However, varying the location of the disc complicated the optimization study because by modifying the propeller's location the mesh could deform unexpectedly and produce a mesh with unacceptable quality to CFX. Therefore, the influence of propeller's position on the system's efficiency will be tested separately.

The main wing's airfoil was chosen based on ATR72, which is close to a standard five digit NACA airfoil (NACA43015) [Ref.31]. However, this airfoil produces high pressure gradients, which could cause flow circulation in not optimized configurations. Therefore, it was decided to move the camber location of the airfoil from 15% chordwise position to 40% chordwise position to decreases the high

pressure gradient of the airfoil and avoid such effects; After obtaining an optimum shape for the secondary wing, NACA43015 was used as the main wing's airfoil. The main wing's chord is chosen equal to the mean aerodynamic chord of the ATR72 [Ref.31].

The secondary wing is a new element added to the OTW based propeller model. The chord length of the secondary wing was selected between 30% to 40% of the main wing's chord length. This boundary was chosen because the secondary wing was defined as a small scaled wing with respect to the main wing according to the study that Hongbo, Xiaoping, and Zhou [Ref.24] conducted. The model's flexibility also limits the secondary wing's chord length range of variation. Changing the secondary chord length could deform the mesh and reduce the mesh quality in the optimization study, which is not desired.

The minimum distance between the wings was assumed to be 30% of the main wing's chord length (chord line to chord line). This number is roughly calculated by presuming that one third of ATR72's intake region of the engine is equal to the intake region of DP system. It is assumed that the required propulsive power of ATR72 is distributed over three different propulsion systems namely DP system over the wing, wingtip, and the tail. Equating only the areas of the intake regions is not enough to estimate the dimensions of the DP's intake region. The array of the engines is assumed to be distributed over 50% of the wingspan minus the width of the fuselage. The assumptions above are just to specify the initial point of the design, and the accuracy of the assumptions in this particular case will not affect the analysis.

Table 2: Calculation of the minimum gap between the wings based on intake area region of ATR72

ATR72 Propeller's diameter	$\approx 3.9\ [m]$
Open rotor intake area divided by three	$A = 2.\pi r^2 = \pi.\frac{(1.6)^2}{3} \approx 4\ [m^2]$
50% of the half wingspan minus the fuselage width	$50\ \%.\frac{27\ [m] - 3[m]}{2} = 6\ [m]$
Spacing between the wings	$\frac{A}{l} = \frac{4[m^2]}{6\ [m]} = 0.667\ [m]$
Spacing normalized by the main wing's chord length	$\frac{0.667\ [m]}{2.11\ [m]} \approx 30\%$

CFD simulations can be very costly, and if not optimized, they can require a tremendous amount of computational power and time. Since this project is based

on CFD simulations, it is necessary to reduce the computational cost of the analysis. However, it is also important not to oversimplify the simulations so that the solver neglects the critical flow features. Therefore, different assumptions were investigated to indicate how much the calculation cost of the simulations could be reduced without a significant increase in the modeling error. The model was initially tested with inviscid flow condition [Ref.32] to decide whether compressibility effects of the flow should be included in the solutions or not. Since the momentum source accelerates the flow, the local flow velocity increased up to the point that the compressibility effects could not be neglected locally. Therefore, based on the simulations performed with inviscid flow conditions in chapter 5.1, it is decided to include the compressibility effects in the simulations [Ref.33].

2.2 Analytical Approaches

The first question that comes up when starting an analytical and numerical study is "what type of numerical approach is suitable to answer the research questions?". It is critical to answer this question immediately in the initial phase of research and define the necessary steps to accomplish the goal of the study. Figure [12] illustrates different types of numerical approaches that one could take to investigate nearly any fluid dynamic problems.

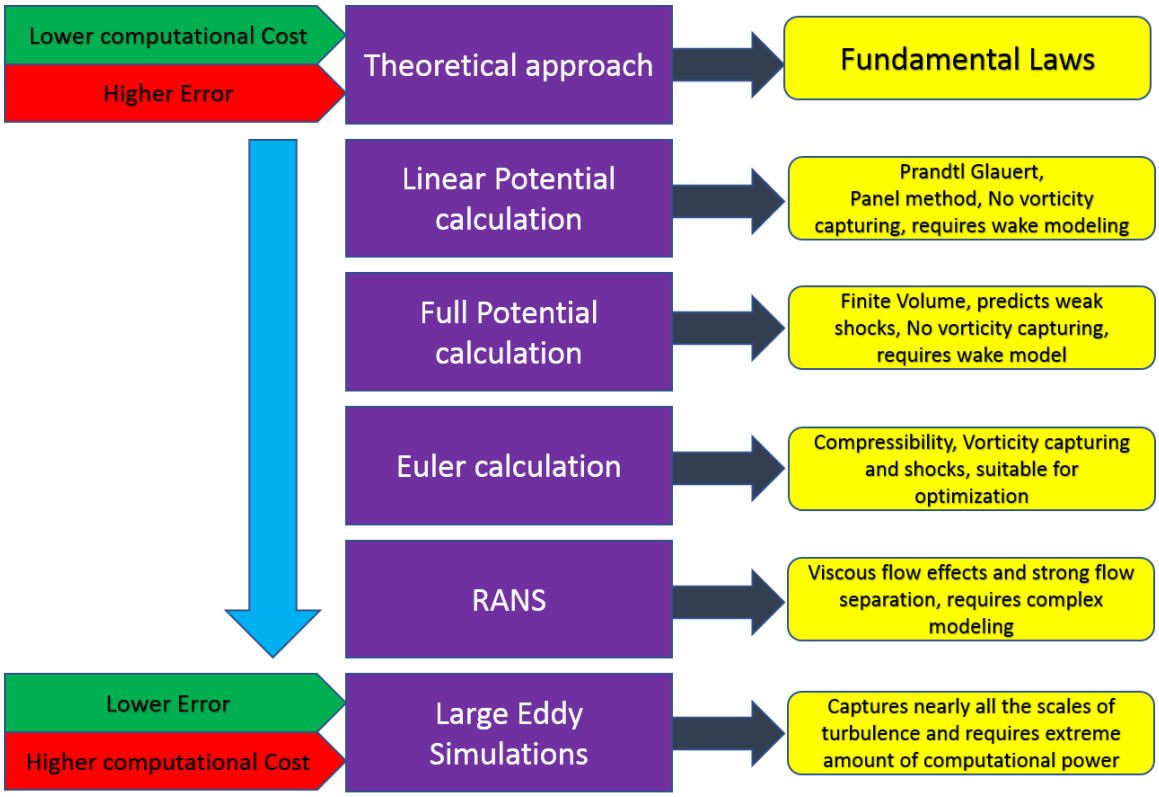

Figure 16: Different mathematical approaches ranked based on the required computational cost

Panel codes are based on the Prandtl-Glauert equations that were converted to Laplace equations by a simple transformation [Ref.34]. Linear potential calculations (Panel codes) could be helpful as a mean to study the on-surface aerodynamic characteristics of different 2D geometry shapes, where the flow is considered subsonic and incompressible. In full potential flow calculations, solvers solve nonlinear equations and require a mesh in the fluid domain unlike the linear potential method (Panel codes). The full potential method requires a coarser mesh and can produce solutions at a low computational cost compared to Euler calculation.

However, simulating a propeller or even an actuator disc could be problematic with full potential method since this type of calculation does not include flow vorticity in the calculation and requires a wake model. Although this method could provide an estimation of interactions between separate body elements, it could not adequately capture the interactions between two wings and a propeller because this method does not include the calculation of wake and vorticity. Assuming that the geometry of the wake is modeled for the wings and the propeller separately, the interactions between the wakes adds to the model's complexity. Developing a wake model to take the interactions of multiple elements into account is complicated and time consuming because the topology of such interactions between multiple elements and a propeller is not yet fully understood. Catalano [Ref.18] [Ref.19] approaches the propeller wing interactions with the help of potential flow calculations and a wake model developed based on experimental data [Ref.35]. These models were developed for known topologies and using them for arbitrary configurations can jeopardize capturing the new flow features.

Euler equations, on the other hand, are based on the conservation laws. Euler equations can simulate compressible flow at low cost, predict strong shocks and capture flow vorticity [Ref.38]. Euler equations are comparable with Navier-Stokes equations where viscosity and thermal conductivity of the flow are set to zero, and flow is considered laminar. Although Euler method lacks in capturing any scales of turbulence, boundary layer or viscous effects, it is proven to be helpful in studying the fluid dynamics problem and interactions between multiple elements [Ref.26]. Moreover, this method is proven effective and inexpensive for the optimization study and capturing the critical flow features due to interaction. However, after reaching an optimum point in the optimization study, viscous effects could be obtained by means of more expensive RANS calculation.

By adding the RANS models and trying to capture the flow's turbulence as well as viscous effects, the simulations become costlier and more complicated. Interpretation of the results, in this case, could be difficult since there is no prior information available for comparison such as Euler solutions. The calculation cost is not the only issue where the RANS models are used. Modeling and meshing become more problematic as the complexity of the simulation increases. The number and the orientation of the cells to capture the flow's boundary layer could become a serious issue while performing a grid convergence study to quantify discretization error. In addition, RANS models have substantial modeling error because they are based on experimental data and correlations. Performing an

optimization study with the help of RANS models could easily fail because this type of numerical method is vulnerable to mesh deformation.

Muller, Heinze, Kožulovic, Hepperle, Radespiel [Ref.20] [Ref.21] [Ref.22], Hongbo, Xiaoping, and Zhou [Ref.24] used RANS calculations as in their studies. However, in their case, the number of simulations was limited so they could construct and execute costlier calculations. However, this project aims to investigate the influence of different parameters on the aerodynamic performance of the model, which requires numerous sets of simulations. Therefore, choosing a less costly method of calculation could broaden the scope of this project.

LES can nearly capture all the scales of turbulence and almost all the critical flow features. However, this type of numerical method requires a considerable amount of computational power that right now is not available to students.

Consequently, Euler calculation was chosen as the mathematical approach to investigate OTW based DP system with addition of a secondary wing. Inviscid flow calculation was used initially to confirm the impact of the compressibility effects on the analysis. The initial test of inviscid calculation showed in chapter 5.1 that this method suffers from significant amount of modeling error. Therefore, Euler equations were used to include the flow's compressibility effects.

2.3 THEORY

In this project, the program ANSYS CFX was used to perform the necessary CFD simulations. This solver is based on the Navier-stokes equations and uses finite volume method to solve these equations. Navier-Stokes equations are based on the fundamental laws of conservation namely, mass, momentum, and energy. This research is required to perform Euler calculations; therefore, the influence of the fluid viscosity was eliminated to reduce the Navier-Stokes equation to Euler equations.

Performing optimization studies with the help of CFX could become extremely costly. The physical flow conditions were altered to exclude the Navier-Stokes energy equation from simulations and reduce the computational cost and time of simulations. The effects of such simplification were investigted in chapter 3.

2.3.1 Navier-Stokes vs. Euler Equations

Euler equations are a set of coupled differential equations that describe the relationship between the velocity, pressure, and density of a moving fluid. These equations can be approximated for a given flow problem by using methods from calculus such as finite element or finite volume method. The following sets of equations are Euler equations in unsteady form [Ref.36].

$$\frac{\partial \rho}{\partial t} + \frac{\partial (\rho u)}{\partial x} + \frac{\partial (\rho v)}{\partial y} + \frac{\partial (\rho w)}{\partial y} = 0 \; [Eq.1]$$

$$\frac{\partial (\rho u)}{\partial t} + \frac{\partial (\rho u^2)}{\partial x} + \frac{\partial (\rho vu)}{\partial y} + \frac{\partial (\rho wu)}{\partial z} = -\frac{\partial p}{\partial x} \; [Eq.2]$$

$$\frac{\partial (\rho v)}{\partial t} + \frac{\partial (\rho uv)}{\partial x} + \frac{\partial (\rho v^2)}{\partial y} + \frac{\partial (\rho wv)}{\partial z} = -\frac{\partial p}{\partial y} \; [Eq.3]$$

$$\frac{\partial (\rho w)}{\partial t} + \frac{\partial (\rho uw)}{\partial x} + \frac{\partial (\rho vw)}{\partial y} + \frac{\partial (\rho w^2)}{\partial z} = -\frac{\partial p}{\partial z} \; [Eq.4]$$

Navier-stokes equations are an extended form of the Euler equations that include the viscosity effects of the moving flow on the velocity, pressure, and density of a moving fluid.

The following sets of equations describe the Navier-Stokes equations in unsteady form that are comparable with Euler equations where (Re) is Reynolds number and (τ_{ij}) is the component of stress tensor [Ref.37].

$$\frac{\partial \rho}{\partial t} + \frac{\partial (\rho u)}{\partial x} + \frac{\partial (\rho v)}{\partial y} + \frac{\partial (\rho w)}{\partial y} = 0 \quad [Eq.5]$$

$$\frac{\partial (\rho u)}{\partial t} + \frac{\partial (\rho u^2)}{\partial x} + \frac{\partial (\rho v u)}{\partial y} + \frac{\partial (\rho w u)}{\partial z} = -\frac{\partial p}{\partial x} + \frac{1}{Re}\left[\frac{\partial \tau_{xx}}{\partial x} + \frac{\partial \tau_{xy}}{\partial y} + \frac{\partial \tau_{xz}}{\partial z}\right] \quad [Eq.6]$$

$$\frac{\partial (\rho v)}{\partial t} + \frac{\partial (\rho u v)}{\partial x} + \frac{\partial (\rho v^2)}{\partial y} + \frac{\partial (\rho w v)}{\partial z} = -\frac{\partial p}{\partial y} + \frac{1}{Re}\left[\frac{\partial \tau_{xy}}{\partial x} + \frac{\partial \tau_{yy}}{\partial y} + \frac{\partial \tau_{yz}}{\partial z}\right] \quad [Eq.7]$$

$$\frac{\partial (\rho w)}{\partial t} + \frac{\partial (\rho u w)}{\partial x} + \frac{\partial (\rho v w)}{\partial y} + \frac{\partial (\rho w^2)}{\partial z} = -\frac{\partial p}{\partial z} + \frac{1}{Re}\left[\frac{\partial \tau_{xz}}{\partial x} + \frac{\partial \tau_{yz}}{\partial y} + \frac{\partial \tau_{zz}}{\partial z}\right] \quad [Eq.8]$$

The right hand side of the Navier-stokes equations was eliminated by equating the fluid's kinematic viscosity (ν), which is a part of Reynolds number, to zero. Therefore, the solver neglected the flow's viscous effects and obtained in this way the Euler solution. Moreover, Euler calculation does not include the turbulence of the flow. Therefore, the flow is considered laminar and no further modeling of the flow's turbulence is required.

2.4 Isothermal vs. Adiabatic flow conditions

As it was mentioned in chapter 1.2, this project aimed to use optimization studies to investigate the influence of secondary wing's shape and position on performance of the system in OTW configuration. Such a study requires to vary the parameters and evaluate the CFD solution after each alteration. Depending on the number of variables, the optimization study demands a massive amount of computational power and time.

Eliminating the influence of Navier-Stokes energy equation from Euler solution and neglecting the energy state of flow in fluid domain could reduce the required computational power of each simulation by half. In this case, the freestream flow conditions were based on ATR72's cruise condition and by assuming that the aircraft had been in steady cruise flight for a long time, the heat transfer between the elements and flow could be neglected. By assuming that the velocity variation of flow does not influence the energy state of fluid and the flow's temperature

remains constant, the evaluation of Navier-Stokes's energy equation could be neglected entirely. However, eliminating the effect of flow velocity on the flow's energy state is a significant compromise to reduce the cost of the optimization study. Therefore, the initial and the optimum point of the optimization study should still be simulated with adiabatic flow conditions.

[Eq.9] shows the Navier-Stokes's energy equation where (q) is heat flux, (E_T) is the total energy of the fluid and (P_r) is the Prandtl number.

$$\frac{\partial(E_T)}{\partial t}+\frac{\partial(uE_T)}{\partial x}+\frac{\partial(vE_T)}{\partial y}+\frac{\partial(wE_T)}{\partial z}=-\frac{\partial(up)}{\partial x}-\frac{\partial(vp)}{\partial y}-\frac{\partial(wp)}{\partial z}$$
$$-\frac{1}{Re.P_r}\left[\frac{\partial q_x}{\partial x}+\frac{\partial q_y}{\partial y}+\frac{\partial q_z}{\partial z}\right]+\frac{1}{Re}\left[\frac{\partial}{\partial x}\left(u\tau_{xx}+v\tau_{xy}+w\tau_{xz}\right)\right.$$
$$\left.+\frac{\partial}{\partial y}\left(u\tau_{xy}+v\tau_{yy}+w\tau_{yz}\right)+\frac{\partial}{\partial z}\left(u\tau_{xz}+v\tau_{yz}+w\tau_{zz}\right)\right] \quad [Eq.9]$$

The Navier-Stokes's energy equation is based on the conservation law of energy and includes the viscosity effects, which are neglected in Euler calculation. If the flow's viscous effects are eliminated, then the Navier-Stokes's energy equation reduces to the following form [Eq10].

$$\frac{\partial(E_T)}{\partial t}+\frac{\partial(uE_T)}{\partial x}+\frac{\partial(vE_T)}{\partial y}+\frac{\partial(wE_T)}{\partial z}=-\frac{\partial(up)}{\partial x}-\frac{\partial(vp)}{\partial y}-\frac{\partial(wp)}{\partial z} \quad [Eq.10]$$

The flow is assumed to be isothermal where the effect of flow velocity on temperature is neglected. However, by including the energy equation in the simulations, the flow is then assumed to be adiabatic, which represents the actual flow condition more accurately. Adiabatic flow condition assumes that variation in flow parameters is small and gradual. Moreover, heat transfer between the flow and the elements is negligible, which was accepted by assuming that the aircraft is flying in a steady cruise condition long enough that the local flow and body surface temperature match.

2.5 Actuator disc model

Simulating an actual propeller requires a significant number of grid elements which adds to the complexity of the analysis. Moreover, complex interaction between propeller blades and flow could make the simulation's convergence problematic [Ref.38].

In this project, the propeller was represented by an actuator disc model, which is an idealized form of a propulsor [Ref.39]. Actuator disc theory or Momentum theory describes a propeller or a rotor as a mathematical model of an ideal actuator disc. According to Momentum theory, the propeller is modeled as an infinitely thin disc that applies momentum into fluid domain.

According to Stevens, Martínez, Tossas and Meneveau [Ref.40], such model can significantly reduce the demanded computational cost of simulations and still generate accurate solutions. Instead of performing simulations by an actual propeller in the fluid domain, the influence of propeller on flow is modeled to reduce the computational cost. In an actuator disc model, the exerted momentum in axial and tangential directions is calculated by another software based on Blade Element Method (BEM) calculation and the resultant forces are distributed over the momentum source subdomain, where the propeller is located. The variation of propeller's inlet flow velocity due to propeller wing interaction determines the influence of body elements on propeller's performance.

2.5.1 Actuator disc Model construction

JavaProp[7] is a free and user-friendly software based on Blade Element Method calculations. This program is validated with the help of NASA technical reports, and the estimated error of this program is in the order of 5%. This program calculates the propeller's thrust and torque profile with the help of the reference aircraft's parameters and the definition of distributed propulsion systems.

This case assumes that one third of ATR72's engine power is distributed over the model's wingspan. Reducing and transforming ATR72's engine to an array of smaller engines is achieved by dividing ATR72's engine power by the number of the engines distributed over the wingspan. Furthermore, the propeller's diameter is chosen based on the calculation in Table [2]. The propeller's diameter is restricted by the wingspan where the distributed propulsion system is placed, which is roughly

[7] JavaProp program and Documentation, https://www.mh-aerotools.de/airfoils/javaprop.htm

six meters long. Assuming that there are ten engines placed over the wingspan with a clearance of 20% (of the propeller's diameter) [Ref.41], the propeller's diameter is estimated to be 0.5 meters. The propeller's clearance is chosen based on NASA distributed propulsion vertical take-off and landing (VTOL) tilt wing aircraft model [Ref.41]. GL10 scaled model for wind tunnel testing uses eight propellers with 9 inches of diameter placed over a wing with 126 inches of wingspan. The spacing between the propeller's tips is variable and between 20% to 38% of the propeller's diameter. The propeller's inflow velocity is initially equated to freestream velocity, which is chosen based on ATR72's cruise condition [Ref.31].

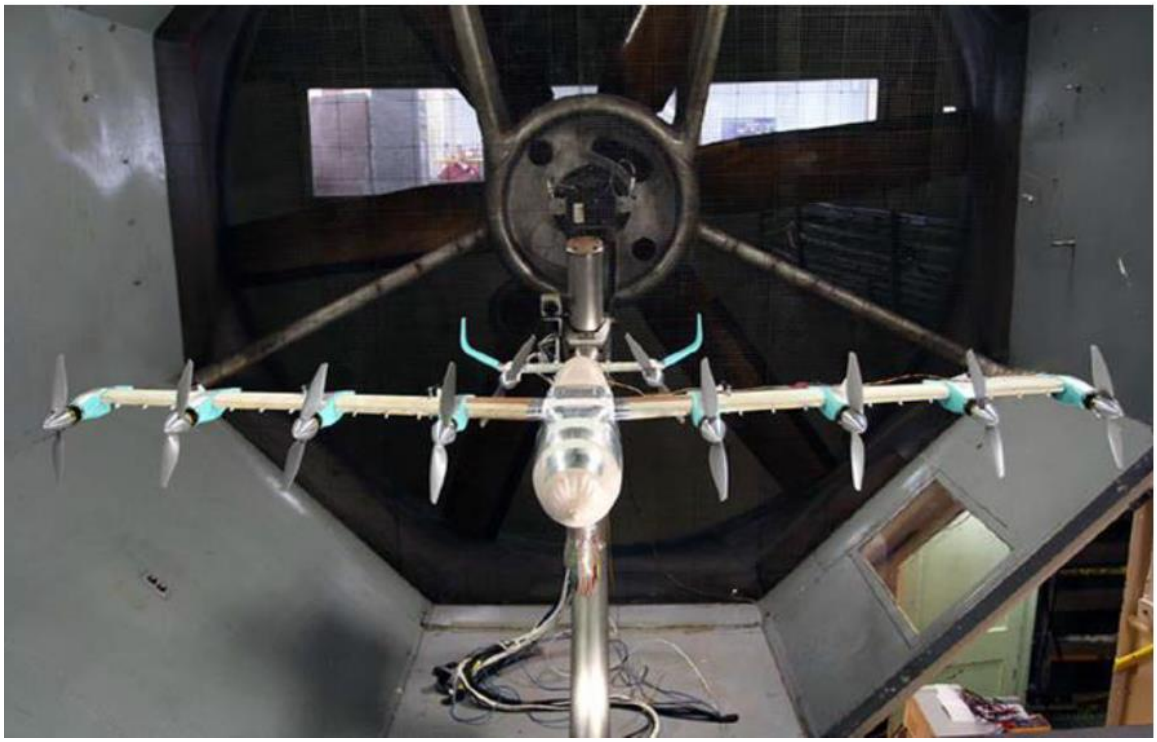

Figure 17: GL-10 28.125% scale tunnel model in NASA Langley's 12-foot Low Speed Wind Tunnel, 9-inch diameter Propeller and a wingspan of 10.5 ft [Ref.41]

Table [3] shows how the required power of each engine in the array of DP system is calculated based on the information provided by the reference aircraft (ATR72). In this case, it is roughly assumed that one third of ATR72's engines power is redistributed over 50% of the wingspan. The remaining power used for namely propulsion systems based on the wing tip and tail of the aircraft [Ref.42]. This assumption is based on the aircraft configuration of NOVAIR project [Ref.43] [Ref.44]. Moreover, it is fair to assume that only 50% of the engine's full power is required during cruise condition. As Table [3] shows, it is assumed that the DP system in this case contains twenty small engines. According to these calculations, each engine requires about 34.166 [kw] of power. With the help of Table [3], the

provided information in Table [4] and a Blade Element Method software (JavaProp), the new propeller's characteristics are calculated.

Table 3: Determining the rescaled engine's required power

Total engine power of ATR72	4100[kw] (2 Engines)
Cruise condition (50% of power required)	4100 [kw] / 2 = 2050 [kw]
Distributed over 3 different propulsion systems (tail, wing tip and DP)	2050 [kw] / 3 = 683.3 [kw]
DP system containing ten engines per half span (20 engines full span)	683.3 [kw] / 20 = 34.166 [kw] per engine

Figure [18] shows that the influence of the propeller's hub is not included in BEM calculation by choosing the "Open hub" option and equating the hub diameter to zero. Including the propeller's hub in the analysis complicates the meshing procedure and increases the number of variables in the optimization study. Moreover, including the hub could shift the focus of the study to optimize the shape of the hub, which is out of the scope of this project.

Table 4: Propeller's specifications and Parameters are based on Pratt & Whitney Pw100 engine and Hamilton standard 568F propeller. The rotational velocity of the propeller was guessed based on trial and error observation to achieve the highest possible propeller

Parameters	Values
Number of blades	6 [-]
Revolutions per minute	10,000 [1/min]
Outer Diameter	0.5 [m]
Freestream Velocity	135 [m/s]
Power	34166 [Watt]

Figure 19: Hamilton standard 568F propeller mounted on Pratt & Whitney Pw100 engine on an ATR72 [Ref.45]

Propeller Name:	P&W scaled		
Number of Blades B:	6	[-]	
Revolutions per minute rpm:	10000	[1/min]	
Diameter D:	0.5	[m]	
Spinner Dia. Dsp:	0	[m]	
Velocity v:	135	[m/s]	
Power P:	34166	[W]	
shrouded rotor	square tip	open hub	

Propeller			
v/(nD)	1.62	v/(ΩR)	0.516
Efficiency η	89.149 %	loading	low
Thrust T	225.62 N	Ct	0.1064
Power P	34.17 kW	Cp	0.1934
Torque Q	32.63 Nm	Cs	2.2502
β at 75%R	41.1°	Pitch H	1.03 m

Figure 18: JavaProp (BEM), on the top half of the picture the required inputs are filled, and on the bottom a table is generated containing the characteristics of the designed propeller

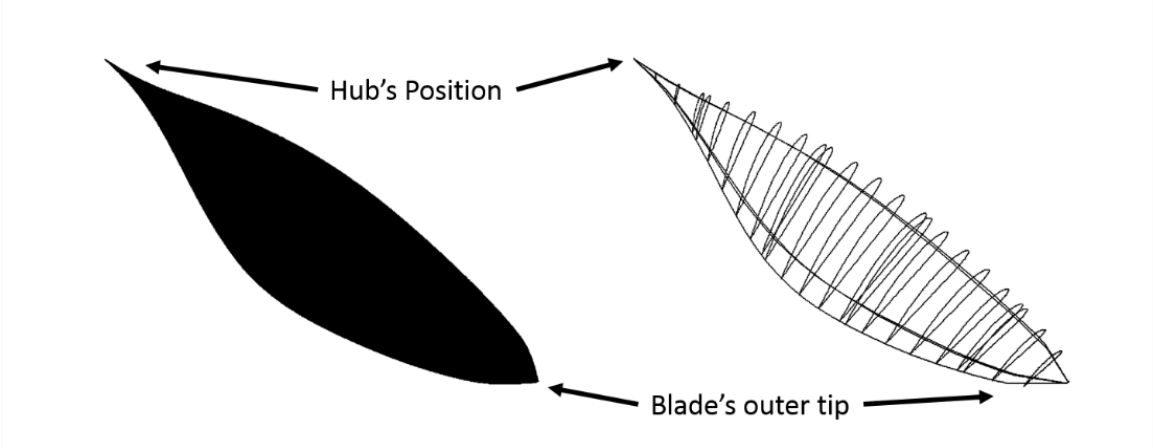

Figure 20: Sketch of the designed blade with the help of JavaProp (the sketch is scaled and rotated for better visualization), On the left side: the solid sketch of the blade, On the right side: the wireframe sketch of the blade

After using these parameters and designing the desired propeller, the thrust and torque coefficient profile over the blade of the propeller is used in CFX to model the actuator disc. As figure [19] and figure [20] illustrate, a trendline of JavaProp's calculated data is produced to implement these parameters in a continuous form in CFX.

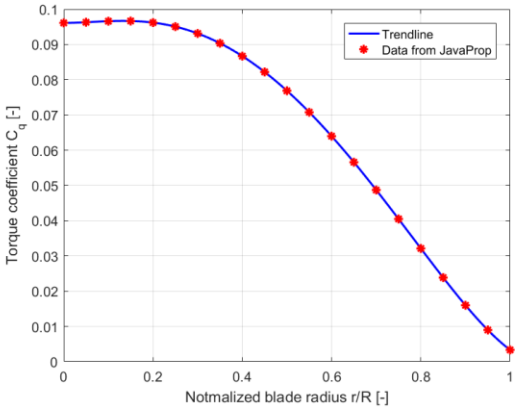

Figure 21: Torque coefficient distributed over the propeller blade

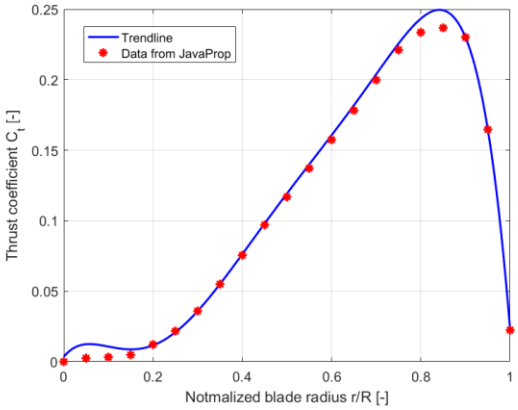

Figure 22: Thrust coefficient distributed over the propeller blade

The polynomial equations represent the torque and thrust coefficient distribution of the propeller's blade, which will be implemented in CFX. Consequently, the torque and thrust distribution over the actuator disc subdomain is introduced in a continuous form to reduce the grid solution's grid dependency.

$$C_q(x) = 4228.3x^6 - 3115x^5 + 1074.9x^4 - 194.71x^3 + 7.76x^2 - 0.0114x + 0.385 \; [Eq.11]$$

$$C_t(x) = -368820x^6 + 24500x^5 - 6215x^4 + 7286.8x^3 - 347.99x^2 + 6.2x + 0.014 \; [Eq.12]$$

There is a difference between the trendline curve and the data points of the thrust coefficient graph. This deviation is not relevant to the objective of this project unless there is a significant difference in the physical behavior of the actuator disc and the predicted Blade Element Method calculation. This difference could easily be compensated by adjusting the required power of the propeller until the average thrust of the propeller matches the integral of the trendline in propeller's subdomain. The propeller's power was increased from 34166 [watt] to 37500 [watt] to compensate for the deviation of the trendline and the data obtained from JavaProp.

[Eq.11] and [Eq.12] were introduced in CFX with the help of CFX Expression Language (CEL). The actuator disc's subdomain was isolated from the rest of the fluid domain and recognized by CFX as a momentum source. The momentum source subdomain requires axial and tangential forces per unit volume [Ref.46], which could be expressed as a constant value or a variable as a function of coordinate points in fluid domain.

The axial and tangential forces that momentum source should introduce into fluid domain were calculated with the help of [Eq.13] and [Eq.14] and then divided by the volume of actuator disc's subdomain. The resulting axial and tangential forces distribution per unit volume over actuator disc's subdomain were then used by CFX to simulate an actuator disc.

$$T(r) = C_t(r).\rho.n^2.D(r)^4 \ [Eq.13] \qquad Q(r) = C_q(r).\rho.n^2.D(r)^4 \ [Eq.14]$$

2.5.2 Actuator Disc thickness

If the exerted propeller's momentum into fluid domain is not distributed over a finite thickness, actuator disc is modeled as a single element geometry. As a result, evaluation of flow properties in the momentum source subdomain becomes more grid dependent, because the first derivative of momentum's distribution function in the momentum source subdomain becomes discontinuous. Depending on the chosen calculation schemes, the solver evaluates these discontinuities which correlate with the mesh size in the corresponding region [Ref.38].

This project considers an actuator disc model with a finite thickness, which means that model distributes thrust and torque over this finite thickness for lower and smoother gradients comparing to a single element geometry.

According to Simisiroglou, Karatsioris, Nilsson, Breton, and Ivanell [Ref.47], changing the thickness of the actuator disc has a negligible effect on the accuracy of the actuator disc model. However, by considering the actuator disc model as a single element geometry, the model becomes more grid dependent. Therefore, it is recommended to define the actuator disc model over a finite thickness. Nevertheless, the thickness of the actuator disc seems not to be a significant parameter, if the solution of the simulation is grid independent [Ref.48]. Section 3.2.4 will later show the influence of the actuator disc's thickness on the simulations.

2.6 Parameters and Objective function definition

In this section, the required parameters and the objective function of the analysis are identified and introduced based on the information and recommendations of the references mentioned earlier in chapter 1.

2.6.1 Secondary wing shape (CST Coefficients)

As Hongbo, Xiaoping, and Zhou [Ref.24] recommended, the influence of the secondary wing on the system's overall performance should be investigated in detail by optimizing the shape of this element.

Characterizing the shape of the secondary wing with CST coefficients is a reliable method to reduce the number of variables as well as reducing the unwanted shapes of an airfoil [Ref.49]. Twelve CST coefficients are used to produce the shape of the secondary wing for the optimization study. These twelve CST coefficients represented the shape of an airfoil accurately with sufficient degree of freedom for the optimization study. However, the number of the coefficients is not too high to increase the calculation cost of the optimization significantly [Ref.50] [Ref.51].

2.6.2 Disc position

According Luijendijk [Ref.29] and Marcus [Ref.30] varying the chordwise position of the propeller significantly affects the system's performance, since changing the position of the propeller alters the propeller's region of influence on the flow field upstream and downstream the propeller. In addition, modifying the surface to propeller spacing is also possible with the established model which could impact the influence of the propeller on the wings.

Moreover, due to the propeller dislocation, the propeller's inlet velocity profile can change and affect the performance of the propeller as well. Modifying the position of the propeller laterally over the span of the wing was not required in this model due to the symmetry and periodic assumptions made on the boundaries of the model.

2.6.3 Objective function

The total lift and drag coefficient of the system were calculated [Eq.15] [Eq.16] based on the planform area of the model as the reference area. Since the secondary wing is on the top of the main wing, the reference area is equal to the main wing's planform area.

$$C_{L_{tot}} = \frac{F_{y_{main}} + F_{y_{sec}}}{q_\infty . S_{ref}} \; [Eq.15] \qquad C_{D_{tot}} = \frac{F_{x_{main}} + F_{x_{sec}}}{q_\infty . S_{ref}} [Eq.16]$$

[Eq.17] shows the definition of the lift to drag ratio, which is considered for this analysis. $C_{D_{ATR72}}$ is the drag coefficient of wingless ATR72, which will be discussed in more detail in section 2.6.4.

$$L/D = \frac{C_{L_{tot}}}{C_{D_{tot}} + C_{D_{ATR72}}} \; [Eq.17]$$

[Eq.18] shows how the overall propulsive efficiency of the system is calculated. The overall propulsive efficiency depends on the sum of the axial forces acting on the system including the main wing and secondary wing's drag and the propeller's thrust.

$$\eta_{pp} = \frac{-V_\infty . F_x}{P} = \frac{-V_\infty . (D_{main} + D_{sec} + T)}{P} [Eq.18]$$

Finally, the objective function of the optimization study was defined as [Eq.19]. The objective of the optimization was to maximize the aerodynamic performance and the overall propulsive efficiency. Considering the overall propulsive efficiency in the objective function of this study, included the effect of wings on the propeller's inflow velocity. The flow accelerates over the upper surface of the main wing and reduces the thrust produced by the propeller according to BEM calculation. Therefore, maximizing the propulsive efficiency could mean minimizing the drag produced by the wing and optimizing the duct shape to reduce the propeller's inflow velocity.

$$J = \frac{1}{2}\left(\frac{\frac{C_L}{(C_D + C_{D_{ATR72}})}}{\frac{C_{L_0}}{(C_{D_0} + C_{D_{ATR72}})}} + \frac{\eta_{pp}}{\eta_{pp_0}} \right) \; [Eq.19]$$

2.6.4 Drag coefficient of ATR72

The initial results in chapter 5.1, and some publications [Ref.24] [Ref.52] [Ref.20] show that the pressure drag due to propeller wing interaction is small and often has a negative value. In this case, another drag component is needed to make the comparison between the results more accessible.

This component is obtained based on the reference aircraft, and it is called the drag coefficient of the wingless aircraft [Ref.31]. According to Nita [Ref.31], the wingless aircraft drag coefficient is roughly calculated to be equal to 0.01107 by only including drag of the fuselage, the vertical and the horizontal tail.

According to Muller [Ref.21], The overall lift to drag ratio of an OTW configuration is sensitive to drag due propeller wing interaction, therefore $C_{D_{ATR72}}$ is used to reduce the dependency of the objective function to the drag coefficient. Moreover, as Muller [Ref.20] shows, the value of the pressure drag due to interaction becomes negative, and it is essential to correct this value for a better comparison between the different cases.

2.7 Boundary Conditions

Freestream flow and fluid domain's boundary conditions are based on ATR72's cruise flight condition. Total pressure of fluid domain's inlet boundary and static pressure of the fluid domain's outlet boundary were calculated based on isentropic relations and freestream Mach number (Assuming that there are no sources of entropy production is present in the fluid domain such as shocks). ATR72's flight altitude is not incorporated in the calculation of the fluid domain boundary properties, and it is assumed that the model is tested in a wind tunnel at sea level.

Initially, it was necessary to establish whether the influence of the compressible flow could be neglected or not. The boundary conditions were chosen so that compressibility effects could be neglected (freestream Mach number does not exceed 0.3), since the density change due to flow velocity is less than 5% in this case [Ref.53] [Ref.54] [Ref.55]. Total pressure of the inlet boundary and static pressure of the outlet boundary of fluid domain were calculated based on freestream Mach number of 0.2 to ensure that the local density change due to flow velocity is smaller than 5%.

$$\frac{P}{P_t} = \left(1 + \frac{\gamma - 1}{2} M^2\right)^{-\gamma/\gamma - 1} \xrightarrow{\gamma = 1.4, M = 0.2, P_t = 1[bar]} P = 0.9724[bar][Eq.\,20]$$

However, the initial tests in chapter 5.1 show that compressibility effects are not negligible since actuator disc induces the flow beyond the Mach number of 0.5. In this case, the freestream conditions are obtained from the reference aircraft cruise condition (Mach number =0.41). The following calculation shows how of the outlet static pressure of fluid domain's outlet boundary is obtained [Ref.53] [Ref.54].

$$\frac{P}{P_t} = (1 + \frac{\gamma - 1}{2} M^2)^{-\gamma/\gamma - 1} \xrightarrow{\gamma=1.4, M=0.41, P_t=1[bar]} P = 0.89[bar][Eq.21]$$

Discussion

As long as isothermal flow assumption does not produce any new flow features, it could be used to simplify the calculations and reduce the cost of the optimization study. The simulations performed under this assumption are not to be interpreted as a genuine finial result. The final and initial point of the analysis and optimization study should be tested with adiabatic flow condition for a final comparison and confirmation.

Modeling and simulating an actual propeller could increase the computational cost of simulations and it can make the grid convergence study quite complicated. Therefore, an actuator disc model was introduced to mimic the influence of a propeller in simulations. According to the work of the previous researchers [Ref.38] [Ref.47], actuator disc models could neglect some of the effects of propeller such as hub effect and tip effect, which are out of the scope of this project. Studying the thickness of actuator disc model could reduce the computational and convergence cost of simulations to the minimum by imposing a smooth gradient over actuator disc's subdomain.

The shape of the wings is defined with twelve CST coefficients to reduce the number design vector elements to the minimum and reduce the cost of the optimization procedure.

The drag coefficient of the wingless aircraft is used to reduce the dependency of the model on the estimated pressure drag. The drag coefficient of the wingless aircraft is also used to correct the negative values of the pressure drag caused by propeller wing interaction. Changing the drag coefficient of the wingless aircraft could help the optimizer to change the criteria of optimization and increase the sensitivity of the model to lift characteristics of the system.

3 Verification and Validation of Numerical Calculations

The CFD simulations are subjected to different sources of error and uncertainty, which are shown in Figure [23]. There are two sources of uncertainty in a CFD simulation namely, input uncertainty and physical model uncertainty. These sources of uncertainty are typically estimated with the help of associating the solution of a simulation to an experiment solution with the same configuration or a verified solution of independent software.

There are also different types of numerical error that should be estimated to verify a CFD simulation namely, discretization error and iterative convergence error. The numerical error is an acknowledged type error, which means that there is a standard procedure to estimate this type of error and it is possible to quantify it. Discretization error and iterative convergence error are two critical types of error that are estimated in this chapter. Round-off error is another type of numerical error in the CFD simulations. Although this type of error is negligible, it can complicate the estimation of discretization error in rare circumstances, which is also addressed in this chapter.

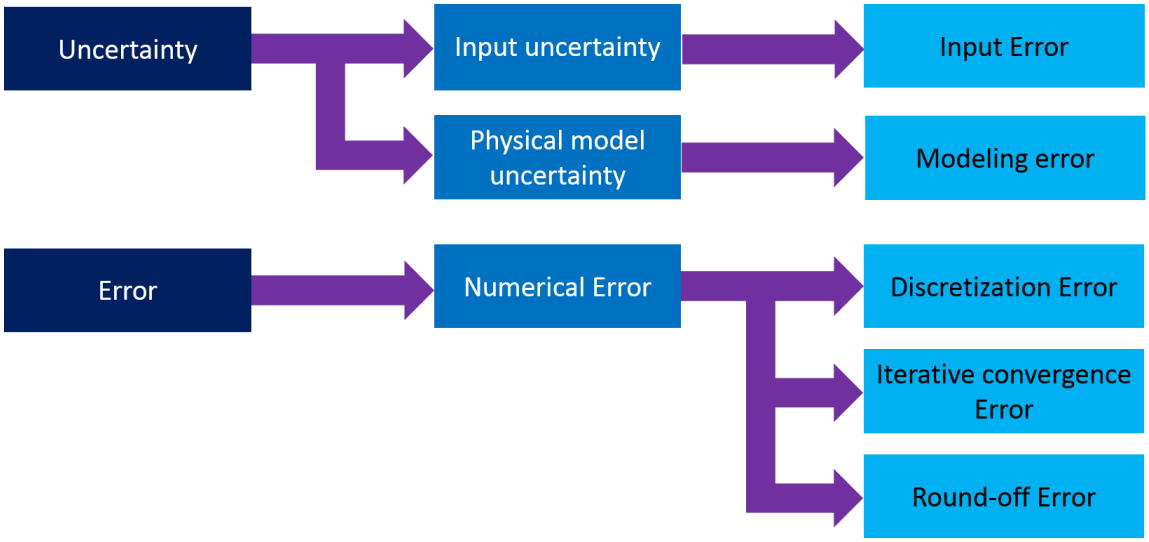

Figure 23: Different sources of error and uncertainty in CFD simulations

3.1 VERIFICATION[8]

After generating the CFD model, it is vital to produce a mesh grid of model for an inexpensive simulation. In other words, solving a discrete form of the problem instead of the continuous form could reduce the cost of analysis significantly. However, the result of discretized function could deviate from its original form. Moreover, this method could eliminate small flow features with smaller scales than the smallest grid size. Therefore, it is imperative to understand what happens to the model while it is out of its continuous form. As an example, the following continuous function [Eq.22] is discretized with the help of differential definition and Taylor series.

$$u\left(\frac{du}{dx}\right) = f_i \; [Eq.22]$$

Rewriting the previous function [Eq.22] in the finite difference expansion results in following form [Eq.23].

$$u_i\left(\frac{u_{i+1} - u_{i-1}}{2\Delta x}\right) = f_i \; [Eq.23]$$

The parameters u_{i+1} and u_{i-1} can be expanded and defined by Taylor series in the following forms of [Eq.24] and [Eq.25].

$$u_{i+1} = u_i + \left[\Delta x \frac{du}{dx}\right]_i + \left[\frac{\Delta x^2}{2!}\frac{d^2u}{dx^2}\right]_i + \left[\frac{\Delta x^3}{3!}\frac{d^3u}{dx^3}\right]_i + \cdots [Eq.24]$$

$$u_{i-1} = u_i - \left[\Delta x \frac{du}{dx}\right]_i + \left[\frac{\Delta x^2}{2!}\frac{d^2u}{dx^2}\right]_i - \left[\frac{\Delta x^3}{3!}\frac{d^3u}{dx^3}\right]_i + \cdots [Eq.25]$$

Substituting the previous terms [Eq.24] [Eq.25] in the finite difference expansion of the initial function results in the modified equation of the partial differential equation. The consistency of discretization is proven when substituting the exact solution into the discrete equations, the only terms that remain are those, which tend to zero as the number of degrees of freedom increases.

[8] Refer to References [38, 56, 57, 58, 59]

In this example, the finite difference expansion of a partial differential equation is approximated by substituting the Taylor series expansion of the exact solution for each solution term, and the result is the modified equation [Eq.26], which includes the truncation error terms too.

$$u_i\left(\frac{u_{i+1}-u_{i-1}}{2\Delta x}\right)=f_i=0+\left[u_i\frac{du}{dx}\right]_i+0+\left[u_i\frac{\Delta x^2}{3!}\frac{d^3u}{dx^3}\right]_i+\cdots[Eq.26]$$

The original partial differential equation appears on the right hand side of the modified equation with an addition of the truncation error that should be solved. The leading truncation error term indicates how the solution will behave. It is crucial to obtain the power of the leading term of the truncation error for the mesh that is analyzed to confirm that the solution is in asymptotic region.

Depending on the chosen advection scheme for the simulations, the power of the leading term of the truncation error can differ. In this case, the central differencing scheme is chosen which contains a leading truncation error term with a power of two. Therefore, obtaining an order of convergence close to two for the grid convergence study could indicate that the results of the simulations are within the asymptotic range of convergence.

3.1.1 Grid convergence study (Incompressible Inviscid flow)

In this study, three simulations of the same model's orientation are performed with three different mesh qualities to estimate the discretization error of the CFD simulation. The mesh density of the coarse grid has been increased locally in the regions of interest, i.e., the regions that the flow velocity, pressure gradients, and geometry curvature are significant, to obtain a mesh with acceptable quality. Finally, the coarse mesh was subjected to refinement globally to create the medium and fine mesh for grid convergence study. The refinement factor is equal to 1.5 to avoid producing a high number of cells in the fine grid. This study was conducted for three different models with different conditions namely isothermal, adiabatic and inviscid flow conditions to estimate the discretization error of the model under different flow conditions.

The following study is conducted for the condition where the inviscid flow characteristics are studied. This study tested a model with the parameters listed in Table [5].

Table 5: Design parameters of the Analyzed model

Main wing Airfoil	NACA0012
Secondary wing Airfoil	NACA0012
Main wing Chord length	2.11[m]
Secondary wing Chord length	30% [cs/C] *
Secondary wing's angle of attack	0 [deg]
Spacing between the two wings	40% [s/C] **
Disc Diameter	0.5[m]
Disc Longitudinal position	100% [x/C] ***
Actuator disc's Thrust	650[N]
Testing Mach number	0.2
Swirl	Accounted
Calculation type	Euler calculations
*Secondary wing chord length normalized by Main wing's chord length **Chord line to Chord line distance between the wings normalized by Main wing's chord length ***Chordwise position of the propeller over the Main wing	

Table 6: Number of elements in each grid

Mesh	Number of elements	Normalized grid spacing
3	900,000	2.25
2	3 million	1.5
1	10 million	1

As it is shown in Table [7], lift and drag coefficient of main wing and secondary wing are considered as parameters and results of this grid study. Table [7] shows the obtained results from three simulations of refined meshes.

Table 7: Values of lift and drag coefficient of the main wing and the secondary wing obtained from different grids

Mesh	$C_{L_{main}}$	$C_{L_{sec}}$	$C_{D_{main}}$	$C_{D_{sec}}$
3	0.257986	-0.736653	0.011956	-0.056103
2	0.262162	-0.751410	0.012125	-0.058405
1	0.264165	-0.757720	0.012202	-0.059364

[Eq.27] determines the order of the convergence, where (r) is the refinement ratio. The theoretical order of convergence is equal to two for a central differencing scheme. However, some factors such as grid quality, shocks or discontinuities could make the calculated order of convergence deviate from the theoretical value. In this case, the order of convergence has converged to two, which is ideal and proves that the results of this study are inside the asymptotic region of convergence.

$$Po = \frac{\ln\left(\frac{f_3 - f_2}{f_2 - f_1}\right)}{\ln(r)} \; [Eq.27]$$

Table [8] shows the calculated order of convergence obtained from the results.

Table 8: Calculated order of convergence from 3 grids of lift and drag coefficient of the main wing and the secondary wing

	$C_{L_{main}}$	$C_{L_{sec}}$	$C_{D_{main}}$	$C_{D_{sec}}$
P_o	1.812	2.095	1.938	2.160

Now with the help of [Eq.28] and the two finest grids, the value of each of these parameters can be estimated at zero grid spacing.

$$P_{r_{h=0}} = f_3 + \frac{f_3 - f_2}{r^p - 1} \; [Eq.28]$$

Table 9: Estimated parameters at zero grid spacing of lift and drag coefficient of the main wing and the secondary wing

	$C_{L_{main}}$	$C_{L_{sec}}$	$C_{D_{main}}$	$C_{D_{sec}}$
$P_{r_{h=0}}$	0.26601	-0.76243	0.01227	-0.06005

[Eq.29] calculates the grid convergence index for the fine grid solution with a safety factor of 1.25 because the order of convergence is calculated with the help of three grids.

$$CGI_{ij} = 1.25 \times \left|\frac{f_i - f_j}{f_i}\right| \times (r^p - 1)^{-1} [Eq.29]$$

Table 10: Grid convergence index of lift and drag coefficient of the main wing and the secondary wing

	$C_{L_{main}}$	$C_{L_{sec}}$	$C_{D_{main}}$	$C_{D_{sec}}$
GC12 *	0.87%	0.78%	0.66%	1.44%
GC23 **	1.84%	1.83%	1.46%	3.52%
GC23/GC12	2.101	2.358	2.208	2.440
*Medium grid to Fine grid ** Coarse grid to Medium grid				

Finally, [Eq.30] can be used to check that the solutions are within the asymptotic range of convergence. If the value of C is close to one, then it can be assumed that the solutions are within the asymptotic range of convergence.

$$C = \frac{CGI_{23}}{(r^p \times CGI_{12})} \; [Eq.30]$$

Table 11: Asymptotic region check

	$C_{L_{main}}$	$C_{L_{sec}}$	$C_{D_{main}}$	$C_{D_{sec}}$
Asym-check	1.008	1.008	1.006	1.016

In conclusion, with the help of the grid convergence study, it is possible to estimate the discretization error band of each parameter.

Table 12: Estimated parameters with the discretization error band (Inviscid flow condition)

	$C_{L_{main}}$	$C_{L_{sec}}$	$C_{D_{main}}$	$C_{D_{sec}}$
Value± Error%	0.26601± 0.87%	-0.76243± 0.78%	0.01227± 0.66%	-0.06005± 1.44%

3.1.2 Grid convergence study (Adiabatic and Isothermal flow condition)

The discretization error of model under the assumption of isothermal and adiabatic flow condition is quantified with the help of the same procedure from chapter 3.1.1. In short, a comparison between the results shows that by considering the compressibility effects, the outcome of the simulations become more dependent on the discretization error of the model.

Table 13: Design parameters of the Analyzed model

Flow condition	Adiabatic	Isothermal
Main wing Airfoil	NACA48015	NACA48015
Secondary wing Airfoil	NACA48015	Optimized Airfoil
Main wing Chord length	2.11[m]	2.11[m]
Secondary wing Chord length	30% [cs/C] *	32.4%[cs/C] *
Secondary wing's angle of attack	0 [deg]	0 [deg]
Spacing between the two wings	33.5% [s/C] **	40% [s/C] **
Disc Diameter	0.5[m]	0.5[m]
Disc Longitudinal position	85% [x/C] ***	85% [x/C] ***
Actuator disc's Thrust	250[N]	250[N]
Testing Mach number	0.41	0.41
Calculation type	Euler calculations	Euler calculations
*Secondary wing chord length normalized by Main wing's chord length **Chord line to Chord line distance between the wings normalized by Main wing's chord length ***Chordwise position of the propeller over the Main wing		

Table 14: Number of elements in each grid depending on the flow conditions

Mesh	Number of cells (Adiabatic)	Number of cells (Isothermal)	Normalized grid spacing
3	2.4 million	1.4 million	2.25
2	8 million	4.7 million	1.5
1	27 million	16 million	1

Table 15: Values of lift and drag coefficient of the main wing and the secondary wing obtained from different grids of adiabatic and isothermal flow conditions

Adiabatic	$C_{L_{main}}$	$C_{L_{sec}}$	$C_{D_{main}}$	$C_{D_{sec}}$
3	0.314853	0.208671	0.002194	-0.005605
2	0.316004	0.209641	0.002063	-0.006093
1	0.316475	0.21003	0.00201	-0.006282
Isothermal	$C_{L_{main}}$	$C_{L_{sec}}$	$C_{D_{main}}$	$C_{D_{sec}}$
3	0.342309	0.154854	0.003786	-0.010603
2	0.342146	0.162127	0.003576	-0.011440
1	0.342080	0.165354	0.003486	-0.011763

Table 16: Calculated order of convergence from 3 grids of lift and drag coefficient of the main wing and the secondary wing of adiabatic and isothermal flow condition

	$C_{L_{main}}$	$C_{L_{sec}}$	$C_{D_{main}}$	$C_{D_{sec}}$
P_o (Adiabatic)	2.204	2.254	2.232	2.339
P_o (Isothermal)	2.230	2.004	2.090	2.346

Table 17: Estimated parameters at zero grid spacing of adiabatic and isothermal flow condition

	$C_{L_{main}}$	$C_{L_{sec}}$	$C_{D_{main}}$	$C_{D_{sec}}$
$P_{r_{h=0}}$ Adiabatic	0.317	0.210	0.002	-0.0064
$P_{r_{h=0}}$ Isothermal	0.34204	0.16793	0.00342	-0.01197

Table 18: Grid convergence index of lift and drag coefficient of the main wing and the secondary wing

Adiabatic	$C_{L_{main}}$	$C_{L_{sec}}$	$C_{D_{main}}$	$C_{D_{sec}}$
GC12 *	0.13%	0.16%	2.24%	2.38%
GC23 **	0.32%	0.39%	5.39%	6.33%
GC23/GC12	2.447	2.498	2.408	2.662
Isothermal	$C_{L_{main}}$	$C_{L_{sec}}$	$C_{D_{main}}$	$C_{D_{sec}}$
GC12 *	0.02%	1.95%	2.42%	2.16%
GC23 **	0.04%	4.47%	5.51%	5.75%
GC23/GC12	2.469	2.299	2.275	2.662
*Medium grid to Fine grid ** Coarse grid to Medium grid				

In conclusion, with the help of the grid convergence study, it is possible to estimate the discretization error band of each parameter.

Table 19: estimated parameters with the discretization error band of adiabatic and isothermal flow condition

	$C_{L_{main}}$	$C_{L_{sec}}$	$C_{D_{main}}$	$C_{D_{sec}}$
Value± Error% (Adiabatic)	0.3168± 0.13%	0.2103± 0.16%	0.002± 2.24%	-0.0064± 2.38%
Value± Error% (Isothermal)	0.34204± 0.02%	0.16793± 1.95%	0.00302± 2.42%	-0.01197± 2.16%

Discussion

This verification study was conducted to ensure that Navier-Stokes equations are solved with an acceptable margin of error. In this study, the model was tested and simulated with three different flow conditions. The grid convergence study was conducted for all flow conditions to ensure that the simulation captures different flow feature under different flow conditions. Moreover, it was crucial to reduce the number of grid elements as much as possible to avoid an unnecessary rise in computational power. The optimization study uses isothermal condition, and therefore the corresponding discretization error and grid orientation are used for the optimization study. Based on the discretization error estimated for isothermal flow condition, the minimum change of variables in the optimization study was defined. However, the initial and optimized point of the optimization study is simulated with adiabatic flow condition, therefore, the discretization error of the adiabatic grid convergence study is used as the error band of final results of the optimization.

3.1.3 Iterative Convergence Error

CFD problems are typically calculated and solved iteratively. In these problems, there are different sources of numerical errors such as convergence error. The difference between the iteratively solved numerical solution and the exact answer is called the convergence error. The difference between the numerical solutions of the last two iterations is called residual, which is an indication of the solution convergence to the exact answer. Table [20] illustrates the iterative solution of a simulation with different residuals. Table [20] shows that as the residual decreases, the solutions converge to a solution. In this case, the maximum residual should not exceed 10^{-5} since the solutions with higher residual deviate more than 5% from the converged value. On the other hand, using a smaller value of residual could increase the number of iterations. Setting a small residual could increase the computational cost of the simulation, which is not desirable for the optimization procedure. It is advised to perfume the final simulations with as low as possible residual to reduce the convergence error to a minimum [Ref.60].

Table 20: Evaluating and performing CFD simulation with different residual to estimate the convergence error, the model uses NACA6415-62 airfoil as the secondary wing shape with 34% (of main wing's chord length) gap between the main wing and the secondary wing, the convergence error is estimated with respect to the residual value of 10^{-7}

NACA 6415-62, 34% gap	1.00E-03	1.00E-04	1.00E-05	1.00E-06	1.00E-07
$C_{L_{main}}$	0.27636	0.30564	0.31915	0.32116	0.32138
$C_{L_{main}}$ iterative error	14.0%	4.9%	0.7%	0.06%	0%
$C_{L_{sec}}$	0.11652	0.20492	0.20925	0.20912	0.20908
$C_{L_{sec}}$ iterative error	44%	2%	0.08%	0.02%	0%
$C_{D_{main}}$	0.02167	0.00449	0.00229	0.00225	0.00226
$C_{D_{main}}$ iterative error	858%	98%	1%	0.88%	0%
$C_{D_{sec}}$	0.001	-0.0016	-0.00376	-0.00384	-0.00381
$C_{D_{sec}}$ iterative error	126%	58%	1.3%	0.78%	0%
$C_{L_{tot}}$	0.31131	0.36712	0.38193	0.3839	0.3841
$C_{L_{tot}}$ iterative error	19%	4.4%	0.56%	0.05%	0%
$C_{D_{tot}}$	0.02196	0.004	0.00125	0.00124	0.00122
$C_{D_{tot}}$ iterative error	1700%	220%	2%	1.6%	0%
L/D	9.42	24.36	31	31.18	31.25
L/D iterative error	70%	22%	0.8%	0.22%	0%
Number of iterations	81	187	326	475	625

3.1.4 Round-off Error

Round-off error is a result of the computational representation of real numbers. This error is generated by accepting only a specified maximum number of digits for a real number. Subtracting almost equal sized large numbers or addition of numbers with a significant difference could increase the influence of Round-off error. As an example, in many CFD codes, it is common to use gauge pressure relative to specific base pressure; This ensures that the pressure values in the domain are of the same order as the pressure difference that drives the flow. However, if the calculation between the cells were performed with comparatively sizeable absolute pressure values, it could result in loss of significant digits [Ref.56].

Round-off error could complicate the estimation of the model's discretization error. In this case, if the grid convergence study requires a coarse mesh with tiny cell size, either locally or globally, for the study to be in the asymptotic region of convergence, the difference between the solution of the medium mesh and the fine mesh could be affected by the round-off error. Figure [24] shows the influence of the round-off error on the grid convergence study.

The red dots and blue dots in Figure [24] represent two different grid convergence studies. The blue dots represent a grid convergence study that is in asymptotic region of convergence, and the red dots represent the grid convergence study that is not in the asymptotic region of convergence due to the influence of the round-off error. In this case, it is assumed that the iterative tolerance is small enough for the solution to be sensitive to round-off error, which does not often happen in reality.

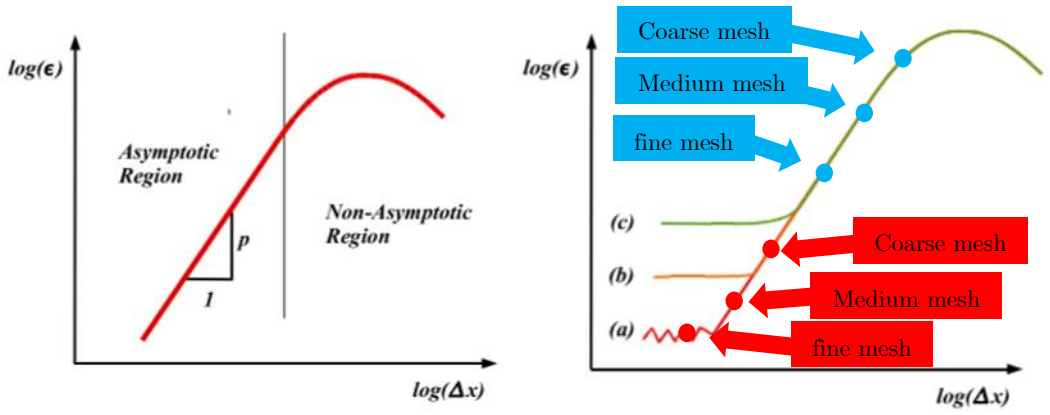

Figure 24: On the left: Log error plotted versus the log of the mesh spacing for a scheme of order p. On the right: Leveling off of convergence due to (a) round-off error, (b) insufficient tolerances for iterative solution procedures, (c) incompatible refinement [Ref.56]

3.2 VALIDATION

3.2.1 Physical Model Uncertainty and Code validation

CFX is a Computational fluid dynamic solver that does not include an inviscid flow model. Therefore, the settings in this program should be chosen accordingly to simplify the Navier-Stokes equations to disregard flow's turbulence, viscosity and wall shear stress Only adopting the setting in a program is not reliable and validating the solution is necessary. To validate the Euler calculations performed by CFX, the solution of a simple 2D simulation should be compared to another validated program such as Xfoil. This simulation is carried out on a NACA08121 airfoil at low speed flow conditions (Mach number=0.2) [Ref.46].

According to Kutta-Joukowski theorem the resultant force acting on a body element is perpendicular to freestream direction, and therefore any force parallel to flow direction is caused by numerical error unless there are other external forces present [Ref.61]. Consequently, the component of the resultant force acting on a body parallel to freestream direction is equal to zero. This validation study associates the component of resultant force acting on the airfoil normal to the freestream direction (lift force) estimated by CFX to the solution of other validated programs. To estimate the lift coefficient of the airfoil by CFX, discretization error should be estimated to realize weather the outcome of the simulation is within the asymptotic region of convergence [Ref.38].

Table 21: CFX code validation for potential flow calculation

Parameter	Coarse mesh 1	Medium mesh 2	Fine mesh 3	P_o	$P_{r_{h=0}}$	GCI12*	GCI23**	Asym. check
$C_{L_{main}}$	0.4586	0.5046	0.5161	1.998	0.52003	0.93%	3.8%	1.022
*Medium grid to Fine grid ** Coarse grid to Medium grid								

According to this study, the estimated lift coefficient of the airfoil by CFX is equal to 0.52±0.93%. The calculated lift coefficient for the same airfoil in Xfoil is equal to 0.5165 which validates the assumptions made in CFX. The drag component calculated in CFX for this model is equal to zero which proves that Kutta-Joukowski theorem holds in this simulation and CFX is purely performing inviscid flow calculations.

3.2.2 Fluid Domain Boundary Error

As it was explained chapter 2.7, the boundary conditions were defined by prescribing total pressure at the fluid domain's inlet boundary and static pressure at the fluid domain's outlet boundary. The effect of constant static pressure at the outlet boundary could influence the solution. Since flow needs to recover its static pressure to reach the boundary condition imposed on the fluid domain's outlet, the length of the fluid domain affects the rate of pressure recovery. This type of modeling error is small and could be considered negligible. After increasing the length of fluid domain by main wing's chord length, the observed difference was extremely small and could not be distinguished from other sources of error. Therefore, the fluid domain was extended by twenty chord lengths, in the next step, to observe the effect of this modeling error on the evaluated parameters.

Table 22: Parameters of two different lengths of the fluid domain, initial case modeled the fluid domain 10 chords long and the second case extends the fluid domain 20 chords from outlet

Case	$C_{L_{main}}$	$C_{L_{sec}}$	$C_{D_{main}}$	$C_{D_{sec}}$
10 chord lengths	0.344379	0.162757	0.0039278	-0.00937004
30 chord lengths	0.35212	0.166768	0.00384276	-0.00925825
Difference	2%	2%	2%	1%

3.2.3 Actuator disc model validation

This section aims to investigate the influence of actuator disc's thickness on actual added momentum in fluid domain. In this case, two actuator disc models with thicknesses of 2% and 10% of propeller's diameter were simulated by CFX. The prescribed thrust by user and the actual added axial momentum to flow were compared in Table [24].

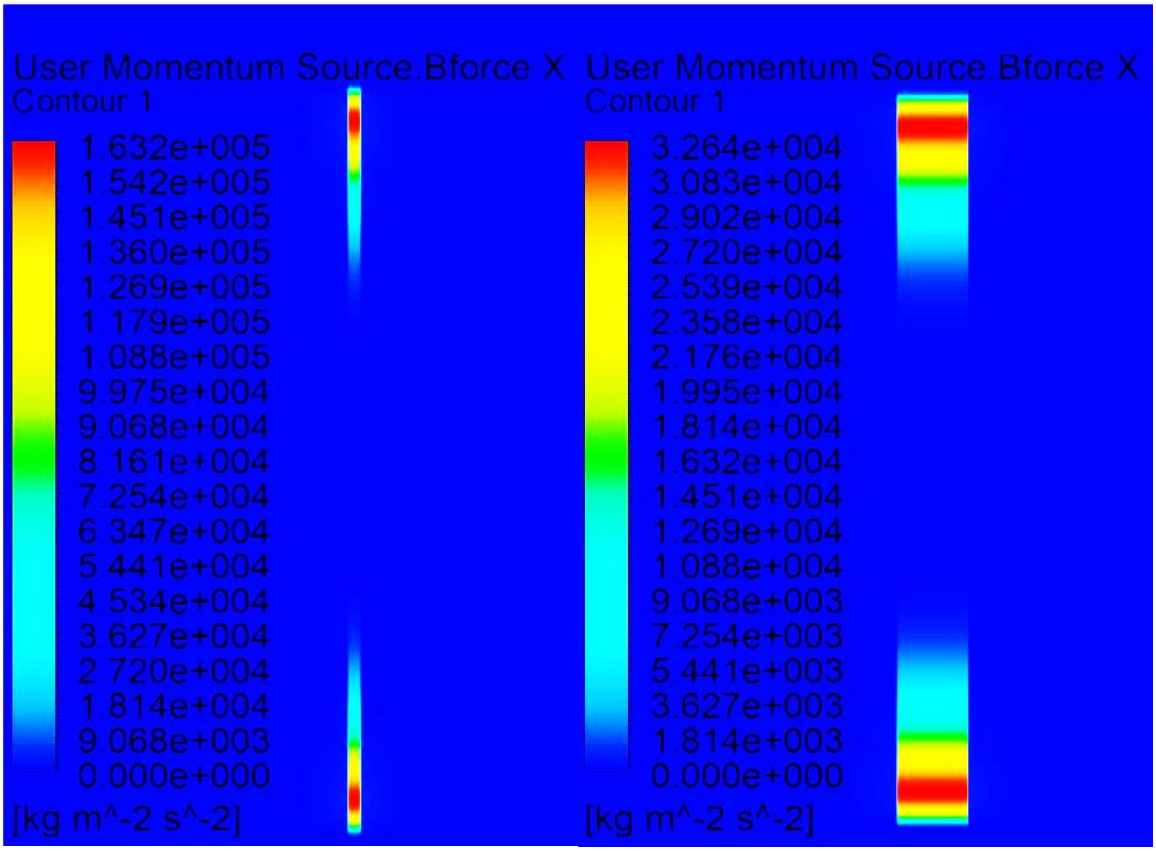

Figure 25: Volumetric axial momentum distribution in disc region for two cases of 2% and 10% disc thickness

As Table [23] shows, by increasing actuator disc's thickness, the difference between actual added momentum and the prescribed value decreases. This means that by increasing actuator disc's thickness, distribution of momentum along disc's thickness becomes smoother and the actuator disc model becomes less grid dependent. It is evident from Figure [25] that the volumetric momentum added in actuator disc's subdomain is smaller in case of 10% disc thickness compared to the disc with 2% thickness since the same momentum was distributed over a larger thickness.

The previous cases considered uniform distribution of momentum along disc's thickness. The first derivative of the distribution function in the previous cases is discontinuous on the bounds of the disc's subdomain, which increases the model's grid dependency. The same momentum is distributed along the disc's thickness with help the following function [Eq.31] to reduce the model's grid dependency.

$$C_T(x) = C_T \times 30\big(x(x-1)\big)^2 \text{ [Eq. 31]}$$

Table [23] shows that by distributing the momentum along the disc's thickness as a function of [Eq.31], simulation became more stable and the actual added momentum to fluid domain is closer to the theoretical value, since the first derivative of the distribution function is continuous in disc's subdomain.

Figure [26] shows the distributed axial momentum in disc's subdomain as a function of $30\big(x(x-1)\big)^2$ along the actuator disc's thickness.

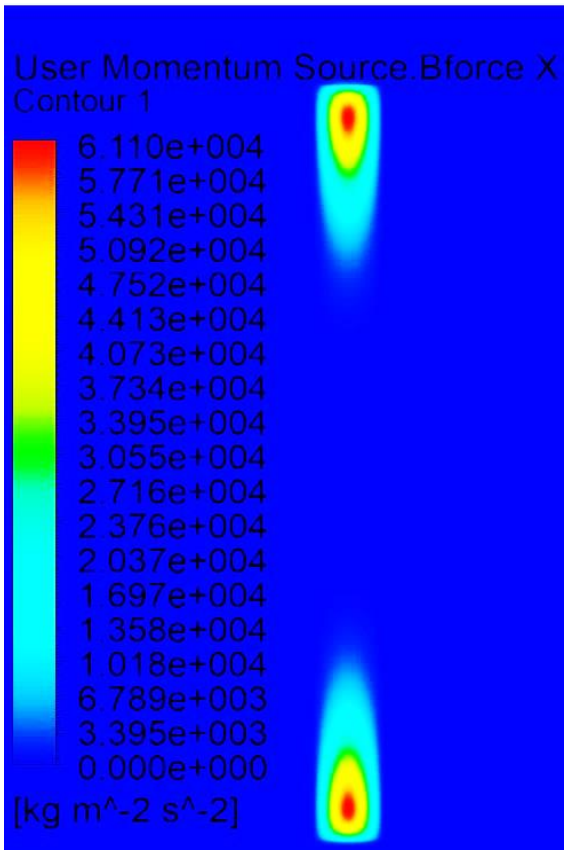

Figure 26: Volumetric axial momentum distributed as a function of $30\big(x(x-1)\big)^2$ over the thickness of the disc

Table 23: Results of the actuator disc's thickness study

Case	Theoretical	Actual added Thrust	Rate of Convergence
2% thickness	130 [N]	118.29 [N]	Unstable
10% thickness	130 [N]	127.57 [N]	Unstable
$30\big(x(x-1)\big)^2$ 10% thickness	130 [N]	129.98 [N]	Stable, fast convergence

3.2.4 CFD vs. Experiment (Modeling Error Estimation)

In this project, many assumptions had to be made to simplify the CFD simulations. However, every assumption could eliminate a different physical phenomenon from the analysis such as viscous effects, compressibility effects, influence of surface roughness, humidity, fluid properties of a nonideal gas, effects of propeller's hub, nacelle, and so forth. A CFD simulation was performed based on an experiment conducted on propeller wing interactions to realize how the constructed model correlates to realistic scenarios. It is challenging to accurately quantify the modeling error since in this scenario the experimental setup did not include a secondary wing. However, a qualitative statement about the differences between the simulations and experimental results could help to establish how the constructed model correlates with real situations. In this case, the following experiment performed by Marcus [Ref.30] [Ref.62] is replicated with help of CFD simulation.

Table 24: Parameters of the experimental setup

Wing chord length	0.6 [m]
Freestream Velocity	41 [m/s]
Advance ratio of the propeller	0.7 [-]
Angle of Attack of the wing	2.08 [Deg]
Thrust Coefficient of the Propeller [C_T]	0.122 [-]
Power Coefficient of the Propeller [C_P]	0.1019 [-]

The four bladed propeller model has a diameter of 0.237 [m], a blade chord of 7.8% of the propeller diameter, and a pitch angle of 23 degrees at 75% of the propeller's radius. The propeller was driven by a 7.5hp three phase induction motor housed in a nacelle with 0.07 [m] diameter [Ref.62].

Figure [27] and Figure [28] illustrate the model's dimensions and the orientation of propeller with respect to the wing. The case where the propeller is placed at 85% chordwise position of the wing is modeled and simulated with help of CFX. There are two main differences between the experimental setup and the CFD model. The CFD analysis did not take the effect of hub and nacelle into account, and also the gap (slot) between the flap and main wing was not modeled.

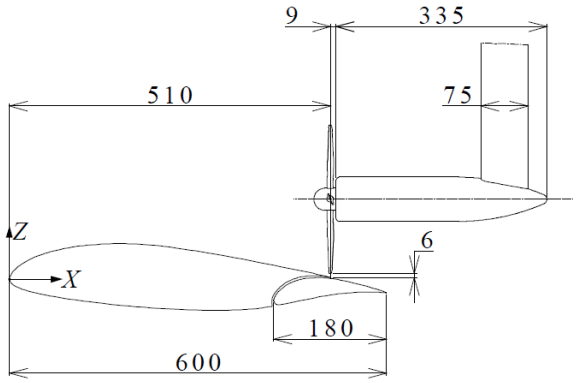

Figure 27: The dimensions and the configuration of the experimental setup, NLF-MOD22B airfoil designed at Delft University of Technology is used as the airfoil of the wing, the propeller is

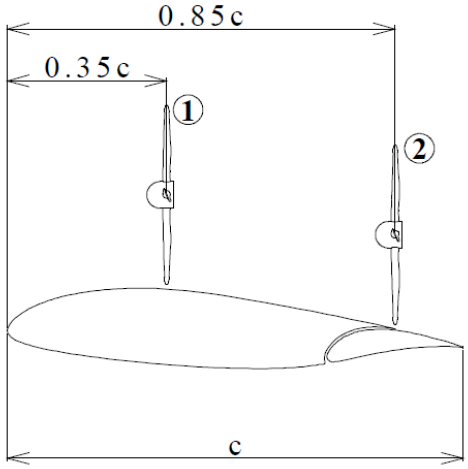

Figure 28: The propeller's location with respect to the wing, the propeller's position of the case number 2 is the subject of this study with chordwise position of 85%

Figure [29] and Figure [30] show the pressure coefficient of the wing at 50% spanwise position in two different situations namely, without the propeller and with the propeller operating. As clean wing graph shows, there are some small differences between the calculated and experimented data. These differences on the pressure side of the wing are caused by the presence of the slot between the main wing and the flap. Moreover, the small deviation between the data on the suction side of the wing could have been created by the presence of the propeller, which is not taken into account in the CFD simulation where the propeller is not operative.

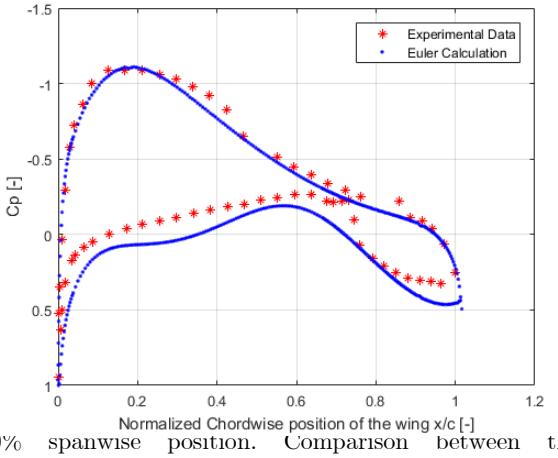

50% spanwise position. Comparison between the experimental data [Ref.30] and Euler calculation performed by CFX of the clean wing (without the influence of the propeller), the slight difference in the pressure coefficient values on the pressure side of the airfoil is due to the gap between the main wing element of the wing and the flap

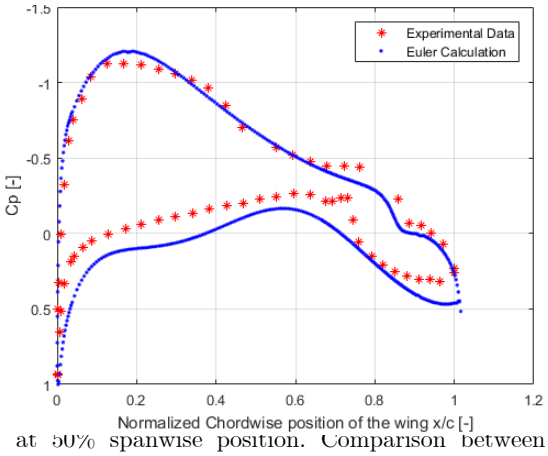

at 50% spanwise position. Comparison between the experimental data [Ref.30] and Euler calculation performed by CFX of the case where the propeller is located over the wing. On the suction side the sudden change in the pressure at 85% chordwise position is due to the influence of the propeller

Figures [31] and Figure [32] show the 3 dimensional pattern of the pressure coefficient over the upper and lower side of the wing. Figure [33] shows the experimental data, which is comparable with Figure [31] and Figure [32]. The spanwise length is normalized by the propeller's diameter for a more straightforward comparison.

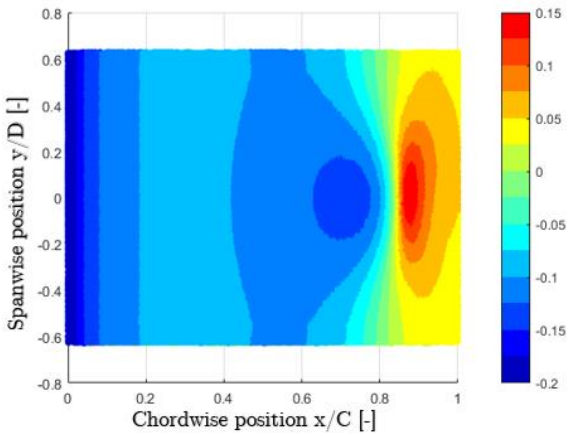

Figure 32: Pressure coefficient (C_p) difference of the suction surface between the clean wing and the wing with the influence of the propeller

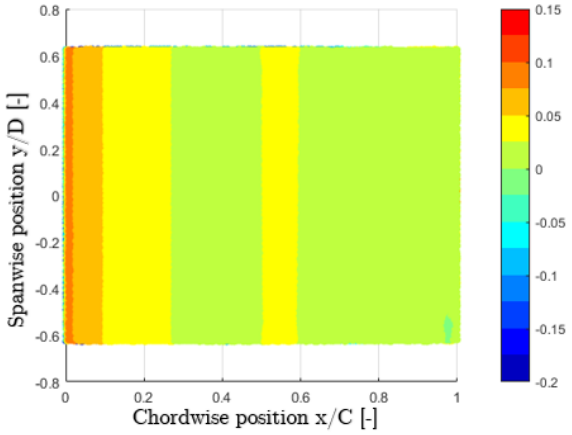

Figure 31: Pressure coefficient (C_p) difference of the pressure surface between the clean wing and the wing with the influence of the propeller

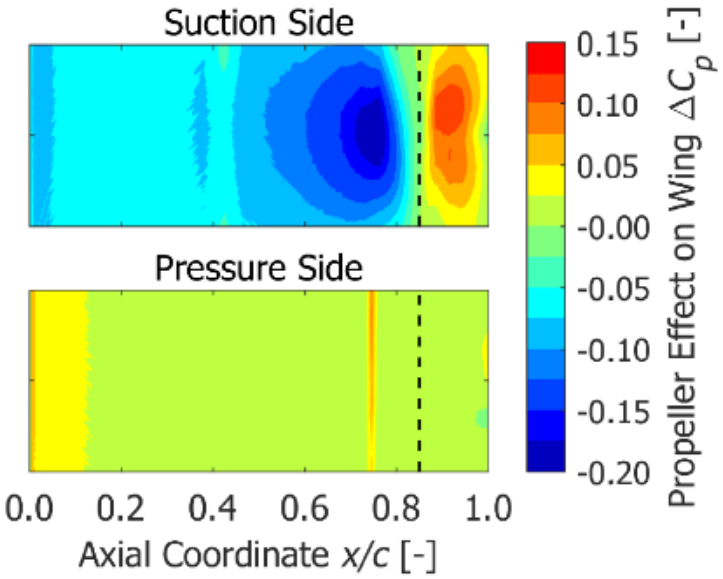

Figure 33: Experimental results [Ref.30], the pressure coefficient difference between the clean wing and the wing with the influence of the propeller on the suction and pressure side, the span length of the wing is 120% of the propeller diameter

As it is shown in Figure [31], Figure [32] and Figure [33], general flow characteristics of propeller wing interaction are captured by the numerical analysis. The outcome of the simulation indicates that the propeller is inducing the flow over the upper surface of main wing, which is in agreement with the experimental data. Moreover, the lower side of the wing shows no significant change in pressure coefficient except on the leading edge, which is slightly overestimated by the CFD simulation.

It is difficult to comment on the source of the differences between the experimental data and the solution of the numerical analysis. However, looking at the modeling differences between the two setups such as influence of the gap between the main wing and the flap, actuator disc model and absence of the propeller in clean wing simulation indicates some of the differences between the numerical solution and the experimental data.

In conclusion, according to this study, the constructed model captures the general flow features of the propeller wing interaction and the CFD simulations adequately represent an actual setup.

4 Effect of the wings on the Propeller

As the propeller's chordwise position, the shape of the secondary wing and the shape of the main wing are modified, the inflow velocity that the propeller experiences changes. These effects can influence the propeller's performance and the amount of thrust that the propeller produces, which can influence pressure forces induced on the wings. Initially, the propeller characteristics were calculated with respect to the freestream flow velocity by which the first iteration and the first CFD simulation was performed.

For the second iteration, the inlet flow velocity of the disc was measured, and the propeller's characteristics were recalculated. This procedure continues until the difference between the inlet flow velocity of the last two simulations was within an acceptable range of error, which was fixed to 1% deviation in this case. This process cold become very costly and could increase the calculation cost by two to four times.

Consequently, it is more desired to perform the optimization procedure with the assumption of constant thrust for the propeller, which could help to reduce the calculation cost, in the beginning. However, the effect of the propulsive efficiency on the objective function and the influence of the change in propeller characteristics could be simplified significantly and change the procedure of the optimizer. Therefore, in the final step, a comparison between the initial and optimum design with the appropriate propeller setting should be performed to include this effect in the calculations as well.

4.1 Uniform Vs. Non-uniform Propeller's inflow velocity

4.1.1 Uniform propeller's inflow velocity

Figure [34] and Figure [35] are the screenshots taken from JavaProp program that applies Blade Element Method calculations to obtain the propeller's characteristics in different conditions. Figure [35] shows the case where the propeller's thrust profile is calculated based on the freestream velocity. Figure [34] shows the propeller's characteristic calculated based on the local surface averaged inlet flow velocity. The average inlet flow velocity of the disc is obtained from the inlet surface of the disc in the CFD simulation where the propeller's characteristics was based on the freestream flow conditions.

The difference between the produced thrust force in the two scenarios is not negligible, and it should be taken into account. In this case, the average flow velocity is used to calculate the propeller's thrust profile and the new propeller's thrust profile is then implemented in the model and used to perform the second CFD simulation.

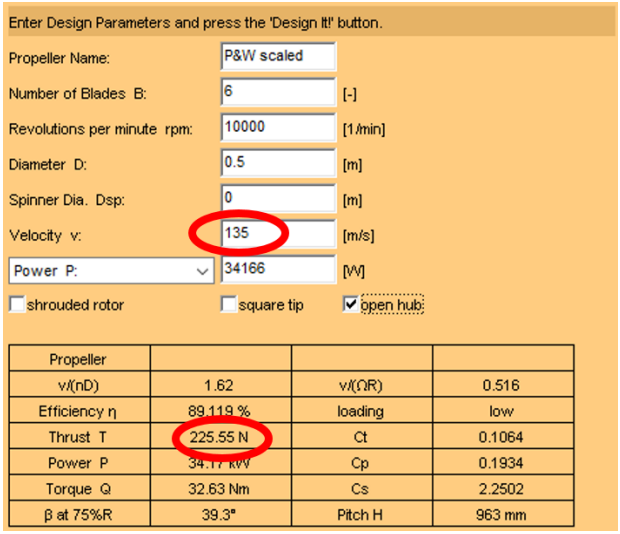

Figure 35: Screenshot taken from JavaProp which is based on Blade Element Method calculation, this particular case calculates the propeller's characteristics based on the freestream velocity

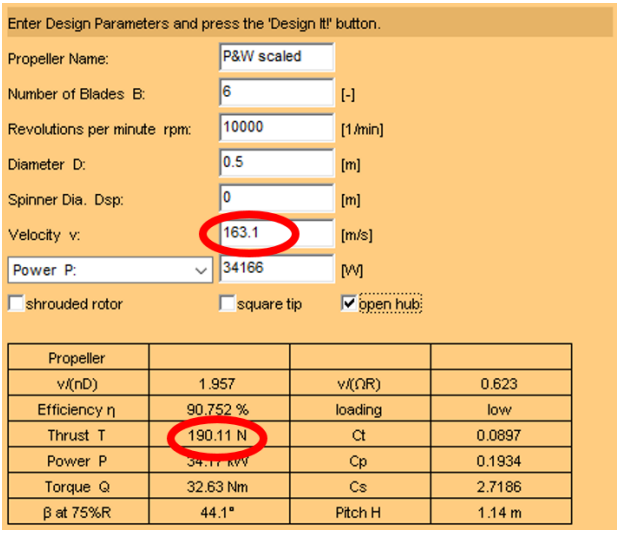

Figure 34: Screenshot taken from JavaProp which is based on Blade Element Method calculation, this particular case calculates the propeller's characteristics based on the local average inlet flow velocity of propeller

4.1.2 Non-uniform propeller's inflow velocity (Disturbed flow)

Figure [36] shows that the propeller's inlet is divided into 16 pieces, and the propeller's characteristics were calculated separately for each of these pieces based on the local inlet flow velocity to obtain the propeller's characteristics based on the disturbed inflow of the propeller. Figure [37] and Figure [38] show the real inlet velocity profile obtained from the actuator disc's surface and the linear trendline that represents the disturbed flow in JavaProp is calculated.

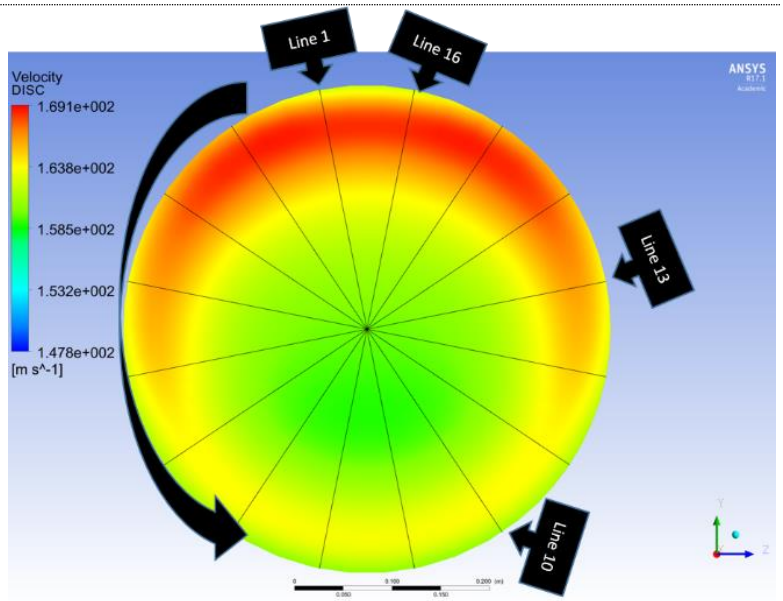

Figure 36: Propeller's inlet divided into 16 pieces to represent the disturbed flow conditions

The software that was used to calculate the thrust profile of the propeller could not handle the actual inlet velocity profile of the propeller. However, it is possible to represent the disturbed flow with a linear trendline in JavaProp software. Figure [37] and Figure [38] are examples of how the disturbed flow is represented in JavaProp.

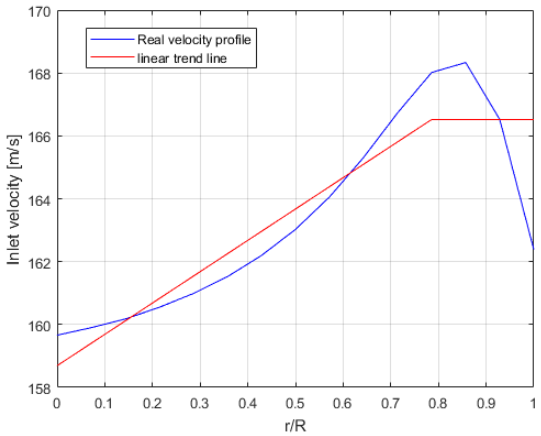

Figure 38: Actual velocity profile and its trendline at line number one specified in figure [68]

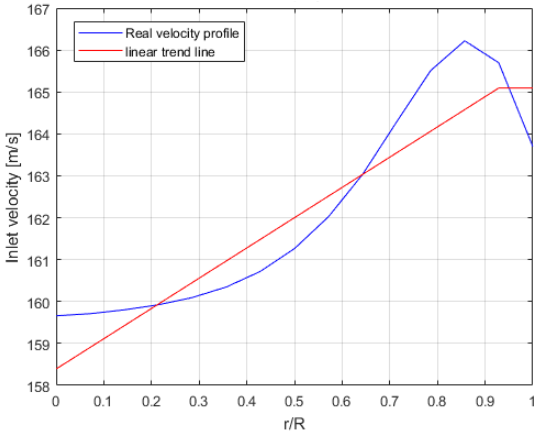

Figure 37: Actual velocity profile and its trendline at line number thirteen specified in figure [68]

Figure [39] demonstrates the necessary steps taken to calculate the propeller's characteristics for each piece of the propeller's inlet. Based on the calculated linear trendline of the inlet velocity profile of the propeller, the shape of the disturbed flow was implemented in JavaProp.

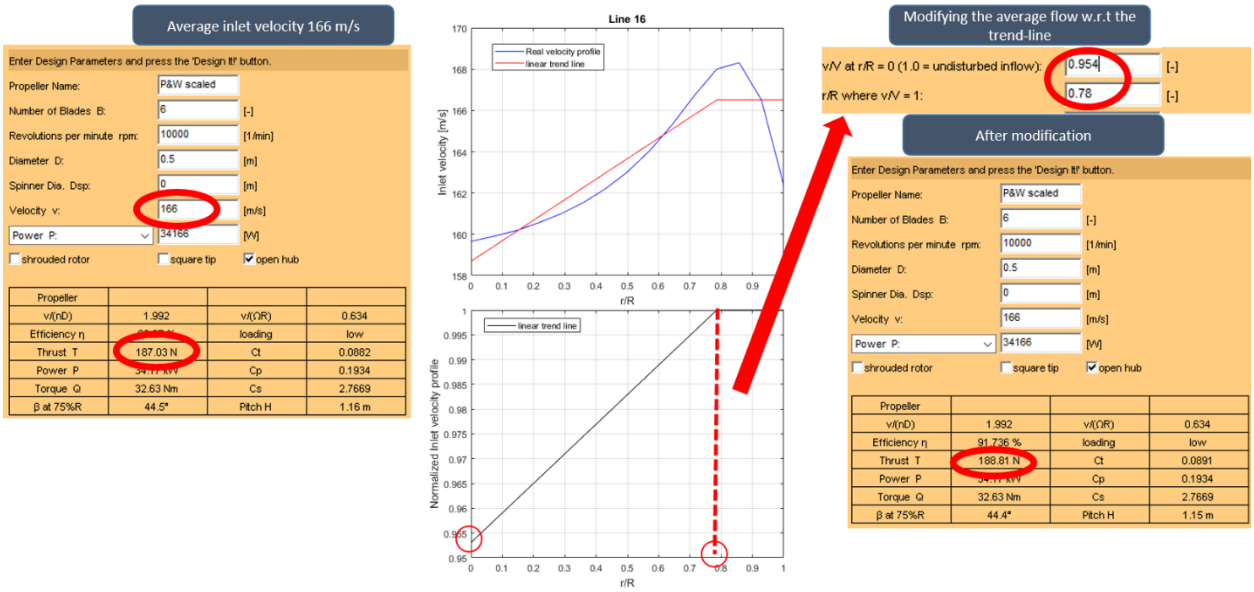

Figure 39: Required steps to calculate the propeller's characteristics for local inlet velocity, the difference between the disturbed and undisturbed flow is not larger than 0.8%

Table [25] shows that there is a small difference between the cases where uniform and non-uniform inflow velocity of the propeller were considered since flow velocity does not fluctuate abundantly in the duct. Considering the complicated procedure of incorporating non-uniform velocity profile in the simulations, it was decided to consider propeller's inflow velocity uniform to calculate the propeller's characteristics.

Table 25: Parameters and results of different assumptions for inlet flow effects

Case	Inlet Velocity	Thrust [N]	η_{prop}*	$C_{L_{tot}}$	$C_{D_{tot}}$
Freestream	133.4 m/s	249.1 [N]	0.885	0.356	0.000441
Uniform	163.1 m/s	213.5 [N]	0.907	0.353	0.000522
Non-uniform	Variable	211.2 [N]	0.907	0.352	0.000525
*Propeller's Efficiency					

4.2 Constant Power Vs. Constant Thrust

In chapter 5.5, the system's performance was examined by varying the propeller's position. In that study, the characteristics of the propeller were obtained under the assumption that propeller was driven with constant power and produces variable thrust depending on the propeller's average inflow velocity. Therefore, the effect of the wings on the disc's performance, which could also influence the system's aerodynamic performance was not neglected. The Figures [75,76,77] show the aerodynamic characteristics of the model where the propeller is operating with constant power as the position, and the inlet flow velocity of the disc varies. This method is very costly to be included in the optimization study. Therefore, the assumption where the propeller operates under constant thrust should be investigated to understand if the model could be simplified for the optimization study within an acceptable margin of error.

4.2.1 Constant Thrust

This section aims to vary the position of propeller with constant thrust assumption for the propeller to investigate the differences between the assumption of constant thrust and constant power for the propeller. Table [26] specifies the propeller's specification obtained from BEM calculation.

Table 26: Propellers specification with constant thrust assumption

Parameters	Values
Number of Blades	6
RPM	10,000
Advance ratio	1.6
Power	Constant ,37500 [watt]
Thrust	Constant, 250 [N]
Inlet flow velocity	Constant, 133.4 [m/s] freestream velocity
Propeller's Efficiency	89.4%
Power Coefficient	0.0689 [-]
Thrust Coefficient	0.0560 [-]

Figure [40] and Figure [41] show the variation of the lift and drag coefficient of the system regarding the propeller's. The total drag coefficient decreased as the propeller was moved forward and the lift coefficient of the system increased as the propeller was moved closer to main wing's surface and rear end of the main wing.

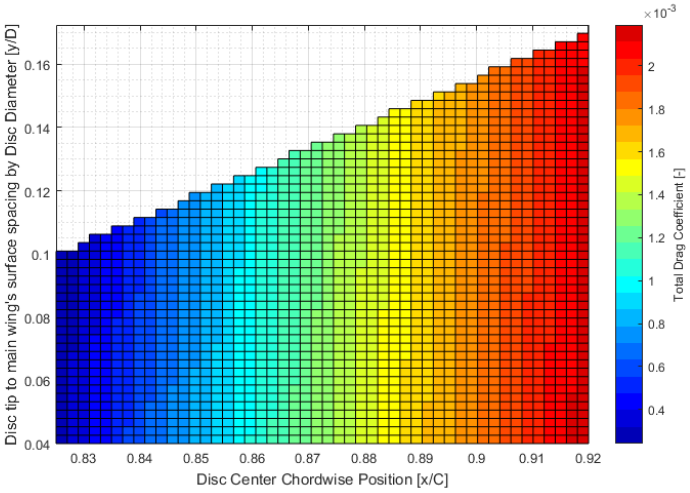

Figure 40: Total drag coefficient of the system as a function of propeller's location, the position of the propeller is defined with the propeller chordwise position and propeller's tip clearance from the main wing's surface normalized by the propeller's diameter, the simulations are performed with adiabatic flow condition and constant thrust assumption for the propeller

Comparing Figure [76] to Figure [41] confirms that in fact, the difference between the lift coefficient estimation of constant thrust assumption and constant power assumption is not significant. The general behavior of the system remaind the same under both assumptions, however, comparing the drag coefficient of the model with Figure [40] and Figure [75] shows that the drag coefficient was overestimated by about 60% by not including the influence of the propeller's inflow effect which could not be overlooked. However, by including the drag coefficient of the wingless aircraft in the objective function, the influence of the drag variations could be dampened and neglecting the propeller's inflow effect could be motivated by reducing the computational cost of the optimization study.

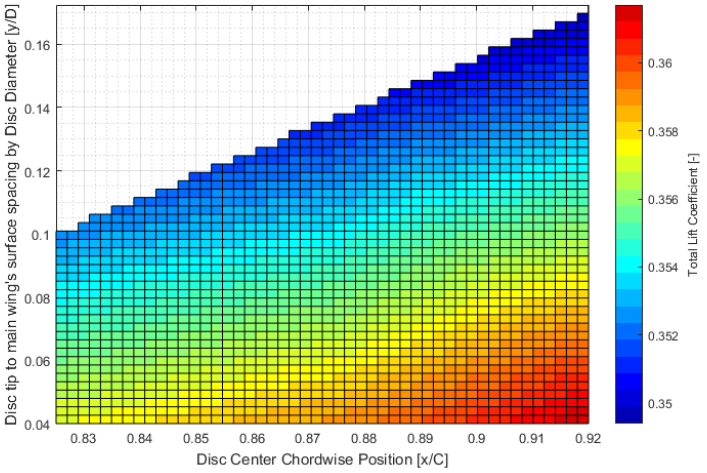

location, the position of the propeller is defined with the propeller chordwise position and propeller's tip clearance from the main wing's surface normalized by the propeller's diameter, the simulations are performed with adiabatic flow condition and constant thrust assumption for the propeller

Figure [42] demonstrates the value of the lift to drag ratio of the system. This graph was used to compare this results of the two cases. The lift to drag ratio was defined with the help of the wingless aircraft's drag coefficient. Since the drag coefficient of the wingless aircraft was only determined with the help of the literature study, the value of the lift to drag ratio alone could not provide enough information about the system's performance.

The total drag coefficient has a higher range of variation compared to the lift coefficient, which proves why this parameter dominates the aerodynamic performance. Comparing Figure [42] and Figure [77] shows that the aerodynamic performance predicted under both assumptions does not exceed $2.4\% \pm 1.5\%$ variation. Therefore, it can be conclusively stated that to reduce the computational cost of the optimization procedure, the propeller's inflow effects could be neglected. However, the initial and the optimum point of the optimization study should be recalculated under the assumption of the constant power and compared to each other to correctly estimate the aerodynamic characteristics of the model.

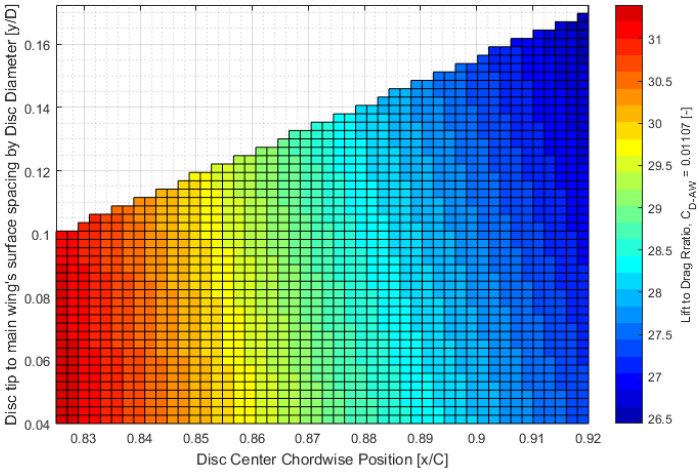

Figure 42: lift to drag of the system as a function of propeller's location, the position of the propeller is defined with the propeller chordwise position and propeller's tip clearance from the main wing's surface normalized by the propeller's diameter, the simulations are performed with adiabatic flow condition and constant thrust assumption for the propeller

Figure [43] and Figure [44] show the difference between the two cases with the assumptions of constant power and thrust. These figures show that the drag performance of the system changes significantly under a different assumption. On the other hand, the lift performance of the model does not vary more than $1\% \pm 0.5\%$. Figures [43,44,45] are obtained by subtracting the solution of the analysis under two different assumption from each other that illustrates the sensitivity of the drag coefficient to the assumptions made.

As Figure [45] shows, the difference between the outcomes of the two propeller's conditions is not more than $2.4\% \pm 1.5\%$ for the aerodynamic performance of the design. Figure [45] confirms the possibility of reducing the computational cost of the model by assuming that the propeller is operating with constant thrust. This difference could be reduced by choosing a higher value of the drag coefficient of a wingless aircraft to dampen the variation of the total pressure drag coefficient due to interaction.

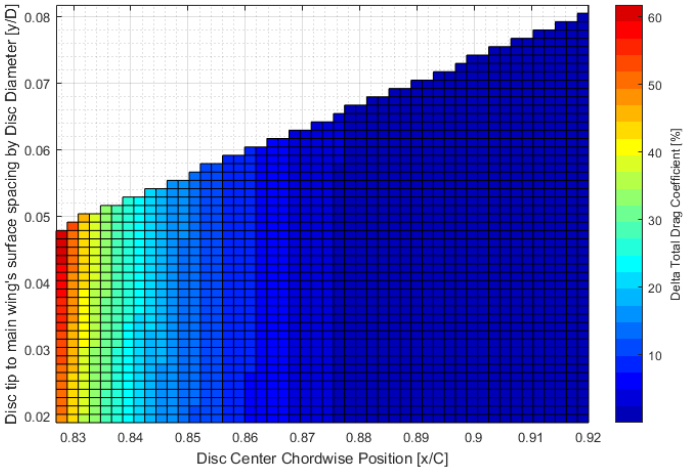

Figure 43: Delta drag coefficient of the system as a function of propeller's location, the simulations are performed with adiabatic flow condition

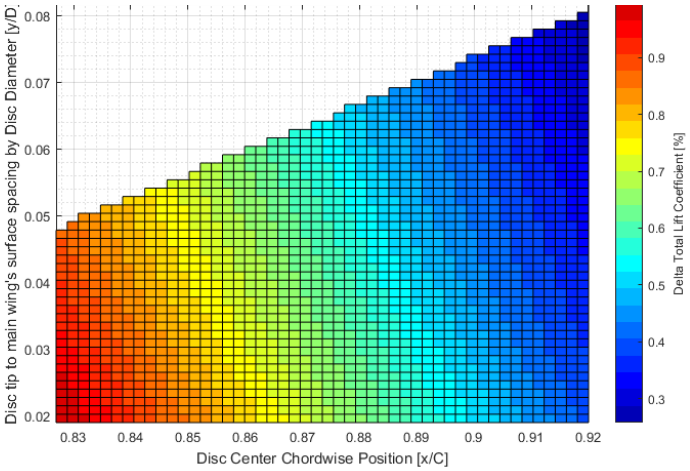

Figure 44: Delta lift coefficient of the system as a function of propeller's location, the simulations are performed with adiabatic flow condition

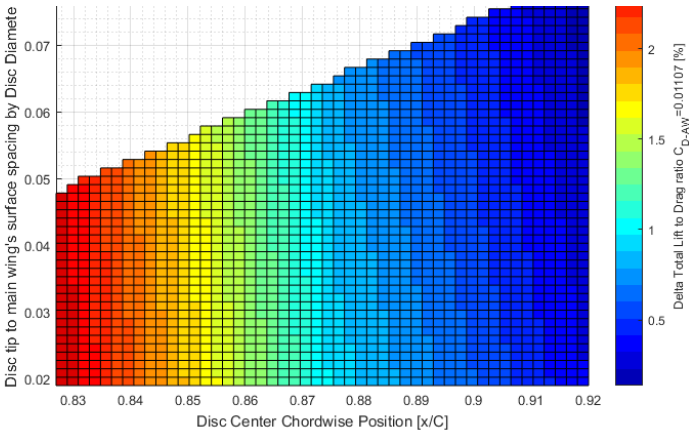

Figure 45: Delta lift to drag ratio of the system as a function of propeller's location, the simulations are performed with adiabatic flow condition

4.2.2 Propeller's Performance

In section 4.2.1, the influence of the propeller on the lift and drag performance of the wings was investigated. In this section, the effect of the wings on the propeller's performance was examined to explain further the difference between the assumptions made to simplify the model.

Figure [46] and Figure [47] show the intake velocity and the thrust coefficient of the propeller. As the propeller moves rearward, it experiences lower inlet flow velocity, which increases the thrust of the propeller.

Figure [48] shows, as the inlet flow velocity of the propeller decreases, the optimizer reduces the propeller's advance ratio to maintain a high propeller's efficiency. This effect causes a lower thrust coefficient as the disc center moves from 88% to 92% chordwise and decreases the overall propulsive efficiency.

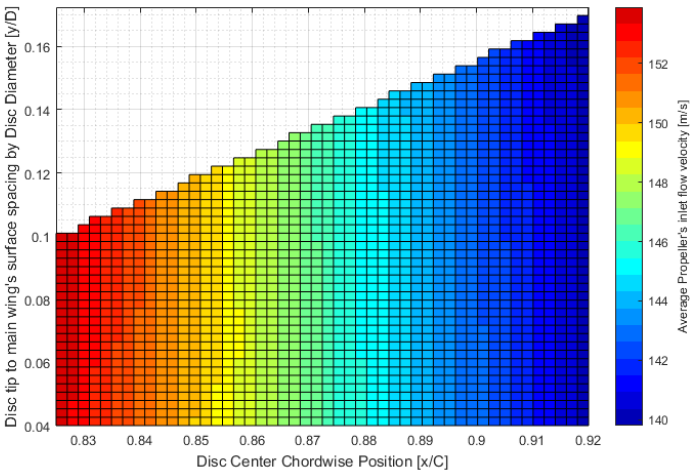

Figure 46: Average inlet flow velocity of the propeller against propeller's location, the simulations are performed with adiabatic flow condition

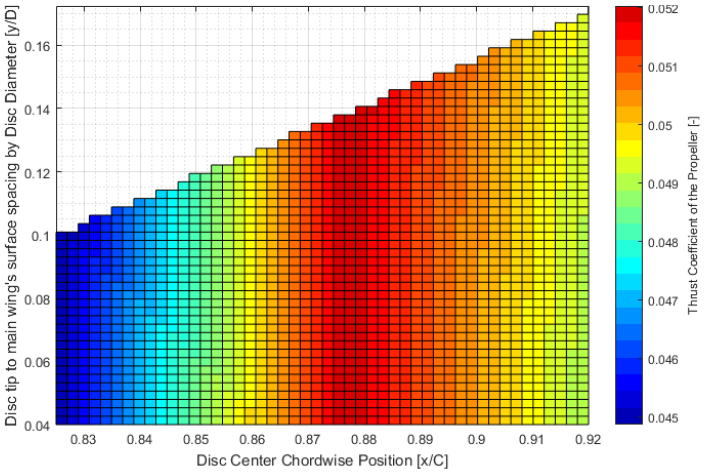

Figure 47: Thrust coefficient of the propeller against propeller's location, the simulations are performed with adiabatic flow condition

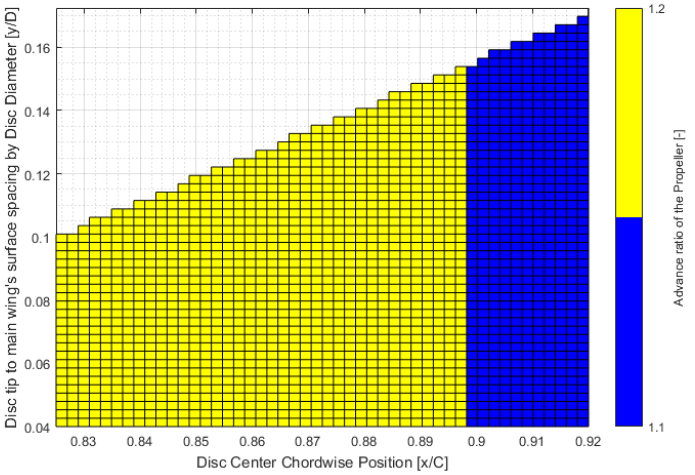

Figure 48: Advance ratio of the propeller against propeller's location

Discussion

The research in this chapter showed that the average flow velocity over propeller's intake represents the disturbed flow in that area accurately. The study that simulates both uniform and non-uniform propeller's inflow velocity shows that this difference does not influence aerodynamic performance and propeller's characteristics because flow velocity fluctuations between the wings is small.

The influence of the wings on the propeller's performance changes the thrust characteristics of the propeller and again this change affects the aerodynamic performance of the whole system. As the geometry shape and the disc position varies, the inlet flow velocity of the thrust characteristics of the propeller remains unchanged. In this case, the propeller is assumed to operate with a constant thrust setting. However, if the influence of the inlet flow velocity on the thrust performance of the propeller is taken into account, the propeller is assumed to operate under constant power assumption. Including this effect could increase the calculation cost of the optimization by a factor of two or sometimes four.

The rotational velocity (RPM) of the propeller was also recalculated, to improve the propeller's efficiency with different inlet velocities. The BEM calculations were performed with a wide range of advance ratio values, and the corresponding advance ratio to the highest propeller's efficiency is chosen to calculate the rotational velocity of the propeller.

This study shows that by not considering the influence of the flow velocity on the propeller's characteristics, the study of the interactions between the wings and the propeller is incomplete and the modeling error of the study could increase by $2.4\% \pm 1.5\%$. If the total drag coefficient of the system is considered as the primary aim of the investigation, then the modeling error could increase even by $60\% \pm 4\%$, which is unacceptable. Therefore, it is recommended to include the influence of the inlet flow velocity of the propeller in the optimization procedure, unless it is necessary to perform the optimization study in a short window of time.

5 Distributed Propulsion Analysis

In this chapter, the influence of multiple parameters on aerodynamic performance and overall propulsive efficiency of the system was studied, i.e., the spacing between the wings, secondary wing shape, secondary wing angle of attack and the camber position of the main wing. The primary goal of these studies was to recognize the parameters that influence propeller wing interaction with an addition of a secondary wing as it was suggested by Hongbo, Xiaoping, and Zhou [Ref.24].

Moreover, it is essential to use the result of this chapter to obtain the initial point of the optimization study. A clear initial point in the optimization study could help to eliminate the unnecessary number of iterations to reach an optimal point.

The analytical studies in this chapter were performed with adiabatic flow condition. The influence of wings on the propeller's inlet flow velocity and the propeller's performance was included by iteratively obtaining the inlet flow velocity of the propeller from CFD simulations and calculating the propeller's characteristics with the help of BEM calculations.

Table [29] shows that the propeller's RPM is varied to obtain the highest possible propeller's efficiency. Based on the calculated RPM and the inlet flow velocity, the advance ratio was calculated. These parameters were then used in a BEM code (JavaProp) to calculate the propeller's characteristics.

Table 27: Specification of the propeller that is used in this chapter based on the study in chapter 4

Parameters	Values
Number of Blades	6
RPM	Variable, (Based on the highest propeller's efficiency)
Advance ratio	Variable, (Based on the highest propeller's efficiency)
Power	Constant ,37500 [watt]
Thrust	Variable, (Calculated)
Inlet flow velocity	Variable, (Obtained from CFD simulation)

5.1 Initial Analysis of the model's configuration

In this section, the parameters that could significantly influence propeller wing interaction were identified and studied. Using symmetrical airfoil (NACA0012) for both the main wing and the secondary wing could help this study to identify the influence of propeller wing interaction on the system's overall performance. In this study, the influence of wings on propeller's performance could be estimated with the help of propeller's inflow velocity variation due to influence of the wings.

The primary focus of this study was to realize the impact of propeller and secondary wing on the main wing and also the effect of secondary wing on the system's overall performance. Table [28] lists the model's description used for this analysis.

Table 28: The specification of the studied model

Main wing Airfoil	NACA0012
Secondary wing Airfoil	NACA0012
Main wing Chord length	2.11[m]
Secondary wing Chord length	30% $[C_{sec}/C_{main}]$ *
Secondary wing's angle of attack	0 [deg]
Spacing between the two wings	40% $[y_s/C_{main}]$ **
Disc Diameter	0.5[m]
Disc position	100% $[x/C_{main}]$ ***
Actuator disc's Thrust	650[N]
Testing Mach number	0.2
Calculation type	Inviscid calculations
Disc center position [Y-direction]	20% $[(y_{p_{main}} + \frac{D_P}{2})/C_{main}]$**
*Secondary wing chord length normalized by Main wing's chord length **Chord line (or disc center) to Chord line distance between the two wings (or main wing and propeller) normalized by Main wing's chord length ***Chordwise position of the propeller over the Main wing	

In chapter 3.1.1, a model was tested to quantify the discretization error of the simulation with inviscid flow condition. The initial simulation shows that disc and secondary wing induced the flow over upper surface of main wing and as a result symmetrical shape of main wing generated lift force. Moreover, the initial test confirmed higher degrees of suction on lower surface of the secondary wing than upper surface due to flow acceleration over the upper surface of main wing.

Figure [49] shows the pressure coefficient plot of the main wing, which illustrates that the presence of the disc and the secondary wing increases the lifting performance of the main wing. The effect of the disc and the secondary wing can be realized by comparing the pressure coefficient plot of the main wing (with the influence of the disc and the secondary wing) and the clean wing. Increasing the influence of the propeller on flow field on the upper surface of the main wing can be beneficial to increase the lift coefficient of the main wing.

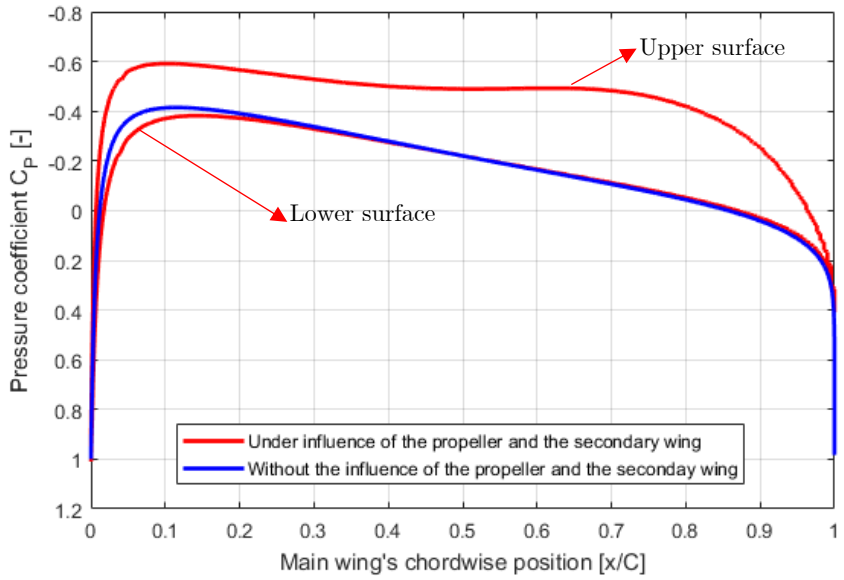

Figure 49: Pressure coefficient plot of the main wing with and without the influence of the propeller and the secondary wing, pressure coefficient plot at 50% spanwise position of a NACA0012 airfoil

At zero degree angle of attack, upper and lower surface of a symmetrical airfoil produces the same pressure coefficient distribution, which means according to [Eq.32] that a symmetrical airfoil does not produce any lifting force.

The difference between the upper and lower surface of the main wing in Figure [49] shows the interaction of the disc and the secondary wing on the main wing. These interactions have a positive effect by increasing the dynamic pressure over the upper surface of the main wing or in other words increasing the suction in that region, causing the main wing to produce lift.

$$C_n = \int_0^1 (C_{p_l}(x) - C_{p_u}(x)) d\left(\frac{x}{c}\right) \quad [Eq.32]$$

Figure [50] shows that the secondary element tends to increase the flow velocity over the upper side of the main wing. The space between the main wing and the secondary wing behaves similarly to a converging-diverging nozzle which increases the flow velocity upstream of the secondary wing until the flow reaches the nozzle's throat and from there the fluid pressure starts recovering. The pressure coefficient plot of the main wing shows (without the influence of the propeller) that the flow velocity increases from 46% to 75% chordwise position over the upper surface of the main wing, and it starts decreasing from 75% chordwise position to the trailing edge. The pressure coefficient plot of the main wing (without the influence of the propeller) indicates that the nozzle's throat is located at 75% chordwise position of the main wing where the maximum suction over the pressure distribution is present.

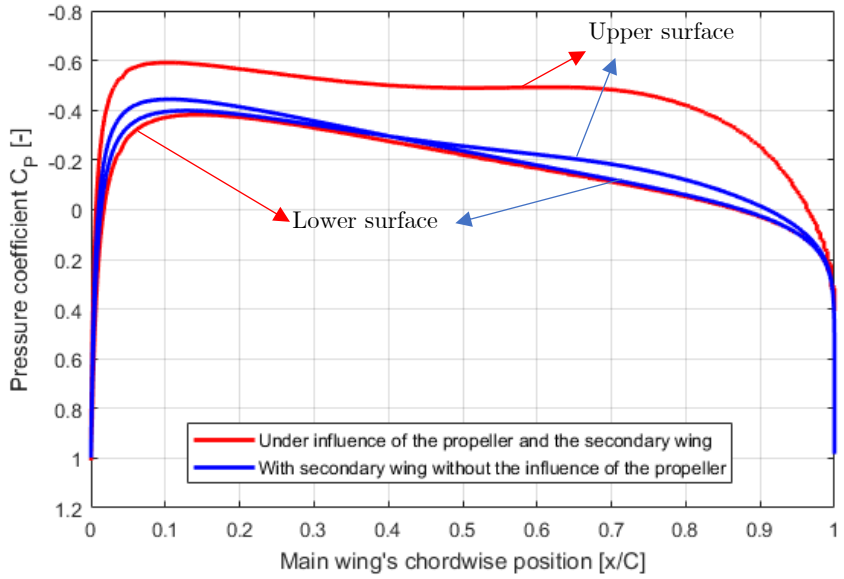

Figure 50: Pressure coefficient plot of the main wing with and without the influence of the propeller

Figure [51] shows the pressure coefficient distribution over the secondary wing and by comparing this plot to a pressure coefficient plot of a symmetrical airfoil reveals the interactions of the main wing and the disc with the secondary wing. Figure [51] shows that the lift coefficient of the secondary wing is in the negative direction. According to [Eq.32], the amount of lift generated by an element is the integrated difference between the upper and lower surface pressure coefficient distributed over the chord length of an airfoil. It is evident that the bottom surface of the secondary wing experiences higher suction than the top surface due to the interaction between the disc and the secondary wing.

Figure [51] further shows that the velocity between the wings is already higher than the suction surface of the secondary wing, and the propeller is only aggravating this effect. The spacing between the wings acts similar to a converging-diverging nozzle, and this speculation could be confirmed by investigating the pressure coefficient graph of the secondary wing without the presence of the propeller. The flow velocity increases rapidly at the leading edge of the secondary wing because the area between the wings suddenly decreases. However, the flow velocity starts to decreases as the space between the wings increases.

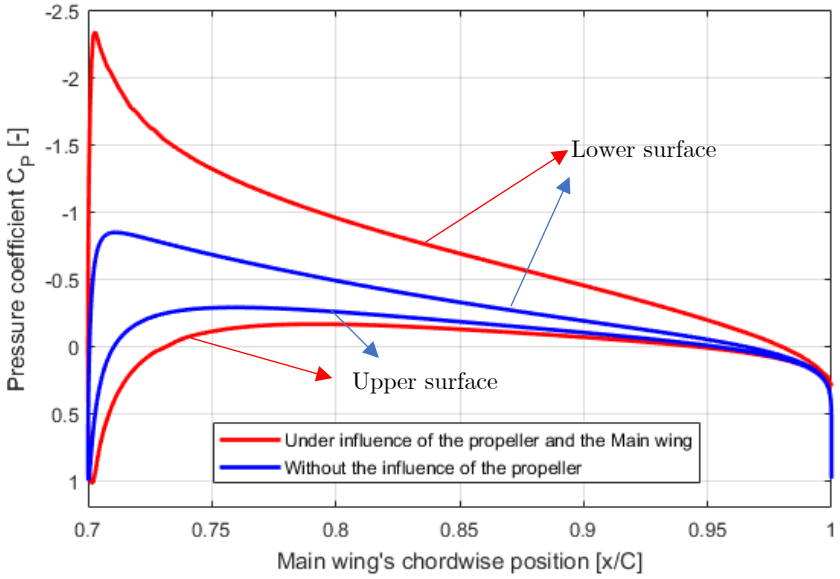

Figure 51: Pressure coefficient plot of the secondary wing with and without the influence of the propeller

Figure [52] illustrates the position of main wing and secondary wing. The shadow of secondary wing is sketched as close as possible to the main wing to show the area change between wings due to their shape and geometry orientation in a clearer picture.

As Figure [52] shows, the spacing between wings on the left section of throat line is decreasing, and on the right hand side of throat line, the spacing between the wings is increasing, which is forming a converging-diverging nozzle. The nozzle's throat is defined at the point where the area between wings starts increasing. The flow velocity is increasing upstream of the throat line and decreasing downstream of the throat line according to the solution of the simulation, which is in agreement with [Eq.33].

According to [Eq.33] as the cross section area of a nozzle decreases the flow velocity increases, where the Mach number is smaller than 1 or the flow is considered subsonic. In this case, the flow upstream the throat line starts to accelerate, and it reaches its maximum value as it passes through the nozzle's throat. However, as the cross section area of the nozzle starts to increase downstream of the throat line, the flow starts to recover its static pressure and slows down. Explaining the flow behavior with the help of [Eq.33] confirms that the position of the throat line is indeed at 75% chordwise position of the main wing. Moreover, relating [Eq.33] to this configuration could help the researcher to understand how the flow behaves in the duct between the wing before performing the simulation.

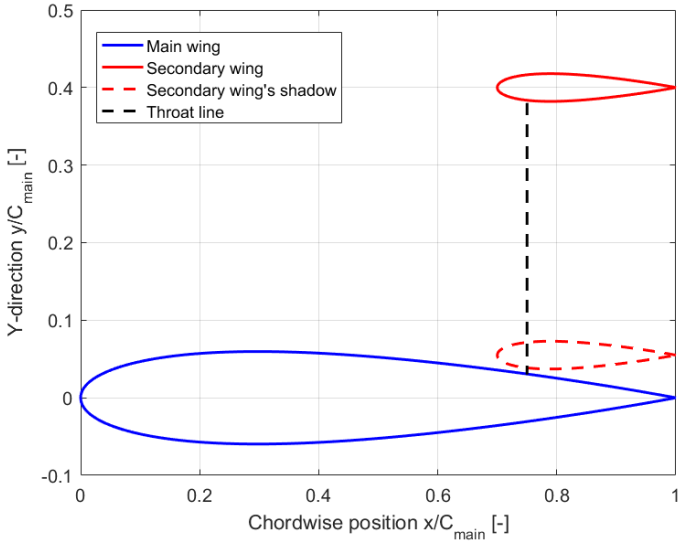

Figure 52: Cross section graph of the initial model's configuration, the dash line sketch of the secondary wing is the shadow of the secondary wing and drawn to show that area variation between the wings in a clearer picture, NACA0012 airfoil is used for both main wing and secondary wing

$$(1 - M^2)\frac{dV}{V} = -\frac{dA}{A} \quad [Eq.33]$$

In conclusion, three notable qualities of this model were discovered in the initial test, i.e., interference effects of the propeller on the main wing that resulted in increasing the lift coefficient of the main wing, interference effects of the propeller on the secondary wing that induced negative lift coefficient on this element and the importance of the secondary wing's shape in forming the duct which influences the flow considerably. As long as there is no shock or secondary flow effects seen in the simulations, the estimated discretization error in chapter 3.1 is assumed to remain unchanged.

5.2 Wing Spacing Analysis

After conducting the necessary steps to verify and validate the numerical analysis, an initial model was tested to observe the significant interactions between the elements. The previous study in chapter 5.1 was conducted with a symmetrical airfoil to observe these effects easier and to reveal some of the critical parameters and useful variables that could affect the objective of this project. In this section, the wing geometry, disc position and the location of each element were chosen from either the reference aircraft or the literature study carried out chapter 1.

The following study focused on the spacing between wings. As it was mentioned in chapter 5.1, the duct that is formed between the main wing and the secondary wing influences the performance of the model. To investigate the influence of the duct on the system's overall performance, the variation of spacing between the wings was studied. Table [29] lists the necessary parameters that are used to construct the CFD model.

The spacing between the main wing and the disc (s_{main}/D_P) was chosen to be as small as possible to increase propeller wing interaction between the main wing and the propeller, which is about 3.3% (≈1.6Cm) of disc's diameter.

Table 29: Parameters of the model based on the reference aircraft's cruise condition and basic geometry

Main wing's airfoil	NACA48015
Secondary wing's airfoil	NACA48015
Main wing's chord length	2.11[m]
Secondary wing's chord length	30% $[C_{sec}/C_{main}]$ *
Secondary wing's angle of attack	0 [deg]
Spacing between the wings	30%-40% $[y_s/C_{main}]$ **
Disc's diameter	0.5[m]
Disc's position	85% $[x/C_{main}]]$ ***
Actuator disc's thrust	250[N]
Freestream Mach number	0.41
*Secondary wing chord length normalized by Main wing's chord length **Chord line (or disc center) to Chord line distance between the two wings (or main wing and propeller) normalized by Main wing's chord length ***Chordwise position of the propeller over the Main wing	

Table 30: The analysis of the secondary wing spacing with the assumption of constant power for the propeller, the propeller has 4% (of it diameter) clearance from the main wing's surface

s/C*	32%	34%	36%	38%	40%
$C_{L_{main}}$	0.286678	0.275803	0.266935	0.259706	0.253653
$C_{L_{sec}}$	-0.54453	-0.497606	-0.457382	-0.422296	-0.390963
$C_{D_{main}}$	0.020081	0.017779	0.015840	0.014189	0.012759
$C_{D_{sec}}$	-0.072705	-0.064141	-0.056895	-0.050689	-0.045296
η_{prop}**	91.7%	91.6%	91.4%	91.3%	91.2%
η_{pp}***	79.8%	79.9%	79.9%	80%	79.9%
$C_{L_{tot}}$	0.1043	0.1091	0.1137	0.1182	0.1227
$C_{D_{tot}}$	-0.001731	-0.001463	-0.001228	-0.001017	-0.00083
L/D	11.2	11.4	11.6	11.8	12
J****	1	1.009	1.017	1.028	1.037
(v/Dn)*****	1.3	1.3	1.3	1.3	1.3

*Chord line (or disc center) to chord line distance between the two wings (or the main wing and the propeller) normalized by the main wing's chord length

** Propeller's Efficiency

*** Overall Propulsive Efficiency of the system

****Objective Function value

*****Advance Ratio of the propeller

Figure [54] illustrates an increase in total lift coefficient as the spacing between the wings was increased. Table [30] and Figure [53] show, as the spacing between the wings was increased, lift coefficient of the main wing decreased. However, the negative lift of the secondary wing also decreased, which indicates that the interaction between the propeller and the secondary wing declined. Since the order of change in the negative lift coefficient of the secondary wing was dominating the total lift coefficient, the system's performance benefited from increasing the spacing between the wings.

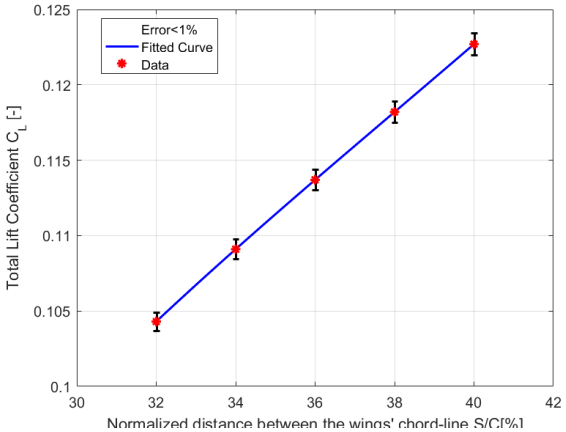

Figure 54: Total Lift coefficient as a function of wing spacing (smaller than 1% Numerical Error)

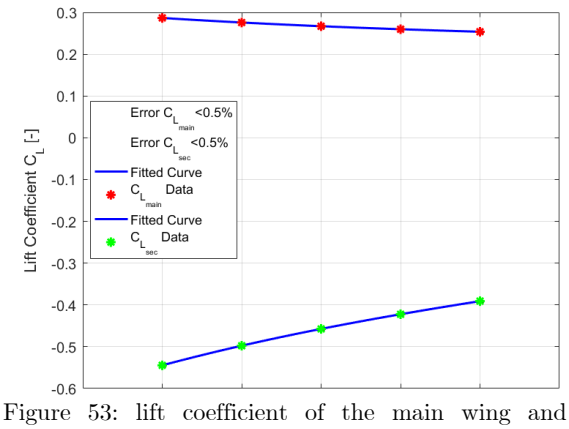

Figure 53: lift coefficient of the main wing and the secondary wing as a function of wing spacing (smaller than 0.5% Numerical Error)

This study shows that the interactions between the propeller and the secondary wing has more influence on the system's lifting performance than the interactions between the main wing and the secondary wing. Therefore, these results explicitly depend on the secondary wing's performance, which is not yet fully optimized and an optimum spacing between the wings could change for different shapes of the secondary wing. Therefore, the only conclusion that could be drawn from these results with certainty was that the secondary wing interaction with the propeller deteriorated the system's lifting performance due to negative lift force generation by the secondary wing.

Figure [55] shows the behavior of the drag force as the spacing between the wings increases. In this case, pressure drag due to propeller wing interaction was calculated by the integral of pressure forces acting on the surface of the wing parallel to the flow direction. The total drag coefficient increased as the spacing between wings was increased which also influences the overall propulsive efficiency because it changes the total axial force component acting on the model. It is important to realize that the drag coefficient of the secondary wing increased as the lift coefficient was improved, which could indicate that the pressure drag due to interactions is also lift dependent and it exists because of the propeller.

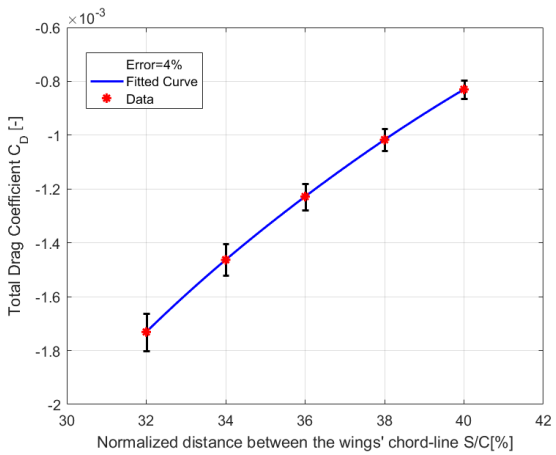

Figure 56:Total Drag coefficient as a function of wing spacing (4% Numerical Error)

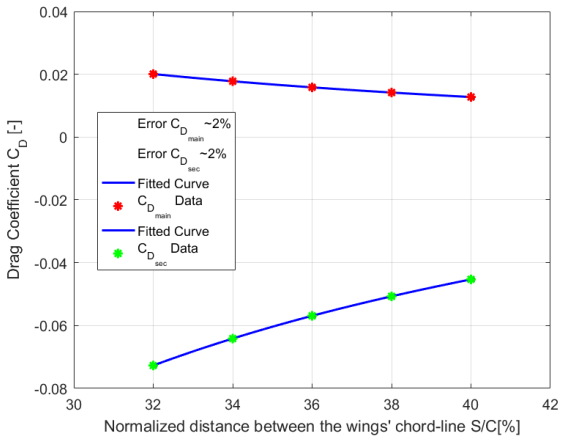

Figure 55:Drag coefficient of the main wing and the secondary wing as a function of wing spacing (4% Numerical Error)

Evaluating the objective function (J) could draw a better picture of advantages and disadvantages of changing the wing spacing by including the influence of the wing spacing on overall propulsive efficiency. In this study the propulsive efficiency and aerodynamic performance were equally worthy, which increased the dependency of the objective function more on the aerodynamic performance factor because overall propulsive efficiency did not change as much as aerodynamic performance of the model.

Figure [58] and Figure [59] illustrate the pressure coefficient of the main wing and the secondary wing to show the local impact of the spacing between the wings on the pressure coefficient of the wings. Figure [58] and Figure [59] show as the spacing between the wings was increased, the dynamic pressure in the duct declined.

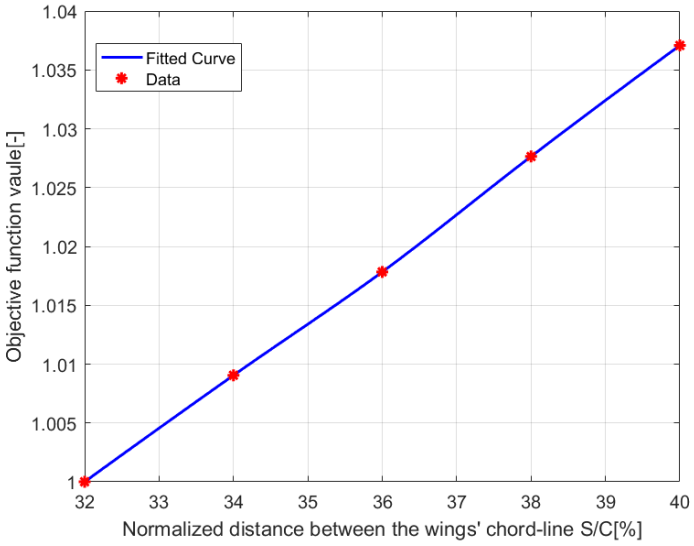

Figure 57:Evaluating the objective function of this project to include the influence of the propulsive efficiency in the calculations

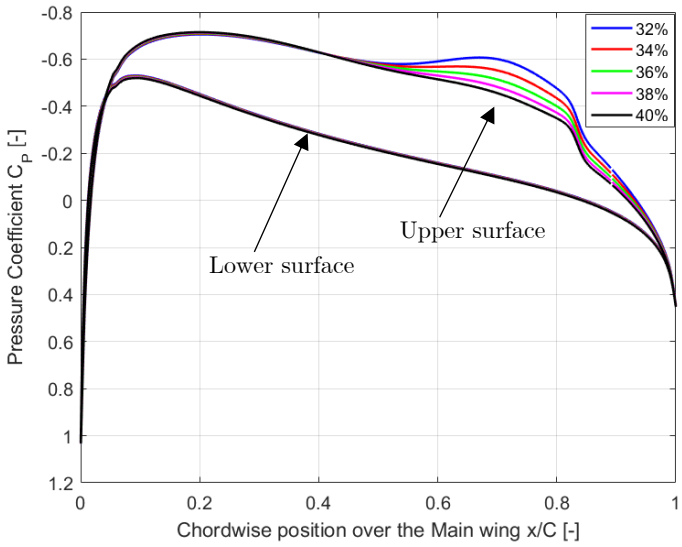

Figure 58: Pressure coefficient over the upper surface of the main wing at 50% spanwise position is influenced by the spacing between the wings. Local changes lead to overall variation of the lift and drag coefficient of the system

Analyzing these figures and understanding the relationship between geometry modification and the system's response showd that by changing the spacing between the wings, cross section area of the duct was modified and the converging part of the nozzle became less effective to accelerate the flow. Reducing the acceleration of the flow upstream of the propeller improved the propeller's thrust production and, as a result, it increased the system's overall propulsive efficiency.

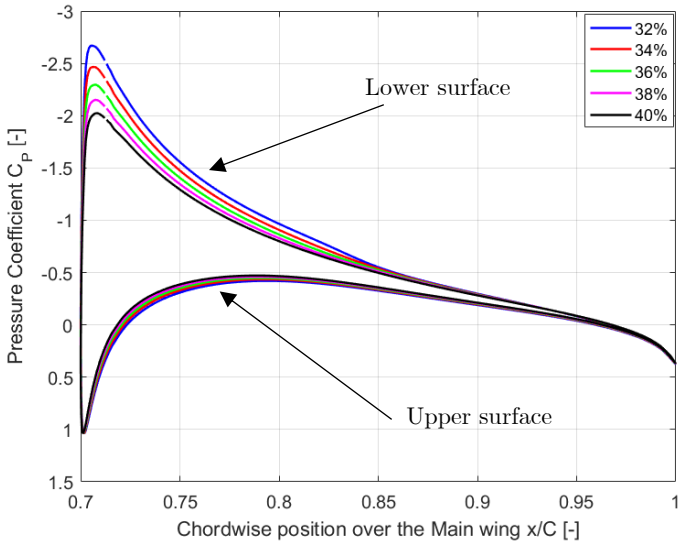

Figure 59: Pressure coefficient over the upper surface and the lower surface of the secondary wing at 50% spanwise position is influenced by the spacing between the wings. The local variations of the pressure coefficient show the influence of the wing spacing on the flow velocity between the wings

5.3 Secondary Wing's Initial Lift Analysis

The study in chapter 5.2 used the same airfoil shape for both the secondary wing and the main wing. The aerodynamic performance and the propulsive efficiency showed high sensitivity to the shape of the secondary wing; This element affects the flow upstream of the disc, and its lower surface is significantly affected by disc interaction. Decreasing the flow velocity by increasing the static pressure in this region could help improve the aerodynamic performance. Moreover, decreasing the velocity in the duct could increase the thrust force of propeller, and as a result, an optimum shape of the secondary wing could improve overall propulsive efficiency. Increasing static pressure under the secondary wing was made possible by increasing the initial lift coefficient of the secondary wing's airfoil.

Table 31: Parameters of the model based on the reference aircraft's cruise condition and geometry

Main wing's airfoil	NACA48015
Secondary wing's airfoil	Variable
Main wing's chord length	2.11[m]
Secondary wing's chord length	30% $[C_{sec}/C_{main}]$ *
Secondary wing's angle of attack	0 [deg]
Spacing between the wings	40% $[y_s/C_{main}]$ **
Disc's diameter	0.5[m]
Disc's position	85% $[x/C_{main}]$ ***
Actuator disc's thrust	250[N]
Freestream Mach number	0.41
*Secondary wing chord length normalized by Main wing's chord length **Chord line (or disc center) to Chord line distance between the two wings (or main wing and propeller) normalized by Main wing's chord length ***Chordwise position of the propeller over the Main wing	

Table [33] shows the results of the study performed to investigate increasing the initial lift coefficient of secondary wing's airfoil at zero degree angle of attack by manipulating secondary wing's camber.

Table 32: The analysis of the secondary wing's initial lift coefficient with the assumption of constant power for the propeller, the propeller has 4% (of it diameter) clearance from the main wing's surface

NACA X8115 C_{L_0}	NACA 48115 $C_{L_0} = 0.354$	NACA 58115 $C_{L_0} = 0.430$	NACA 68115 $C_{L_0} = 0.505$	NACA 78115 $C_{L_0} = 0.580$	NACA 88115 $C_{L_0} = 0.655$
s/C*	40%	40%	40%	40%	40%
$C_{L_{main}}$	0.246654	0.24442	0.242239	0.240196	0.237998
$C_{L_{sec}}$	-0.139317	-0.0508326	0.0406606	0.133357	0.234451
$C_{D_{main}}$	0.00742048	0.00559768	0.00374977	0.00190591	-0.0000695
$C_{D_{sec}}$	-0.0248757	-0.0177643	-0.0103546	-0.0029396	0.00519557
η_{prop}**	90.9%	90.8%	90.7%	90.6%	90.5%
η_{pp}***	78.6%	78%	77.1%	76.2%	74.9%
$C_{L_{tot}}$	0.2000	0.2274	0.2559	0.2849	0.3165
$C_{D_{tot}}$	-0.0000422	0.0002684	0.0006434	0.001024	0.001489
L/D	18.14	20.06	21.84	23.56	25.2
J****	1	1.05	1.09	1.13	1.17
(v/Dn)*****	1.2	1.2	1.2	1.2	1.2

*Chord line (or disc center) to chord line distance between the two wings (or the main wing and the propeller) normalized by the main wing's chord length
** Propeller's efficiency
*** Overall propulsive efficiency
****Objective function value
*****Advance ratio of propeller

In this case, the propeller's performance is calculated under the assumption of constant power consumption and variable thrust. The rotational velocity of the propeller is calculated iteratively to achieve the highest possible propeller's efficiency as the inlet flow velocity of propeller changes.

Figure [60] and Figure [61] show the system's response to the variation of the secondary wing's initial lift coefficient as the camber of this element increases. The overall lifting performance seems to be dependent on secondary wing's lift coefficient and by increasing the secondary wing's initial lift coefficient, the main wing's lifting performance was not affected significantly.

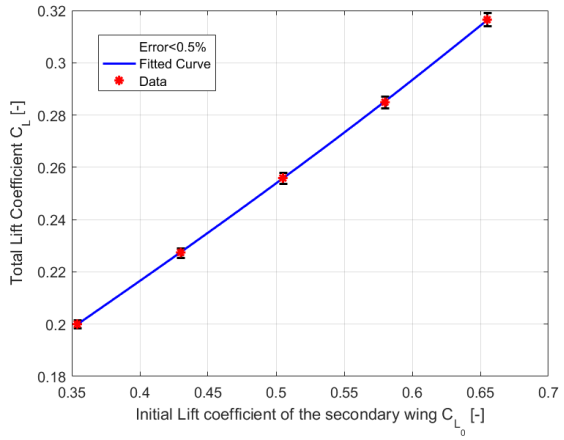

Figure 60: The overall lift coefficient of the system as a function of initial lift coefficient of the secondary wing with less than 1% Numerical Error

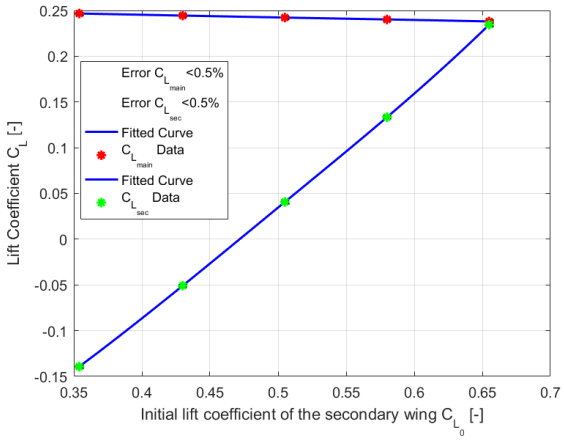

Figure 61: The green dots represent the secondary wing and the red dots represent the main wing's lift coefficient with less than 0.5% Numerical error

Figure [63] and Figure [62] illustrate that by increasing the initial lift coefficient of the secondary wing, the drag coefficient of the system increases. Figure [62] shows that the system's drag performance is dominated by the secondary wing's drag coefficient in this case.

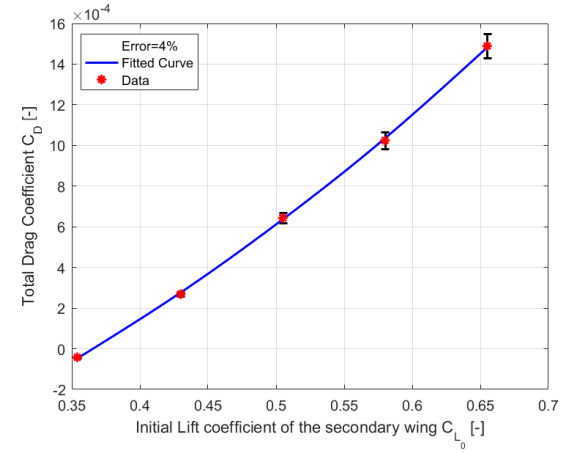

Figure 63: The overall drag coefficient of the system as a function of initial lift coefficient of the secondary wing with 4% Numerical Error

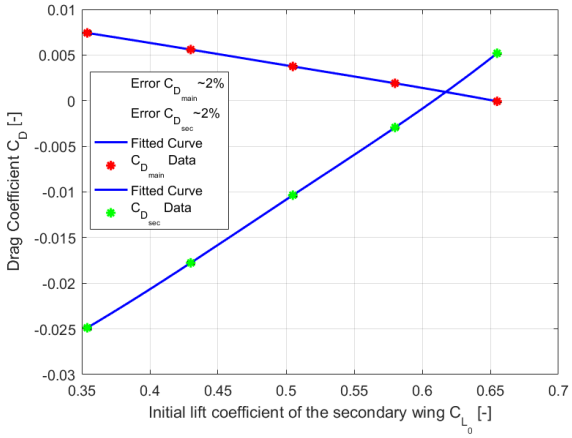

Figure 62:The green dots represent the secondary wing and the red dots represent the main wing's drag coefficient with about 2% Numerical error

Evaluating the objective function (J) in Figure [64] could draw a better picture of the advantages and disadvantages of the changing the initial lift coefficient of the secondary wing by including the influence of this parameter on the propulsive efficiency. In this study the system's propulsive efficiency and aerodynamic performance were equally worthy, which increased the dependency of the objective function more on the aerodynamic performance factor, since the order of lift to drag ratio's variation was higher than the propulsive efficiency.

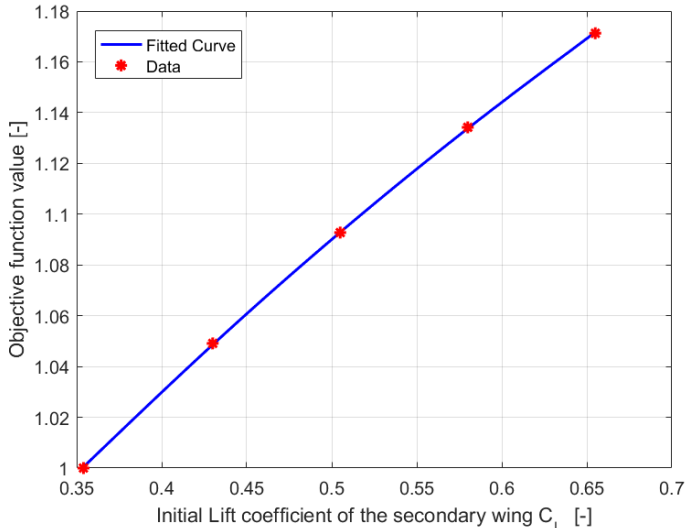

Figure 64: Evaluating the objective function of this project to include the influence of the propulsive efficiency in the calculations

Figure [65] shows that by increasing the secondary wing's initial lift coefficient, the suction on the main wing's surface decreased. Increasing the camber of the secondary wing's airfoil results in higher pressure on the secondary wing's lower surface and also lower flow velocity in the duct. Increasing the flow's static pressure in on the suction side of the main wing could damage the lifting performance of the main wing, which was not significant in this case. However, keeping in mind that indefinitely increasing the secondary's initial lift coefficient could increase the dependency of system's lifting performance on the secondary wing, which is not desired from the structural point of view. Moreover, Figure [62] shows that increasing the initial lift coefficient of the secondary wing increases the total drag coefficient of the system, which damaged overall propulsive efficiency.

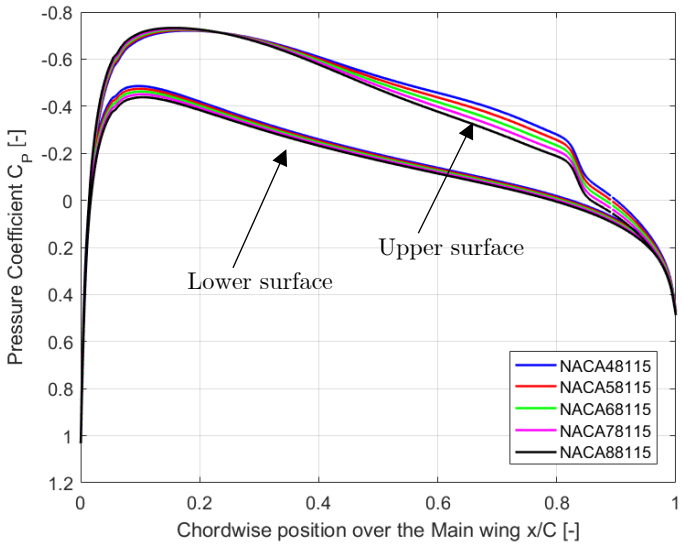

Figure 65: Pressure coefficient over the upper surface of the main wing at 50% spanwise position is influenced by the secondary wing's initial lift coefficient (camber). Local changes lead to overall variation of the overall lift and drag coefficient of the system

Figure [66] shows the pressure coefficient over the secondary wings surface. As the secondary wing's initial lift coefficient was increased, the pressure on the lower surface of the secondary wing increases. Figure [51] in chapter 5.1 showed that the pressure coefficient on the secondary wing's lower surface and leading edge have a lower value than the upper side. However, by increasing the initial lift coefficient of the secondary wing the pressure coefficient values shift their orientation. After the intersecting point of the pressure coefficients of the lower and the secondary wing's upper surface, the wing produces positive lifting force, which is desirable for the system's lifting performance. Therefore, moving this intersecting point as close as possible to the leading edge could improve the system's lifting performance by dedicating a higher surface area of the wing to lift force generation in a positive direction. As Figure [66] shows, the intersecting point is moving forward from 77.5% to 74% chordwise position as the secondary wing's initial lift coefficient increases.

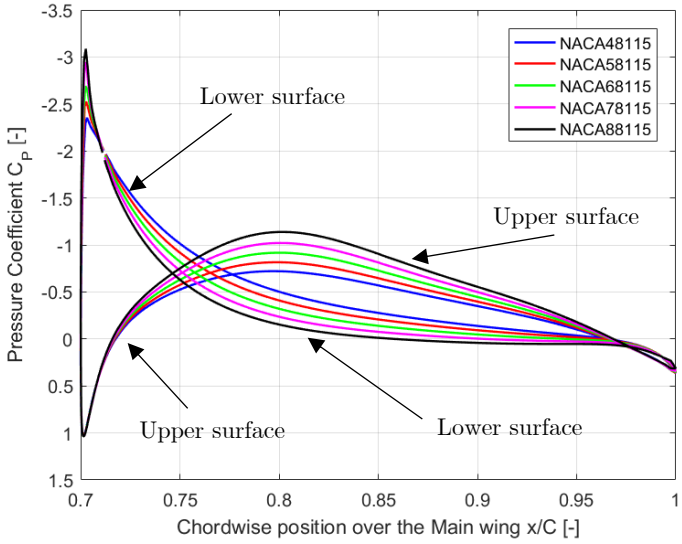

Figure 66: Pressure coefficient over the upper surface and the lower surface of the secondary wing at 50% spanwise position is influenced by the initial lift coefficient of the secondary wing (camber). The local variations of the pressure coefficient show the influence of the wing spacing on the flow velocity between the wings

Discussion

In this case, the camber of the secondary wing was varied to modify the pressure distribution on the pressure side of this element. The system's performance was improved compared to the case where the secondary wing shape was similar to the main wing. Which indicates that an optimized secondary wing could increase the aerodynamic performance of the design. However, since this element produces forces parallel to the flow direction (drag force due to the interaction of wing and propeller), it could put the propulsive efficiency of the system in disadvantage. Therefore, it is not desired to indefinitely increase the initial lift coefficient of the secondary wing.

5.4 Secondary wing's Angle of Attack Analysis

Table [35] shows the tested model's specification and the parameters required to construct this model. Analyzing the secondary wing's angle of attack was complicated without an optimized secondary wing shape. As it was mentioned in chapter 5.1, the presence of the secondary wing formed a converging-diverging duct that increased the flow velocity upstream of this element and decreased the flow velocity between the wings. The velocity gradients are not controlled by an arbitrary shape of the secondary wing, and they could result in flow circulation. Analyzing the secondary wing's angle of attack, with an arbitrary shape, resulted in flow circulation and an unstable simulation. Therefore, the shape of the secondary wing was first optimized (chapter 6), and then the system's response to the variation of angle of attack was studied.

In this study, propeller's power was considered to be constant, and the variation of the average inlet flow velocity was taken into account. This effect was examined in the detail in chapter 4.

Table 33: The specification of the studied model and its geometry orientation

Main wing's airfoil	NACA48015
Secondary wing's airfoil	Optimized Airfoil from chapter 6
Main wing's chord length	2.11[m]
Secondary wing's chord length	32.4% $[C_{sec}/C_{main}]$ *
Secondary wing's angle of attack	Variable
Spacing between the wings	33.5% $[y_s/C_{main}]$ **
Disc's diameter	0.5[m]
Disc's position	82.5% $[x/C_{main}]$ ***
Actuator disc's thrust	250[N]
Freestream Mach number	0.41
*Secondary wing chord length normalized by main wing's chord length **Chord line to chord line distance between the wings normalized by main wing's chord length ***Chordwise position of propeller over the main wing	

Table 34: The analysis of the secondary wing's angle of attack with the assumption of constant power for the propeller, the propeller has 4% (of it diameter) clearance from the main wing's surface

α_{sec}*	-2	-1	0	1	2
s/C**	33.5%	33.5%	33.5%	33.5%	33.5%
$C_{L_{main}}$	0.304278	0.292462	0.280275	0.268574	0.257436
$C_{L_{sec}}$	-0.078006	0.066807	0.21901	0.369242	0.516921
$C_{D_{main}}$	0.008303	0.004936	0.001243	-0.002392	-0.005956
$C_{D_{sec}}$	-0.027506	-0.015799	-0.002542	0.010842	0.024206
η_{prop}***	91.3%	91.1%	90.9%	90.7%	90.4
η_{pp}****	75.3%	76.4%	76.6%	76.3%	75.8%
$C_{L_{tot}}$	0.2781	0.3148	0.3536	0.3923	0.4306
$C_{D_{tot}}$	0.000052	0.000196	0.00048	0.000861	0.001306
L/D	25	27.9	30.6	32.9	34.8
J	1.000	1.066	1.121	1.164	1.200
(v/Dn)	1.3	1.2	1.2	1.2	1.2

*Secondary wing angle of attack in degrees

** Chord line (or disc center) to chord line distance between the two wings (or the main wing and the propeller) normalized by the main wing's chord length

*** Propeller's efficiency

**** Overall propulsive efficiency

The lower side of the secondary wing is exposed to high dynamic pressure and decreasing that could increase the pressure recovery in the duct. Figure [68] illustrates the total lift coefficient of the system as a function of secondary wing's angle of attack. As the secondary wing's angle of attack increases, the total lift coefficient of the system increases, which is dominated by the secondary wing's lift performance shown in Figure [67].

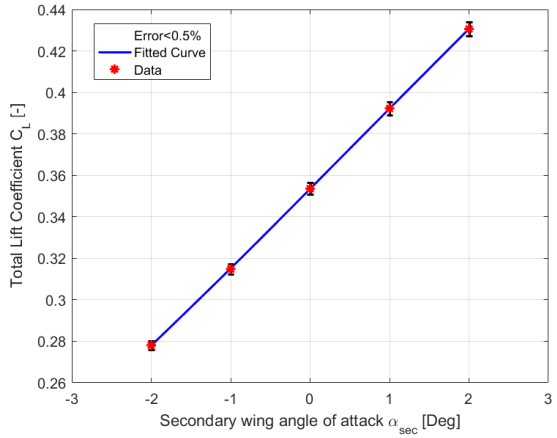

Figure 68: The overall lift coefficient of the system as a function of the secondary wing's angle of attack with less than 1% Numerical Error

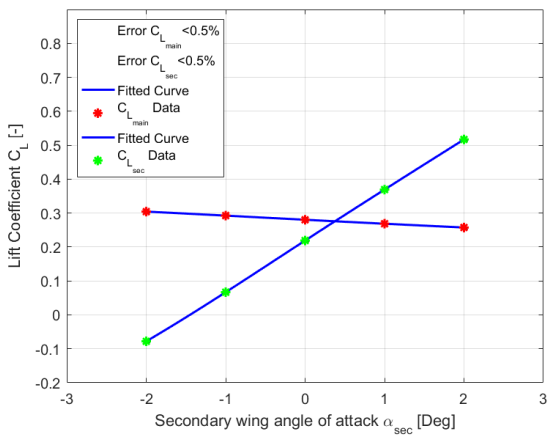

Figure 67: The green dots represent the secondary wing and the red dots represent the main wing's lift coefficient with less than 0.5% Numerical error

Figure [69] is showing the drag behavior of the model as a function of the secondary wing's angle of attack. Similar to the lifting performance, the drag performance response to the angle of attack variation is increasing. As Figure [70] shows, the secondary wing angle of attack increases the drag coefficient of the secondary wing, which dominates the system's overall drag performance.

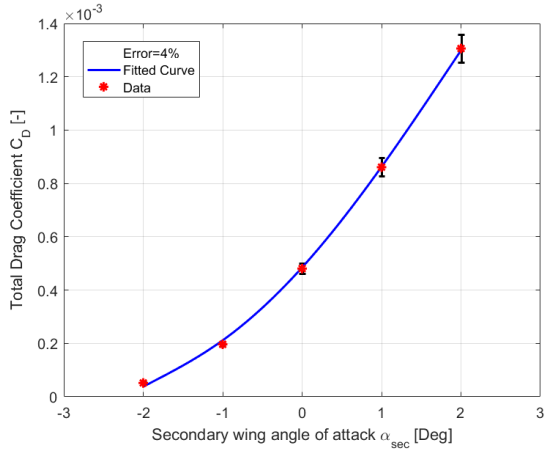

Figure 69: The overall drag coefficient of the system as a function of the secondary wing angle of attack with 4% Numerical Error

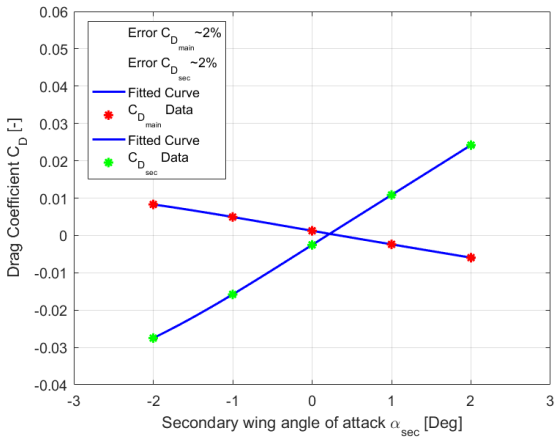

Figure 70: The green dots represent the secondary wing and the red dots represent the main wing's drag coefficient with about 2% Numerical error

Figure [71] shows the lift to drag ratio of the model as a function of the secondary wing's angle of attack. The total lift coefficient order of change seems to be higher than the drag coefficient. Figure [56] shows the effect of the total lift coefficient on the lift to drag ratio of the system. The lift to drag ratio is increasing as the secondary wing angle of attack increases. The model did not have the freedom to increases the secondary wing angle attack to higher values, which limits this study. However, the aircraft is assumed to be at cruise conditions. Therefore, the secondary wing angle of attack could be constrained by the structural and mechanical factors. It is fair to assume that the secondary wing angle of attack does not exceed the defined range. As Figure [53] shows, the total lift coefficient of the system is nearly doubled comparing the cases with -2 [deg] and 2 [deg] angle of attack, which means that the applied force on the secondary wing was increased dramatically.

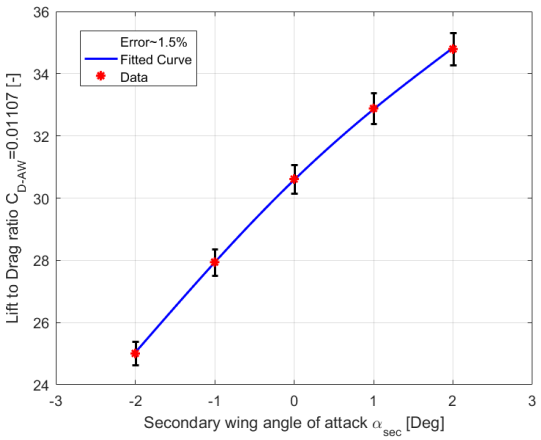

Figure 71: Lift to drag ratio of the system with 1.5% Numerical Error. Including the drag coefficient of the wingless aircraft to reduce the influence of the drag coefficient's numerical Error

According to the Blade Element Method calculations, as the inlet velocity of the propeller decreases the thrust coefficient of the propeller increases, assuming that the propeller is operating with a constant power coefficient. Figure [72] indicates the effects of the wing on the propeller in a different angle of attack. As Figure [73] shows, the duct reduced the flow velocity as the secondary wing's angle of attack was increased.

In this case, the lower side of the secondary wing experienced higher pressure as the angle of attack was increased and the propeller's inlet velocity decreases. This easily translates to a higher thrust production by the propeller with the same amount of power. However, the secondary wing angle of attack did not influence the system's overall propulsive efficiency significantly because as the secondary wing angle of attack was increased the drag coefficient of the system increased too. Therefore, the influence of the drag increase on the overall propulsive efficiency is compensated by the increase in thrust as the average inlet flow velocity of the propeller decreases.

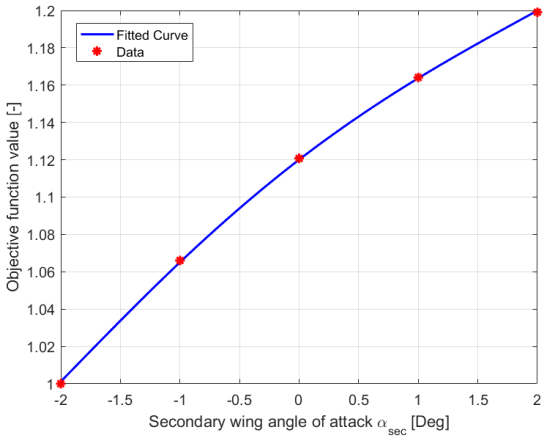

Figure 72: Evaluating the objective function of this project to include the influence of the propulsive efficiency in the calculations

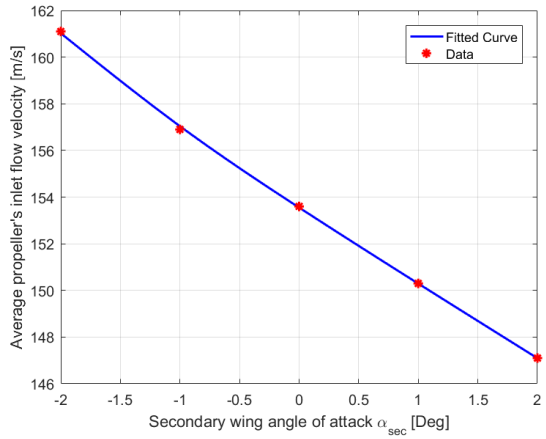

Figure 73: Average inlet flow velocity of the propeller measured on the actuator disc's inlet surface as the secondary wing's angle of attack changes

Discussion

Although the influence of the secondary wing angle of attack is significant, its range of variation should be limited. Indefinitely increasing the secondary wing's angle of attack could lead to boundary layer separation. The viscous effects are neglected in this project; However, it is sensible to constrain this particular variable to avoid cases with impractical solutions. Moreover, by increasing the secondary wing angle of attack the exerted force on this element was increased and it could make the structural and mechanical design of this element difficult.

Increasing the secondary wing's angle of attack increased the inlet area of the duct between the wings, and it reduced the acceleration of the flow upstream of this element. Therefore, it is possible to control the flow velocity over the suction side of the main wing with the help of this parameter efficiently. Moreover, the drag increase due to the change in the secondary wing's angle of attack and its influence of the overall propulsive efficiency is partially compensated by the influence of the secondary wing's angle of attack on the velocity profile in the duct and the average inlet flow velocity of the disc.

5.5 Disc Position Analysis

The following analysis investigated the effect of the propeller's position in the spacing between wings. Figure [74] shows the boundaries in which the propeller's position was varied. The propeller's center represents the location of the propeller in this case. The boundaries of this analysis were chosen based on the limitations of the mesh deformation and the geometry of the model. This analysis uses adiabatic flow conditions and assumes that the propeller is operating with constant power.

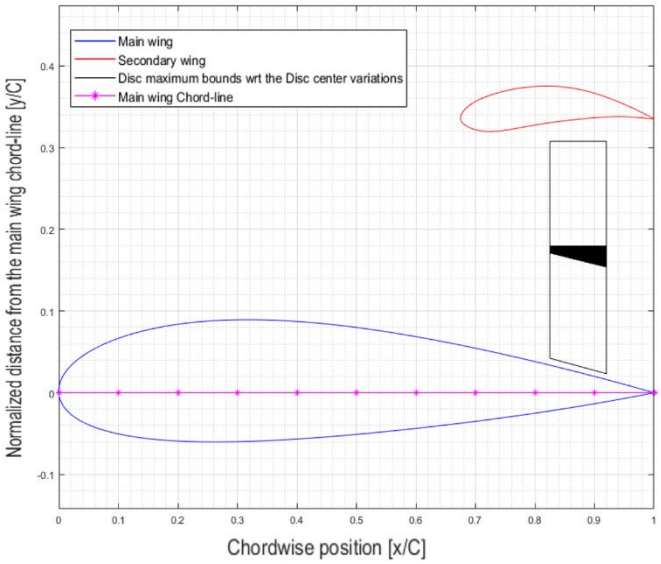

Figure 74: Model's configuration and disc's center and surfaces boundaries are specified

Table 35: The specification of the studied model and its geometry orientation

Main wing's airfoil	NACA48015
Secondary wing's airfoil	Optimized Airfoil from chapter 6
Main wing's chord length	2.11[m]
Secondary wing's chord length	32.4% $[C_{sec}/C_{main}]$ *
Secondary wing's angle of attack	0 [Deg]
Spacing between the wings	33.5% $[y_s/C_{main}]$ **
Disc's diameter	0.5[m]
Disc's position	Variable $[x/C_{main}]$ ***
Actuator disc's thrust	250[N]
Freestream Mach number	0.41
*Secondary wing chord length normalized by main wing's chord length **Chord line to chord line distance between the wings normalized by main wing's chord length ***Chordwise position of the propeller over the main wing	

Figure [75] and Figure [76] illustrate the variation of the system's lift and drag coefficient regarding the position of the propeller. The drag coefficient decreased as the propeller was moved forward on the chordwise position and the lift coefficient increased as the propeller's lower tip was moved closer to the main wing surface and the rear end of the main wing.

A comparison between Figure [75] and Figure [76] shows that by decreasing the system's total lift coefficient, the drag coefficient did not necessarily increase. For example, by comparing the drag and lift coefficient of the case where the propeller was placed at 92% chordwise position with 16% tip clearance from the main wing's surface, it could be observed that even though the lift coefficient of the system was decreasing the drag coefficient due to interaction remained similar.

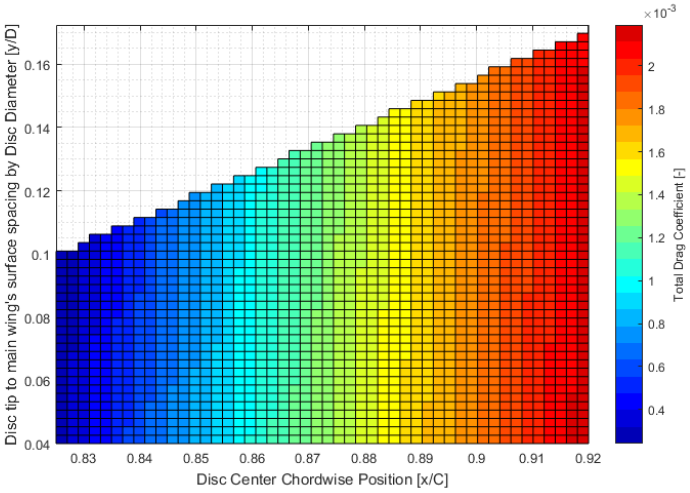

Figure 75: Total drag coefficient of the system as a function of propeller's location, the position of the propeller is defined with the propeller chordwise position and propeller's tip clearance from the main wing's surface normalized by the propeller's diameter, the simulations are performed with adiabatic flow condition and constant power assumption

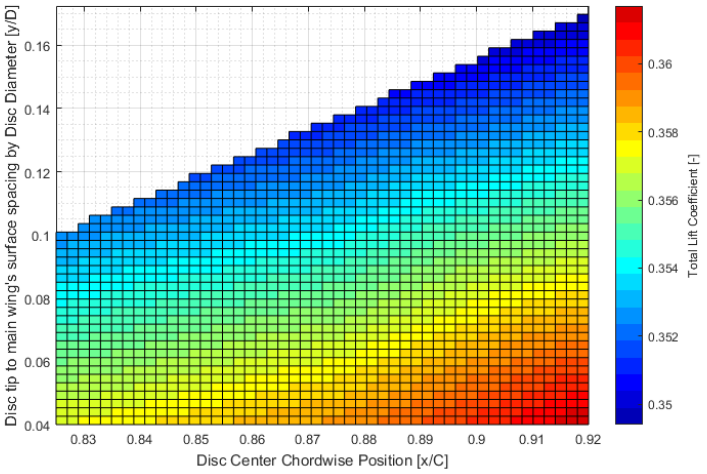

Figure 76: Total lift coefficient of the system as a function of propeller's location, the position of the propeller is defined with the propeller chordwise position and propeller's tip clearance from the main wing's surface normalized by the propeller's diameter, the simulations are performed with adiabatic flow condition and constant power assumption for the propeller

Figure [77] demonstrates the value of the lift to drag ratio of the system. This graph is only useful to compare the lift and drag coefficient's order of variation. The lift to drag ratio of the system is defined with the help of the wingless aircraft drag coefficient. Increasing the wingless aircraft drag coefficient could reduce lift to drag ratio sensitivity to drag and decreasing this value has the opposite effect. Since the drag coefficient of the wingless aircraft is only determined with the help of the literature study, the value of the lift to drag ratio alone could not provide enough information about the system's performance. However, this parameter could be useful when different cases with different conditions are compared to each other.

The drag coefficient of the system has a higher order of variation compared to the lift coefficient, which proves why this parameter dominates the system's aerodynamic performance behavior. Figure [77] shows that the total drag coefficient dominates the behavior of the system and the aerodynamic performance of the model depends on this parameter.

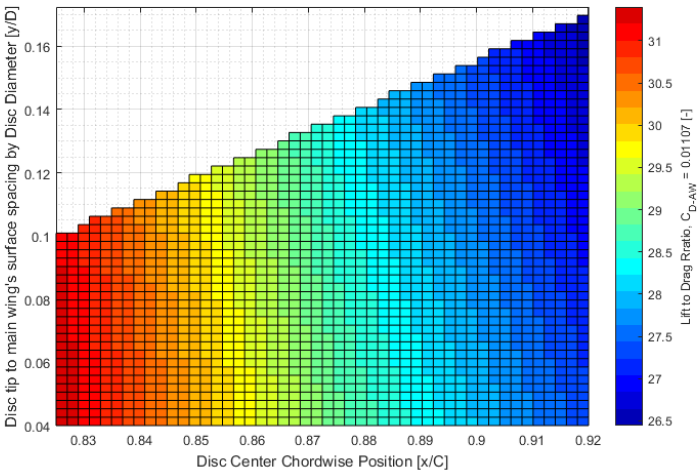

Figure 77: Lift to drag ratio of the system as a function of propeller's location, the position of the propeller is defined with the propeller chordwise position and propeller's tip clearance from the main wing's surface normalized by the propeller's diameter, the simulations are performed with adiabatic flow condition and constant power assumption for the propeller

5.6 Main wing's initial lift Analysis

The main wing's airfoil was chosen to represent the shape of the ATR72 (NACA43015) wing. However, this airfoil produces a high suction peak, and the influence of the propeller and the secondary wing aggravates this effect by accelerates the flow over the suction side of the wing. The camber position of the airfoil was moved more aft to smoothen the suction peak of the airfoil. This could prevent flow circulation due to high pressure gradients, which was problematic at the beginning of the research since the secondary wing was not yet fully optimized. However, the secondary wing airfoil and the position of the disc was optimized in chapter 6.2 and therefore studying the effect of the main wing's camber position on the system's aerodynamic performance is more straightforward.

This study aimed to relate the constructed model one step closer to the reference aircraft and also investigate the effect of the main wing's camber position.

Table 36: The specification of the studied model and its geometry orientation

Main wing's airfoil	Variable
Secondary wing's airfoil	Optimized Airfoil from chapter 6
Main wing's chord length	2.11[m]
Secondary wing's chord length	32.4% $[C_{sec}/C_{main}]$ *
Secondary wing's angle of attack	0 [deg]
Spacing between the wings	33.5% $[y_s/C_{main}]$ **
Disc's diameter	0.5[m]
Disc's position	82.5% $[x/C_{main}]$ ***
Actuator disc's thrust	250[N]
Freestream Mach number	0.4
*Secondary wing chord length normalized by main wing's chord length **Chord line to chord line distance between the wings normalized by main wing's chord length ***Chordwise position of propeller over the Main wing	

In this study, the propeller was operating under the condition of constant power, which means that the inlet flow velocity effects of the propeller were taken into account. The position of the main wing's camber was varied from 20% to 40% chordwise position, and the results conclude that the total lift performance of the system depends on the main wing's initial lift coefficient.

The effect of the secondary wing and propeller on the main wing did not change, and the initial lift coefficient of the main wing was increased with a nearly constant offset.

Table 37: The analysis of the main wing's camber position with the assumption of constant power for the propeller, the propeller has 4% (of it diameter) clearance from the main wing's surface

x/C^*	20%	25%	30%	35%	40%
$C_{L_{main}}$	0.607839	0.655535	0.662612	0.576994	0.280275
$C_{L_{sec}}$	-0.027496	-0.082212	-0.100677	-0.023716	0.21901
$C_{D_{main}}$	0.011787	0.014619	0.015572	0.011426	0.001243
$C_{D_{sec}}$	-0.034688	-0.044321	-0.047947	-0.035177	-0.002542
η_{prop}**	91.1%	91.2%	91.2%	91.1%	90.9%
η_{pp}***	70.1%	69.6%	69.9%	72.2%	76.6%
$C_{L_{tot}}$	0.554125	0.579319	0.579875	0.523379	0.3536
$C_{D_{tot}}$	0.001035	0.000992	0.000891	0.000654	0.00048
L/D	45.1	47.4	47.9	44.4	30.6
J ****	1.000	1.022	1.030	1.007	0.885
(v/Dn)	1.2	1.2	1.2	1.2	1.2

*Chordwise position of the main wing's camber
** Propeller's efficiency
*** Overall propulsive efficiency
****Objective function value

Figure [78] and Figure [79] examine the effect of clean wing lift coefficient on the aerodynamic performance of the system. The system's overall lifting performance is dominated by the initial lift coefficient of the main wing. As Figure [78] shows, the total lift coefficient behaves similarly to the lift coefficient of the clean main wing.

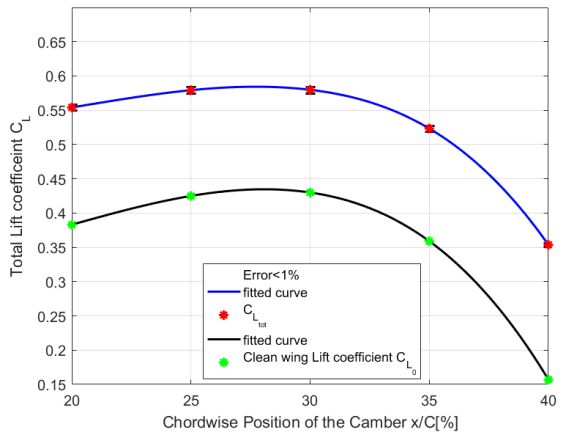

Figure 78: Total lift coefficient of the system seems to depend on the initial clean wing lift coefficient of the main wing

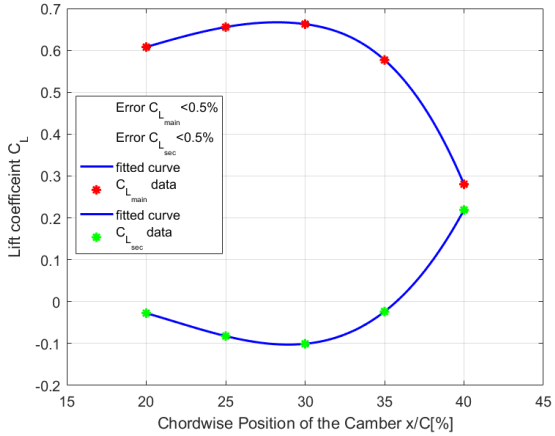

Figure 79: The green dots represent the secondary wing and the red dots represent the main wing's lift coefficient with less than 0.5% Numerical error

Moreover, Figure [79] shows, that the secondary wing's lift coefficient is also influenced by this the initial lift coefficient of the main wing.

As Figure [80] and Figure [81] show, the behavior of the pressure drag seems not to follow the same reasoning as the lift coefficient. It seems that pressure drag due to interaction, in this case, depends more on the velocity and pressure gradients closer to the leading edge of the wings. As the suction peak of the clean main wing decreases due to shifting of the main wing's camber rearward, the pressure drag coefficient decreases.

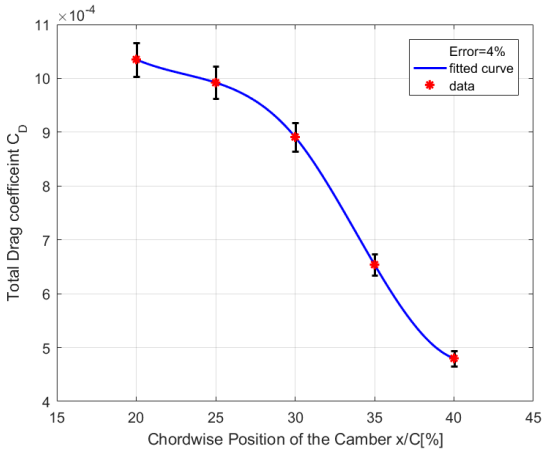

Figure 80: Drag coefficient of the system due to interaction of the wings and the propeller including 4% Numerical Error

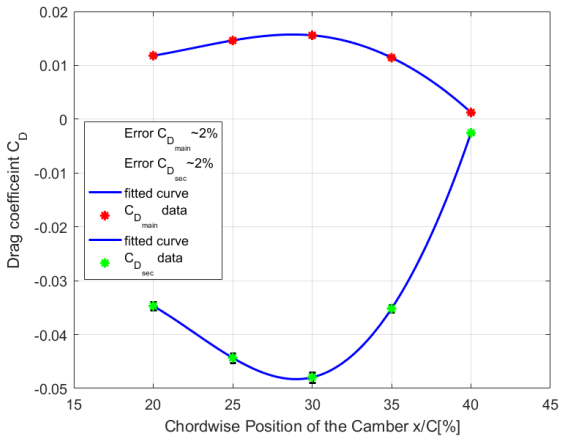

Figure 81: The green dots represent the secondary wing and the red dots represent the main wing's drag coefficient with about 2% Numerical error

Figure [82] also shows that the system's overall performance depends on the main wing's aerodynamic performance. As Figure [82] shows, the behavior of the objective function follows the lifting performance of the main wing and the propulsive efficiency does not influence the objective function as much. The change in lift coefficient, in this case, seems to be dominating the performance of the whole system.

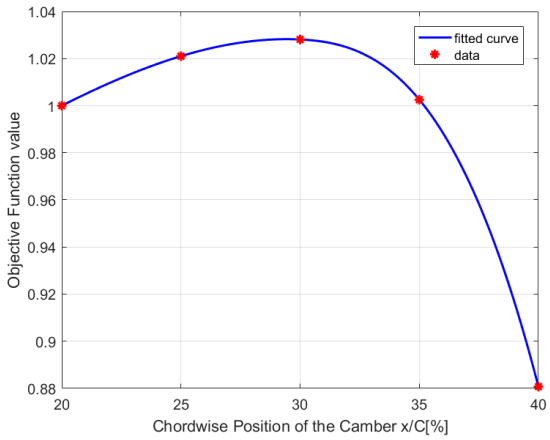

Figure 82: Evaluating the objective function of this project to include the influence of the propulsive efficiency in the calculations

6 Optimization

This chapter focused on the shape optimization of the secondary. The procedure of the optimization is simplified as much as possible to construct an inexpensive algorithm. If the velocity and pressure gradients were not controlled, they could produce unpredictable flow features such as strong vortices and circulation. The drag coefficient of the system directly correlates with the velocity gradients of the flow according to Muller and his colleagues [Ref.20] [Ref.21] [Ref.22]. It is recommended not to increase the drag coefficient of the wingless aircraft so that the optimizer chooses to decrease the drag coefficient of the system. If the optimizer chooses to increase the lift coefficient of the objective function instead of decreasing the drag coefficient, the shape of the wing may get modified in a way that the velocity gradients increase and the simulations become unstable due to flow circulation.

However, considering this parameter alone could lead to a configuration with low lifting performance, because the value of the drag coefficient relates to the system's lifting performance as well. Therefore, it is decided to maximize the lift to drag ratio of the model with a suitable drag coefficient of the wingless aircraft value.

The overall propulsive efficiency is also included in the objective function. Meanwhile, the propeller's thrust is considered constant, the drag force included in the overall propulsive efficiency influences the objective function of this optimization.

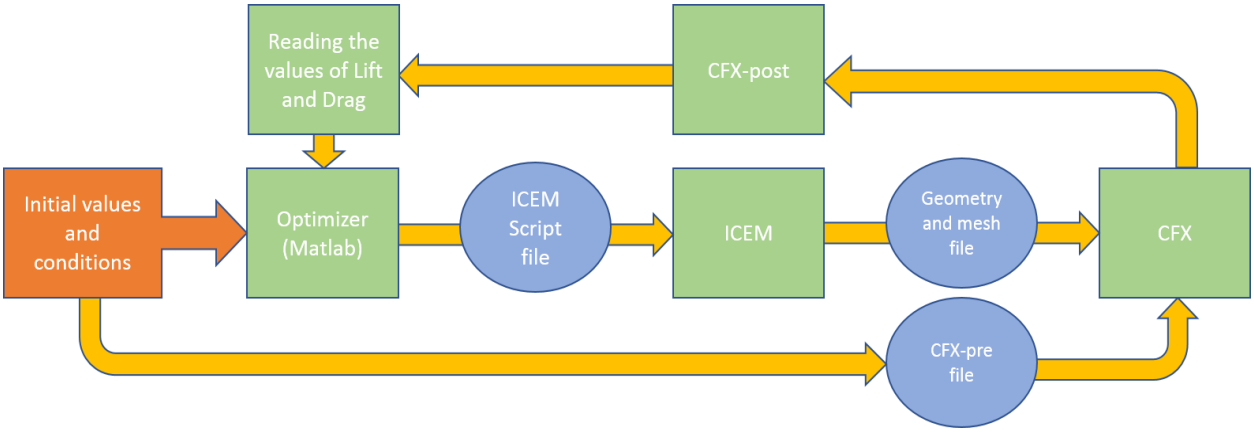

Figure 83: Optimization procedure diagram, the green blocks represent the programs that are connected to each other by the script files (blue circles), these script files are altered by the optimizer

6.1 Connecting Matlab to ANSYS

The ANSYS subprograms such as CFX solver, CFX post, CFX pre, and ICEM could directly be called from the command window of Matlab or by using the scripts shown in Table [38] to run these programs in batch mode. However, the required script files to generate the desired CFD simulation and conditions should be made beforehand (FILENAME.xxx) and saved. Each of these programs required a different type of script file with different extensions to execute the program. However, in some cases, some of these programs needed an additional file to define the conditions and the settings of the software. The required modifications were made in these script files to change the geometry and the conditions of the simulation for the optimization procedure.

Table 38: required commands in MATLAB to execute each program from ANSYS suite

ICEM	!"C:\Program Files\ANSYS Inc\v171\icemcfd\win64_amd\bin\icemcfd.bat" -batch -script FILENAME.rpl
CFX pre	!"C:\Program Files\ANSYS Inc\v171\CFX\bin\cfx5pre.exe" -batch FILENAME.pre
CFX solver	!"C:\Program Files\ANSYS Inc\v171\CFX\bin\cfx5solve.exe" -batch -def FILENAME.def
CFX post	!"C:\Program Files\ANSYS Inc\v171\CFX\bin\cfx5post.exe" -batch FILENAME.cse

6.1.1 ICEM

The geometry and the required mesh was produced with the help of ICEM. An initial model was developed manually, and the ICEM script of this model was recorded. Later this script file was altered by the optimizer to produce different orientations of the model. The flexibility of the model was examined to observe the effect of the maximum and minimum changes of the geometry on the mesh quality and the discretization error of the grid. Based on this observation, the boundaries of the geometry and mesh modification were established and implemented inside the optimizer as a guideline to avoid unwanted situations. Finally, after modifying the ICEM script file with the help of the optimizer, the ICEM script file was saved with (rpl) extension and was executed with the first command line on Table [38]. The mesh and the geometry files were produced and ready to be used for the simulation.

6.1.2 CFX pre

The conditions of the simulations and the definition of the boundaries were recorded in the CFX pre's script file with a (ccl) extension. This file was also subjected to the modification by the optimizer. The position of the actuator disc's subdomain and the effect of the inlet flow velocity on the propeller performance were incorporated in the simulation by modifying the CFX pre's script file. The CFX pre's script file was changed accordingly to account for the mentioned modifications. However, the (ccl) file only included the definitions and the conditions of the simulation. Therefore a second script file was required to execute the program with a (pre) extension. After producing these files with the help of Matlab, the second command line from Table [38] was used to produce the necessary CFX files.

6.1.3 CFX solver & CFX post

The necessary files to start the CFD simulation were produced with a (def) extension from CFX pre. The third command line in Table [38] was used to execute the CFD simulation with the help of CFX solver. When the simulation was finished, the result file was automatically produced by CFX solver. The resulting file was then subjected to post processing procedure to extract the required results. This procedure was recorded manually and saved with a (cst) extension. CFX post required another execution file with a (cse) extension which could also be recorded manually and used to run and export the required data from the CFX result file to a text file. This text file was read by the optimizer to obtain the required data such as lift coefficient, drag coefficient and the inlet flow velocity of the actuator disc.

6.2 Secondary wing's shape Optimization

The analyses in chapter 5 showed that the effect of the secondary wing on the system's overall performance is significant. Moreover, the shape of the secondary wing could alter the flow velocity that the propeller experiences. The shape of the secondary wing was defined with the help of twelve CST coefficients to reduce the number of variables.

Table [43] shows the initial and optimized values of the secondary wing shape parameters. According to the outcome of this study in Table [40], the total drag coefficient decreased substantially compared to the lift coefficient. The optimized secondary wing shape provided the opportunity to investigate the effect of the wings on the propeller and the propeller on the wings more in-depth because it reduces the chance of flow circulation and made the simulations more stable.

Table 39: The required parameters to construct the model, the initial and optimized shape of the secondary wing could be found in Table [41]

Main wing's airfoil	NACA 48015
Main wing's chord length	2.11[m]
Secondary wing's chord length	32.4% $[C_{sec}/C_{main}]$
Secondary wing's angle of attack	0 [deg]
Spacing between the wings	33.5% $[y_s/C_{main}]$
Disc's diameter	0.5[m]
Disc's position	82.5% $[x/C_{main}]$
Actuator disc's thrust	250[N]
Freestream Mach number	0.4

Table 40: Initial and optimized model parameters of the secondary wing shape and disc position optimization study performed with adiabatic flow condition and constant thrust assumption for the propeller

Parameters	Initial point	Normalized	Optimized point	Normalized
$C_{L_{tot}}$	0.379751	1	0.355153	0.935
$C_{D_{tot}}$	0.00135	1	0.00029844	0.221
η_{prop}	0.8929	1	0.8949	1.002
η_{pp}	0.8217	1	0.8712	1.06
J	1	-	1.041	-
Main wing's Airfoil	NACA48015		NACA48015	
Secondary wing's Airfoil	NACA 63A-515		Optimized Airfoil	

Table 41: Initial and final point of the optimization's design vector

Secondary wing shape	Initial	Optimized	Normalized
CST - lower surface 1	-0.168539	-0.142068	0.843
CST - lower surface 2	-0.197322	-0.243598	1.234
CST - lower surface 3	0.1776214	0.1343	0.756
CST - lower surface 4	-0.1629881	-0.175561	1.077
CST - lower surface 5	0.16860178	0.154086	0.914
CST - lower surface 6	0.04811248	0.0481125	1
CST - Upper surface 1	0.33280003	0.235324	0.707
CST - Upper surface 2	0.31384085	0.286821	0.914
CST - Upper surface 3	0.28825002	0.288429	1.0006
CST - Upper surface 4	0.40551232	0.427306	1.054
CST - Upper surface 5	0.34809308	0.365098	1.049
CST - Upper surface 6	0.41615891	0.403511	0.9696
Secondary wing chord length*	0.35	0.3254	0.935
*Secondary wing chord length normalized by the main wing's chord length			

Figure [85] and Figure [84] show the initial and optimized secondary wing airfoils. Apparently, the thickness and the chord length of the secondary wing decreases slightly to reduce the pressure drag due to propeller wing interaction. Moreover, the nose radius of the airfoil is also decreased to reduce suction peak. These changes lead to a lower acceleration of the flow and as result lower drag coefficient.

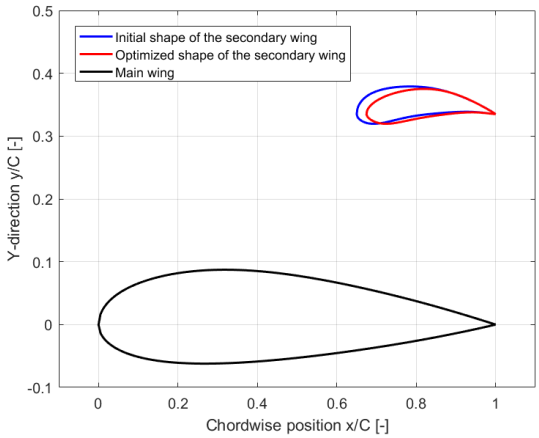

Figure 85: 2D plot of the initial and optimized model

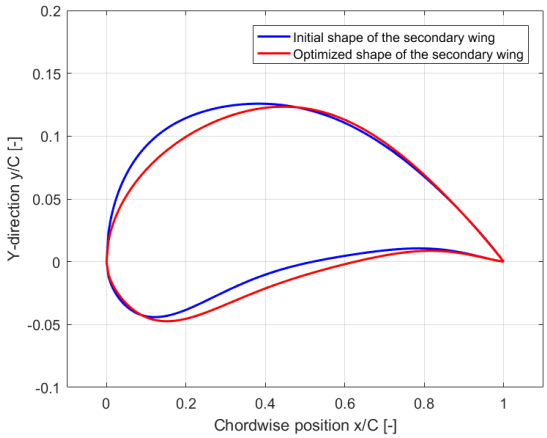

Figure 84: Initial and optimized secondary wing's shape

6.3 Adiabatic vs. Isothermal flow condition

In this section, the initial and final points of the optimization were recalculated with adiabatic flow conditions to study the effect of isothermal flow assumption on the outcome of the optimization study. Comparing the result of the optimization with different flow conditions shows that the lifting performance and the propulsive efficiency of the propeller were not affected significantly by the assumption of isothermal flow condition. However, there is entropy production present in the simulations with isothermal flow condition which translates directly into dissipation and drag. The estimation of the model's drag coefficient is majorly damaged by this aspect, and it is recommended to repeat the initial and final points of the optimization procedure to control this effect.

Establishing the difference between the isothermal and adiabatic flow condition could be difficult because in different cases the entropy production depends on the pressure and velocity gradients, which determines the variance between pressure drag in isothermal and adiabatic flow condition. Table [42] suggests that the initial point of the optimization suffers from higher pressure and velocity gradients than the optimized point.

Table 42: Isothermal vs. adiabatic drag prediction

Total Drag coefficient $C_{D_{tot}}$	Isothermal	Adiabatic	Difference [%]
Initial Point	0.003386	0.00135	60.1%
Optimized Point	0.000441	0.0002984	32.3%

As Table [43] shows, the difference between total lift coefficient of the isothermal and the adiabatic case does not exceed 11% difference. Therefore, it is safe to say that if the objective of the optimization is to improve the lifting performance of a system, the isothermal flow condition could be used. Moreover, regarding the demanded computational cost, it is more efficient to conduct the optimization study with isothermal flow condition than adiabatic flow condition. However, it is still recommended to recalculate the initial and the final point of the optimization procedure to determine the difference between the outcome of the two conditions.

Table 43: Isothermal vs. adiabatic lift coefficient prediction

Total Lift coefficient $C_{L_{tot}}$	Isothermal	Adiabatic	Difference [%]
Initial Point	0.4242	0.379751	10.5%
Optimized Point	0.3978	0.355153	10.7%

Discussion

This study resulted in two important finding namely, the impact of the secondary wing's shape on the aerodynamic performance and influence of the isothermal flow condition on the solution of the simulations. The objective function of the optimization included the drag coefficient of the wingless aircraft. However, the objective function remained sensitive to the variation of drag coefficient. Therefore, the optimizer chose to minimize drag coefficient instead of maximizing lift coefficient. Since the optimization was done under the assumption of constant thrust, the propeller's thrust was not affected by the variation of the inlet flow velocity, and therefore a high value of propulsive efficiency was achieved.

This optimization resulted in a secondary wing shape that reduced the total drag coefficient by reducing flow acceleration upstream the converging part of the duct.

This optimization study was conducted with isothermal flow condition and later after the optimum point of the optimization was reached, the initial and optimized point were simulated with adiabatic flow conditions. Performing the optimization study with isothermal flow condition could reduce the computational cost of the optimization by half. However, it seems that such assumption could be inaccurate when the objective of the optimization is to minimize the drag coefficient. Therefore, it is recommended to use adiabatic flow condition for Euler calculation, unless the time of study is constrained.

7 Multidisciplinary Design Optimization

In this study, the effectiveness of the parameters and variables that defined the geometry and the position of the secondary wing were investigated. In chapter 5, different aspects of the model were examined to test the assumptions used to reduce the computational cost of the CFD simulations. Figure [86] illustrates the algorithm of this optimization procedure, which includes the effect of the inlet flow velocity on the propeller. In this case, CFX was not the only discipline of this optimization procedure. A BEM based program (JavaProp) was also required to calculate and alter the propeller's performance as the inlet velocity of the propeller changed to take the influence of the propeller's inlet flow velocity into account.

Table 44: Initial conditions of the optimization study

Main wing's airfoil	NACA43015
Secondary wing's airfoil	Optimized airfoil from chapter 6
Main wing's chord length	2.11[m]
Disc's position	82.5% $[x/C_{main}]$
Freestream Mach number	0.4

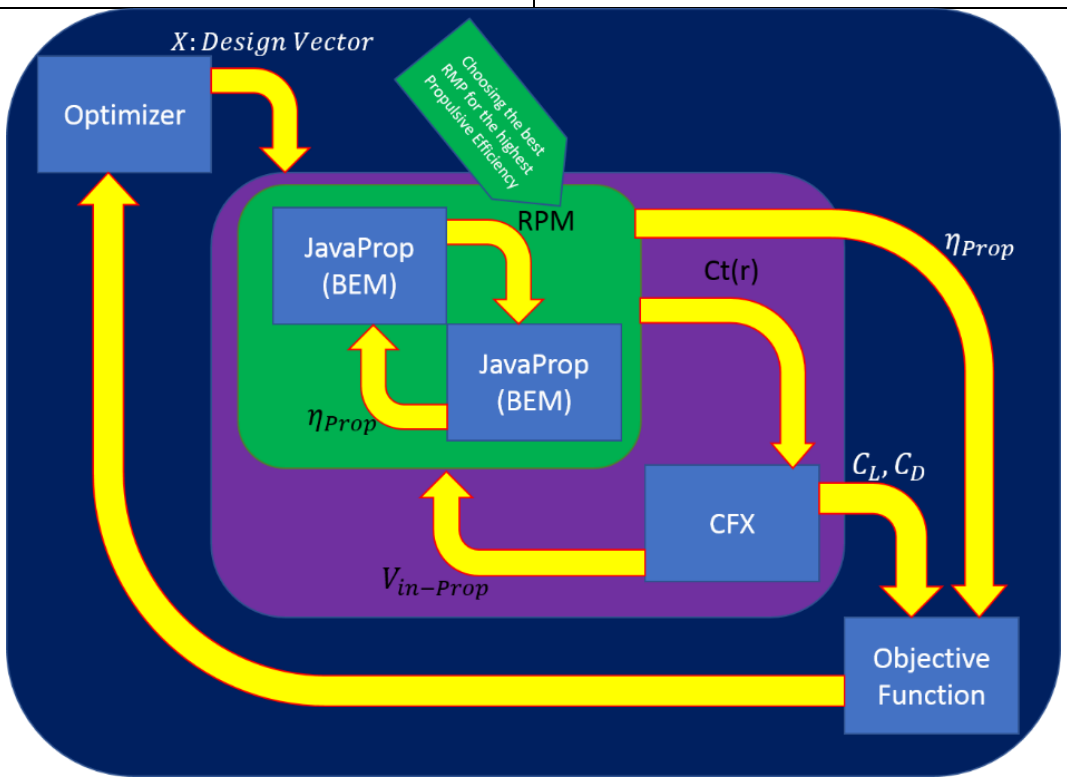

Figure 86: Optimization algorithm flowchart: the green square contains the loop to calculate the highest possible propeller's efficiency based on the corresponding propeller's RPM, the purple square contains the loop to incorporate the effect of propeller's inflow velocity on the propeller's performance

7.1 Design Vector

In this study, the secondary wing's shape and chord length and the spacing between the wings were subjected to optimization to increase the system's aerodynamic performance and propulsive efficiency. The airfoil shape of the secondary wing was defined with the help of twelve CST coefficients to reduce the calculation cost of the optimization. The spacing between the wings was defined as the distance between the chord lines of the wings normalized by the main wings chord length. Also, the chord length of the secondary wing was normalized by the main wing's chord length to make this parameter dimensionless.

7.2 Bounds and constraints

The mesh flexibility and requirements bounded the design vector elements. The maximum upper and lower bound were chosen not to interfere with the mesh construction and also not to produce unwanted mesh deformities that could influence the discretization error of the model. Table [45] shows the lower and upper bounds of the design vector elements.

Table 45: Maximum upper and lower bounds of the Design vector elements

Design vector element	Maximum lower bound	Maximum upper bound
CST - lower surface 1	70%	140%
CST - lower surface 2	70%	140%
CST - lower surface 3	70%	140%
CST - lower surface 4	70%	140%
CST - lower surface 5	70%	140%
CST - lower surface 6	70%	140%
CST - Upper surface 1	70%	140%
CST - Upper surface 2	70%	140%
CST - Upper surface 3	70%	140%
CST - Upper surface 4	70%	140%
CST - Upper surface 5	70%	140%
CST - Upper surface 6	70%	140%
Secondary wing chord length*	95%	110%
Wing spacing	96%	110%

Table [47] shows the maximum possible variation of the design vector element with respect to its initial value. These boundaries were set by observing and testing the influence of the element's variation on the construction of the model and the mesh.

Table 46: The value of design vector elements before and after the optimization

Design vector element	Initial point	Normalized	Optimized point	Normalized
CST - lower surface 1	-0.142068	1	-0.174289	1.22679
CST - lower surface 2	-0.243598	1	-0.246007	1.00989
CST - lower surface 3	0.1343	1	0.1204	0.896504
CST - lower surface 4	-0.175561	1	-0.177473	1.01089
CST - lower surface 5	0.154086	1	0.145326	0.943147
CST - lower surface 6	0.0481125	1	0.0481125	1
CST - Upper surface 1	0.235324	1	0.259681	1.1035
CST - Upper surface 2	0.286821	1	0.300199	1.04664
CST - Upper surface 3	0.288429	1	0.301882	1.04664
CST - Upper surface 4	0.4269	1	0.40263	0.943147
CST - Upper surface 5	0.365098	1	0.511133	1.39999
CST - Upper surface 6	0.403511	1	0.564911	1.39999
Chord length	0.32543	1	0.35797	1.09999
Wing spacing	0.335	1	0.3685	1.09999
*Secondary wing chord length normalized by the main wing's chord length				

Table [48] shows the initial and final state of the variables of optimization study. The last four elements of the design vector increased up to the maximum possible bound which means that the results of this study do not represent a global maximum value of the objective function. In this optimization study, the wingless aircraft's drag coefficient is increased to force the optimizer to improve the system's lifting performance.

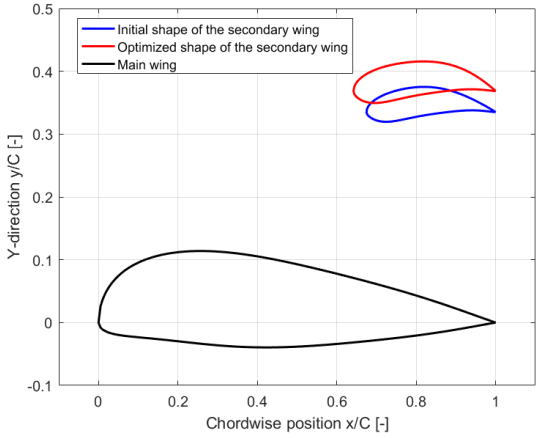

Figure 87: Initial and optimized design configuration

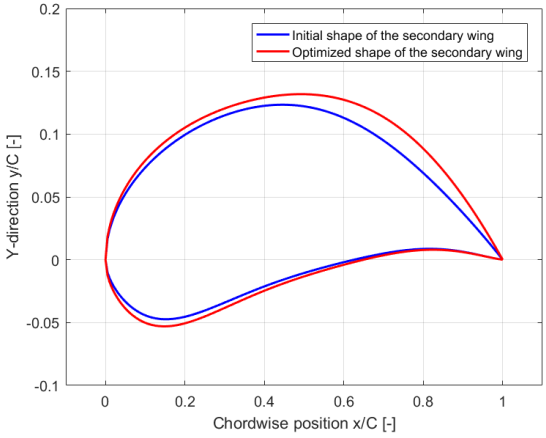

Figure 88: initial and optimized secondary wing's airfoil

This study aimed to maximize the lifting performance of the model. Therefore, $C_{D_{ATR72}}$ was increased to reduce the sensitivity of the objective function to the drag coefficient. The value of $C_{D_{ATR72}}$ was chosen from the literature study [Ref.31], which set equal to 0.027403. In this case the total drag coefficient of the wingless aircraft was considered by including the effect of the engine casing and nacelle and the zero-lift drag coefficient of the wing.

As figure [87] shows, the overall thickness of the wing, the chord length and the spacing between the wings were increased. According to a previous study in chapter 5.2, as the spacing between the wings was increased the system's lifting performance improved. The same behavior could be observed in this study.

The optimized airfoil shows small overall thickness growth. However, a noticeable improvement in the optimized airfoil was that the thickness of the airfoil's rear upper surface was increased. Compared to the optimization study in chapter 6.2 of the secondary wing that studied the drag characteristic, the modifications of the optimizer were entirely in the opposite direction.

As the Table [47] shows, the optimizer chose to increase the lift coefficient over the drag coefficient. The initial point of the optimization could in many aspects represent ATR72 with a distributed propulsion system and an addition of a secondary wing element.

Table 47: Outcome of the optimization compared to the initial point (adiabatic flow condition)

Parameters	Initial point	Normalized	Optimized point	Normalized
$C_{L_{tot}}$	0.559612	1	0.660661	1.1805
$C_{D_{tot}}$	0.00083	1	0.00182116	2.1941
η_{prop}*	0.9042	1	0.9093	1.005
η_{pp}**	69.6%	1	70.5%	1.012
J ***	1	-	1.073	-
(v/Dn)	1.925	1	1.2	0.6234
$V_{prop_{inlet}}$****	161.6[m/s]	1	154.7[m/s]	0.9573
Propeller's Thrust [N]	209 [N]	1	220 [N]	1.052
* Propeller's efficiency ** Overall propulsive efficiency ***Objective function value ****Average inlet flow velocity of propeller				

Discussion

Multidisciplinary design optimization was meant to include propeller's inflow velocity effects in the optimization study. Also, including a BEM based discipline in the optimization algorithm could help optimizing the propeller's performance based on the inlet flow velocity. Moreover, this study was meant to optimize the lift characteristics of system by restraining the pressure drag's influence on the model.

The overall thickness of the secondary wing was increased by the optimizer which was contradictory to the results of the study where the system's drag behavior was dominant (Chapter 6.2).

It was interesting to observe that even though the drag coefficient of system was significantly increased, the overall propulsive efficiency of system was maintained due to the influence of wings on propeller's performance. This study shows, that by increasing the lift coefficient of the secondary wing, flow velocity in the duct decreased, which increased the generated thrust force by the propeller and as result the overall propulsive efficiency was maintained.

8 Conclusion and Discussion

One engine in the array of OTW based DP system was modeled and analyzed with the help of CFD simulations to investigate propeller wing interactions. Moreover, identifying the critical parameters and their influence on the system, reducing calculation cost of simulations for an inexpensive and successful optimization study and estimating the effect of different simplifications were also the subject of this research.

This study showed that the presence of a secondary wing could majorly improve the aerodynamic characteristics of OTW based propellers. From the initial test of this configuration, it was confirmed that by implementing a second wing above the propeller, the space between main wing and this newly added element functions similar to a converging-diverging nozzle. The secondary wing alone could accelerate the flow to improve the lifting performance and also reduce flow velocity in the duct between wings (depending on its shape) to increase the overall propulsive efficiency.

Identifying the parameters alone is not enough to perform an intensive analysis. As the number of variables increased, the optimization's cost amplified linearly. With the resources in hand, it was not possible to include and calculate all the flow features. Therefore, some assumption and simplifications were made to reduce calculation cost of the analysis. However, the effect of these simplifications was studied in order to understand the degree of compromises. The following is a lift of the assumptions that were made to reduce the computational cost of the simulation.

1. *Euler calculations:* This form of analysis was chosen to reduce the computational cost and complexity of the model. Performing viscous flow calculations or using RANS models could make interpretation of solutions challenging without Euler solutions. Including RANS models could increase the calculation cost of the simulation roughly by a factor of 4 to 8. Because evaluating RANS model alone increases the number of equations required to reach the solution and therefore the required computational cost of the simulation. Also, evaluation of the RANS models demands a much finer spatial and temporal discretization, which raises the calculation cost of the simulations.
2. *Compressible flow:* Including the compressibility effects in simulations decreases the modeling error of the analysis. It is evident from initial tests that the propeller accelerates the flow in fluid domain and increases freestream Mach number up to 0.3. This means that there is roughly an 8% difference between the cases of compressible and incompressible flow conditions. Therefore, it was chosen to include the compressibility effects in simulations.

3. *Isothermal flow condition:* As the pressure of flow changes in fluid domain, the volume and temperature of fluid is affected. The influence of the pressure change on the volume of fluid translates to compressibility effects, which is included in the calculations. However, the energy state of fluid is also affected due to the fluid's pressure changes. In order to reduce the computational cost of simulations, the influence of the flow velocity on the energy state of flow was neglected, and therefore the flow was considered to be isothermal. Influence of this assumption was significant on the estimation of drag coefficient. Therefore, after the optimization process, the initial and optimum point of the study were recalculated with adiabatic flow condition to confirm and validate the solution of the optimization study.
4. *Actuator disc model:* Modeling an actual propeller in CFD simulations requires a considerable amount of computational power and validating the model can be time consuming. Since the engine that is used in this project is a rescaled model of a conventional engine, the propeller shape should be designed, which would expand this project beyond its requirements. In order to reduce the complexity of the model and also to focus more on propeller wing interaction rather than designing a propeller, an actuator model was implemented in the model. According to the references, such a model could accurately represent a propeller if appropriately constructed (Chapter 2.5).
5. *The inlet flow velocity of the propeller:* As the chosen parameters were varied to optimize the model's shape and orientation, the inflow velocity of propeller experienced fluctuations. After a careful evaluation of different cases, it was concluded that the influence of the local inlet flow velocity of propeller is significant and should be taken into account. Neglecting this effect could damage the pressure drag prediction by $60\% \pm 4\%$ and the estimation of the model's lift to drag ratio by $2.5\% \pm 1.5\%$ depending on the chosen drag coefficient of the wingless aircraft.

After providing necessary context to motivate this project's approach, the research question could be answered.

1. How do the main wing and secondary wing geometry variations affect overall propulsive efficiency and aerodynamic performance of the system?

The first research question aimed to evaluate the influence of geometry change on the system's aerodynamic performance and propulsive efficiency. This question was divided into three sub questions so that it could be answered more efficienctly. Firstly, it is necessary to separate the desirable and undesirable aspect of the studied model and only then try to improve the advantageous factors and to eliminate the aspects that damage the efficiency of the model. Therefore, the sub questions are expressed as follows.

1.1 By including the secondary wing, is this model's orientation comparable to any known topology?
1.2 What are the advantages and disadvantages of propeller wing interactions in this particular orientation?
1.3 How do the main wing and the secondary wing influence performance of the propeller?

The addition of the secondary wing forms a duct between two wings, which is comparable to a converging-diverging nozzle. According to the study in chapter 4.1, the flow was accelerated upstream the secondary wing and decelerated by the duct. This flow behavior was examined by comparing pressure coefficient plots of the main wing and the secondary wing and correlating the cross sectional area change between wings to [Eq.33].

As it was discussed in chapter 4.1, the main advantage of OTW based DP system was that the propeller induced the flow over the upper surface of main wing and improved the lift coefficient. Moreover, the addition of a secondary wing increased this effect by creating a converging-diverging duct between wings. The converging part of the duct increased the flow velocity upstream of the secondary wing, which improved the lifting performance of the main wing. As flow passes through diverging part of the duct, it recovered its static pressure, which has a desirable effect on the propeller's performance. According to BEM calculation, as the inlet flow velocity of the propeller decreases, the generated thrust of that propeller increases.

However, increasing flow velocity on the upper surface of the main wing could damage lifting performance of the secondary wing. Flow velocity in the duct could increase beyond the value of the flow velocity on the suction surface of the secondary wing and cause this element to produce negative lift. Moreover, increasing the effectiveness of the converging

part of duct could also damage the propeller's performance and increase the drag coefficient.

The propeller performance is affected by the main wing and the secondary wing's shape. The wings could accelerate or decelerate the flow upstream of propeller and affect the inlet flow velocity of the propeller, which directly influences the generated thrust. It is desirable to increase the pressure on the lower surface of the secondary wing to decelerate the flow upstream of the propeller by increasing the secondary wing's angle of attack (Chapter 4.4), increasing the secondary wing's camber (Chapter 4.3) and reducing the secondary wing's nose radius (Chapter 6.2).

2. Which design changes can provide desired velocity profile over the upper surface of the main wing to result in an optimum interaction between both wings and propeller?
2.1 What is the impact of the secondary wing's orientation on aerodynamic performance and propulsive efficiency of the system?
2.2 What is the impact of the propeller's position on aerodynamic performance and propulsive efficiency of the system?

The first question is answered by the studies conducted in chapter 4.2, chapter 4.3, chapter 4.4 and chapter 6.2. Chapter 4.2 showed, as the spacing between the wings was increased, the effectiveness of the duct's converging part decreased. As a result, the flow decelerated at higher rate in the duct (also accelerated less upstream the secondary wing) and the lifting performance of the secondary wing increased. Moreover, increasing the spacing of the wings damaged the lifting performance of the main wing, which was compensated by the improvement of the secondary wing's lifting performance.

Increasing the secondary wing's angle of attack (Chapter 4.4) and its initial lift coefficient (Chapter 4.3), increased flow's pressure on the lower side of this element, which increased the effectiveness of the diverging part of the duct. In this case, flow velocity was decreased in the duct and the total lift coefficient and the propeller's performance were improved. The secondary wing's angle of attack could directly change the duct's shape between the wings by widening the throat area of the nozzle, which results in accelerating the flow upstream of the secondary wing at a lower rate.

The optimization study in chapter 6.2 shows that by reducing secondary wing's nose radius, thickness and chord length, the total drag coefficient could be reduced. This study further shows that drag coefficient's sensitivity to the secondary wing's shape. In this study, the total lift coefficient was reduced by $6.5\% \pm 0.5\%$ and the drag coefficient

reduced by about $78\% \pm 4\%$, which improved the objective function of this project by about $4\% \pm 0.75\%$.

The influence of propeller's position on the aerodynamic performance was evaluated in chapter 4.5 and chapter 5 under two different assumptions of constant power and constant thrust. The chordwise location of the disc, as well as the spacing between the propeller and the main wing surface, influenced the aerodynamic characteristics of the model. As the disc was moved closer to the trailing edge of main wing and as propeller's clearance from main wing's surface was reduced, the propeller induced the flow over the upper surface of the main wing at a higher rate and improved the lifting performance. The model's configuration required to confine the propeller between two wings and therefore, the chordwise position of the wing was only varied behind the nozzle throat line where the pressure recovery was highest. It could be observed from this analysis that the drag coefficient decreased as the disc was moved forward. The total drag coefficient's rate of improvement is higher than the lift coefficient's rate deterioration as the disc was moved further away from the trailing edge. Therefore, the behavior of lift to drag ratio was dominated by the total drag coefficient.

3.Does the CFD simulation resemble and capture the reality of the physical phenomenon and occurrences? (CFD simulation validation and verification)

In chapter 3.1.1 and chapter 3.1.2, discretization error of the model was estimated for three different flow conditions, namely inviscid flow condition, isothermal flow condition and adiabatic flow condition. The grid convergence study resulted in three different grids within the asymptotic region of convergence and a maximum discretization error of 1% and 4% to respectively estimate total lift coefficient and total drag coefficient. Moreover, the study in chapter 3.1.3 shows that total lift and drag coefficient respectively have less than 1% and about 2% iterative convergence error. The verification study shows the Navier-Stokes formulas as solved with an acceptable margin of error.

Moreover, the model is validated with the help of experimental data in chapter 4.2.5 to show that by eliminating the influence of fluid's viscosity and propeller's hub and representing the propeller with an actuator disc, the model could still successfully capture the general flow characteristics.

Optimization studies

The optimization study was performed under two different conditions, and the results were impressive. The first optimization study in chapter 6 is performed with the assumption of constant thrust with a small chosen $C_{D_{ATR72}}$. In this case the optimizer chose to decrease the total drag coefficient, which as a result increased the system's overall propulsive efficiency. However, in the second optimization study in chapter 7, $C_{D_{ATR72}}$ was increased to force the optimizer to increase the overall lift coefficient. It was expected to observe a reduction in overall propulsive efficiency since the total drag coefficient was increased. Nonetheless, as the secondary wing's lift coefficient was improved, the flow velocity in the duct decreased, which influenced the propeller's performance and increased thrust force of the propeller. This effect compensated for the added drag and helped the optimizer to maintain the propulsive efficiency and even improve it by about $1.2\% \pm 0.1\%$.

It can be conclusively stated, that the influence of propeller's inflow velocity on the propeller's performance cannot be ignored in the optimization studies. Because in some cases propulsive efficiency may remain constant due to inflow velocity variation and by neglecting this effect, propulsive efficiency may decrease.

Recommendations

The attention of this project was divided into two main aspects, i.e., computational cost reduction and performance improvement of OTW based distributed propulsion system with an addition of a secondary wing. Reducing the computational cost of simulations by investigating different assumptions and their influence could help this research to perform a thorough analysis. Also, this could help the future projects to have a better understanding of the opportunities and limitations of studying propeller wing interaction.

It is recommended to perform viscous flow calculations with the help of RANS models. Including RANS models in the simulations could undoubtedly increase the computational cost of simulations. Therefore, it is more practical to conduct the optimization studies with the help of Euler calculation with the designed algorithm in chapter 7 and simulate the initial and final point of the optimization study with RANS models.

Due to the shortage of time, this research failed to investigate the influence of propeller's angle of attack. This parameter could significantly influence overall propulsive efficiency and lifting performance of the model.

It is also recommended to simulate this particular model at low speed flight condition to investigate the effectiveness of secondary wing and propeller's angle of attack during take-off and landing.

9 References

[1] S. W. Ashcraft, Andres S. Padron, Kyle A. Pascioni, and Gary W. Stout, Jr., Dennis L. Huff, Review of Propulsion Technologies for N+3 Subsonic Vehicle Concepts Glenn Research Center, Cleveland, Ohio.,2011

[2] E. Obert, "Aerodynamic Design of Transport Aircraft," Delft University of Technology, Faculty of Aerospace Engineering, ISO Press b.v., 2016

[3] H. D. Kim, J. L. Felder, M. T. Tong," Revolutionary Aero-propulsion Concept for Sustainable Aviation: Turboelectric Distributed Propulsion," NASA Glenn Research Center Cleveland, Ohio, U.S.A. 2013

[4] G. Ameyugo, M. Taylor, R. Singh, Cranfield University, "DISTRIBUTED PROPULSION FEASIBILITY STUDIES," Rolls-Royce plc, ICAS 2006

[5] C. Rossow, J. L. Godard, H. Hoheisel, V. Schmitt, Investigation of Propulsion Integration Interference Effects on a Transport Aircraft Configuration, DLR, Institut fur Entwurfsaerodynamik, D-38108, Braunschweig, Germany, ONERA, F-92322 Chatillon, France, 1994

[6] A. Ko, J.A. Schetz and W. H. Mason, Assessment of the Potential Advantages of Distributed-Propulsion for Aircraft, Multidisciplinary Analysis and Design Center for Advanced Vehicles Virginia Polytechnic Institute and State University Blacksburg, VA 24061-0203, 2003

[7] H. D. Kim, Distributed Propulsion Vehicles, NASA Glenn Research Center Cleveland, Ohio, USA, 27th International Congress of the Aeronautical Science, 2017

[8] A. S. Gohardani, G. Doulgeris, R. Singh," Challenges of future aircraft propulsion: A review of distributed propulsion technology and its potential application for the all-electric commercial aircraft," Department of Power and Propulsion, School of Engineering, Cranfield University, Bedfordshire MK430AL, United Kingdom 2010.

[9] A. Isyanov, A. Lukovnikov, and A. Mirzoyan, Development challenges of distributive propulsion systems for advanced aeroplanes, Propulsion & A/C Matching Department, CIAM, Moscow, Russian Federation

[10] K. Reynolds, N. Nguyen, E. Ting, and J. Urnes Sr, Wing shaping concepts using distributed propulsion, NASA Ames Research Center, Moffett Field, California, USA, Boeing Research & Technology, Platform and Networked Systems Technology, Saint Louis, Missouri, USA

[11] H. D. Kim, J. L. Felder, M. T. Tong," Revolutionary Aero-propulsion Concept for Sustainable Aviation: Turboelectric Distributed Propulsion," NASA Glenn Research Center Cleveland, Ohio, U.S.A. 2013

[12] J. L. Felder, G. V. Brown, H. D. Kim, J. Chu. "Turboelectric Distributed Propulsion in a Hybrid Wing Body Aircraft." American Institute of Aeronautics and Astronautics, Inc. (NASA report). 2011

[13] R. Kirner, L. Raffaelli, A. Rolt, P. Laskaridis, G. Doulgeris, R. Singh, "An assessment of distributed propulsion: Advanced propulsion system architectures for conventional aircraft configurations," Cranfield University, Rolls-Royce plc., 2015

[14] R. Kirner, L Raffaelli, A. Rolt, P. Laskaridis, G. Doulgeris, R. Singh, "An assessment of distributed propulsion: Part B – Advanced propulsion system architectures for blended wing body aircraft configurations," Cranfield University, Rolls-Royce plc., 2015

[15] A. Ko, L.T. Leifsson, J.A. Schetz, W.H. Mason and B. Grossman and R.T. Haftka," MDO of a Blended-Wing-Body Transport Aircraft with Distributed Propulsion," Virginia Polytechnic Institute and State University and University of Florida. AIAA's 3rd Annual Aviation Technology, integration, and operations, November 2003

[16] Leo Veldhuis, "Propeller Wing Aerodynamic Interference," Doctoral Dissertation, Delft University of Technology, June 2005

[17] F. M. Catalano, "On the effects of an installed propeller slipstream on wing aerodynamic characteristics," Acta Polytechnica, Vol.44, 2004

[18] F. M. Catalano, M. G. Maunsell "Numerical and experimental analysis of the effect of a pusher propeller on a wing and body," AIAA, Aerospace Sciences Meeting, and Exhibit, 1997

[19] F. M. Catalano, J. L. Stollery, "The effect of a High thrust pusher propeller on the flow over a straight wing," College of Aeronautics, Cranfield, Bedford, England, 2004

[20] L. Muller, D. Kožulovic, R. Radespiel, "Aerodynamic performance of an over-the-wing propeller configuration at increasing Mach number," German Aerospace Center, Technical University of Brunswick, 2014

[21] L. Müller, D. Kožulovic, M. Hepperle, R. Radespiel, "Installation Effects of a Propeller Over a Wing with Internally Blown Flap." AIAA Journal. 2012

[22] L. Muller, W. Heinze, D. Kožulovic, R. Radespiel, m. Hepperle, "Aerodynamic installation effects of an over-the-wing propeller on a high lift configuration," German Aerospace Center, Technical University of Brunswick, 2014

[23] E.C. Olson, B.P. Selberg, "Experimental Determination of improved Aerodynamic characteristics utilizing biplane wing configuration," University of Missouri-Rolla, Rolla, Journal of Aircraft, Vol.13, 1976

[24] W. Hongbo, Z. Xiaoping, Z. Zhou, "Numerical simulation of the propeller/wing interactions at low Reynolds number," School of Aeronautics and Science and technology in UAV Laboratory, Northwestern Polytechnic University Xi'an, China, 2016

[25] Aircraftcompare.com, https://www.aircraftcompare.com/aircraftimage/ATR-72-600-Photo-1/1760, 2015

[26] K.K. Mani, "Design using Euler Equations," Lockheed-California Company, Burbank, AIAA 2nd applied Aerodynamics Conference, Seattle, Washington, 1984

[27] R. Acharya, Investigation of Differences in Ansys Solvers CFX and Fluent, Royal Institute of Technology, KTH Stockholm, June 2016

[28] L. Leifsson, A. Ko, W.H. Mason, J.A. Schetz, B. Grossman, R.T. Haftka, Multidisciplinary design optimization of blended-wing-body transport aircraft with distributed propulsion, Aerospace Science and Technology, volume 25, issue 1, March 2013

[29] A.P.M Luijendijk, “Propeller-wing interference study for over the wing positioned propeller configuration,” Delft University of Technology, Faculty of Aerospace July 2002.

[30] P. Marcus, "Aerodynamic modelling and performance analysis of over-the-wing propellers" Master Thesis project, Faculty of Aerospace engineering, Delft University of Technology, 2018

[31] M. F. Nita, D. Scholz, “Aircraft Design Studies Based on the ATR72”, Department of Automotive and Aeronautical Engineering, Hamburg University of Applied Sciences

[32] D. Küchemann, “The aerodynamic design of aircraft. American Institute of Aeronautics and Astronautics”, chapter 2.3, 2012

[33] D. Küchemann, “The aerodynamic design of aircraft. American Institute of Aeronautics and Astronautics”, chapter 2.5, 2012

[34] D. R. McDaniel, R. M. Cummings, S. A. Morton, and W. H. Mason, “Applied Computational Aerodynamics: A Modern Engineering Approach,” Cambridge University Press, 2015, chapter 4

[35] B. R. Williams.: The Prediction of Separated Flow Using a Viscous-Inviscid Interaction Method, R.A.E. Tech. Memo. Aero 2010, Farnborough, Dec. 1984.

[36] N. Hall, Euler Equations, https://www.grc.nasa.gov/www/k-12/airplane/eulereqs.html, Glenn Research Center, NASA, 2015

[37] N. Hall, Navier-Stokes Equations, https://www.grc.nasa.gov/www/k-12/airplane/nseqs.html, Glenn Research Center, NASA, 2015

[38] S.J Hulshoff, Private communications

[39] Q. R. Wald, “The aerodynamic of Propellers”, Progress in Aerospace Science, 102 Cape George Road, Port, Townsend, WA 98368 USA, 2006

[40] R. J.A.M. Stevens, L. A. Martínez-Tossas, C. Meneveau, “Comparison of wind farm large eddy simulations using actuator disk and actuator line models with wind tunnel experiments”, Department of Physics, Mesa Institute, and J. M. Burgers Centre for Fluid Dynamics, University of Twente, Department of Mechanical Engineering & Center for Environmental and Applied Fluid Mechanics, Johns Hopkins University,2016

[41] P. M. Rothhaar, P. C. Murphy, B. J. Bacon, I. M. Gregory, J. A. Grauer, R. C. Busan, and M. A. Croom, “NASA Langley Distributed Propulsion VTOL Tilt-Wing Aircraft Testing”, Modeling, Simulation, Control, and Flight Test Development, NASA Langley Research Center, Hampton, Virginia, 23681

[42] A. Seitz, J. Bijewitz, S. Kaiser, G. Wortmann, “Conceptual investigation of a propulsive fuselage aircraft layout”, Visionary Aircraft Concepts Bauhaus Luftfahrt e.V. and Munich, Germany, Munich Aerospace e.V.Munich, Germany

[43] L.L.M Veldhuis and R. Vos, MANTA, and NOVAIR projects, https://www.tudelft.nl/en/2016/lr/manta-and-novair-two-successful-clean-sky-2-proposals/, Delft University of Technology, May 2016

[44] A. Filippone, “CFD actuator disk solutions for a helicopter rotor in hover flight,” Master thesis, UMIST, Stockholm, 2013

[45] S. Wilkinson, http://concierge.typepad.com/cntraveler__perrinpost/2007/12/propeller-head.html, December 2007

[46] ANSYS User Guide Manual and Guide to CEL Programming

[47] N. Simisiroglou, M. Karatsioris, K. Nilsson, S.P. Breton, S. Ivanell, The actuator disc concept in PHOENICS, 13th Deep Sea Offshore Wind R&D Conference, EERA DeepWind'2016, 20-22 January 2016, Trondheim, Norway

[48] A. Jameson and L. Martinelli, N.A. Pierce, "Optimum Aerodynamic Design Using the Navier–Stokes Equations," Theoretical and Computational Fluid Dynamics, Springer-Verlag 1998

[49] R. M. Hicks, Preston A. Hennet, "Wing Design by Numerical Optimization," Journal of Aircraft, VOL. 15, NO. 7, JULY 1978

[50] A. Jameson, "Efficient Aerodynamic Shape Optimization," 10th AIAA Multidisciplinary Analysis and Optimization Conference, 30 August - 1 September 2004, Albany, New York

[51] D. A. Masters, N. J. Taylory, T. C. S. Rendall, C. B. Allen and D. J. Poole, "Review of Aerofoil Parameterization Methods for Aerodynamic Shape Optimization," 53rd AIAA Aerospace Sciences Meeting, 5-9 January 2015, Kissimmee, Florida

[52] A. T. Wick, J. R. Hooker, and C. J. Hardin, "Integrated Aerodynamic Benefits of Distributed Propulsion", Lockheed Martin Aeronautics Company, Marietta, GA, 30063 Cale H. Zeune§ Air Force Research Laboratory, Wright-Patterson AFB, OH, 45433

[53] D. Küchemann, "The aerodynamic design of aircraft. American Institute of Aeronautics and Astronautics", chapter 2.1, 2012

[54] D. Küchemann, "The aerodynamic design of aircraft. American Institute of Aeronautics and Astronautics", chapter 2.2, 2012

[55] J. D. Anderson, "Fundamentals of Aerodynamics", McGraw–Hill, 4th Edition,2007

[56] S. J. Hulshoff, "Computational Modelling", Aerodynamic Group Faculty of Aerospace engineering, Delft University of Technology

[57] T. J. Barth, H. Deconinck, "Error Estimation and Adaptive Discretization Methods in Computational Fluid Dynamics", Springer-Verlag Berlin Heidelberg

[58] M. Hafez, K. Morinishi, J. Periaux, Computational Fluid Dynamics for the 21st Century, Proceedings of a Symposium honoring Prof. Satofuka on the Occasion of his 10th birthday, Kyoto, Japan, 15-17 July 2000

[59] W. L. Oberkampf, T. G. Trucano, Verification and Validation in computational fluid dynamics, Validation/Optimization and Uncertainty Estimation Department, Sandia National Laboratories, 2002

[60] H. K. Versteeg, W. Malalasekera, An Introduction to Computational Fluid Dynamics, Pearson Education, Second Edition Published 2007, Chapter 10

[61] Xfoil program and documentation, http://web.mit.edu/drela/Public/web/xfoil/

[62] E.A.P. Marcus, R. de Vries, A. Raju Kulkarni, L.L.M. Veldhuis, “Aerodynamic Investigation of an Over-the-Wing Propeller for Distributed Propulsion,” AIAA Aerospace Sciences Meeting 8-12 January, Delft University of Technology, Delft, 2629 HS, The Netherlands

[63] A. Elham, Private communications

[64] L.L.M. Veldhuis, Private communications

[65] H. Lomax, T. H. Pulliam, D. W. Zingg, “Fundamentals of Computational Fluid Dynamics,” 1999

[66] S. Prudhomme, J. T. Oden, “Computable Error Estimators and Adaptive Techniques for Fluid Flow Problems,” Texas Institute for Computational and Applied Mathematics, The University of Texas at Austin, Austin, Texas 78712, U.S.A.

[67] L. Muller, J. Friedrichs, D. Kožulovic. "Unsteady Flow Simulations of an Over-the-wing Propeller Configuration." AIAA Journal of Propulsion and Energy.2014

[68] A. M. Stoll,” Comparison of CFD and Experimental Results of the LEAPTech Distributed Electric Propulsion Blown,” Joby Aviation, Santa Cruz, California, 95060, 15th AIAA Aviation Technology, Integration, and Operations Conference, 22-26 June 2015, Dallas, TX

Appendix A: Blocking and Meshing

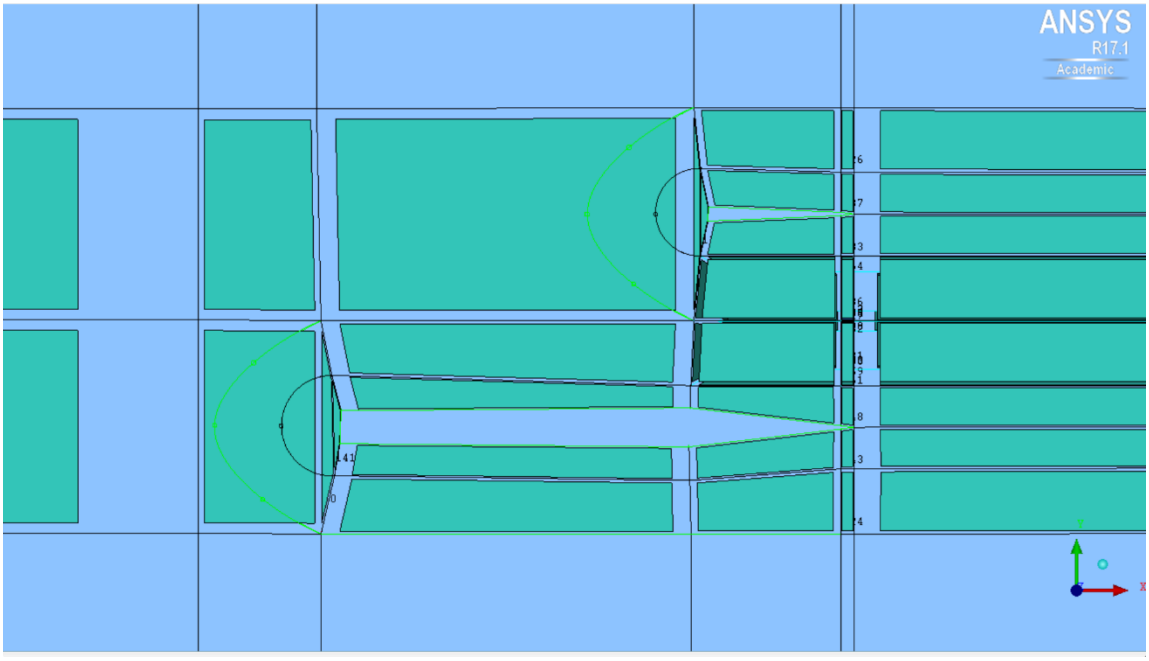

Figure A-1: Side view (2D view) of the CFD model's blocks in the fluid domain (ICEM)

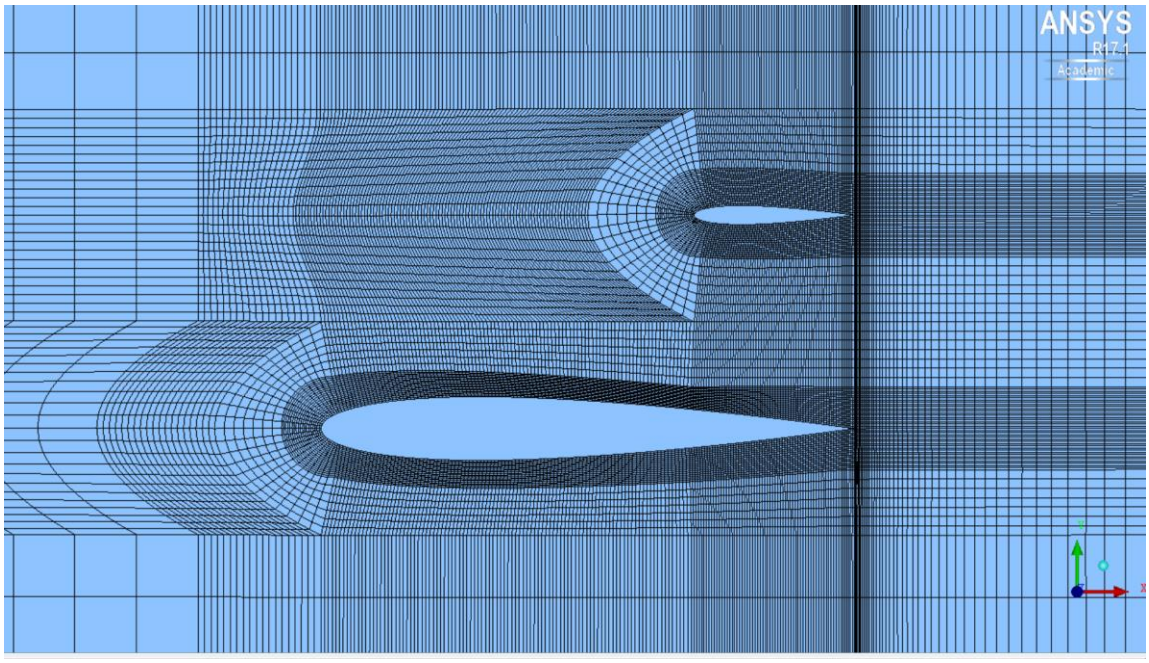

Figure A-2: Side view (2D view) of the CFD model's mesh in the fluid domain (ICEM), using C-grid topology to increase the grid quality around the wings

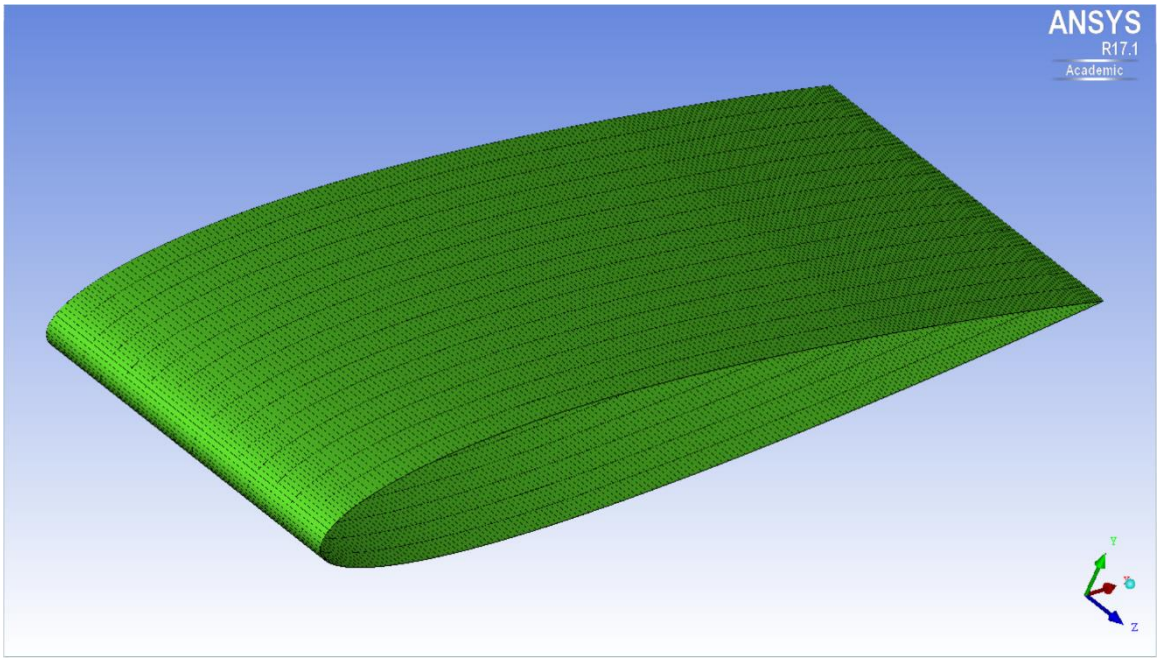

Figure A-3: 3D view of the main wing's surface mesh

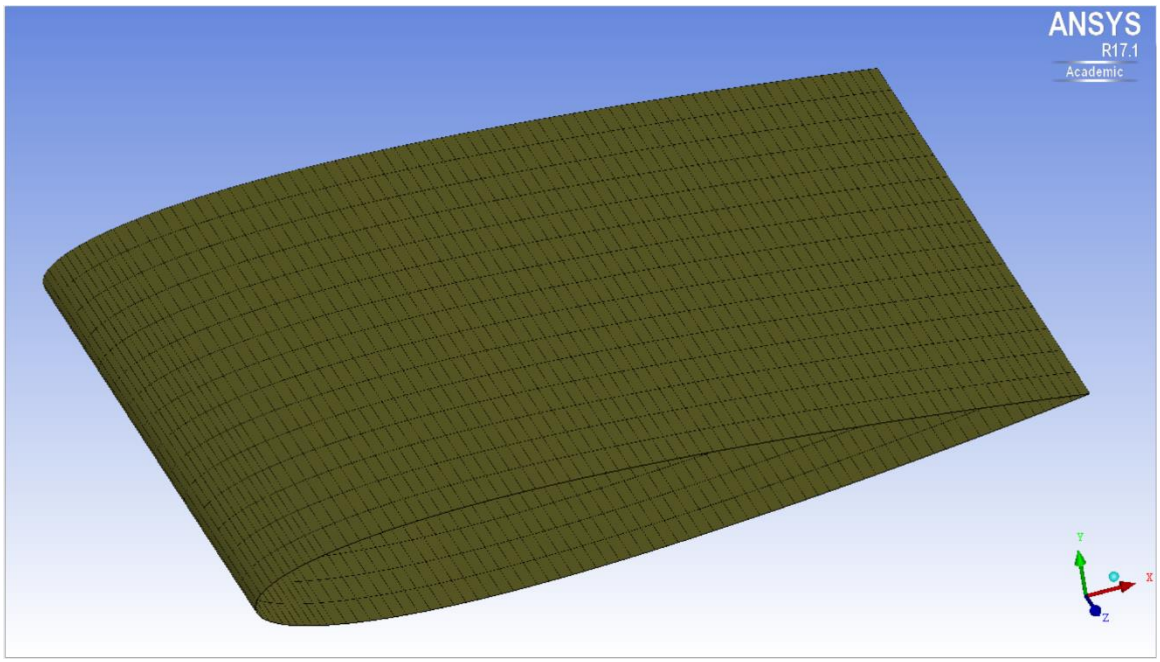

Figure A-4: 3D view of the secondary wing's surface mesh

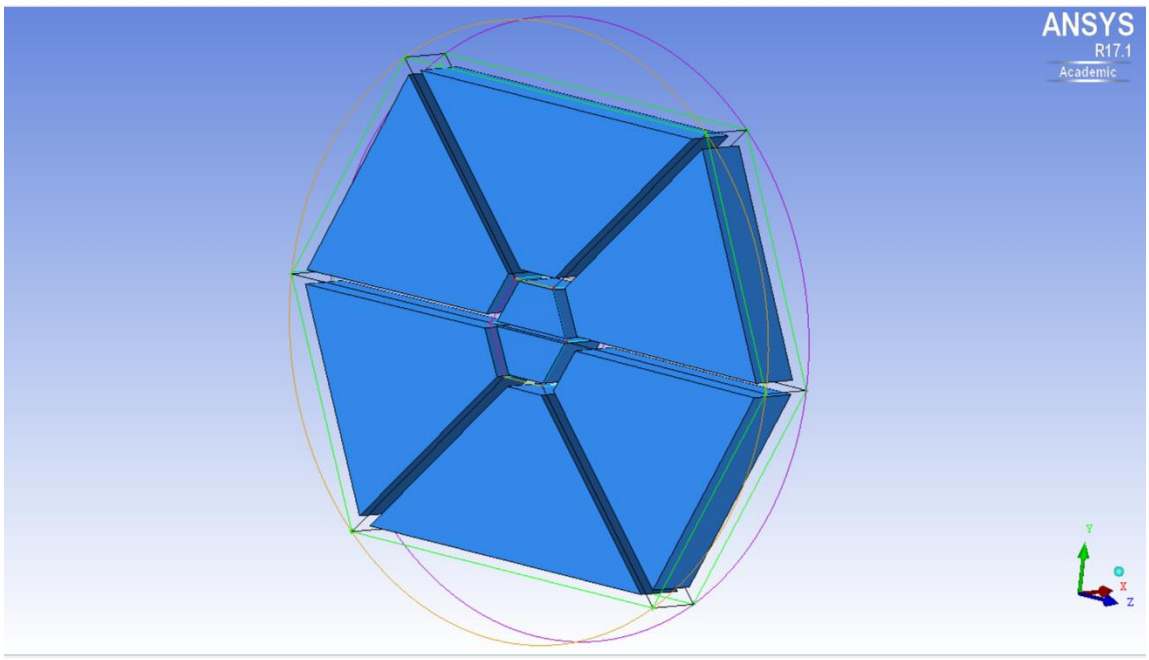

Figure A-5: Actuator disc's blocking orientation, to increase the mesh quality in this region a hexagonal frame was drawn in the middle of the disc and an O-grid was created around this frame

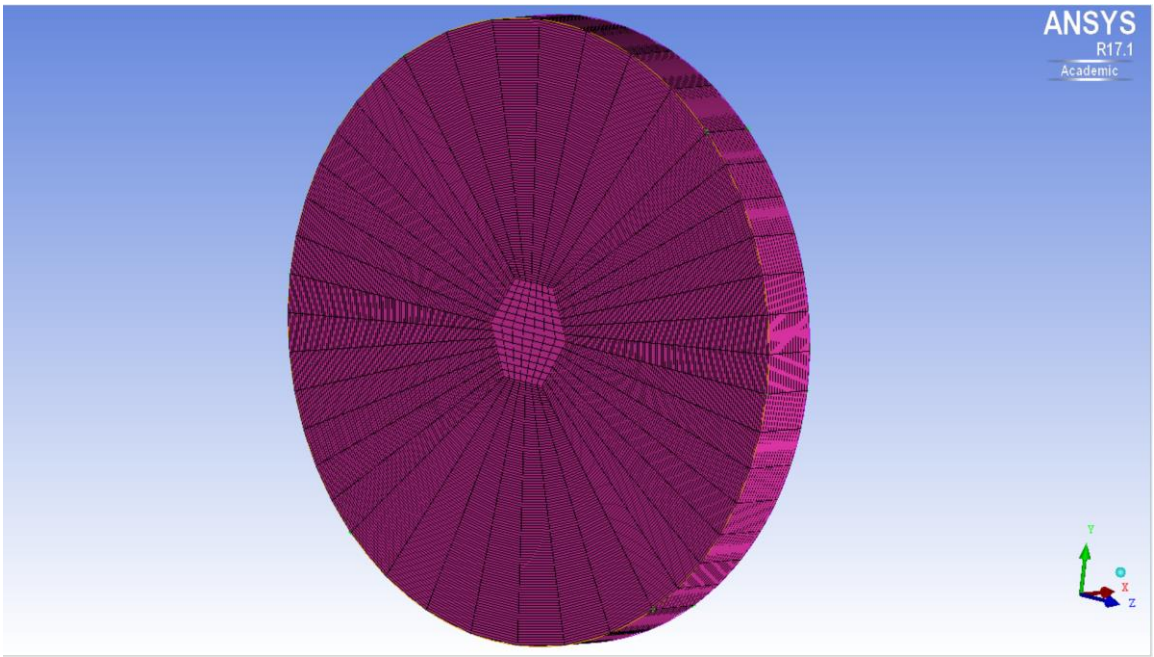

Figure A-6: 3D view of the actuator disc's surface mesh

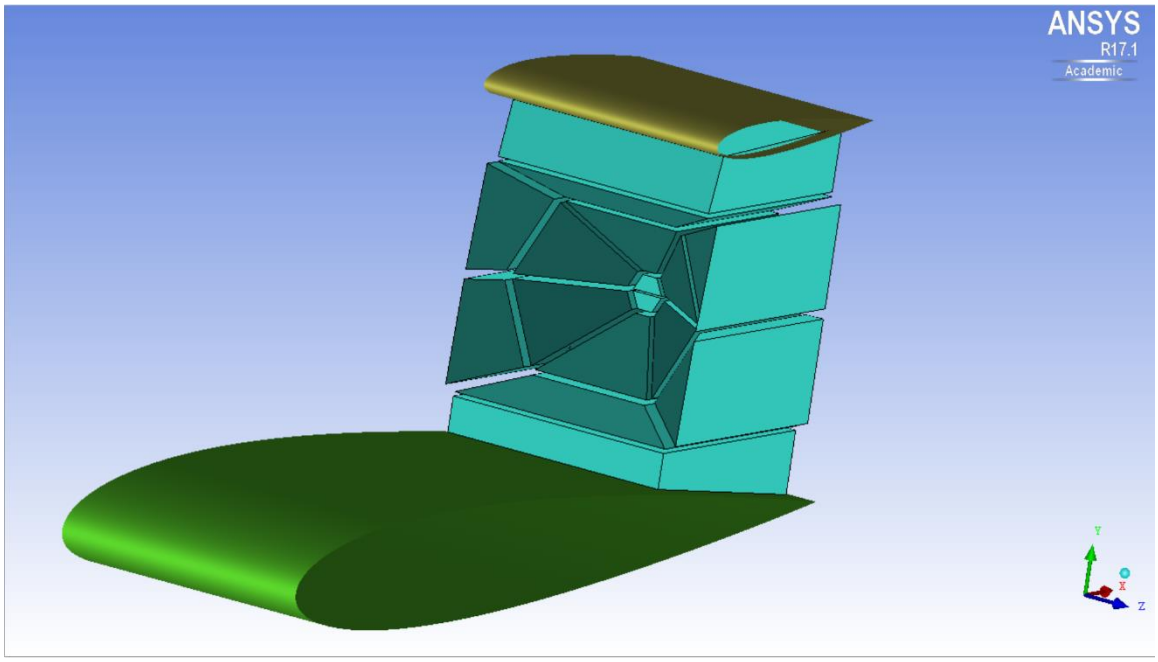

Figure A-7: 3D view of the duct's blocking orientation, two O-grids were required to construct this topology to improve the in the duct region mesh quality

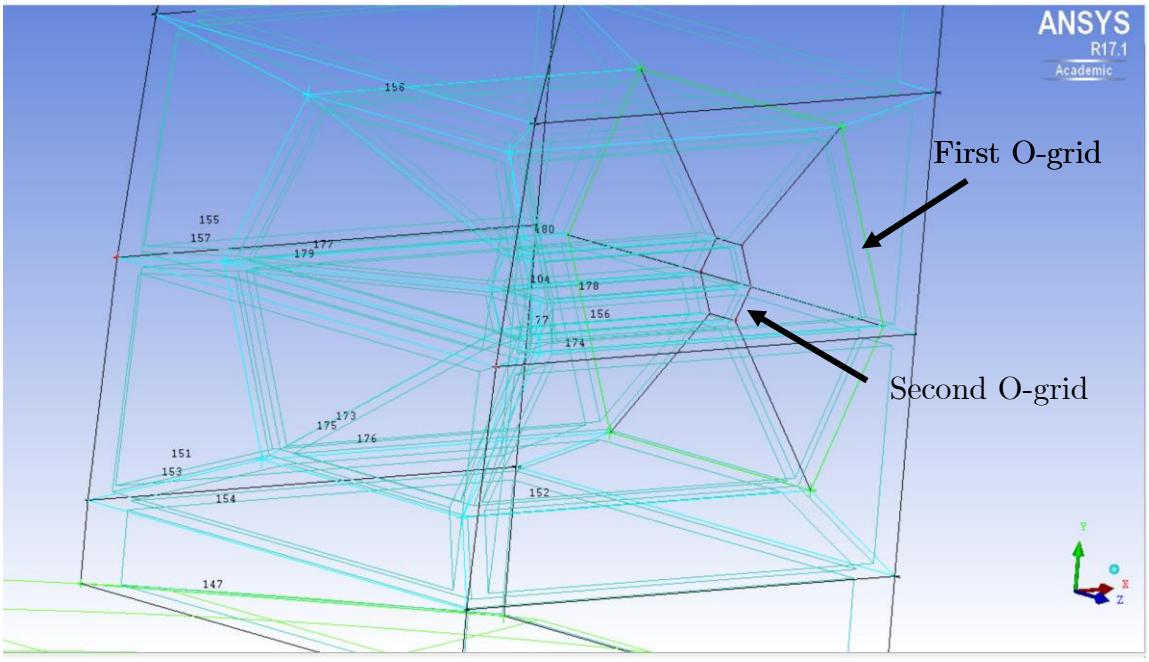

Figure A- 8: 3D wireframe view of the duct's blocking orientation, the first O-grid is created around the disc and the second O-grid is created in the middle of the actuator disc

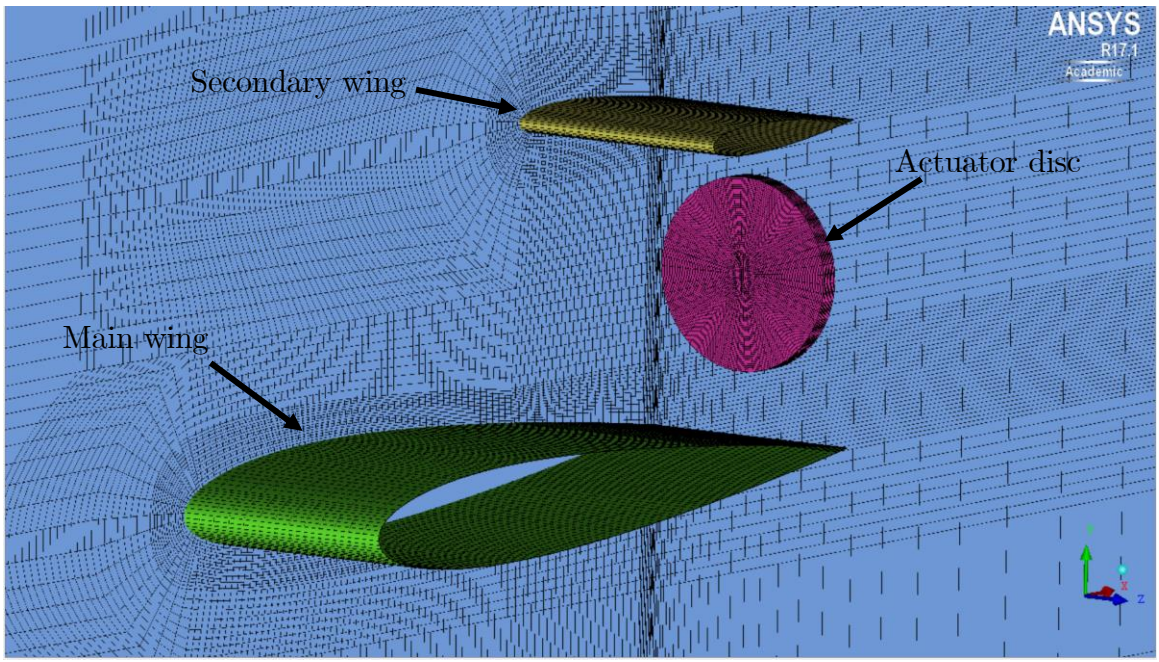

Figure A-9: 3D view of the whole system's structured mesh including the actuator disc in pink, main wing in green, secondary wing in yellow and the fluid domain in blue

Appendix B: CFD Contours

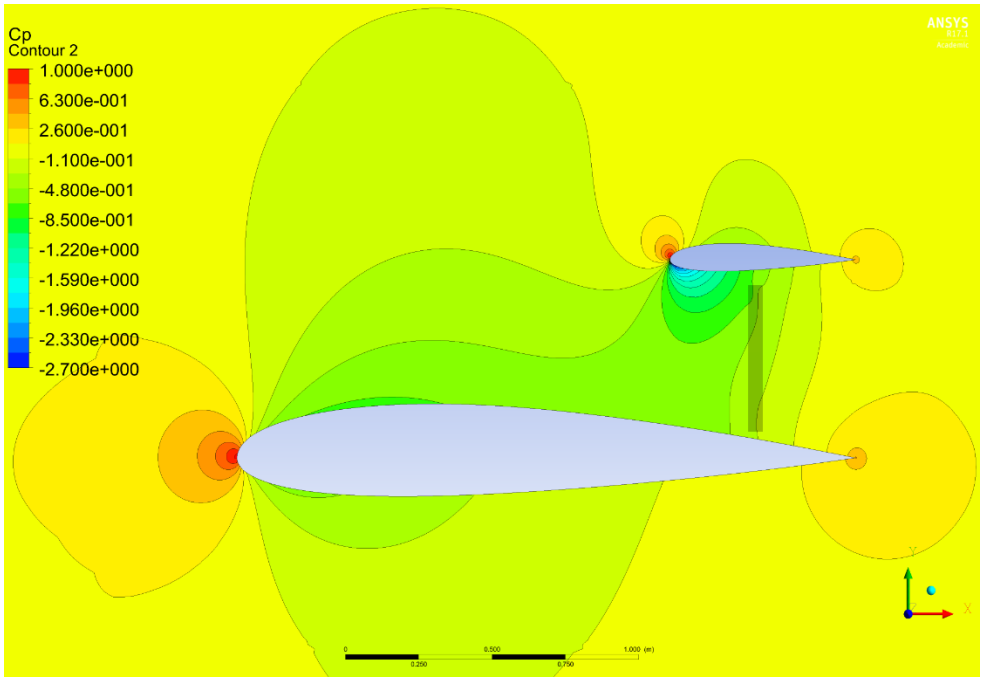

Figure A- 10: Chapter 5.2: wing spacing analysis, $C_p$contour, 50% spanwise position (middle of the disc), 32% wing spacing, 85% chordwise position of the propeller

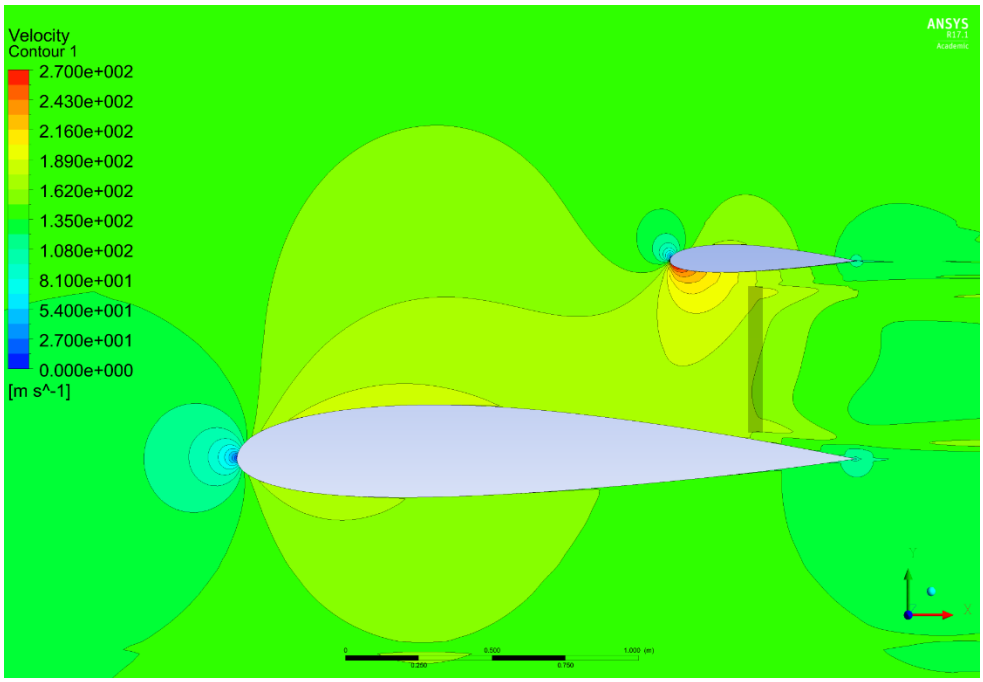

Figure A- 11: Chapter 5.2: wing spacing analysis, velocity contour, 50% spanwise position (middle of the disc), 32% wing spacing, 85% chordwise position of the propeller

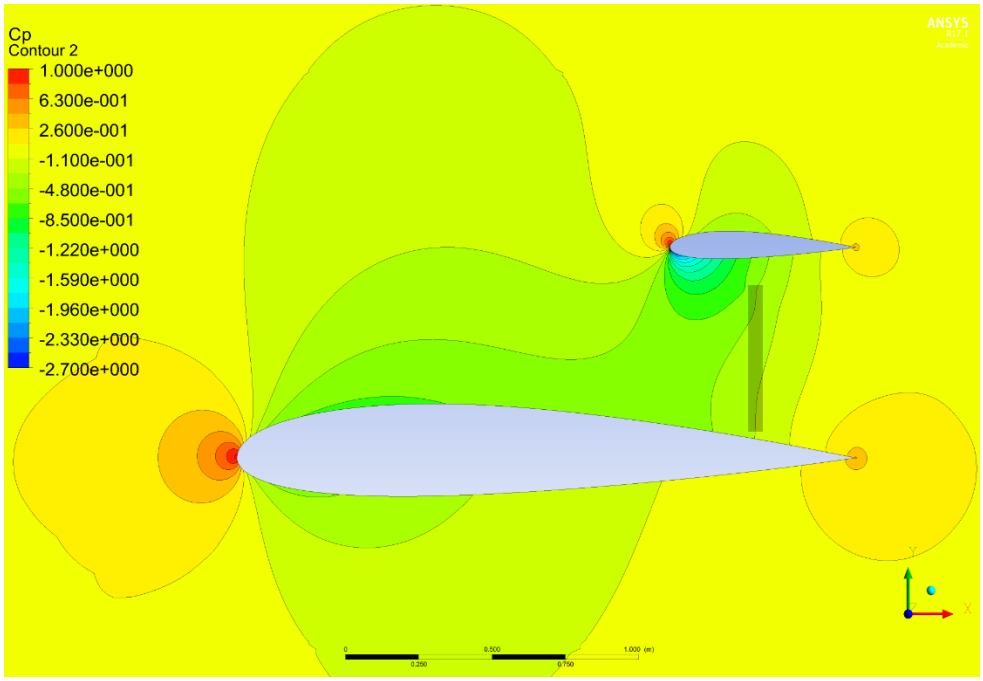

Figure A- 12: Chapter 5.2: wing spacing analysis, $C_p$contour, 50% spanwise position (middle of the disc), 34% wing spacing, 85% chordwise position of the propeller

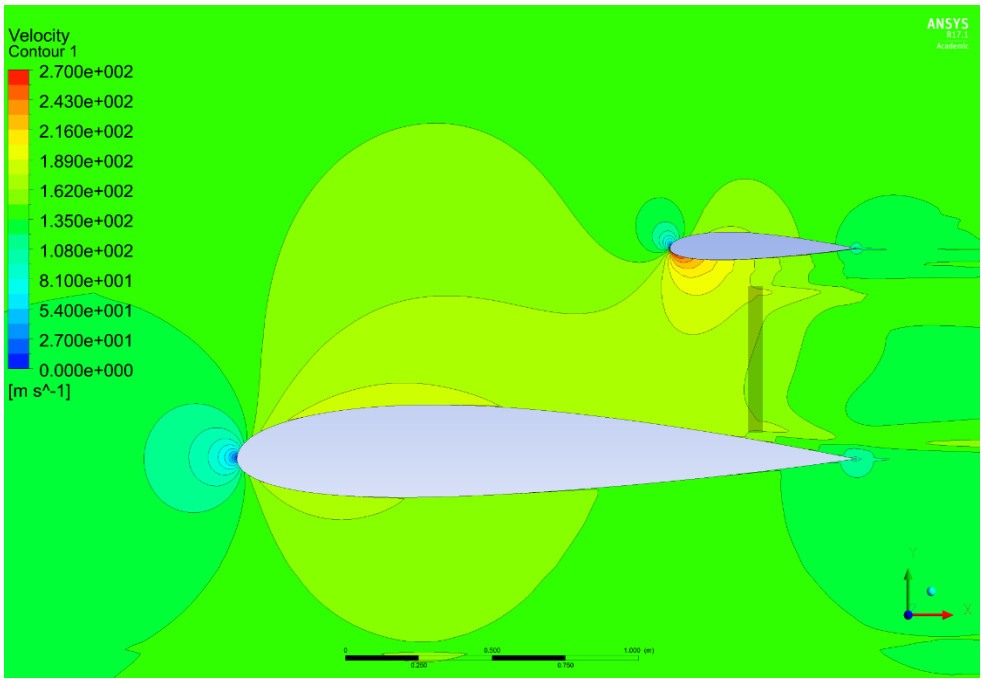

Figure A- 13: Chapter 5.2: wing spacing analysis, velocity contour, 50% spanwise position (middle of the disc), 34% wing spacing, 85% chordwise position of the propeller

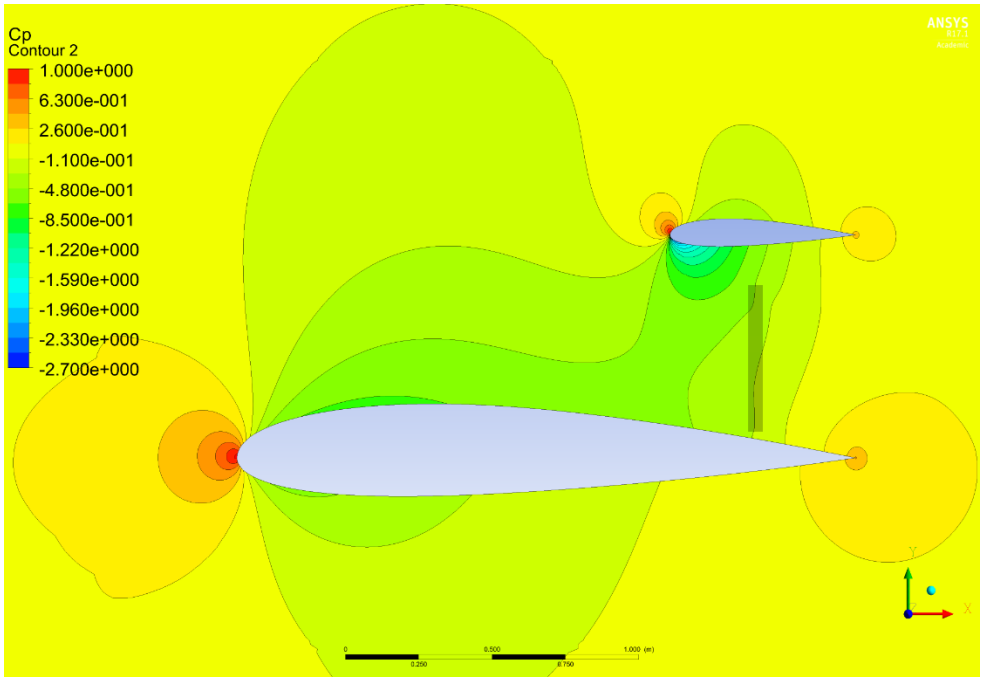

Figure A- 14: Chapter 5.2: wing spacing analysis, $C_p$contour, 50% spanwise position (middle of the disc), 36% wing spacing, 85% chordwise position of the propeller

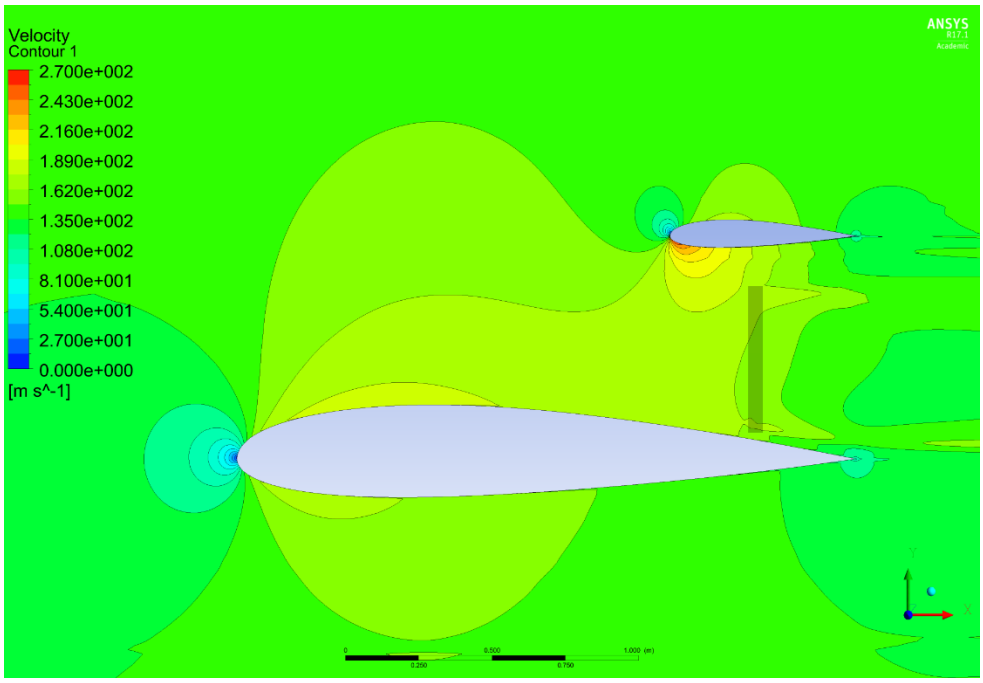

Figure A- 15: Chapter 5.2: wing spacing analysis, velocity contour, 50% spanwise position (middle of the disc), 36% wing spacing, 85% chordwise position of the propeller

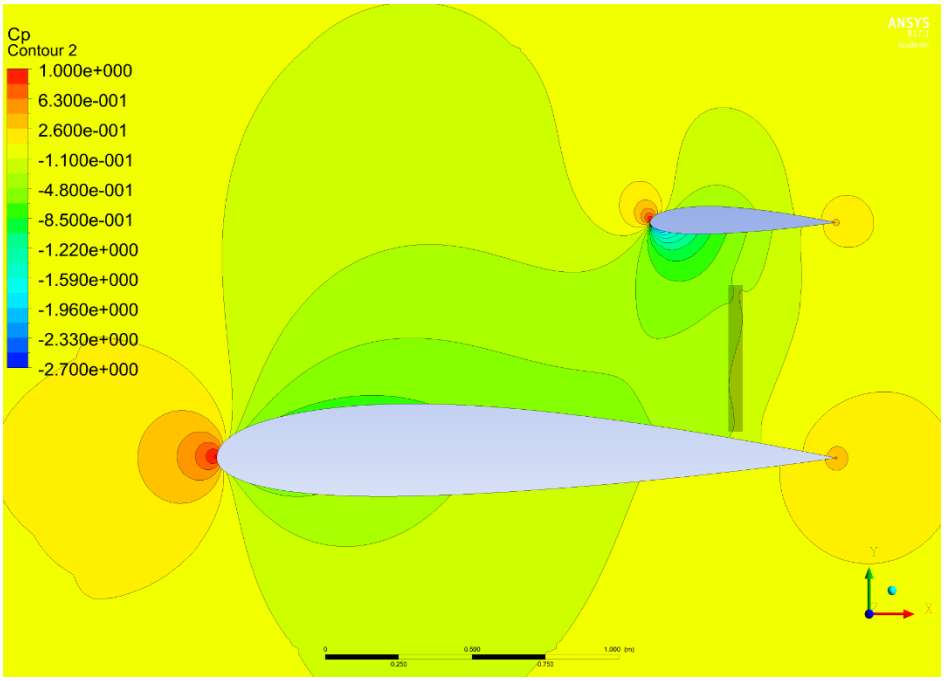

Figure A- 16: Chapter 5.2: wing spacing analysis, $C_p$contour, 50% spanwise position (middle of the disc), 38% wing spacing, 85% chordwise position of the propeller

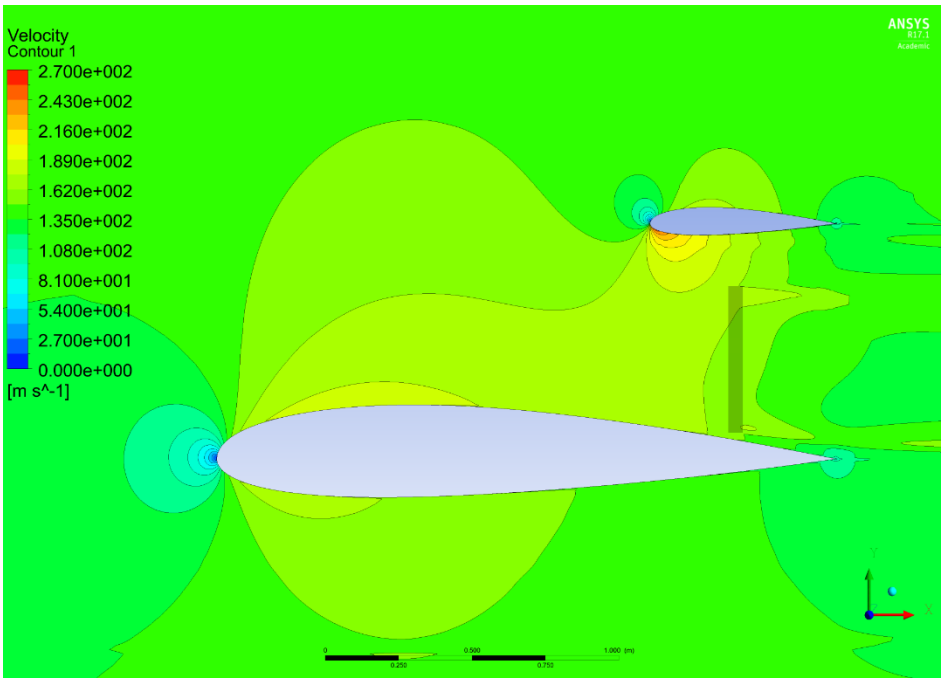

Figure A- 17: Chapter 5.2: wing spacing analysis, velocity contour, 50% spanwise position (middle of the disc), 38% wing spacing, 85% chordwise position of the propeller

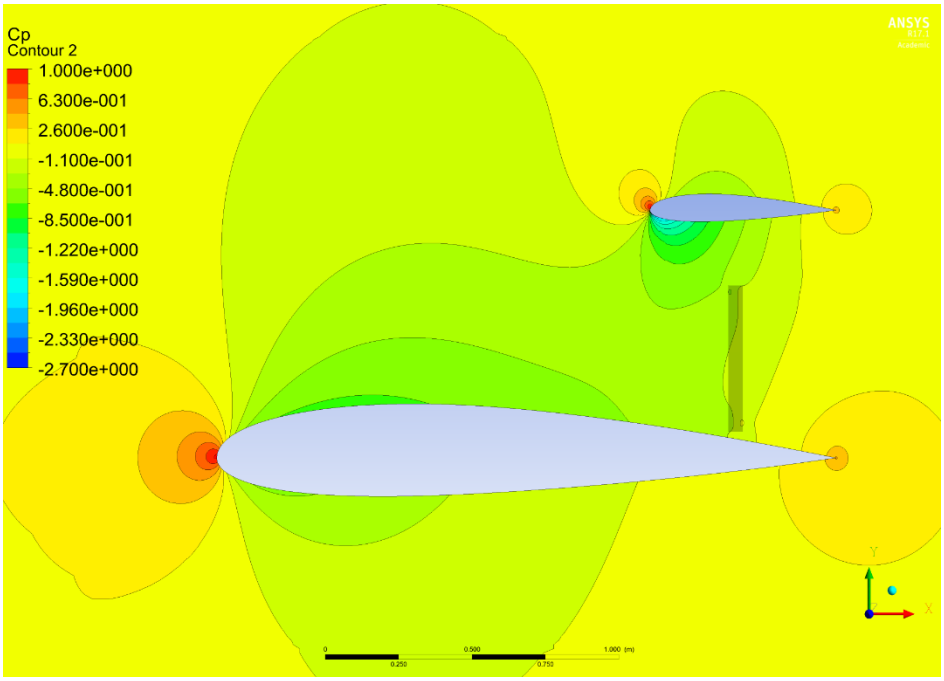

Figure A- 18: Chapter 5.2: wing spacing analysis, $C_p$contour, 50% spanwise position (middle of the disc), 40% wing spacing, 85% chordwise position of the propeller

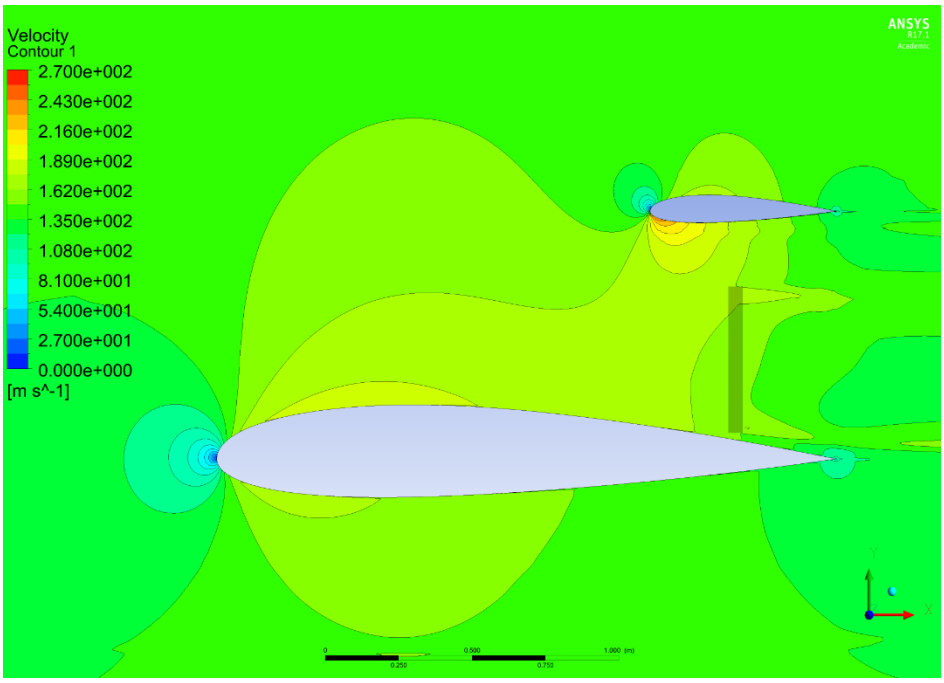

Figure A- 19: Chapter 5.2: wing spacing analysis, velocity contour, 50% spanwise position (middle of the disc), 40% wing spacing, 85% chordwise position of the propeller

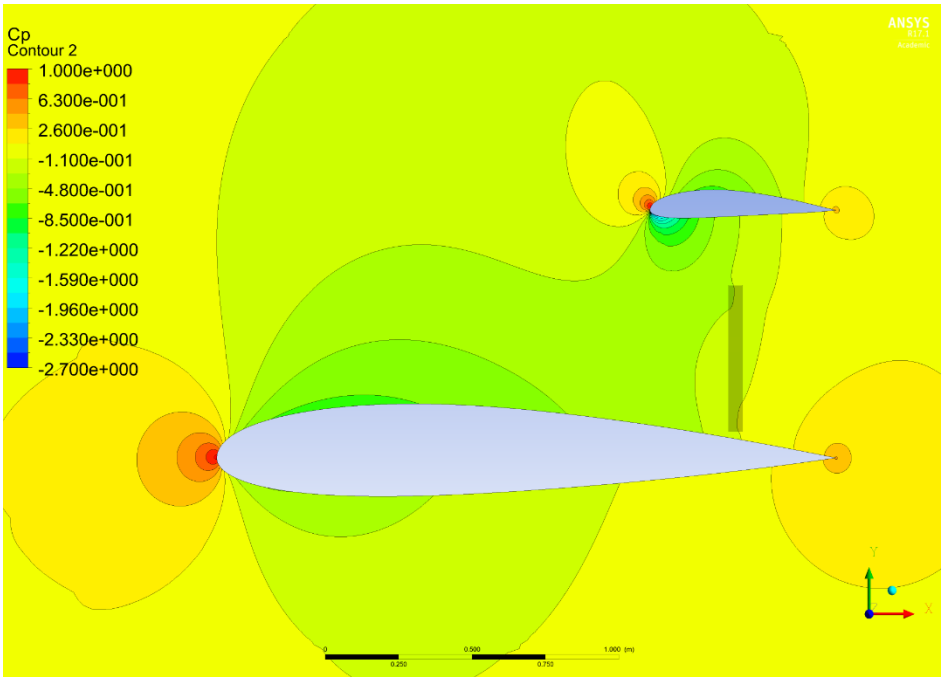

Figure A- 20: Chapter 5.3: Secondary wing's initial lift analysis, C_P contour, 50% spanwise position (middle of the disc), 40% wing spacing, 85% chordwise position of the propeller, Secondary wing's $C_{L_o} = 0.354$

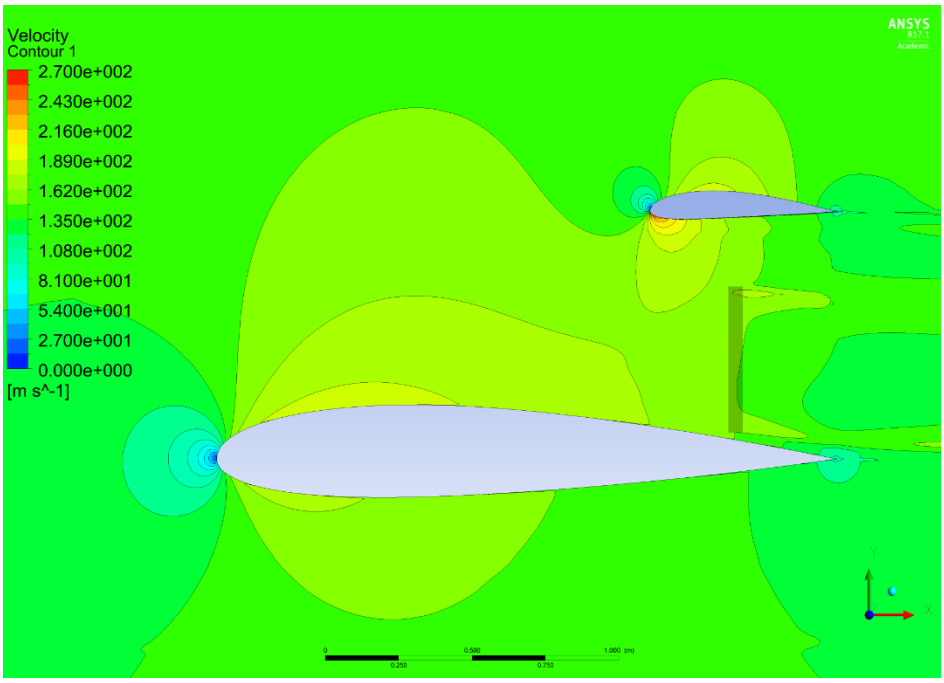

Figure A- 21: Chapter 5.3: Secondary wing's initial lift analysis, velocity contour, 50% spanwise position (middle of the disc), 40% wing spacing, 85% chordwise position of the propeller, Secondary wing's $C_{L_o} = 0.354$

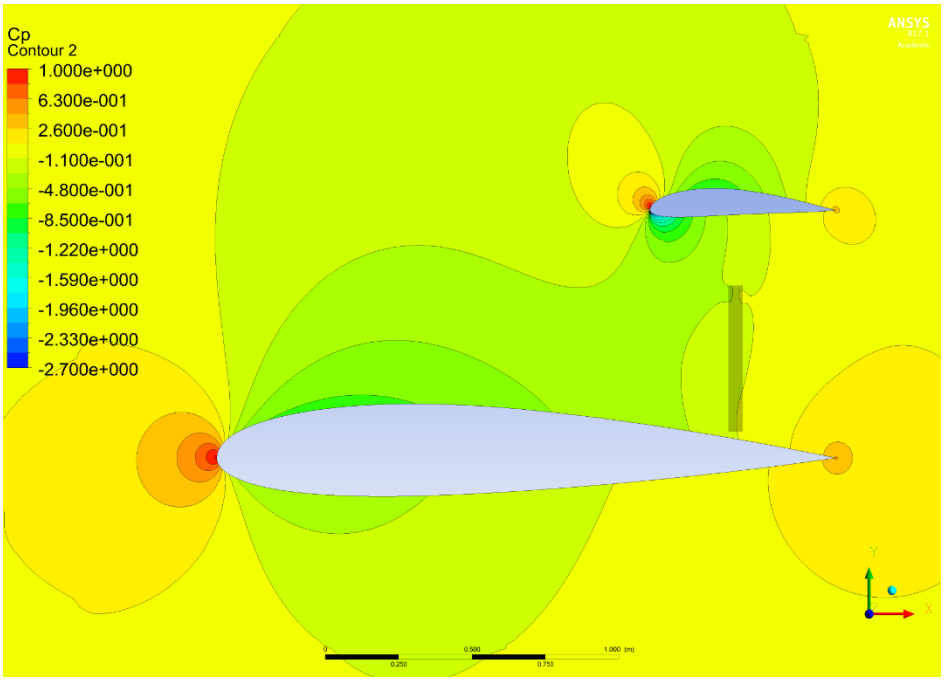

Figure A- 22: Chapter 5.3: Secondary wing's initial lift analysis, C_P contour, 50% spanwise position (middle of the disc), 40% wing spacing, 85% chordwise position of the propeller, Secondary wing's $C_{L_0} = 0.43$

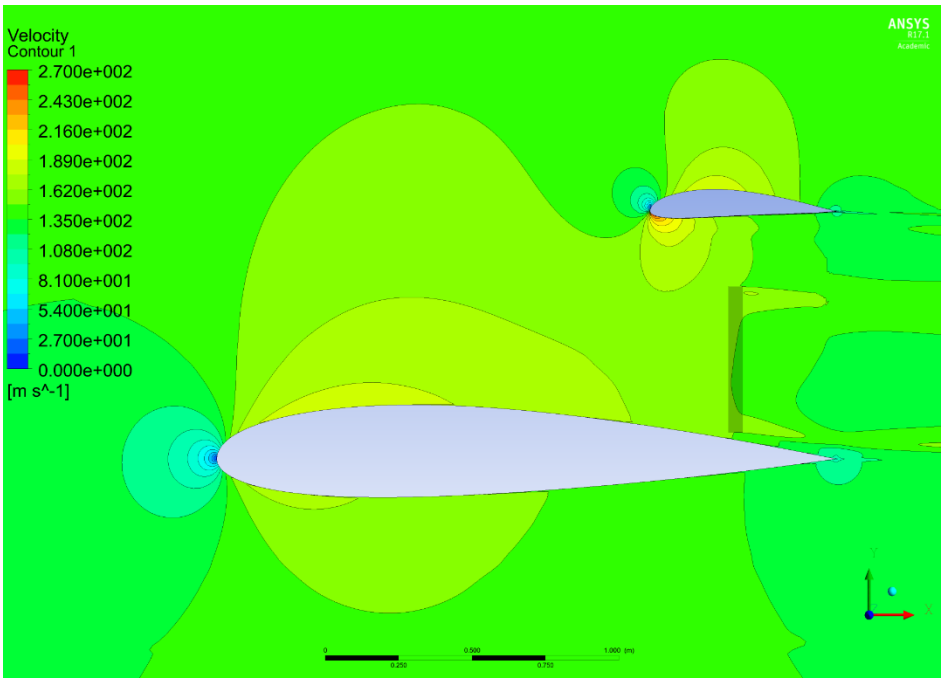

Figure A- 23: Chapter 5.3: Secondary wing's initial lift analysis, velocity contour, 50% spanwise position (middle of the disc), 40% wing spacing, 85% chordwise position of the propeller, Secondary wing's $C_{L_0} = 0.43$

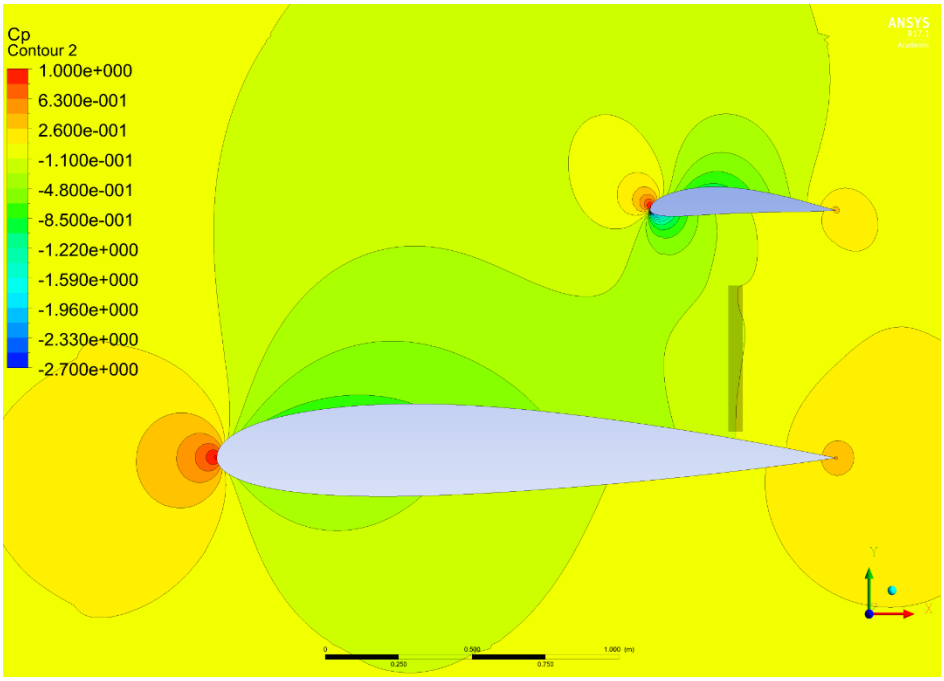

Figure A- 24: Chapter 5.3: Secondary wing's initial lift analysis, C_P contour, 50% spanwise position (middle of the disc), 40% wing spacing, 85% chordwise position of the propeller, Secondary wing's $C_{L_o} = 0.505$

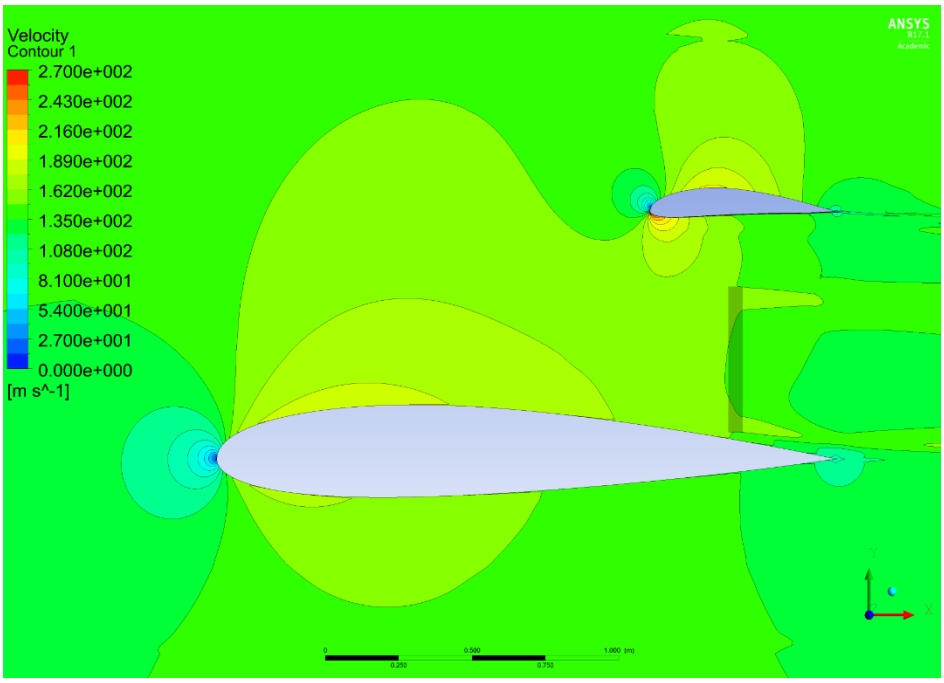

Figure A- 25: Chapter 5.3: Secondary wing's initial lift analysis, velocity contour, 50% spanwise position (middle of the disc), 40% wing spacing, 85% chordwise position of the propeller, Secondary wing's $C_{L_o} = 0.505$

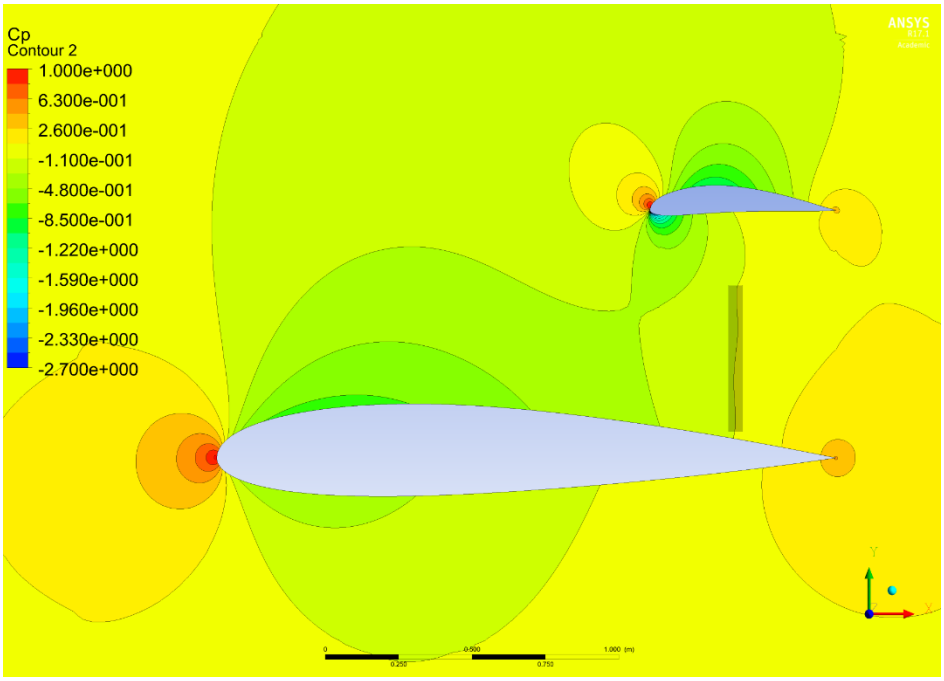

Figure A- 26: Chapter 5.3: Secondary wing's initial lift analysis, C_P contour, 50% spanwise position (middle of the disc), 40% wing spacing, 85% chordwise position of the propeller, Secondary wing's $C_{L_0} = 0.58$

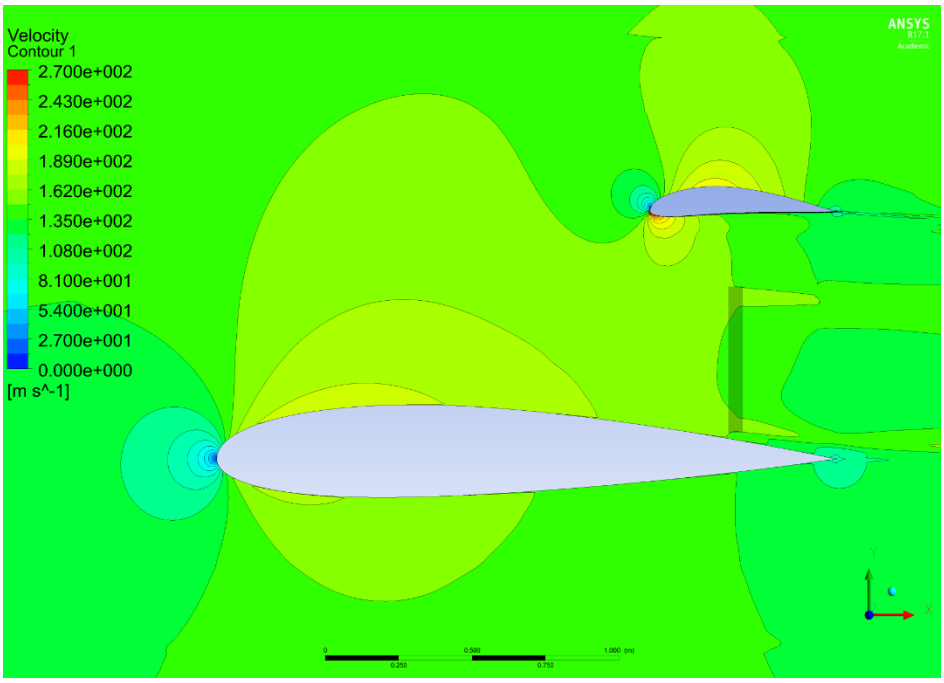

Figure A- 27: Chapter 5.3: Secondary wing's initial lift analysis, velocity contour, 50% spanwise position (middle of the disc), 40% wing spacing, 85% chordwise position of the propeller, Secondary wing's $C_{L_0} = 0.58$

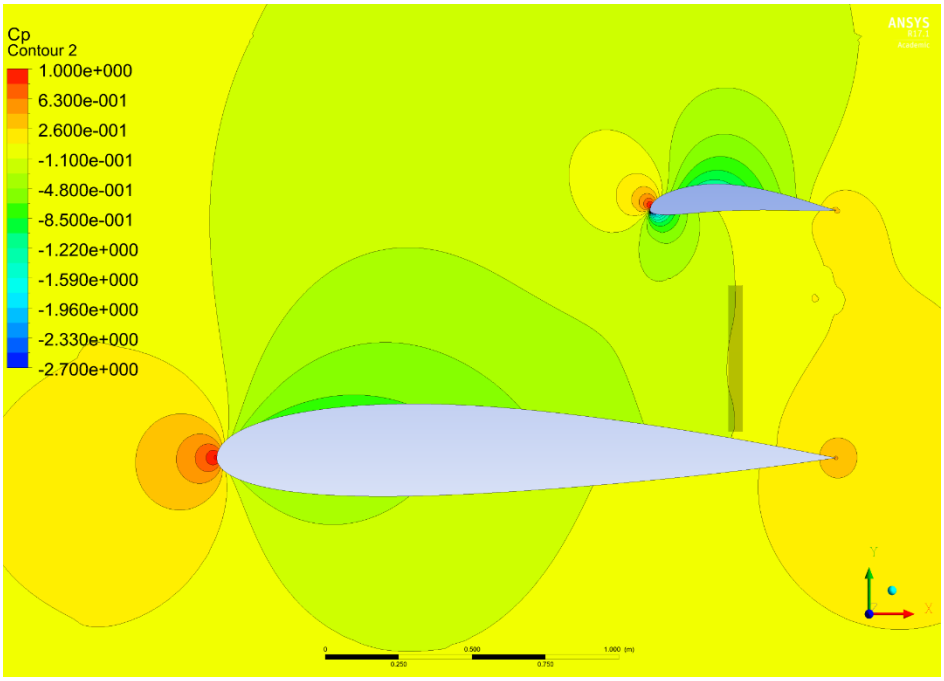

Figure A- 28: Chapter 5.3: Secondary wing's initial lift analysis, C_P contour, 50% spanwise position (middle of the disc), 40% wing spacing, 85% chordwise position of the propeller, Secondary wing's $C_{L_o} = 0.655$

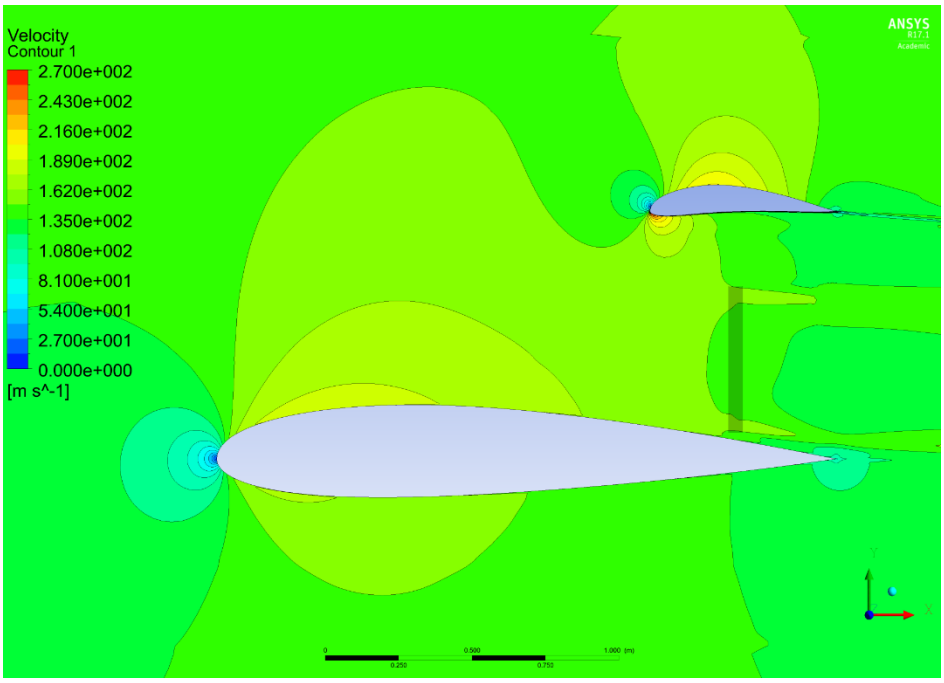

Figure A- 29: Chapter 5.3: Secondary wing's initial lift analysis, velocity contour, 50% spanwise position (middle of the disc), 40% wing spacing, 85% chordwise position of the propeller, Secondary wing's $C_{L_o} = 0.655$

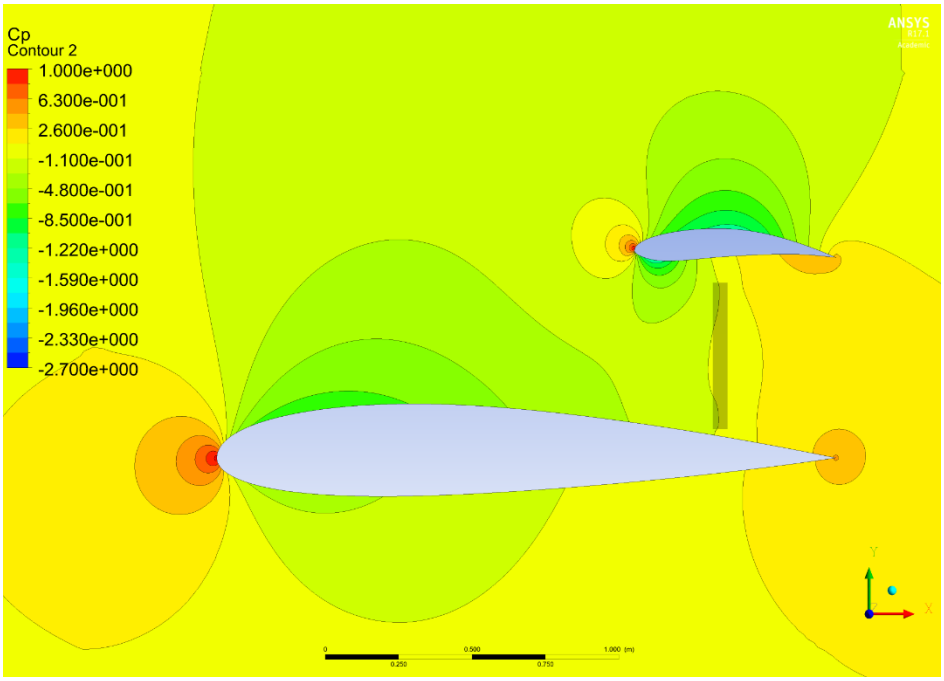

Figure A- 30: Chapter 5.4: Secondary wing's angle of attack analysis, $C_p$contour, 50% spanwise position (middle of the disc), 33.5% wing spacing, 82.5% chordwise position of the propeller, secondary wing's angle attack 2 degrees

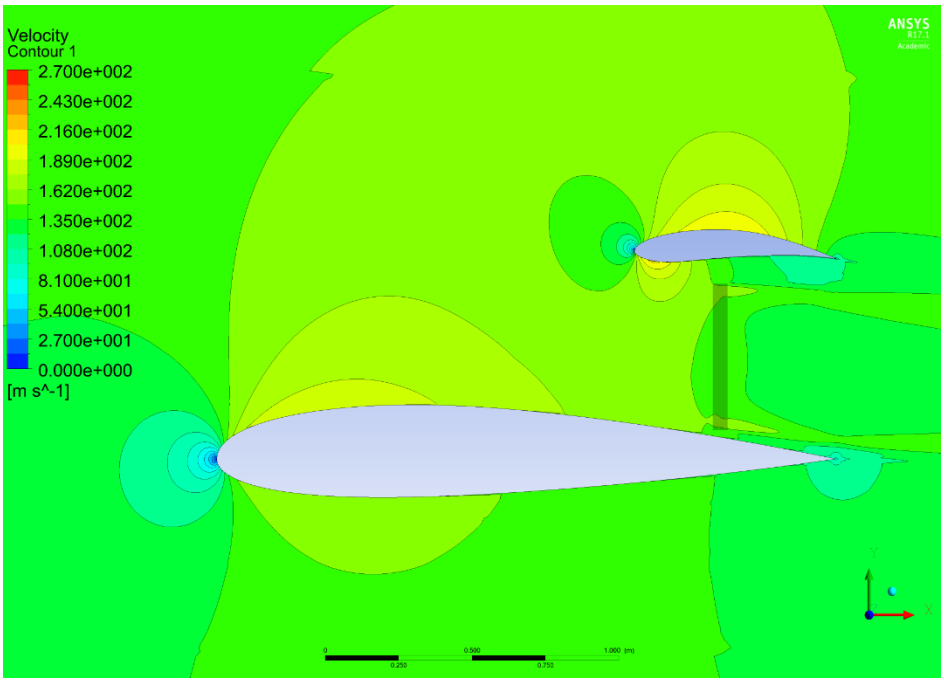

Figure A- 31: Chapter 5.4: Secondary wing's angle of attack analysis, velocity contour, 50% spanwise position (middle of the disc), 33.5% wing spacing, 82.5% chordwise position of the propeller, secondary wing's angle attack 2 degrees

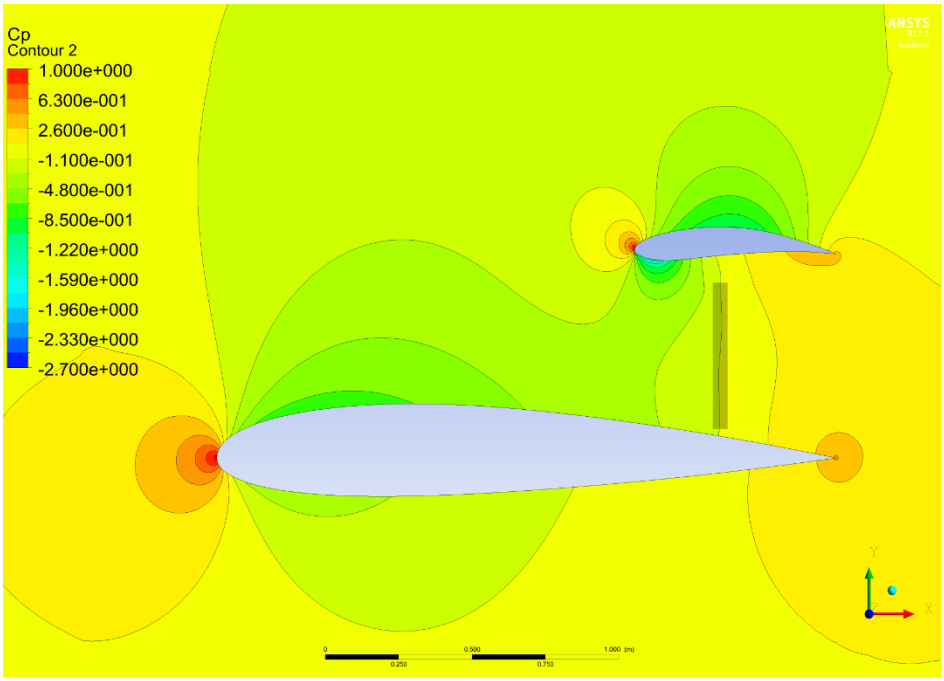

Figure A- 32: Chapter 5.4: Secondary wing's angle of attack analysis, $C_p$contour, 50% spanwise position (middle of the disc), 33.5% wing spacing, 82.5% chordwise position of the propeller, secondary wing's angle attack 1 degrees

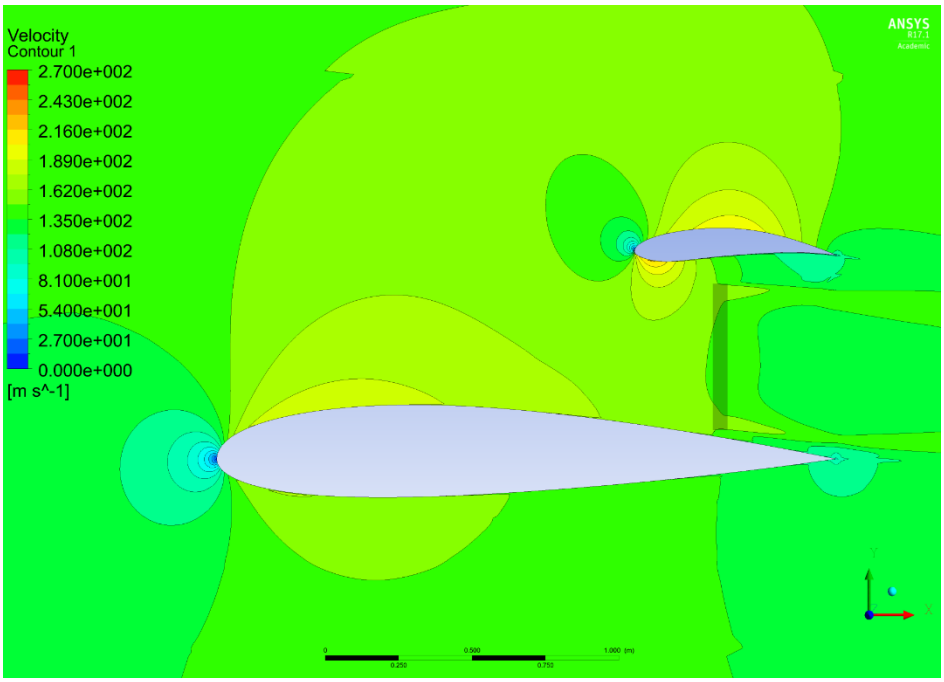

Figure A- 33: Chapter 5.4: Secondary wing's angle of attack analysis, velocity contour, 50% spanwise position (middle of the disc), 33.5% wing spacing, 82.5% chordwise position of the propeller, secondary wing's angle attack 1 degrees

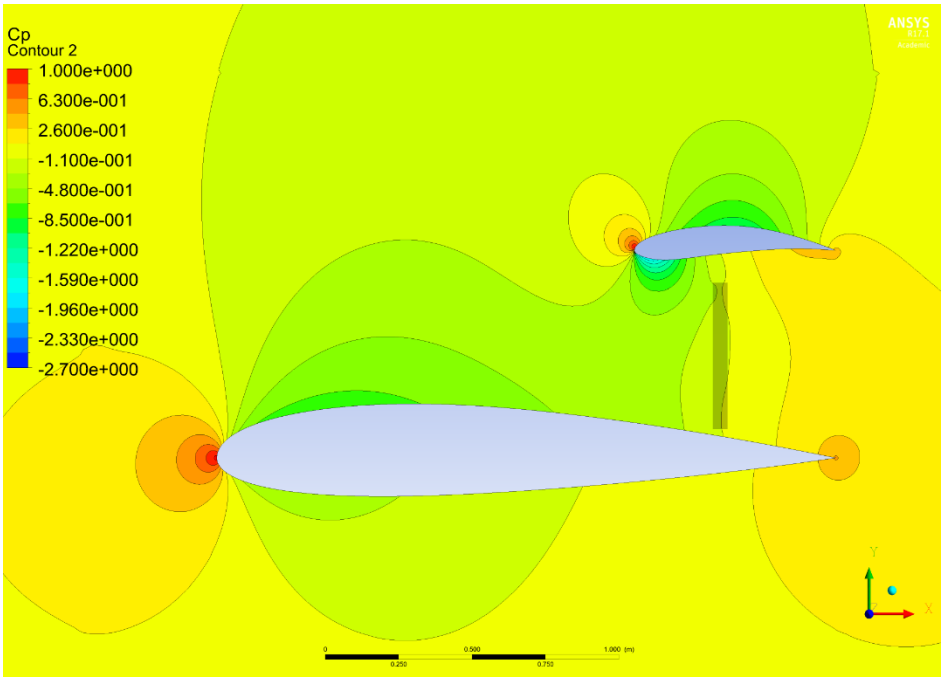

Figure A- 34: Chapter 5.4: Secondary wing's angle of attack analysis, $C_p$contour, 50% spanwise position (middle of the disc), 33.5% wing spacing, 82.5% chordwise position of the propeller, secondary wing's angle attack 0 degrees

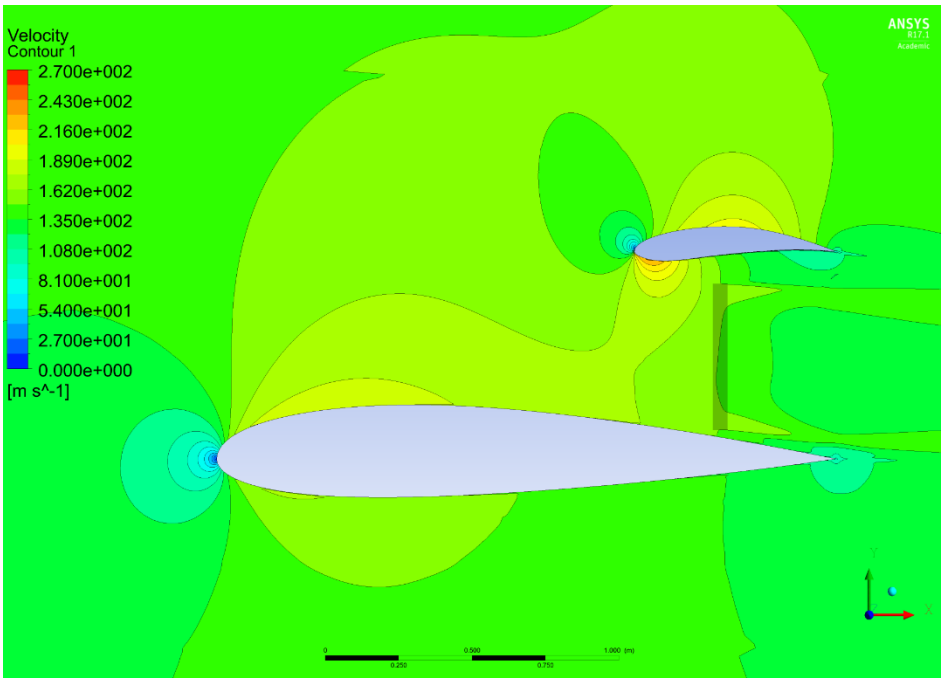

Figure A- 35: Chapter 5.4: Secondary wing's angle of attack analysis, velocity contour, 50% spanwise position (middle of the disc), 33.5% wing spacing, 82.5% chordwise position of the propeller, secondary wing's angle attack 0 degrees

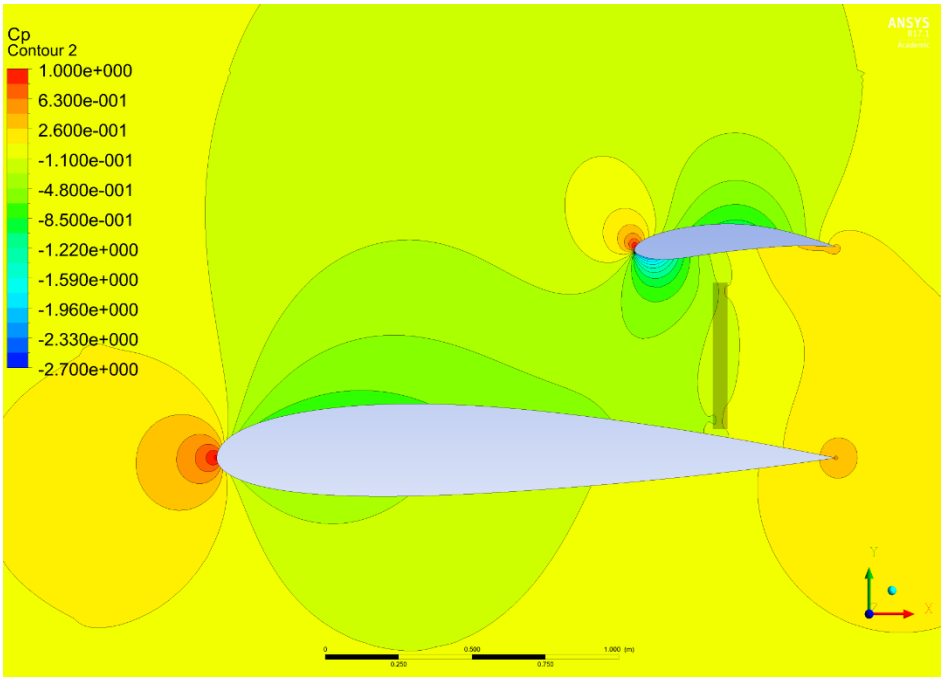

Figure A- 36: Chapter 5.4: Secondary wing's angle of attack analysis, $C_p$contour, 50% spanwise position (middle of the disc), 33.5% wing spacing, 82.5% chordwise position of the propeller, secondary wing's angle attack -1 degrees

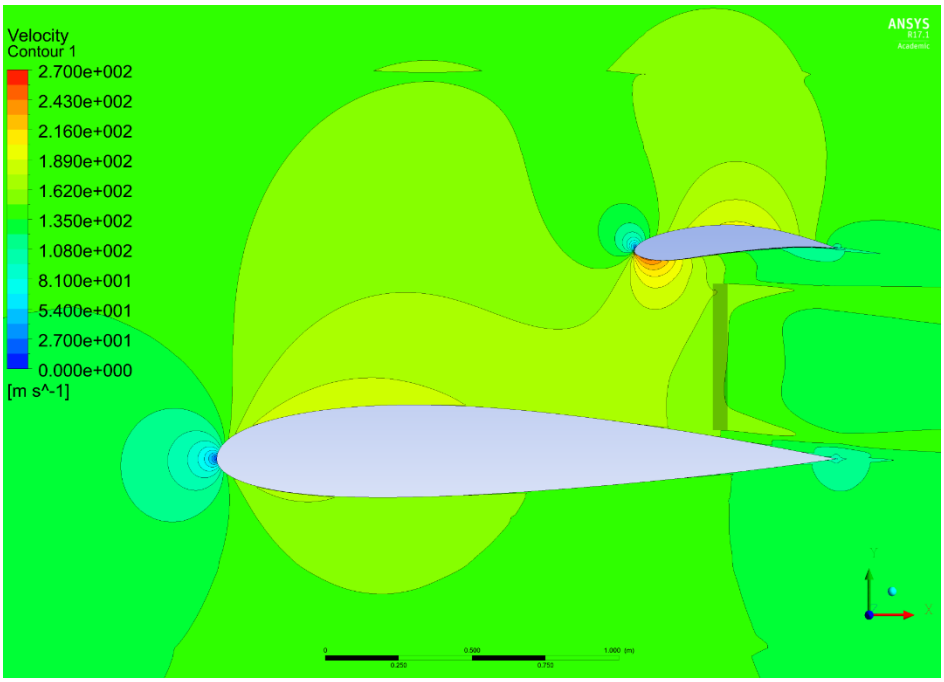

Figure A- 37: Chapter 5.4: Secondary wing's angle of attack analysis, velocity contour, 50% spanwise position (middle of the disc), 33.5% wing spacing, 82.5% chordwise position of the propeller, secondary wing's angle attack -1 degrees

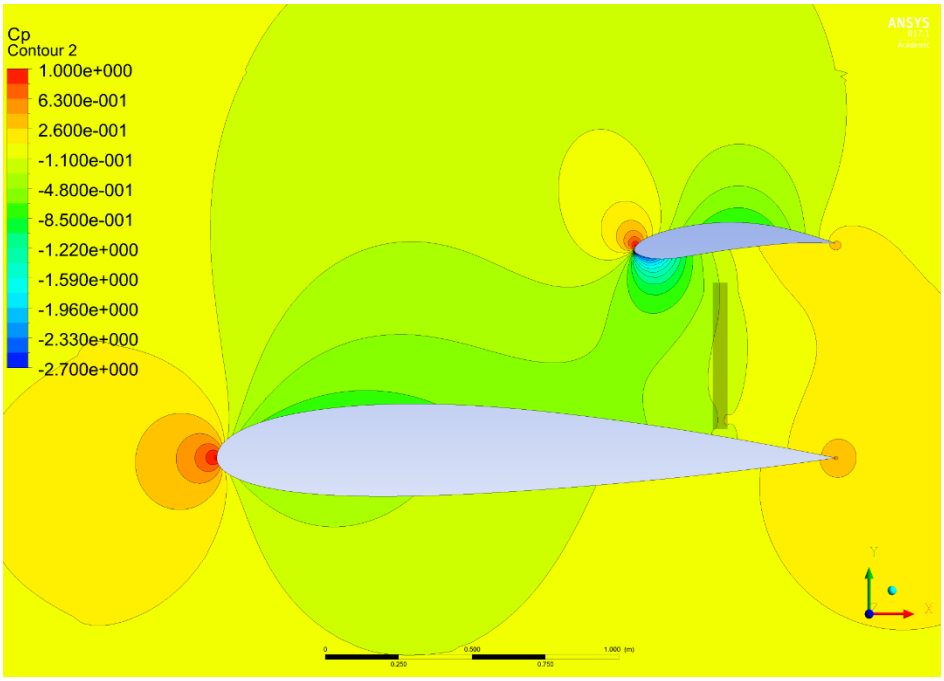

Figure A- 38: Chapter 5.4: Secondary wing's angle of attack analysis, $C_p$contour, 50% spanwise position (middle of the disc), 33.5% wing spacing, 82.5% chordwise position of the propeller, secondary wing's angle attack -2 degrees

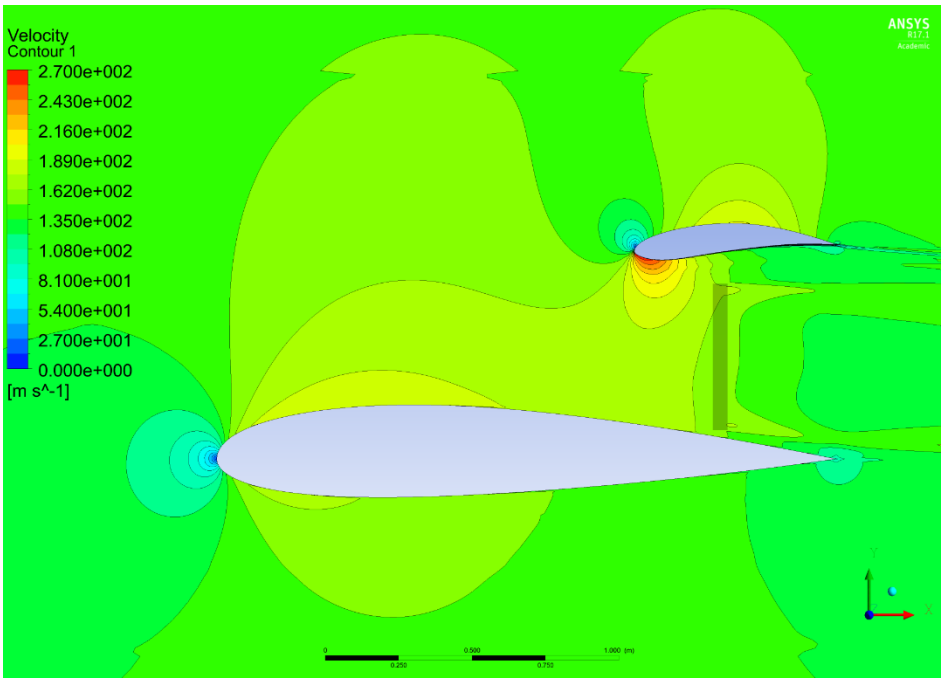

Figure A- 39: Chapter 5.4: Secondary wing's angle of attack analysis, velocity contour, 50% spanwise position (middle of the disc), 33.5% wing spacing, 82.5% chordwise position of the propeller, secondary wing's angle attack -2 degrees

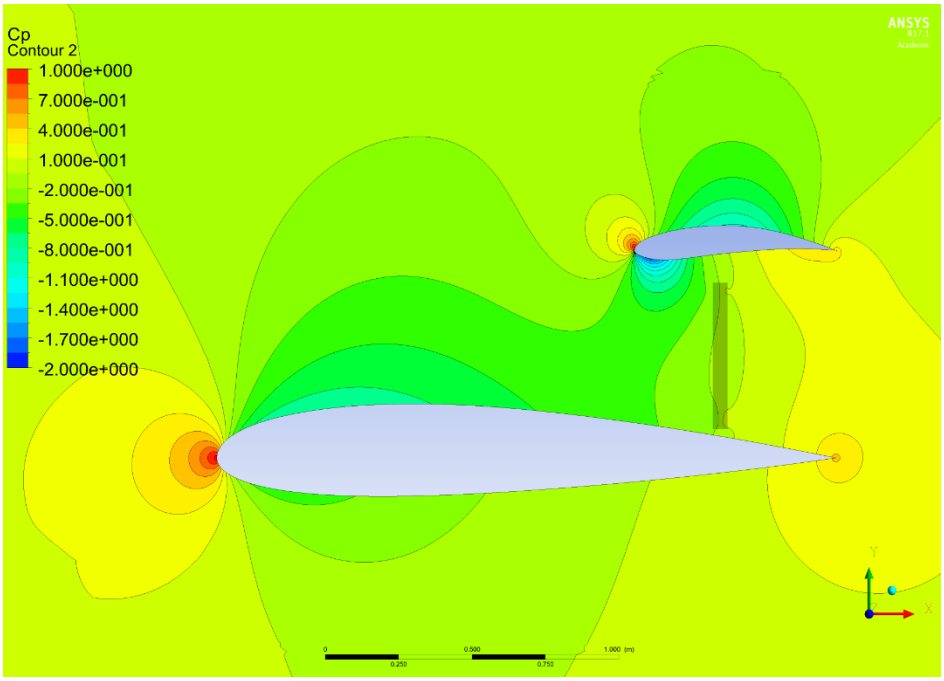

Figure A- 40: Chapter 5.5: Disc position analysis, $C_P$contour, 50% spanwise position (middle of the disc), 33.5% wing spacing, 82.5% chordwise position of the propeller, 4% [y/D_p] disc tip to main wing's surface spacing

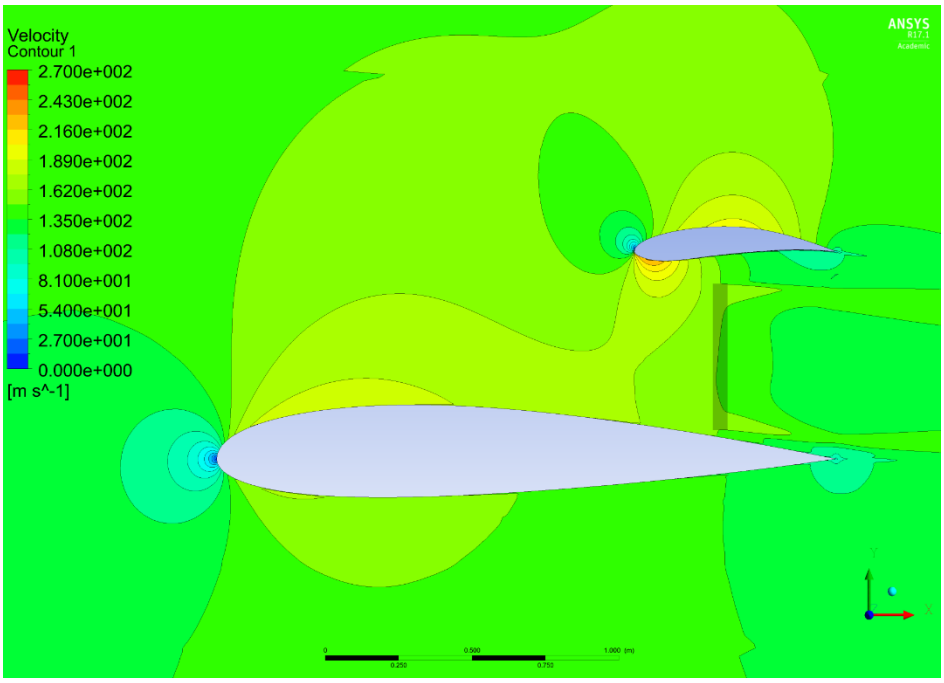

Figure A- 41: Chapter 5.5: Disc position analysis, velocity contour, 50% spanwise position (middle of the disc), 33.5% wing spacing, 82.5% chordwise position of the propeller, 4% [y/D_p] disc tip to main wing's surface spacing

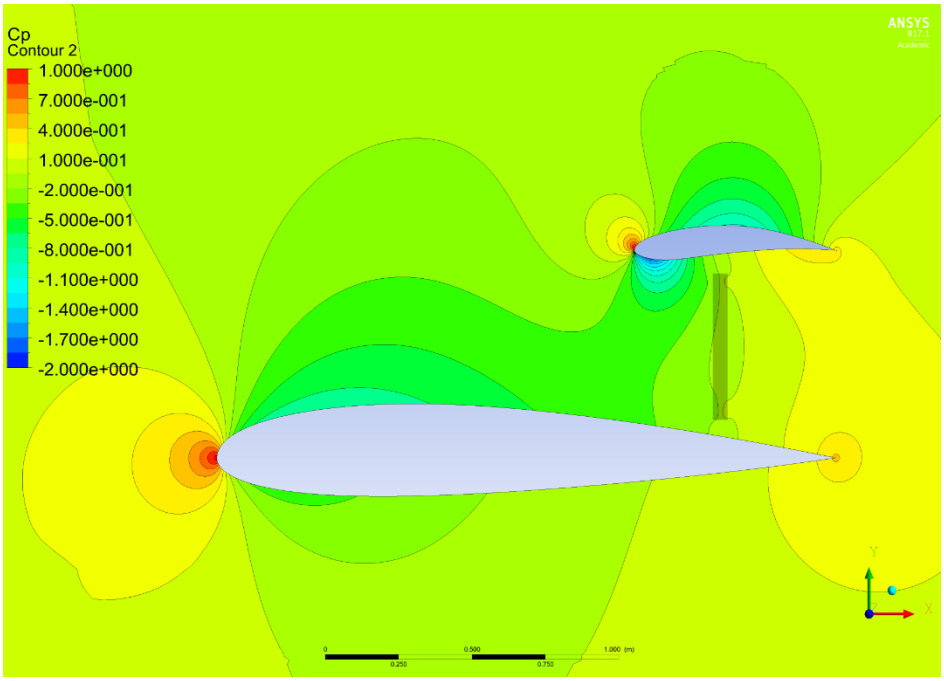

Figure A- 42: Chapter 5.5: Disc position analysis, $C_P$contour, 50% spanwise position (middle of the disc), 33.5% wing spacing, 82.5% chordwise position of the propeller, 10% [y/D_p] disc tip to main wing's surface spacing

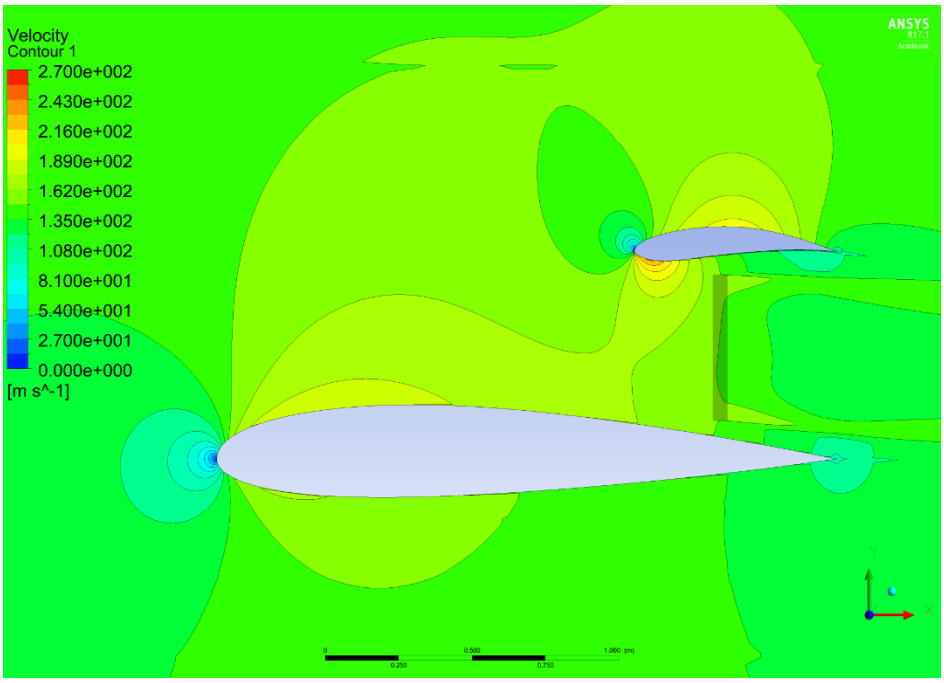

Figure A- 43: Chapter 5.5: Disc position analysis, velocity contour, 50% spanwise position (middle of the disc), 33.5% wing spacing, 82.5% chordwise position of the propeller, 10% [y/Dp] disc tip to main wing's surface spacing

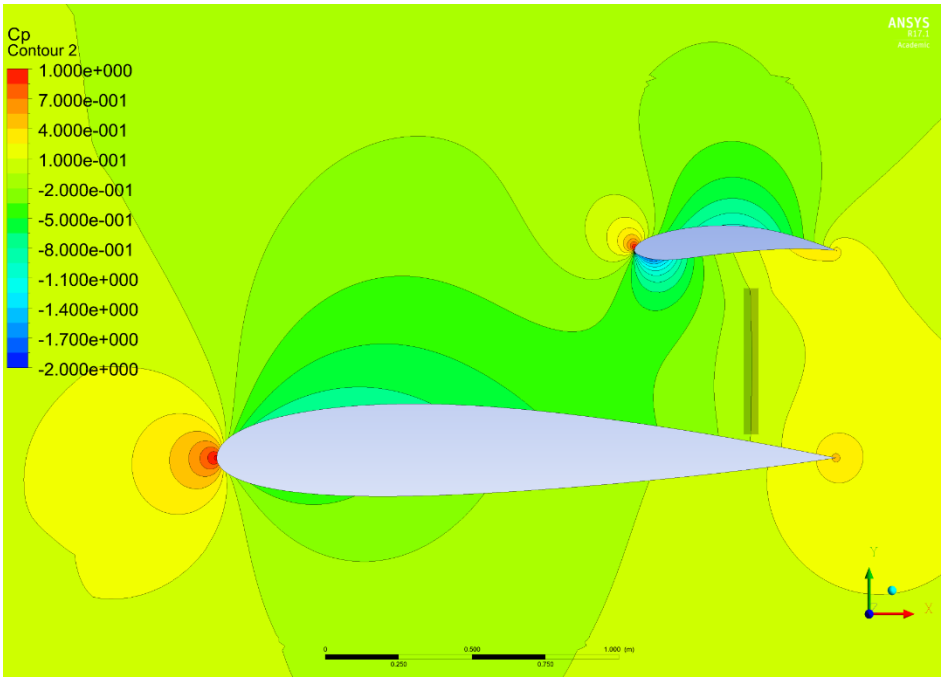

Figure A- 44: Chapter 5.5: Disc position analysis, $C_P$contour, 50% spanwise position (middle of the disc), 33.5% wing spacing, 87.5% chordwise position of the propeller, 4% [y/D_p] disc tip to main wing's surface

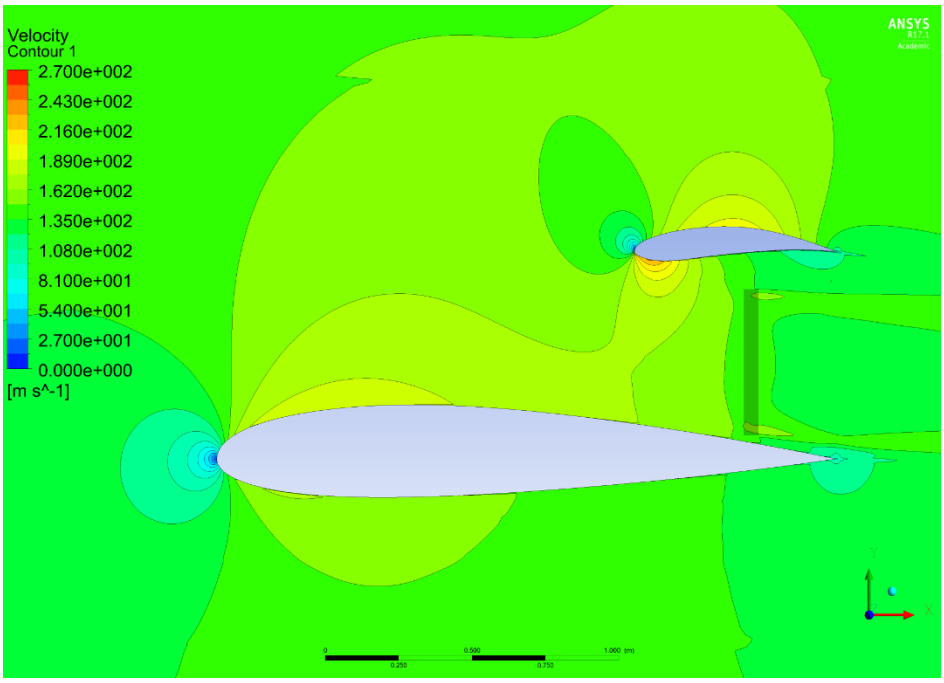

Figure A- 45: Chapter 5.5: Disc position analysis, velocity contour, 50% spanwise position (middle of the disc), 33.5% wing spacing, 87.5% chordwise position of the propeller, 4% [y/D_p] disc tip to main wing's surface

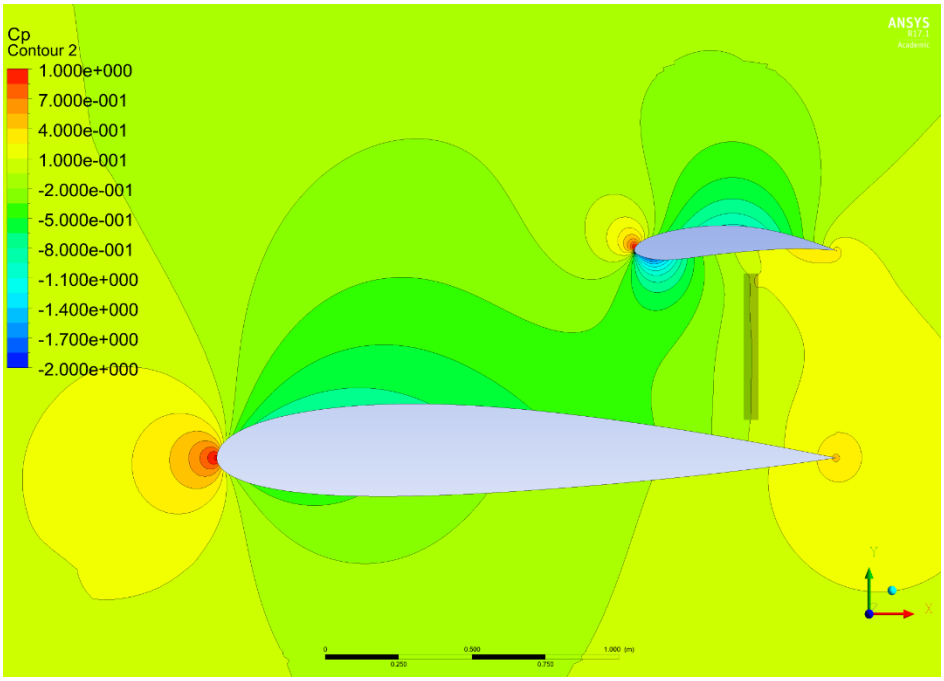

Figure A- 46: Chapter 5.5: Disc position analysis, $C_P$contour, 50% spanwise position (middle of the disc), 33.5% wing spacing, 87.5% chordwise position of the propeller, 14% [y/D_p] disc tip to main wing's surface

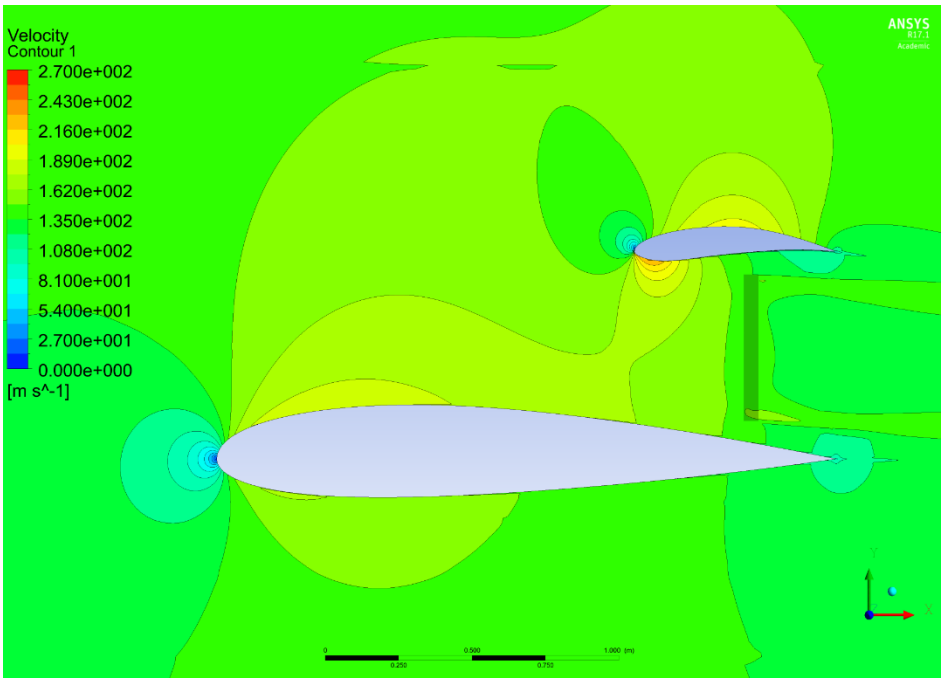

Figure A- 47: Chapter 5.5: Disc position analysis, velocity contour, 50% spanwise position (middle of the disc), 33.5% wing spacing, 87.5% chordwise position of the propeller, 14% [y/D_p] disc tip to main wing's surface

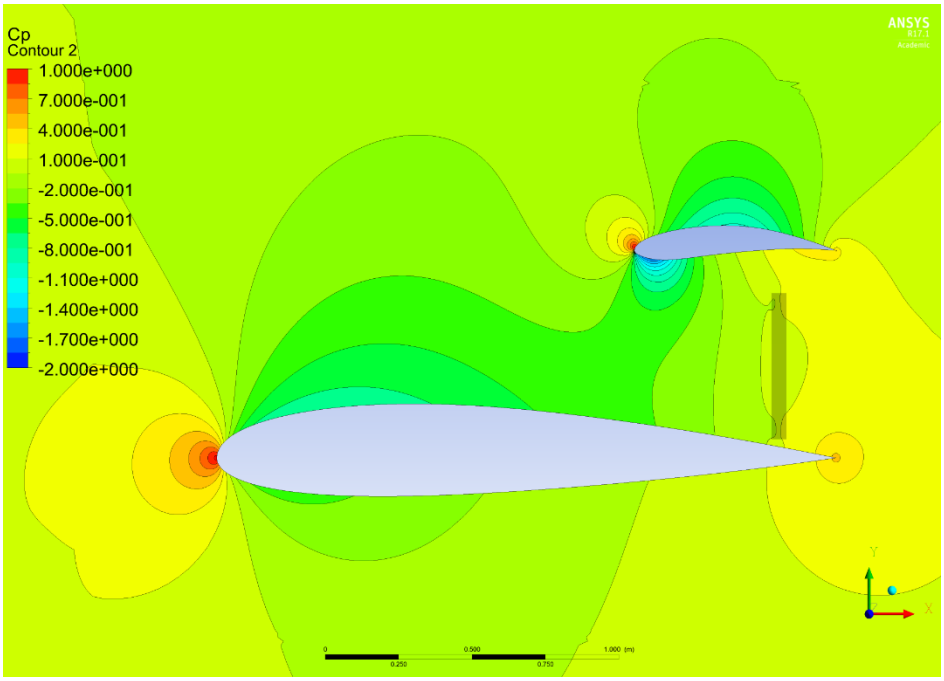

Figure A- 48: Chapter 5.5: Disc position analysis, $C_p$contour, 50% spanwise position (middle of the disc), 33.5% wing spacing, 92% chordwise position of the propeller, 4% [y/D_p] disc tip to main wing's surface

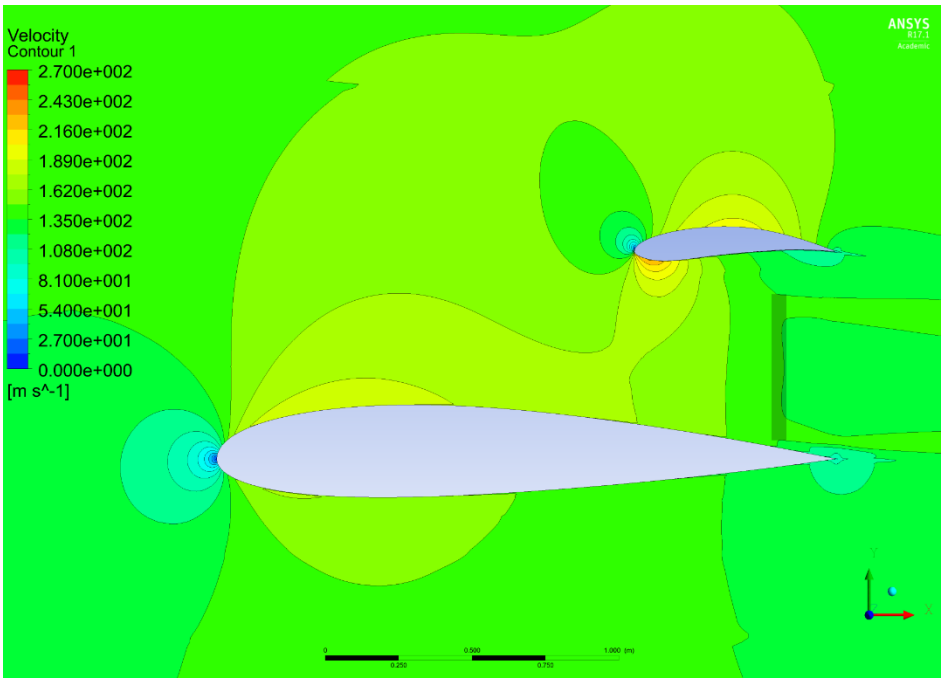

Figure A- 49: Chapter 5.5: Disc position analysis, velocity contour, 50% spanwise position (middle of the disc), 33.5% wing spacing, 92% chordwise position of the propeller, 4% [y/D_p] disc tip to main wing's surface

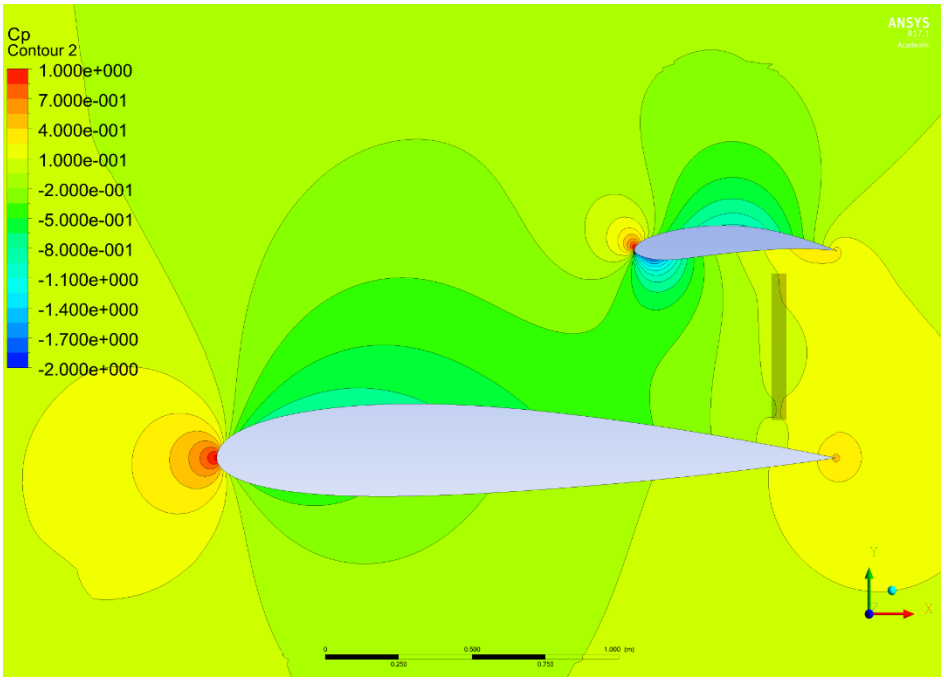

Figure A- 50: Chapter 5.5: Disc position analysis, $C_p$contour, 50% spanwise position (middle of the disc), 33.5% wing spacing, 92% chordwise position of the propeller, 17% [y/D_p] disc tip to main wing's surface

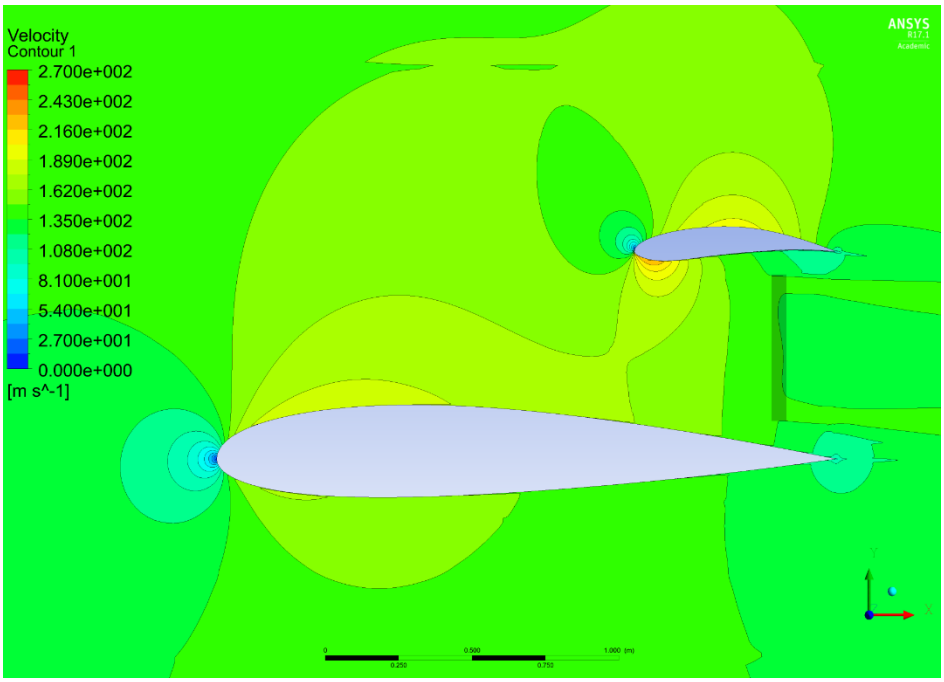

Figure A- 51: Chapter 5.5: Disc position analysis, velocity contour, 50% spanwise position (middle of the disc), 33.5% wing spacing, 92% chordwise position of the propeller, 17% [y/D_p] disc tip to main wing's surface

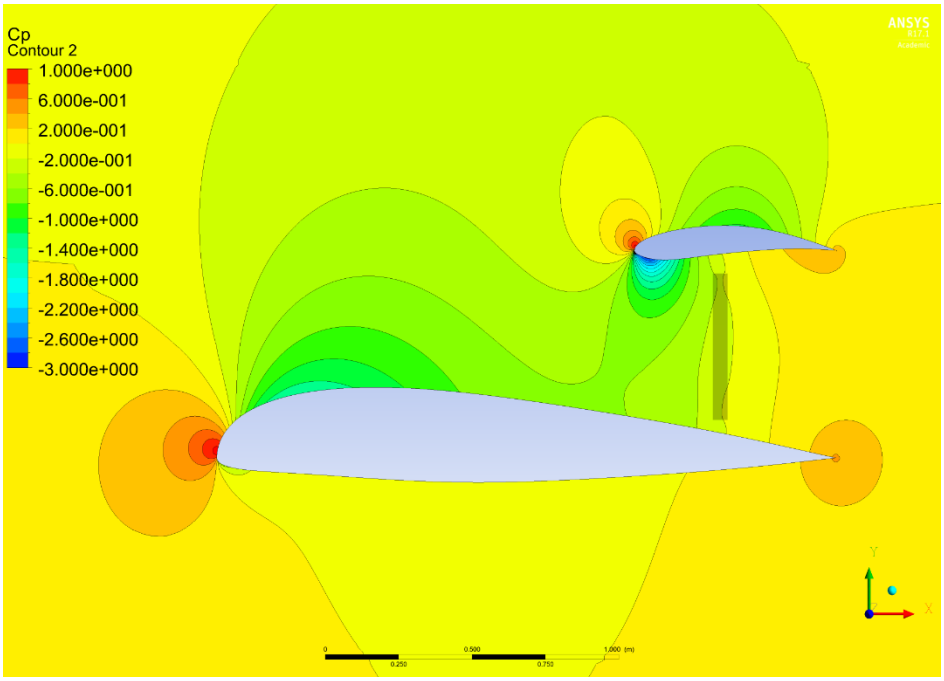

Figure A- 52: Chapter 5.6: Main wing's initial lift analysis, $C_P$contour, 50% spanwise position (middle of the disc), 33.5% wing spacing, 82.5% chordwise position of the propeller, Main wing's camber position at 20% [x/C_{main}]

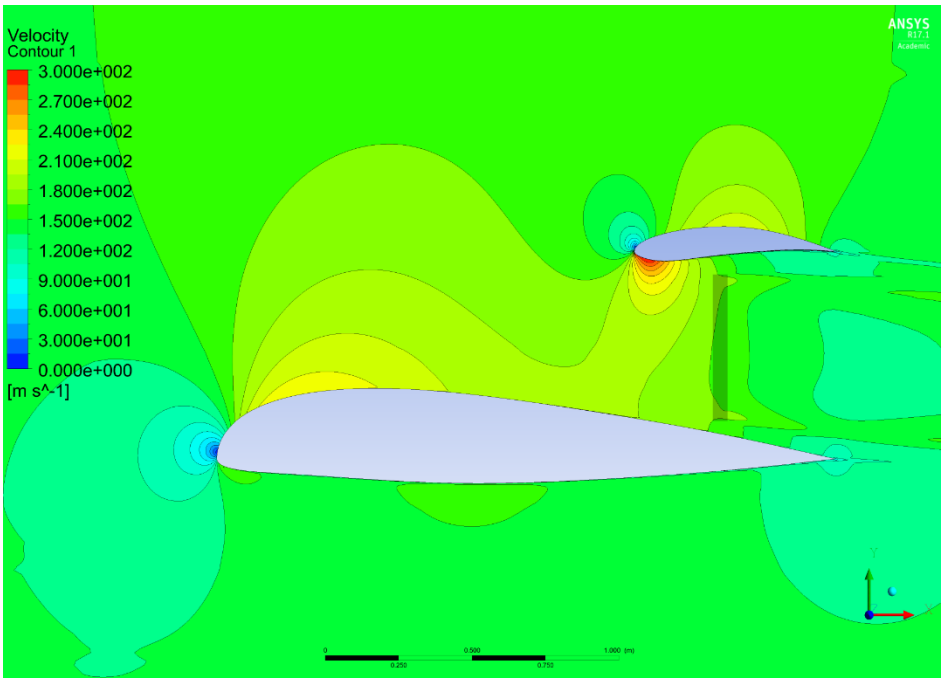

Figure A- 53: Chapter 5.6: Main wing's initial lift analysis, velocity contour, 50% spanwise position (middle of the disc), 33.5% wing spacing, 82.5% chordwise position of the propeller, Main wing's camber position at 20% [x/C_{main}]

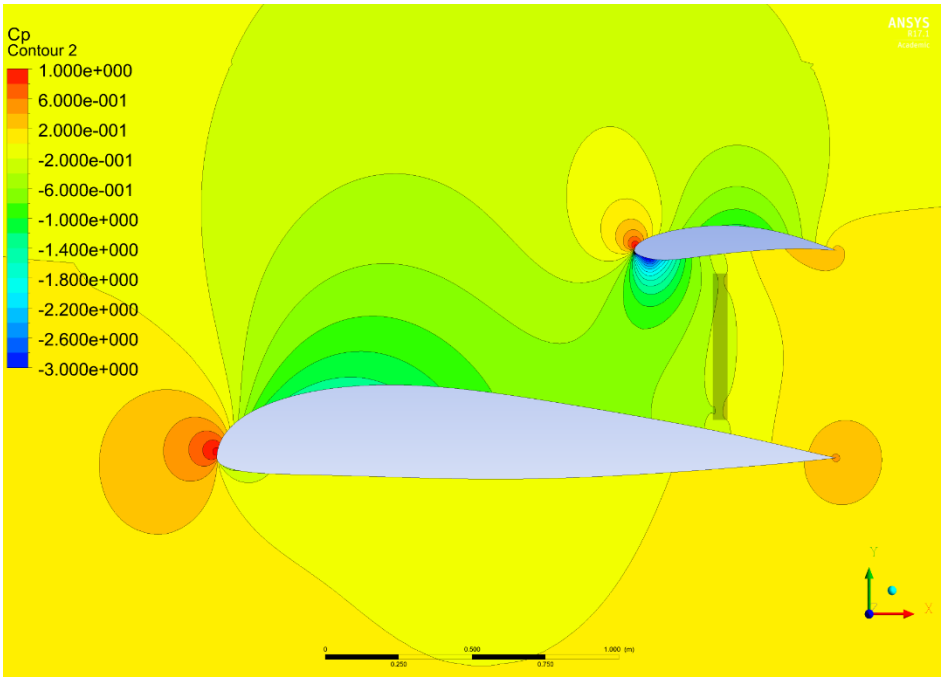

Figure A- 54: Chapter 5.6: Main wing's initial lift analysis, $C_P$contour, 50% spanwise position (middle of the disc), 33.5% wing spacing, 82.5% chordwise position of the propeller, Main wing's camber position at 25% [x/C_{main}]

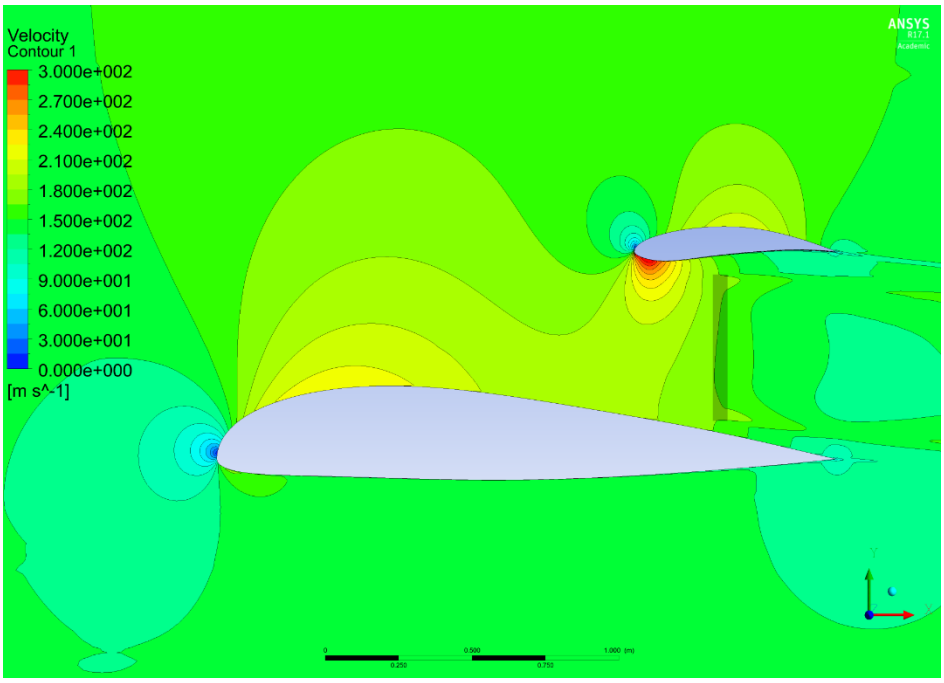

Figure A- 55: Chapter 5.6: Main wing's initial lift analysis, velocity contour, 50% spanwise position (middle of the disc), 33.5% wing spacing, 82.5% chordwise position of the propeller, Main wing's camber position at 25% [x/C_{main}]

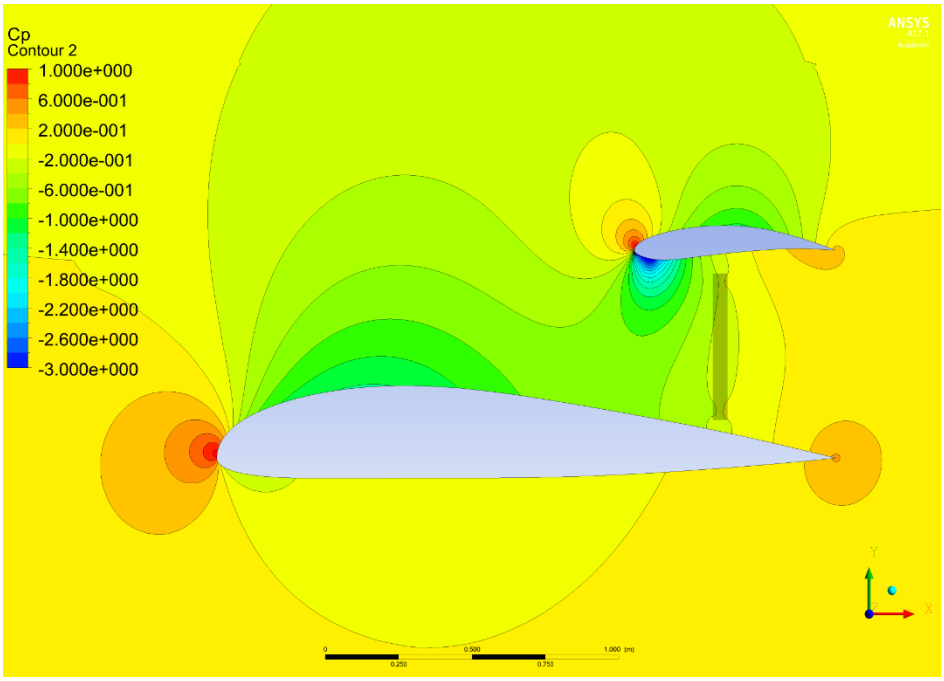

Figure A- 56: Chapter 5.6: Main wing's initial lift analysis, C_P contour, 50% spanwise position (middle of the disc), 33.5% wing spacing, 82.5% chordwise position of the propeller, Main wing's camber position at 30% [x/Cmain]

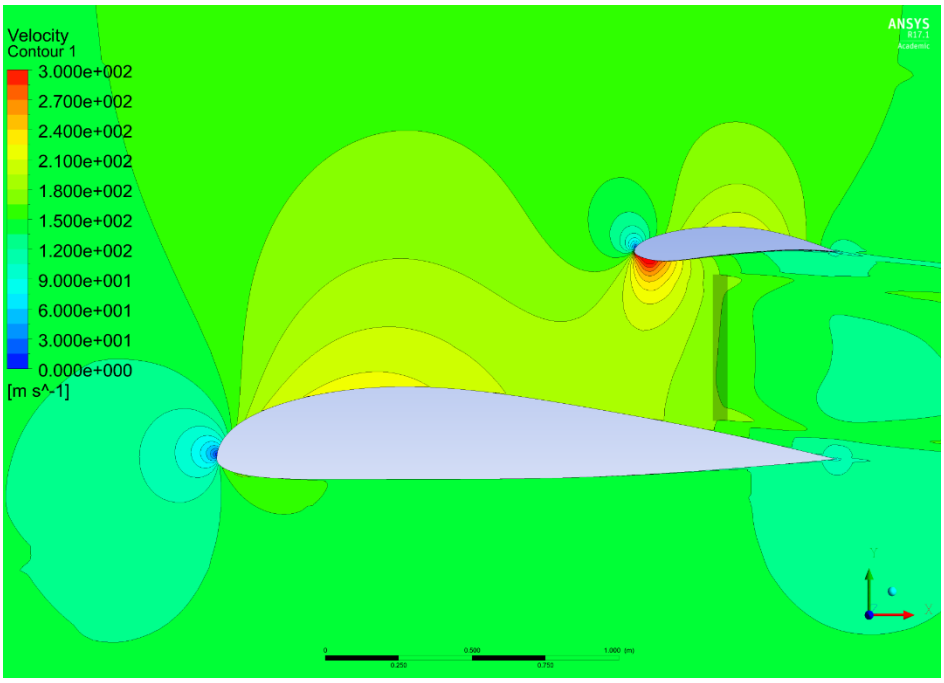

Figure A- 57: Chapter 5.6: Main wing's initial lift analysis, velocity contour, 50% spanwise position (middle of the disc), 33.5% wing spacing, 82.5% chordwise position of the propeller, Main wing's camber position at 30% [x/Cmain]

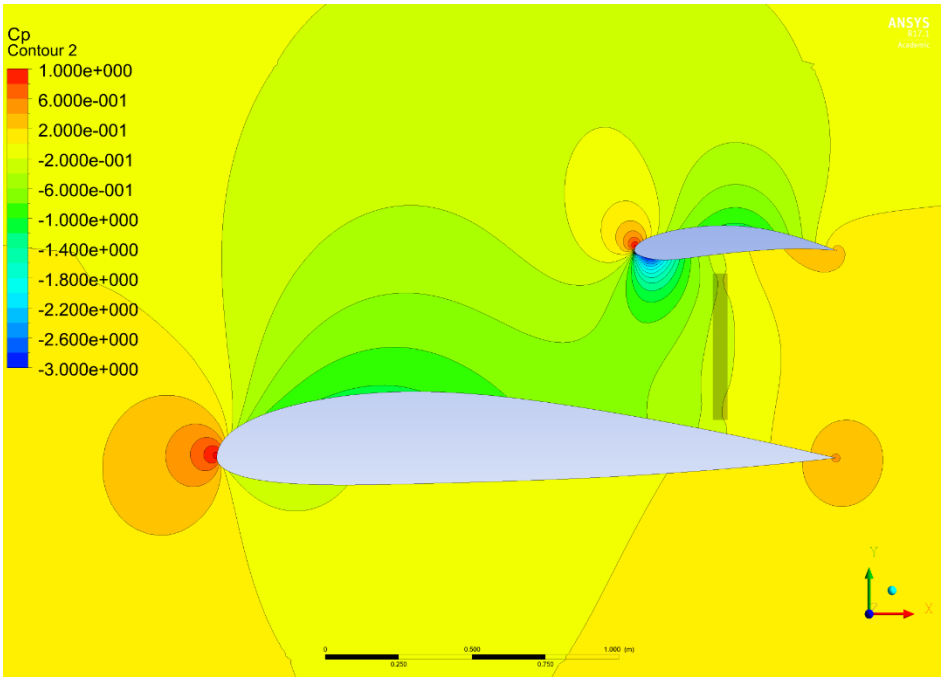

Figure A- 58: Chapter 5.6: Main wing's initial lift analysis, C_P contour, 50% spanwise position (middle of the disc), 33.5% wing spacing, 82.5% chordwise position of the propeller, Main wing's camber position at 35% [x/Cmain]

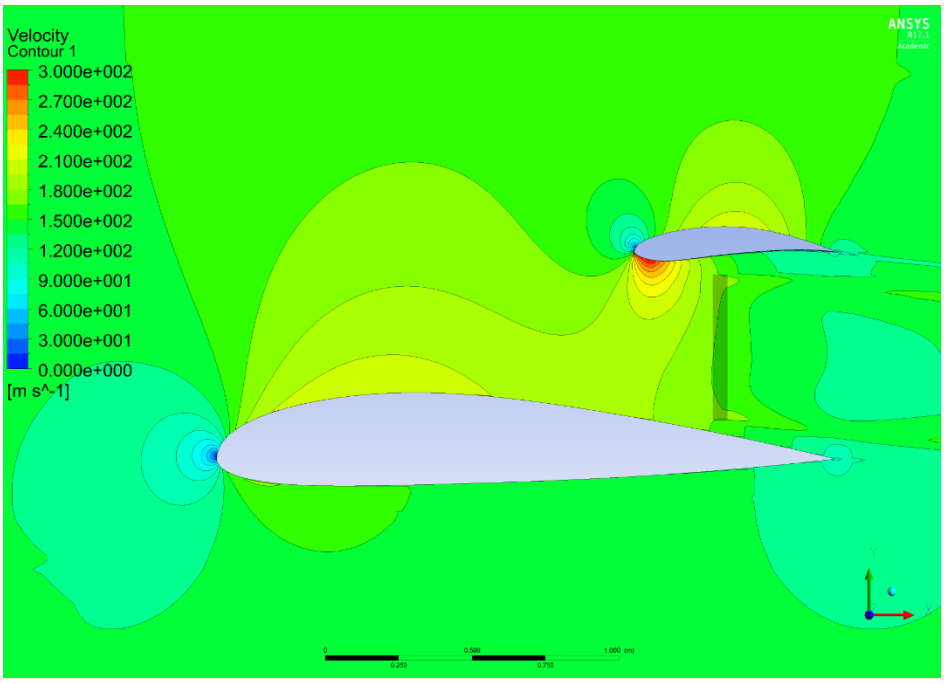

Figure A- 59: Chapter 5.6: Main wing's initial lift analysis, velocity contour, 50% spanwise position (middle of the disc), 33.5% wing spacing, 82.5% chordwise position of the propeller, Main wing's camber position at 35% [x/Cmain]

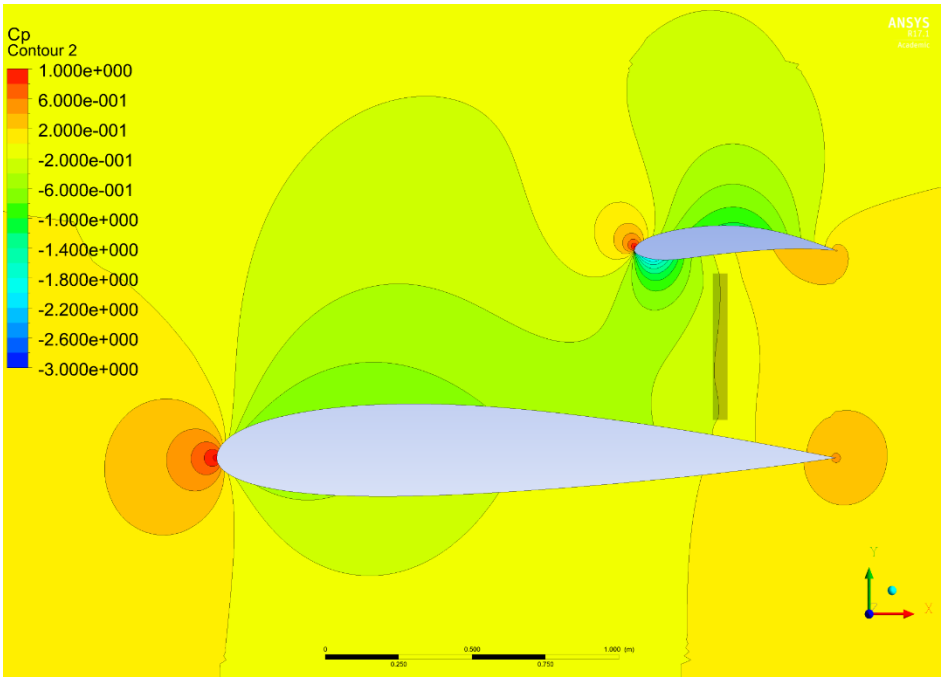

Figure A- 60: Chapter 5.6: Main wing's initial lift analysis, C_P contour, 50% spanwise position (middle of the disc), 33.5% wing spacing, 82.5% chordwise position of the propeller, Main wing's camber position at 40% [x/Cmain]

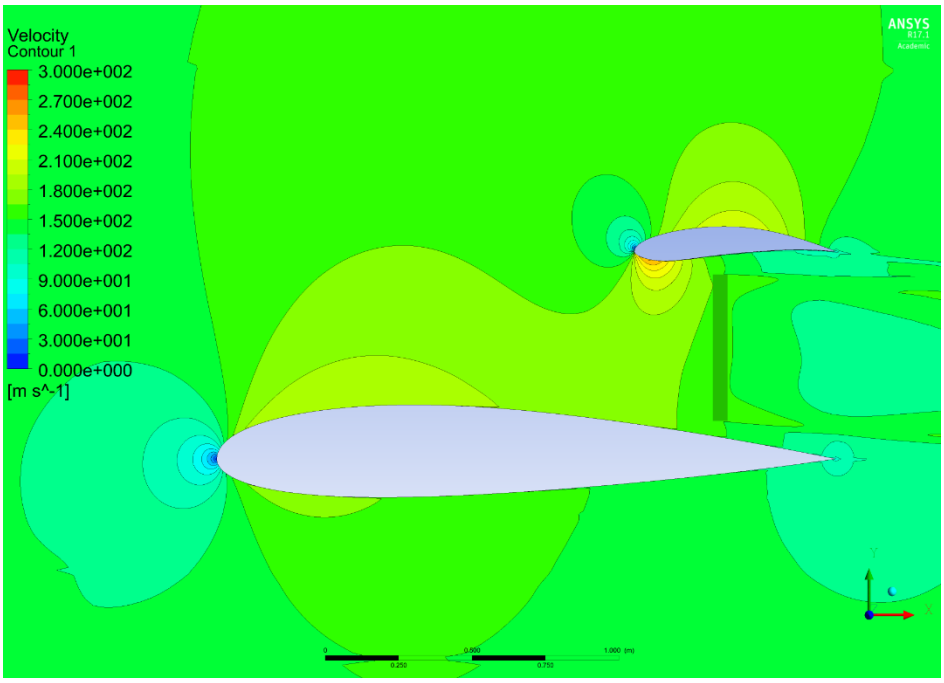

Figure A- 61: Chapter 5.6: Main wing's initial lift analysis, velocity contour, 50% spanwise position (middle of the disc), 33.5% wing spacing, 82.5% chordwise position of the propeller, Main wing's camber position at 40% [x/Cmain]

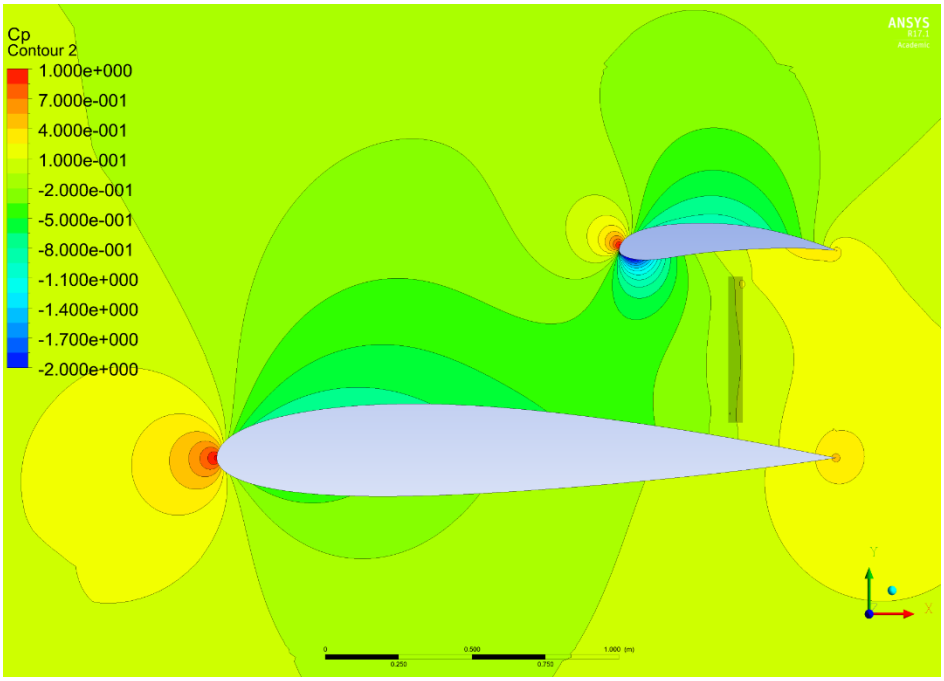

Figure A- 62: Chapter 6.2: Secondary wing's shape optimization, C_P contour, 50% spanwise position (middle of the disc), 33.5% wing spacing, 82.5% chordwise position of the propeller, initial point of the optimization

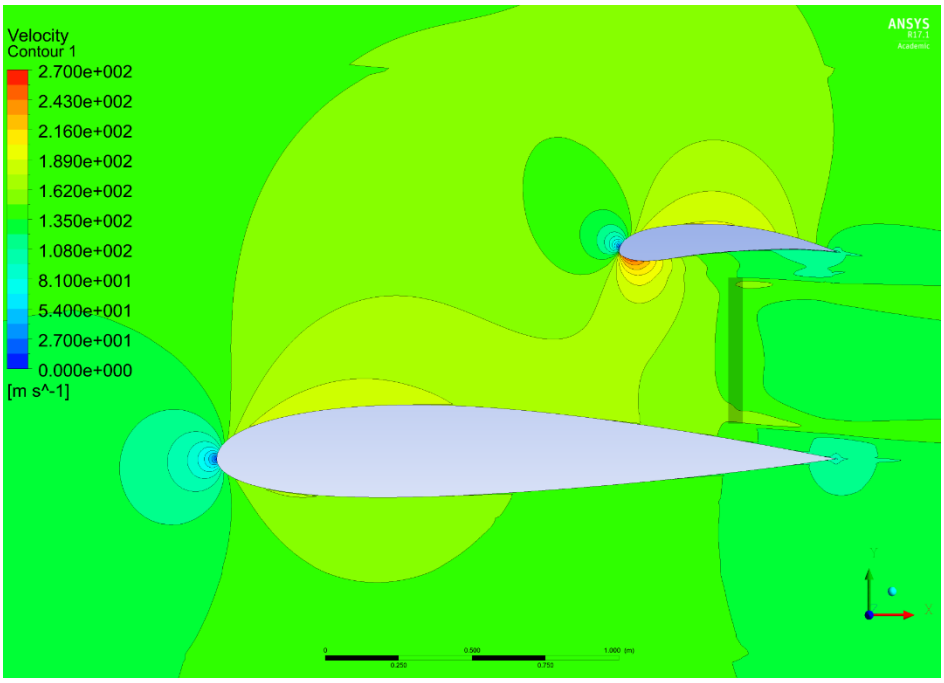

Figure A- 63: Chapter 6.2: Secondary wing's shape optimization, velocity contour, 50% spanwise position (middle of the disc), 33.5% wing spacing, 82.5% chordwise position of the propeller, initial point of the optimization

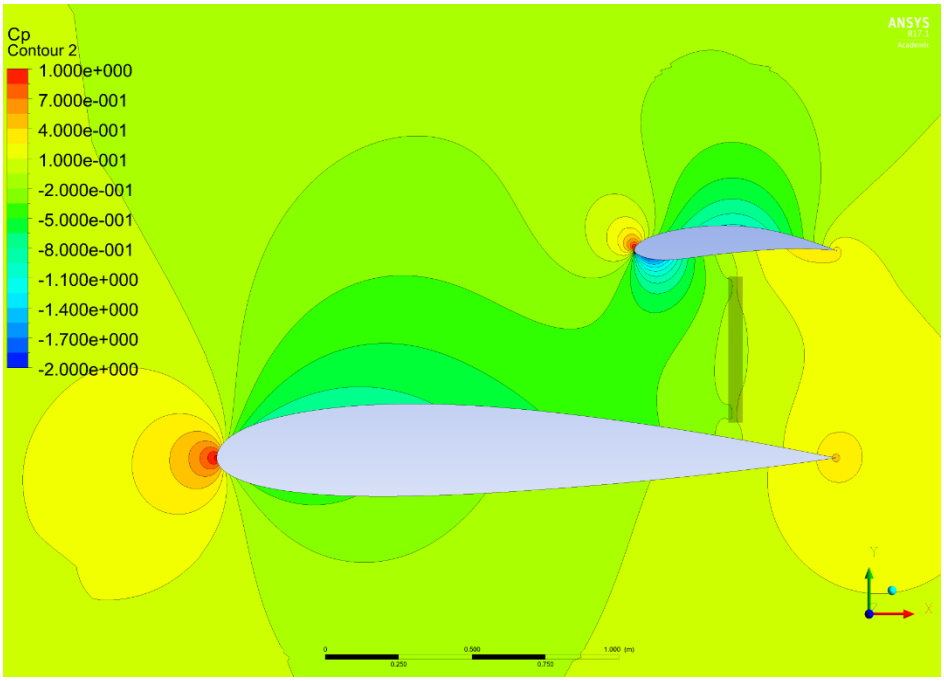

Figure A- 64: Chapter 6.2: Secondary wing's shape optimization, C_P contour, 50% spanwise position (middle of the disc), 33.5% wing spacing, 82.5% chordwise position of the propeller, optimum point of the optimization

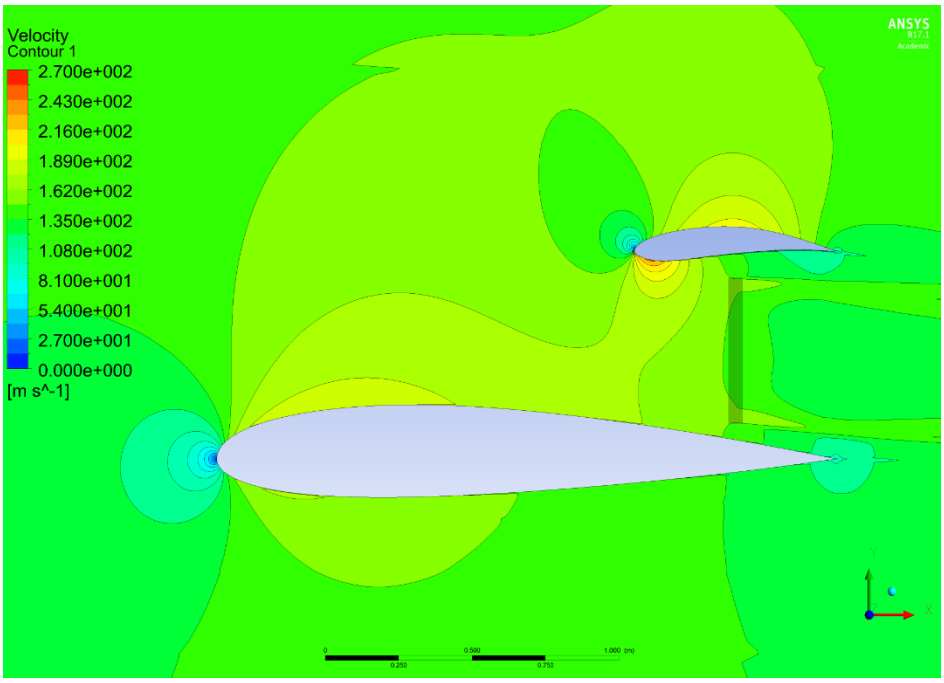

Figure A- 65: Chapter 6.2: Secondary wing's shape optimization, velocity contour, 50% spanwise position (middle of the disc), 33.5% wing spacing, 82.5% chordwise position of the propeller, optimum point of the optimization

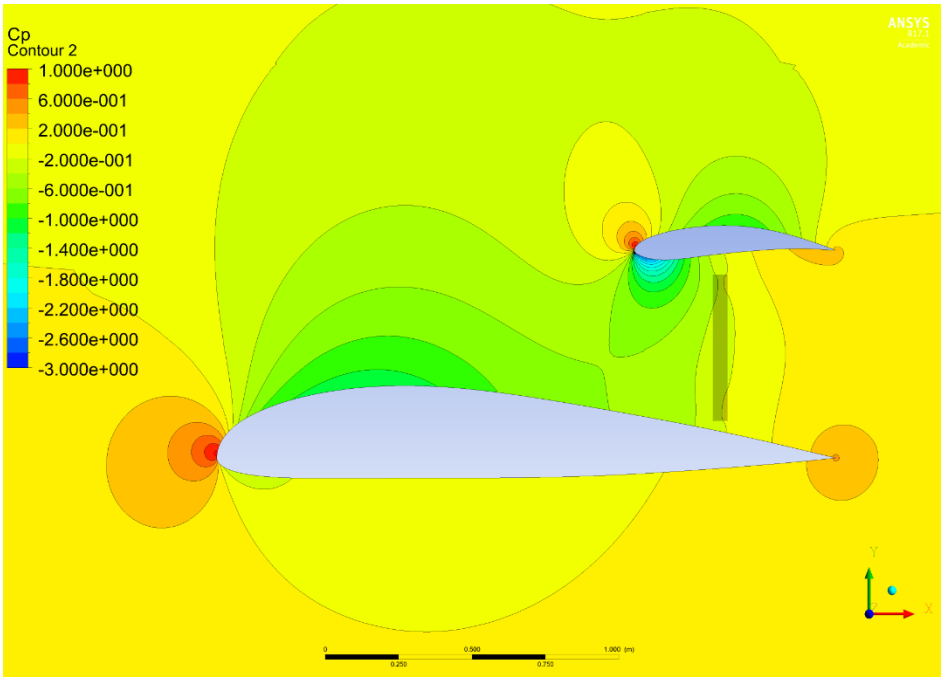

Figure A- 66: Chapter 7: Multidisciplinary design optimization, C_P contour, 50% spanwise position (middle of the disc), 33.5% wing spacing, 82.5% chordwise position of the propeller, initial point of the optimization

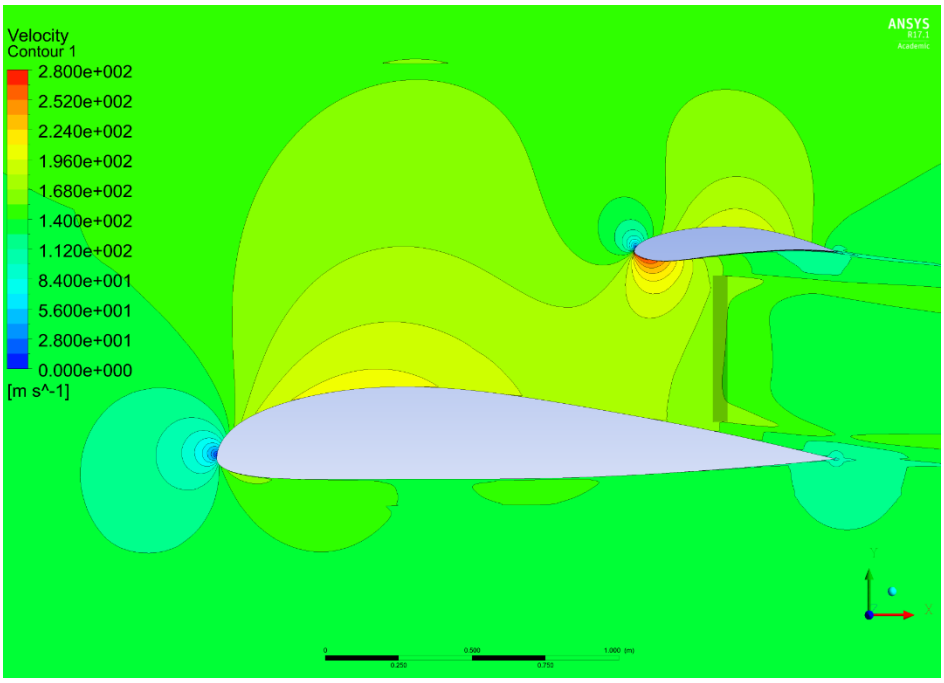

Figure A- 67: Chapter 7: Multidisciplinary design optimization, velocity contour, 50% spanwise position (middle of the disc), 33.5% wing spacing, 82.5% chordwise position of the propeller, initial point of the optimization

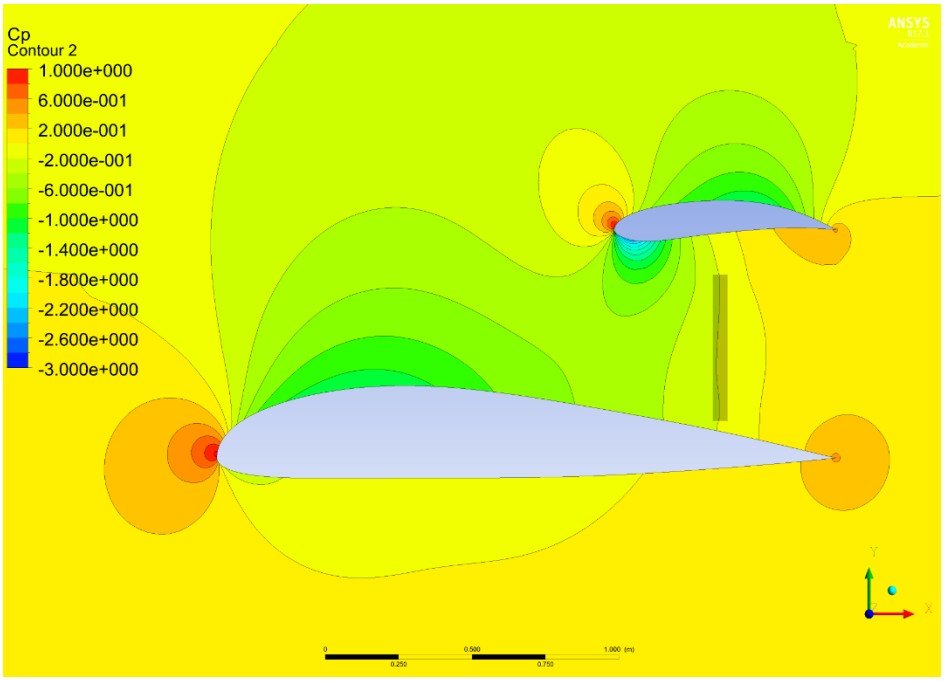

Figure A- 68: Multidisciplinary design optimization, C_P contour, 50% spanwise position (middle of the disc), 36.85% wing spacing, 82.5% chordwise position of the propeller, optimum point of the optimization

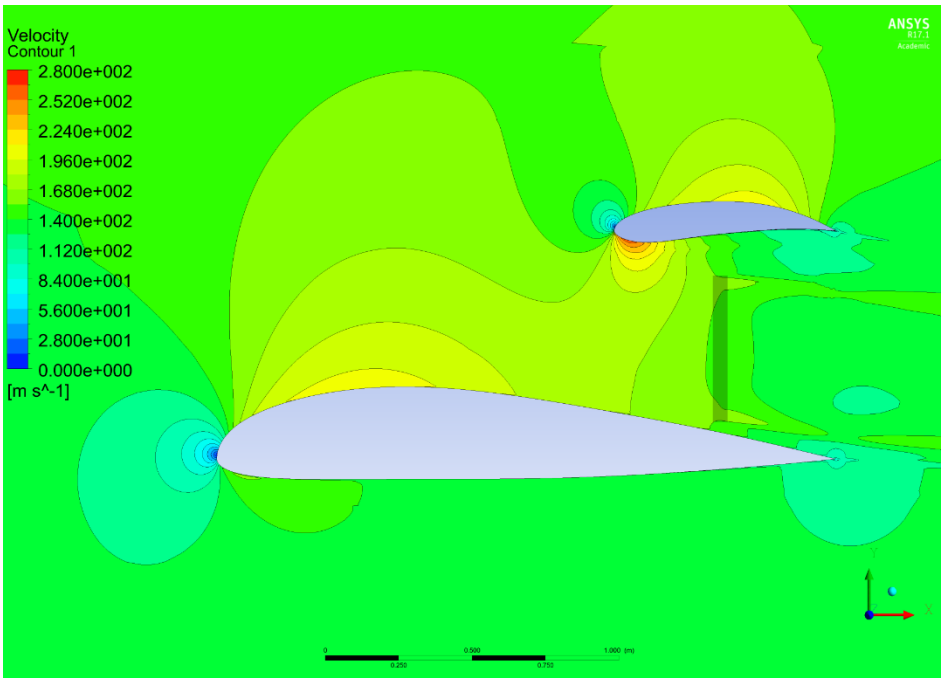

Figure A- 69: Multidisciplinary design optimization, velocity contour, 50% spanwise position (middle of the disc), 36.85% wing spacing, 82.5% chordwise position of the propeller, optimum point of the optimization

Appendix: C: Optimization studies

MDO of secondary wing's shape (Maximizing lift to drag ratio)

Table 48: Initial and final point of secondary wing's shape optimization to increase lift and decrease drag coefficient of the system simultaneously by choosing an appropriate drag coefficient of wingless aircraft $C_{D_{ATR72}} = 0.01107$

Design vector element	Initial point	Normalized	Optimized point	Normalized
CST - lower surface 1	-0.1421	1	-0.1715	1.2073
CST - lower surface 2	-0.2436	1	-0.2855	1.1719
CST - lower surface 3	0.1343	1	0.1214	0.9039
CST - lower surface 4	-0.1756	1	-0.1769	1.0078
CST - lower surface 5	0.1541	1	0.1478	0.9593
CST - lower surface 6	0.0481	1	0.0534	1.1103
CST - Upper surface 1	0.2353	1	0.2579	1.0959
CST - Upper surface 2	0.2868	1	0.2624	0.9148
CST - Upper surface 3	0.2884	1	0.2953	1.0238
CST - Upper surface 4	0.4269	1	0.4628	1.0840
CST - Upper surface 5	0.3651	1	0.3973	1.0882
CST - Upper surface 6	0.4035	1	0.5306	1.3150
Chord length*	0.3254	1	0.2766	0.8500
*Secondary wing chord length normalized by the main wing's chord length				

Parameters	Initial point	Normalized	Optimized point	Normalized
$C_{L_{tot}}$	0.554	1	0.5694	1.03
$C_{D_{tot}}$	0.001474	1	0.001446	0.98
η_{prop}	0.908	1	0.908	1
η_{pp}	0.72	1	0.7274	1.01
J	1	-	1.02	-
Main wing's Airfoil	NACA43015		NACA43015	
Secondary wing's Airfoil	Chapter 6.2		Optimized Airfoil	
x_P/C_{main}	0.8225 [-]			
s_{main}/D_P	0.04 [-]			
y_s/C_{main}	0.4 [-]			

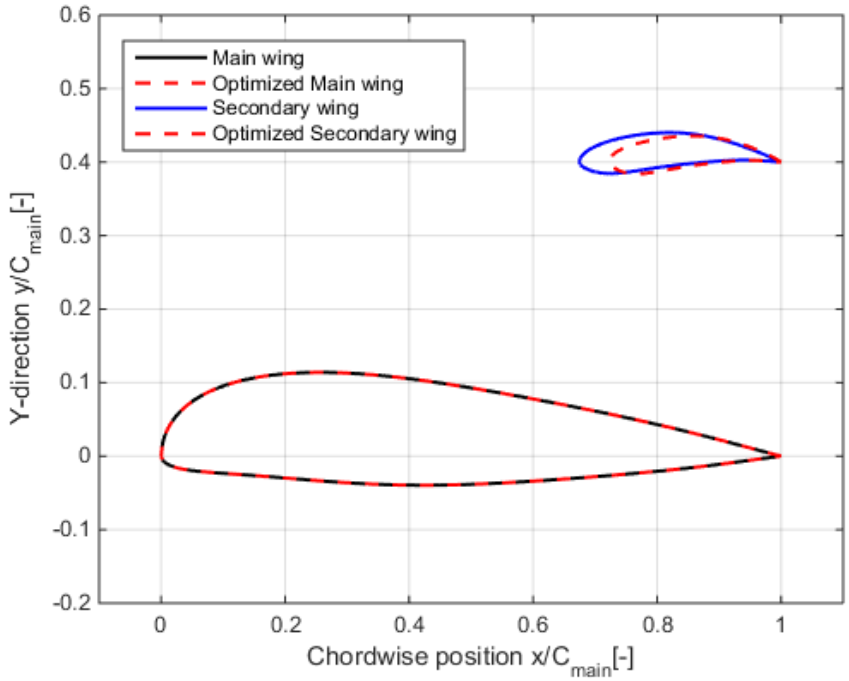

Figure A- 70: Initial and optimized cross section sketch of secondary wing's shape optimization study to increase lift and decrease drag simultaneously by choosing an appropriate drag coefficient of wingless aircraft $C_{D_{ATR72}} = 0.01107$

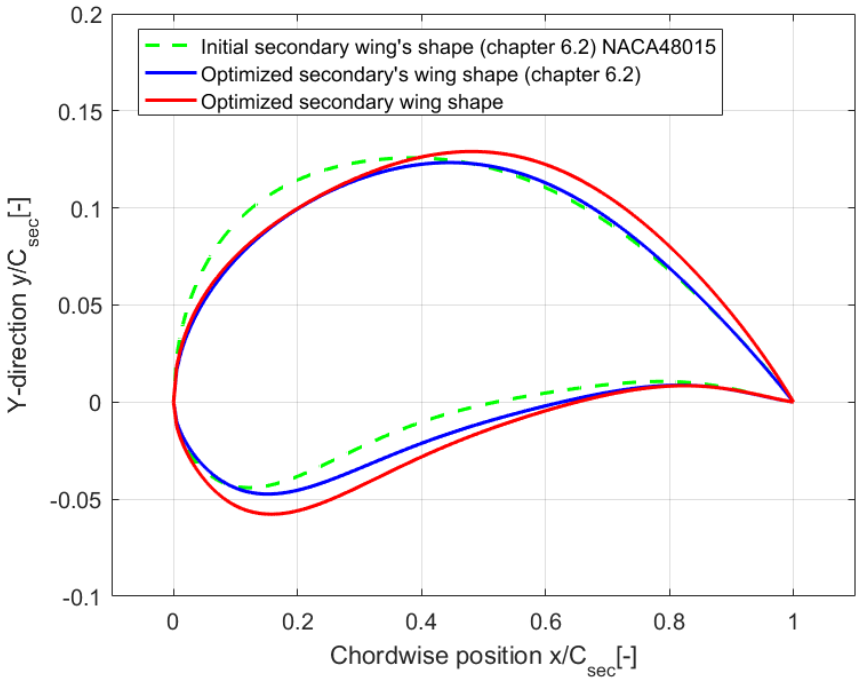

Figure A- 71: Initial and optimized shape of the secondary wing compared to the optimization study in chapter 6.2

MDO of main wing's shape (Minimizing drag)

Table 49: Initial and final point of main wing's shape optimization to decrease the total drag coefficient of system by choosing an appropriate drag coefficient of wingless aircraft $C_{D_{ATR72}} = 0$

Design vector element	Initial point	Normalized	Optimized point	Normalized
CST - lower surface 1	-0.1156	1	-0.1965	1.7000
CST - lower surface 2	0.0092	1	0.0094	1.0168
CST - lower surface 3	-0.2290	1	-0.3058	1.3353
CST - lower surface 4	-0.0220	1	-0.0228	1.0371
CST - lower surface 5	-0.1566	1	-0.1916	1.2234
CST - lower surface 6	-0.1068	1	-0.0983	0.9200
CST - Upper surface 1	0.3683	1	0.1473	0.4000
CST - Upper surface 2	0.2833	1	0.1133	0.4000
CST - Upper surface 3	0.3186	1	0.1275	0.4000
CST - Upper surface 4	0.1812	1	0.0725	0.4000
CST - Upper surface 5	0.2806	1	0.4769	1.7000
CST - Upper surface 6	0.2146	1	0.3648	1.7000

Parameters	Initial point	Normalized	Optimized point	Normalized
$C_{L_{tot}}$	0.5524	1	0.5519	0.999
$C_{D_{tot}}$	0.001452	1	-0.0007096	-
η_{prop}	0.908	1	0.916	1.01
η_{pp}	0.72	1	0.75	1.04
J	1	-	1.127	-
Main wing's Airfoil	NACA43015		Optimized Airfoil	
Secondary wing's Airfoil	Chapter 6.2		Chapter 6.2	
x_P/C_{main}	0.8225 [-]			
s_{main}/D_P	0.04 [-]			
y_s/C_{main}	0.4 [-]			

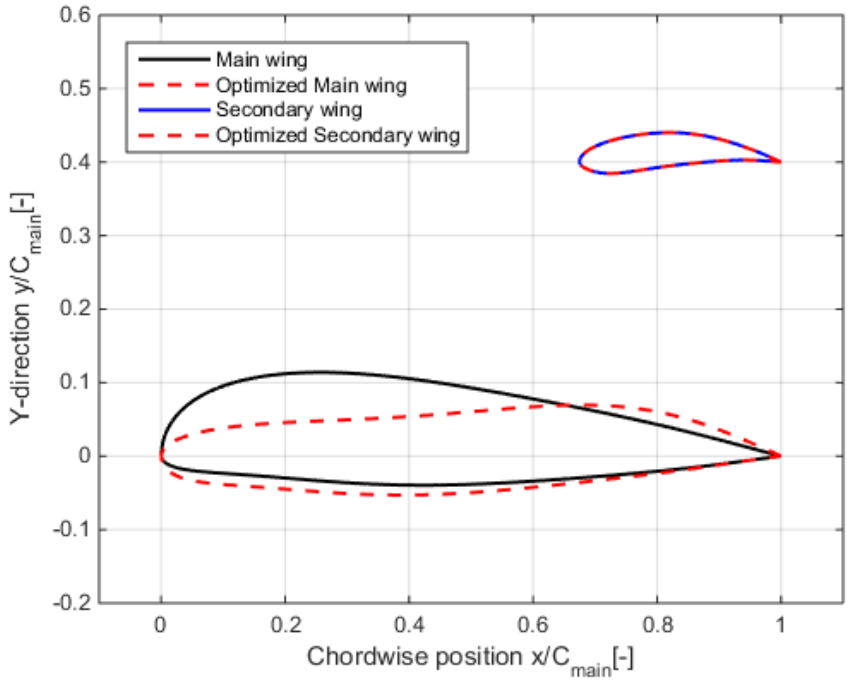

Figure A- 72: Initial and optimized cross section sketch of main wing's shape optimization study to decrease the total drag coefficient of system by choosing an appropriate drag coefficient of wingless aircraft $C_{D_{ATR72}} = 0$

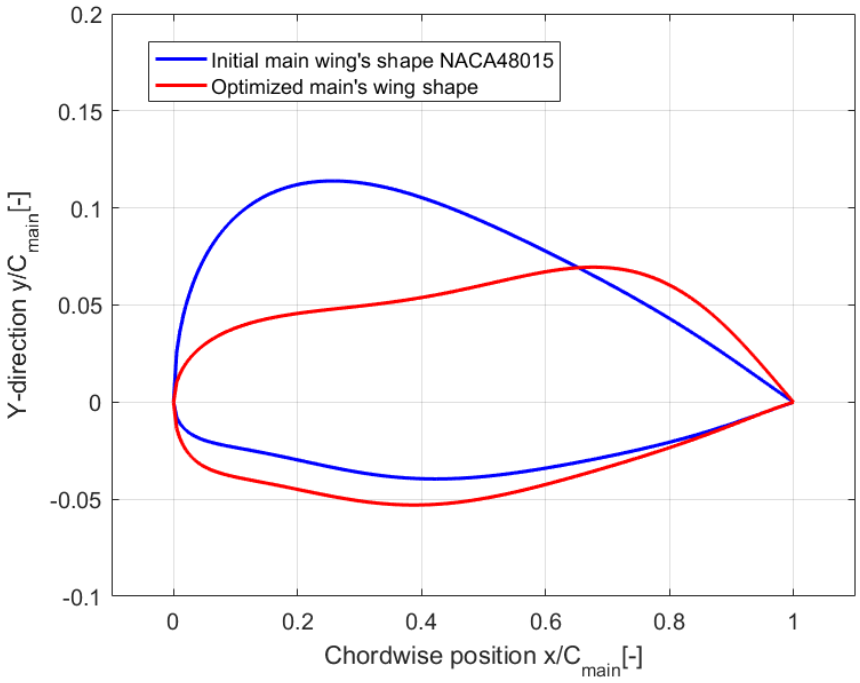

Figure A- 73: Initial and optimized shape of the main wing

MDO of main wing's shape (Maximizing lift to drag ratio)

Table 50: Initial and final point of main wing's shape optimization to increase lift and decrease drag coefficient of the system simultaneously by choosing an appropriate drag coefficient of wingless aircraft $C_{D_{ATR72}} = 0.01107$

Design vector element	Initial point	Normalized	Optimized point	Normalized
CST - lower surface 1	-0.1156	1	-0.1375	1.1895
CST - lower surface 2	0.0092	1	0.0094	1.0173
CST - lower surface 3	-0.2290	1	-0.1696	0.7405
CST - lower surface 4	-0.0220	1	-0.0217	0.9833
CST - lower surface 5	-0.1566	1	-0.1160	0.7405
CST - lower surface 6	-0.1068	1	-0.0713	0.6673
CST - Upper surface 1	0.3683	1	0.3864	1.0491
CST - Upper surface 2	0.2833	1	0.2762	0.9751
CST - Upper surface 3	0.3186	1	0.3342	1.0490
CST - Upper surface 4	0.1812	1	0.2002	1.1050
CST - Upper surface 5	0.2806	1	0.4241	1.5116
CST - Upper surface 6	0.2146	1	0.3648	1.7000

Parameters	Initial point	Normalized	Optimized point	Normalized
$C_{L_{tot}}$	0.5524	1	0.7807	1.41
$C_{D_{tot}}$	0.001452	1	0.001102	0.76
η_{prop}	0.908	1	0.9174	1.01
η_{pp}	0.72	1	0.662	0.92
J	1	-	1.18	-
Main wing's Airfoil	NACA43015		Optimized Airfoil	
Secondary wing's Airfoil	Chapter 6.2		Chapter 6.2	
x_P/C_{main}	0.8225 [-]			
s_{main}/D_P	0.04 [-]			
y_s/C_{main}	0.4 [-]			

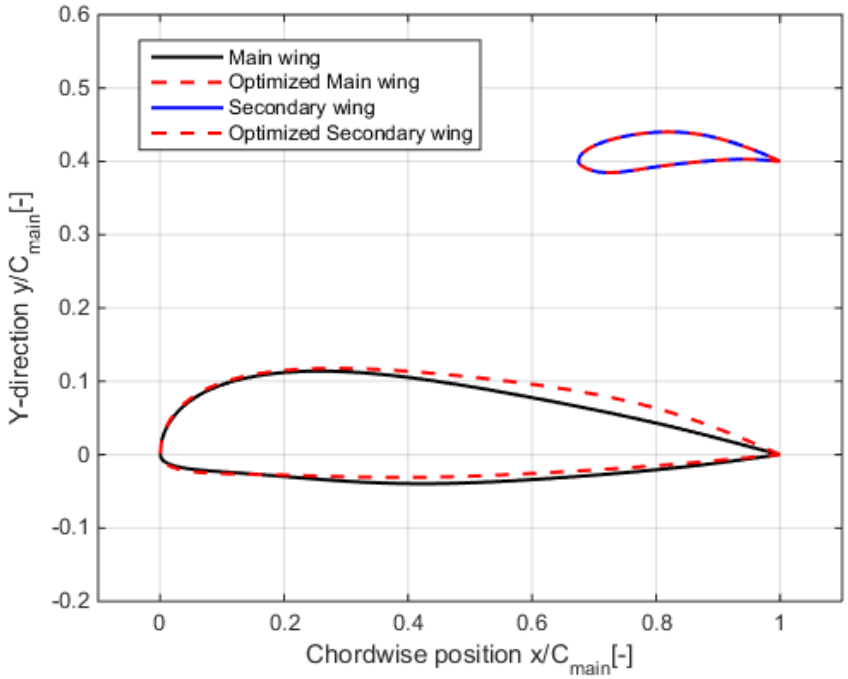

Figure A- 74: Initial and optimized cross section sketch of main wing's shape optimization study to increase lift and decrease drag coefficient of the system simultaneously by choosing an appropriate drag coefficient of wingless aircraft $C_{D_{ATR72}} = 0.01107$

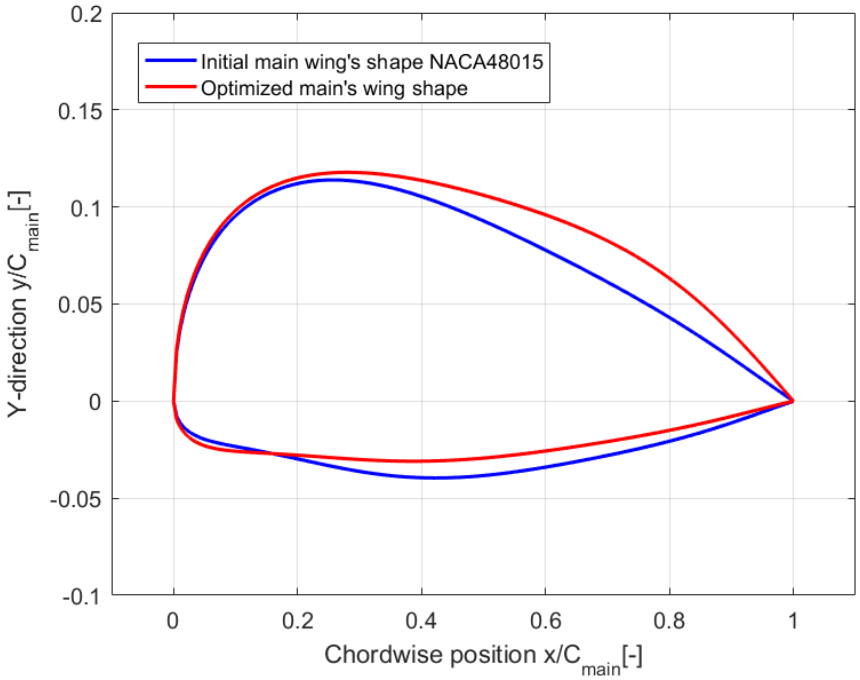

Figure A- 75: Initial and optimized shape of the main wing